


博士研究生国家奖学金申请审批表

基本情况	姓名	郝宇杰	性别	女	出生年月	1992.04
	政治面貌	党员	民族	汉	入学时间	2018.09
	学院	理学院	专业	物理学	学号	11849469
	学制	4 年	攻读学位	博士	学生类别	全日制
	是否在 2021 年 9 月 30 日前完成开题且未完成预答辩：是 <input checked="" type="checkbox"/> 否 <input type="checkbox"/>					
	身份证号					
申请理由	<p>研究生期间，在导师的指导下，我一直在各个方面严格要求自己，积极认真，努力向上，也取得了一定的成绩，总结如下：</p> <p>生活方面，我始终保持乐观的生活态度，喜欢和朋友谈心，相互鼓励。</p> <p>学习方面，成绩优良 GPA3.81，无不及格课程。对于想要了解的知识，会通过书籍、文献、网络、与他人讨论等方式，进行深入研究。</p> <p>科研方面，勤劳且爱动脑，以第一作者身份在 Physical Review X (PRX) 上发表一篇论文，该论文自 2019 年发表以来，已被引用九十多次；还以合作者身份在 Science、PRL、PRX、PRB、ACS Nano、Adv. Mater. 上发表九篇论文；目前有文章正在撰写中。同时我也积极报名参加学术会议，在 2020 年广东省物理学年会上张贴海报，并获得“三等奖”，在 2021 年第五届全国磁性材料与器件大会上做口头报告，并获得“研究生学术新锐奖”。</p> <p>实践方面，为了使实验装样更加的顺利和方便，利用绘图软件设计装样器，并利用 3D 打印机获得实物，现在一直在实验室使用中；为了使样品可以一直在一个超高真空的环境下进行转移，我们设计了一款新型多样品转移装置，并成功申请到实用新型专利。另外，在取得优异的学习成绩和科研成绩的同时，我还在实验室担任安全员，负责实验室的实验垃圾分类与回收等事情。</p> <p>综上所述，我认为自己在研究生期间认真努力，在各个方面都有所进步，未来我还会继续努力的，加油！</p> <p style="text-align: right;">申请人签名：郝宇杰</p> <p style="text-align: right;">2021 年 10 月 8 日</p>					

推荐意见	<p>郝同学在我们课题组工作期间对待科研学习工作认真刻苦，永远热情满满，还积极主动承担课题组的公共日常维护工作，积极热情的帮助组内其他成员，是我们课题组十分宝贵的一员。根据其在博士研究生期间的表现和丰硕的科研成果，我积极推荐郝宇杰同学参加这次奖学金的评定。</p> <p style="text-align: right;">推荐人（导师）签名：刘畅 2021 年 10 月 8 日</p>	
审核意见	<p>学生所在党支部意见：</p> <p>支部书记签名： 年 月 日</p>	<p>基层党委意见：</p> <p>党委书记签名（公章）： 年 月 日</p>
评审情况	<p>经评审，并在本单位内公示 5 个工作日，无异议，推荐该同学获得研究生国家奖学金。</p> <p style="text-align: right;">评审委员会主任委员签名： 年 月 日</p>	
基层单位意见	<p>经评审，并在本单位内公示 5 个工作日，无异议，本单位申报该同学获得研究生国家奖学金。现报请研究生国家奖学金评审领导小组审定。</p> <p style="text-align: right;">基层单位主管领导签名： (基层单位公章) 年 月 日</p>	
培养单位意见	<p>经审核，并在本单位公示 个工作日，无异议，现批准该同学获得研究生国家奖学金。</p> <p style="text-align: right;">(培养单位公章) 年 月 日</p>	

Southern University of Science and Technology

Transcript for PhD Students

Name	Yujie Hao	Gender	female	Date of birth	13/04/1992		
Student ID. No	11849469		Admission Date	03/09/2018			
Partner University in Joint program		Harbin Institute of Technology					
Academic Unit		Department of Physics					
Course Code	Course Title	Credit Hours	Credits	Grade	Grade Point	Note	
PHY5004	Advanced Solid State Physics	64	4	85	3.7		
PHY5031	Introduction to Microelectronic Fabrication	48	2	87	3.7		
GGC5016	Topics for Advanced Research	32	2	92	4		
GGC5003	Literature Searching and scientific Papers Writing	32	2	99	4		
GGC5021	Chinese Marxism and Contemporary	32	2	82	3.3		
PHY5006	Computational Physics	48	3	94	4		
PHY5001	Advanced Quantum Mechanics	64	4	88.72	3.7		
PHY5005	The Principles and Application of Physics Instruments	64	4	94	4		
Course credits completed/Total credits completed				23/23			
GPA	3.81						
Note	1. Courses start with GCC are required courses by the Graduate School; with ACA are required components; others are faculty/departmental courses.						

The Graduate School, Southern University of Science and Technology (Stamp)

Date: 12-25-2019



Gapless Surface Dirac Cone in Antiferromagnetic Topological Insulator MnBi_2Te_4

Yu-Jie Hao¹, Pengfei Liu¹, Yue Feng¹, Xiao-Ming Ma¹, Eike F. Schwier², Masashi Arita², Shiv Kumar^{1,2}, Chaowei Hu,³
 Rui'e Lu,¹ Meng Zeng,¹ Yuan Wang¹, Zhanyang Hao¹, Hong-Yi Sun,¹ Ke Zhang,² Jiawei Mei,¹ Ni Ni,³
 Liusuo Wu¹, Kenya Shimada², Chaoyu Chen^{1,*}, Qihang Liu,^{1,4,†} and Chang Liu^{1,‡}

¹Shenzhen Institute for Quantum Science and Engineering (SIQSE) and Department of Physics,
 Southern University of Science and Technology (SUSTech), Shenzhen, Guangdong 518055, China

²Hiroshima Synchrotron Radiation Center, Hiroshima University,
 2-313 Kagamiyama, Higashi-Hiroshima 739-0046, Japan

³Department of Physics and Astronomy and California NanoSystems Institute,
 University of California, Los Angeles, California 90095, USA

⁴Guangdong Provincial Key Laboratory for Computational Science and Material Design,
 Southern University of Science and Technology, Shenzhen, Guangdong 518055, China



(Received 10 July 2019; revised manuscript received 7 August 2019; published 21 November 2019)

The recently discovered antiferromagnetic topological insulators in the Mn-Bi-Te family with intrinsic magnetic ordering have rapidly drawn broad interest since its cleaved surface state is believed to be gapped, hosting the unprecedented axion states with a half-integer quantum Hall effect. Here, however, we show unambiguously by using high-resolution angle resolved photoemission spectroscopy that a gapless Dirac cone at the (0001) surface of MnBi_2Te_4 exists inside the bulk band gap. Such an unexpected surface state remains unchanged across the bulk Néel temperature, and is even robust against severe surface degradation, indicating additional topological protection. Through symmetry analysis and *ab initio* calculations we consider different types of surface reconstruction of the magnetic moments as possible origins giving rise to such linear dispersion. Our results unveil the experimental topological properties of MnBi_2Te_4 , revealing that the intrinsic magnetic topological insulator hosts a rich platform to realize various topological phases by tuning the magnetic or structural configurations, and thus push forward the comprehensive understanding of magnetic topological materials.

DOI: [10.1103/PhysRevX.9.041038](https://doi.org/10.1103/PhysRevX.9.041038)

Subject Areas: Condensed Matter Physics,
 Materials Science,
 Topological Insulators

I. INTRODUCTION

The integration of magnetic order and topological non-triviality has received much attention since the dawn of the topological era in condensed matter physics [1–4]. In these systems, the absence of time-reversal symmetry (\mathcal{T}) brings about a series of exotic quantum phases such as a Chern insulator [5] and axion insulator [6], leading to potential applications in the fields of spintronics and quantum computing. As a renowned example, the quantum anomalous Hall (QAH) effect in Chern insulators promises novel emergent phenomena such as Majorana fermions and

anyon statistics [7]. Another distinct topological phase is the axion insulator state, signified by a gapped surface state by magnetization but half-quantized surface Hall conductance, which was proposed to host the topological magnetoelectric effect and axion electrodynamics [6,8]. The QAH insulator was first discovered in a magnetically doped topological insulator (TI) at an ultralow temperature of 30 mK [9]. Proposals of heterostructure engineering based on magnetic insulators and TIs are also expected to realize the QAH effect through magnetic proximity effects, but are challenging in the material choice and interface fabrication [6]. On the other hand, the realization of an axion insulator requires a TI layer sandwiched by two magnetic layers whose moments point to opposite directions [10]. Though the QAH effect and the axion state have been discovered in TIs and magnetic topological heterostructures where ferromagnetically ordered moments are induced by chemical doping [9–13], an intrinsic, stoichiometric magnetic topological insulator (MTI) is highly desired in both cases, as the emerging temperatures of these macroscopic quantum states would otherwise be severely suppressed due to disorder.

*chency@sustech.edu.cn

†liuqh@sustech.edu.cn

‡liuc@sustech.edu.cn

Published by the American Physical Society under the terms of the [Creative Commons Attribution 4.0 International](https://creativecommons.org/licenses/by/4.0/) license. Further distribution of this work must maintain attribution to the author(s) and the published article's title, journal citation, and DOI.

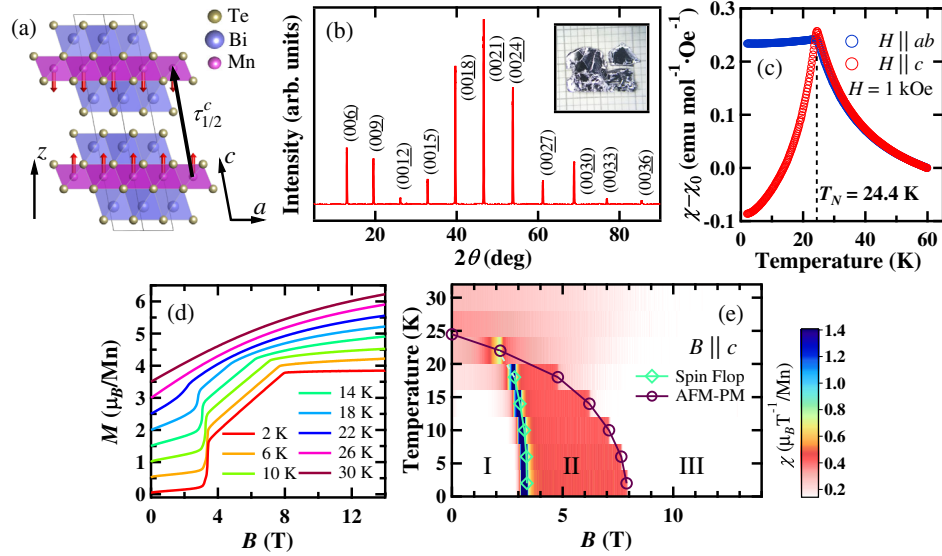


FIG. 1. Crystal characterization and magnetic responses of MnBi₂Te₄. (a) Crystal structure and A-type AFM magnetic configuration. (b) Single crystal x-ray diffraction data. Inset: Crystal against a millimeter grid. (c) Magnetization curves in two different configurations, $H \parallel ab$ and $H \parallel c$. The susceptibility at 60 K (χ_0) is subtracted. (d) Field dependence of magnetization M , measured at different T , with field along the c axis. (e) The field-temperature phase diagram with applied field along the c axis. As B increases, the system evolves from an A-type AFM state (I) to a spin-flop AFM state (II), then to a high- T PM state (III).

For both QAH insulators and axion insulators, materials that best fit the above requirement should be magnetic layered compounds having net magnetization and zero magnetization, respectively. Interestingly, both conditions can be achieved in a single material base comprising A-type antiferromagnetism (AFM) with out-of-plane magnetic moments, in which the two distinct topological phases can be switched simply by controlling the number of layers. Such a three-dimensional material base is an AFM TI characterized by a novel \mathbb{Z}_2 topological invariant protected by the product of \mathcal{T} and a half-cell translation along the c axis $\tau_{1/2}^c$, named $\mathcal{S}^c = \mathcal{T}\tau_{1/2}^c$ [14]. While layered AFM insulators like CrI₃ fulfill the magnetic structure but lack a nonzero topological invariant [15], a novel family of van der Waals layered single crystalline materials MnBi_{2n}Te_{3n+1} ($n = 1, 2, \dots$) [16,17], exemplified by MnBi₂Te₄ [18–36], has been established very recently to be stoichiometric TIs with an A-type AFM ground state. The basic magnetic building block of MnBi₂Te₄ consists of seven atomic layers that arrange as Te-Bi-Te-Mn-Te-Bi-Te [18–21], called a septuple layer (SL) [Fig. 1(a)]. Its magnetic moments in the bulk are theoretically predicted [22,23], and then confirmed by neutron diffraction experiments [24], to be ferromagnetically (FM) ordered within a Mn plane pointing along the out-of-plane z direction but antiferromagnetically aligned between adjacent Mn layers [Fig. 1(a)]. It was experimentally found that few-SL films of MnBi₂Te₄ can realize not only the axion state but a topological transition between the axion state and the QAH state when switching the number of SLs between even and odd numbers [25,26]. Furthermore, nine layers of

MnBi₂Te₄ is experimentally reported to be a higher-order Chern insulator [27]. Such rich emergent physics render MnBi₂Te₄ an ideal platform for studying the interplay between magnetism and topology.

Now that several theoretical predictions and experimental observations point to a simple A-type AFM ground state in bulk MnBi₂Te₄, there are still substantial discrepancies between the ideal scenario and realistic quantum transport behaviors. For example, while the QAH effect was predicted to appear in an odd number of MnBi₂Te₄ layers with uncompensated A-type AFM configuration, such an effect was observed experimentally only under a strong magnetic field (> 5 T) that forces the AFM ground state to a FM one [25,26]. This implies that the inherent magnetic configuration, including the magnitude, orientation, domain, and bulk-surface correspondence, adds complication to the full understanding of intrinsic MTIs such as MnBi₂Te₄. Since the key property for the realization of an axion state is the gapped Dirac cone induced by intrinsic magnetization, it is crucial to verify the existence of such a gapped surface state in bulk MnBi₂Te₄. In this paper, we profile the topological nature of MnBi₂Te₄ by our experimental discovery of the unexpected bulk-surface correspondence using high-resolution angle resolved photoemission spectroscopy (ARPES). Unlike previous theoretical predictions and experimental observations claiming a sizable magnetic gap at the (0001) surface state where \mathcal{S}^c is broken [18–20,28], we show unambiguously that there exists an X-shaped, gapless, Dirac cone at this surface, traversing the bulk band gap of MnBi₂Te₄. This state is intrinsic to the MnBi₂Te₄ crystals, reproducible in all samples we

measured, free of k_z dispersion, unchanged across the bulk magnetic ordering temperature, and is even robust against severe surface degradation. The gapped bands observed by previous works near the Dirac point, on the other hand, are proven to be of bulk nature, having clear k_z dispersion. By performing symmetry analysis and density functional theory (DFT) calculations, we attribute the origin of the observed gapless Dirac cone to surface-mediated reconstruction of magnetic moments that differ from the bulk, with the discussion of several proposed occasions including spin disorder, A-type AFM with in-plane moment and intralayer AFM. The possibility of surface structural deformation is also discussed. Our work reveals an important factor that can significantly affect the topological property of MnBi_2Te_4 , i.e., the surface magnetic or structural reconstruction, and thus brings about a more comprehensive understanding of magnetic topological materials in general.

II. CRYSTAL AND MAGNETIC PROPERTIES OF BULK MnBi_2Te_4

We begin our discussion by presenting the physical properties measured on the MnBi_2Te_4 samples used in our ARPES measurements. It is important to point out that our samples were grown by two different research groups [University of California, Los Angeles (UCLA) and Southern University of Science and Technology (SUSTech)] using slightly different growth procedures, yet the transport, magnetic, and ARPES measurements reveal quantitatively the same results, each on multiple samples, signifying the reliability and repeatability of our data. Figure 1(b) presents the single crystal x-ray diffraction data, as well as the appearance of the crystals, which agree quantitatively with those in the literature. No signal from other crystalline phases is seen. This proves that our photoemission data do not come from impurity phases.

In Figs. 1(c)–1(e) we present the magnetic measurement results, demonstrating that MnBi_2Te_4 has an AFM ground state and a rich magnetic phase diagram. Figure 1(c) shows the magnetization versus temperature curves for two different configurations, $H\parallel ab$ and $H\parallel c$. An AFM-paramagnetic (PM) transition is found at $T_N = 24.4$ K, consistent with data from other groups. Figure 1(d) illustrates the isothermal magnetizations of MnBi_2Te_4 as a function of applied field along the c axis ranging from 2 to 30 K. All the magnetization curves for $T < T_N$ show an abrupt change around the field between 2 and 3.6 T. This suggests the occurrence of a spin-flop-type transition, below which the spin direction of Mn ions turns perpendicular to the easy axis (c axis). Finally, the magnetization approaches saturation around $M = 3.8 \mu_B/\text{Mn}$ at 2 K above 8 T, well consistent with previous results [24,29,30]. The field-temperature phase diagram of MnBi_2Te_4 is depicted in Fig. 1(e). Below T_N , the critical field of the spin-flop transition B_{c1} divides the phase diagram into two regions.

At region I, MnBi_2Te_4 shows an A-type AFM order consisting of FM layers coupled antiferromagnetically along the c axis [24]. Above B_{c1} (region II), it is possible that the moments first turn perpendicular to the c axis due to the lower ground energy, then rotate continuously towards the field direction. When the critical field B_{c2} is reached, all the moments are polarized along the applied field (region III).

III. ROBUST SURFACE DIRAC CONE BY ARPES MEASUREMENTS

We show in Fig. 2 the electronic structure of MnBi_2Te_4 obtained by high-resolution ARPES experiments. Figure 2(a) illustrates a typical ARPES k - E cut through the surface zone center $\bar{\Gamma}$ we obtained with high-resolution laser ARPES [37] below T_N ($h\nu = 6.3$ eV, $T = 10$ K). Even at the first glance, one notices that there undoubtedly exists a gapless state between the electronlike and holelike conduction and valence bands, whose dispersion is even more linear than conventional TIs like Bi_2Se_3 and Bi_2Te_3 . The two branches of this state intersect at $\bar{\Gamma}$ at a binding energy of 0.290 eV, forming a prototypical Dirac cone at $\bar{\Gamma}$ without any trace of gap. This band is one of the sharpest electronic states ever seen in topological materials, with a full width half maximum (FWHM) of 0.010 \AA^{-1} (detailed in Ref. [38]). Note that an ungapped Dirac cone is also reported in Ref. [22] for few-SL films of MnBi_2Te_4 , yet the measurements there were done only at the PM state above T_N . The main purpose of the present paper is to study the spectroscopic properties of this state and to propose, based on reasonable symmetry arguments and DFT calculations, the origin of this state.

Having established the existence of the gapless Dirac state, an important question is whether this gapless band remains unchanged for all k_z 's in the Brillouin zone (i.e., it is a 2D state), or if it gradually opens a gap as k_z varies (i.e., it is a 3D state). We prove that this state is in fact a quasi-2D state with little k_z dispersion by performing a detailed photon energy dependent ARPES map from 6 to 20 eV, corresponding to $3.7 < k_z < 5.8$ (in unit of $2\pi/c$), covering more than two Brillouin zones in the k_z direction [Fig. 2(b)]. Note that the lattice constant c here represents the height of a single SL of MnBi_2Te_4 ($c = 1.37$ nm), which is about 1/3 the height of the conventional unit cell. For all k_z values within this range where the Dirac state is resolvable, we see negligible change in the (k, E) position of the Dirac band [38]. Therefore, the Dirac state behaves as a quasi-2D, surfacelike electronic state. On the other hand, the bands that form a gap at $\bar{\Gamma}$, especially the one below the Dirac band, show clear periodic dispersion along k_z [Fig. 2(b)]. As a result, the size of the $\bar{\Gamma}$ gap varies between 0.13 eV at the bulk Γ and 0.20 eV at Z [Figs. 2(c)–2(e)]. In light of this behavior, we assign this gapped band to be a bulklike electronic state.

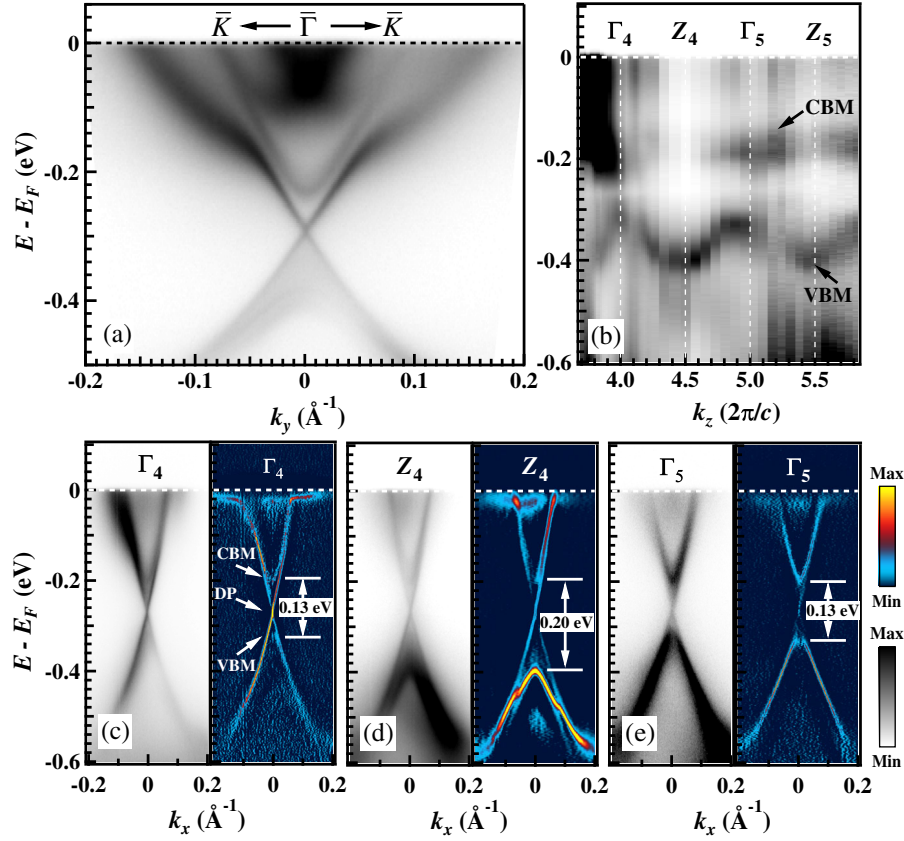


FIG. 2. Surface and bulk electronic structure of MnBi₂Te₄. (a) A typical ARPES k - E map along \bar{K} - $\bar{\Gamma}$ - \bar{K} (k_y), taken at 10 K under photon energy $h\nu = 6.3$ eV. A linear, X-shaped, gapless state exists between the valence and the conduction bands. The Dirac point (DP) energy locates at $E_D = 288$ meV for this sample. (b) k_z dispersion map at $\bar{\Gamma}$, taken with 6–20 eV photons. VBM, valence band maxima; CBM, conduction band minima. Periodic dispersion pattern on the VBM is seen clearly. The bulk Γ and Z points are determined by assigning an inner potential $V_0 = 9$ eV, estimated from the total bandwidth of the valence bands. (c)–(e) k - E maps along \bar{M} - $\bar{\Gamma}$ - \bar{M} (k_x) taken at the Γ_4 , Z_4 , and Γ_5 points marked in (b) (corresponding to $h\nu = 7.5$, 10.5, and 13.5 eV, respectively). It is clear that the gapless state forming the Dirac cone has no k_z dispersion, while the VBM evolves from -0.33 eV (Γ) to -0.4 eV (Z), consequently changing the bulk gap from 0.13 to 0.20 eV.

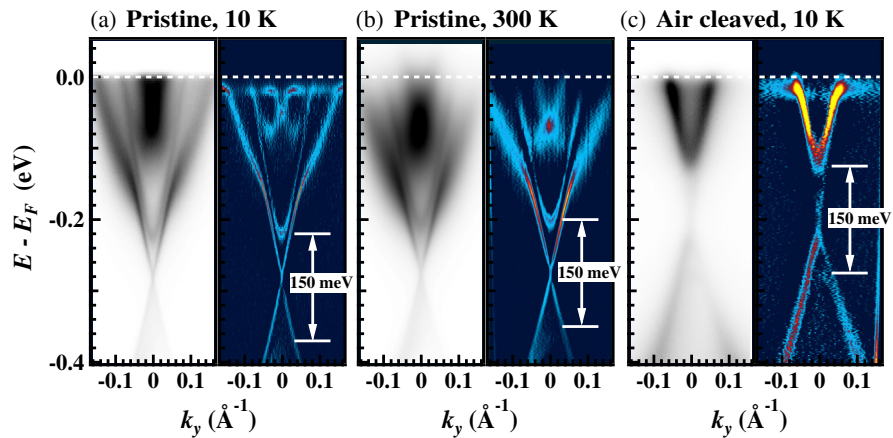


FIG. 3. Robustness of the Dirac surface state. ARPES raw (left) and second derivative (right) k - E maps taken with 6.3 eV laser light along \bar{K} - $\bar{\Gamma}$ - \bar{K} (k_y) for (a) a pristine sample cleaved and measured at 10 K (below T_N), (b) a pristine sample cleaved and measured at 300 K (well above T_N), and (c) a sample cleaved in air at room temperature, and measured at 10 K. Despite the overall carrier doping induced by different cleaving conditions, the gapless Dirac cone is clearly seen for all cases, along with an unchanged bulk band gap sized 150 meV.

Next we study whether this Dirac state remains across the magnetic transition temperature, and whether it is robust against considerable surface perturbation. Figure 3 gives positive answers to both questions. When an as-grown, pristine MnBi_2Te_4 crystal is cleaved *in situ* at 10 K (below T_N), it shows a clear ungapped Dirac cone whose Dirac point lies at $E_b = 0.28$ eV [Fig. 3(a)] [50]. In case of 6.3 eV photons, the bulk gap measures to be 150 meV. When we raise the temperature to 300 K [Fig. 3(b)], the Dirac point energy changes to $E_b = 0.27$ eV, yet the gapless nature of the Dirac band, as well as the size of the bulk gap, remains. Therefore, being in the AFM ground state or the high-temperature PM state does not seem to affect the integrity of the cone. To further test the robustness of the cone, we cleave a sample in air at room temperature before loading it into the vacuum chamber, and measure the band structure of the disturbed surface at 10 K [Fig. 3(c)]. Although the band structure becomes significantly *p* doped compared with the pristine one, the Dirac surface state is still visible, without any sign of gap opening. The bulk gap also keeps its size of 150 meV. The message here is that this Dirac state is as robust as those in prototypical nonmagnetic TIs like Bi_2Se_3 [51]. Therefore, it is highly likely that this state is topologically protected by a symmetry of the crystal.

IV. PROPOSED GAPLESS DIRAC CONE FROM DIFFERENT SURFACE MAGNETIC STRUCTURES

Next we discuss the possible physical origin of the gapless (0001) surface Dirac cone in MnBi_2Te_4 from the perspective of surface spin reorientation. For 3D magnetic-doped TIs, it is reported that the helical surface electrons can induce a FM order at the surface through Ruderman-Kittel-Kasuya-Yosida interaction even when the bulk is not magnetically ordered [52–55]. In MnBi_2Te_4 , previous neutron diffraction measurements confirmed an A-type AFM spin configuration with the magnetization along the *c* axis [24], which supports a massive surface Dirac cone if the bulk magnetic configuration remains at the surface [Fig. 4(a)]. Therefore, our results suggest that the surface-mediated spin configuration at the few top layers differs from that in the bulk state, hosting topology-protected gapless surface states which can be detected by our surface-sensitive ARPES technique. In the following we consider several possible magnetic states of the surface layers that can support the linear-dispersed, gapless surface Dirac cone, and then discuss their chance of happening based on the current experimental observations and our corresponding total energy calculations. They are summarized in Figs. 4(b)–4(d) and Table I.

Before proposing the possibilities, we make a basic assumption that the gapless surface states are protected by \mathcal{T} , crystalline symmetry, or their combinations. Starting from nonmagnetic MnBi_2Te_4 having the same space group of Bi_2Te_3 ($R\bar{3}m$), there are in total five types of symmetry operations, i.e., threefold rotation along the *z* axis \mathcal{C}_{3z} ,

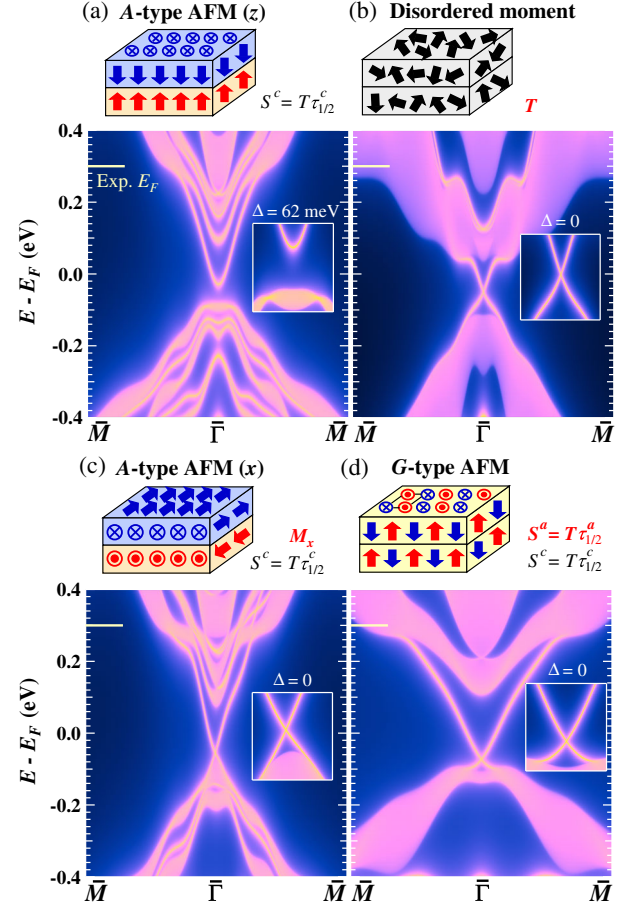


FIG. 4. DFT-calculated surface states of MnBi_2Te_4 for four prototypical magnetic configurations. (a) A-type AFM with the magnetic moments along the *z* axis, (b) disordered magnetic moments, (c) A-type AFM with the magnetic moments along the *x* axis, and (d) G-type AFM. The top drawing in each panel specifies the magnetic configuration and the symmetries that preserve in bulk (black) and (0001) surface (red). \mathcal{T} , time reversal; $\tau_{1/2}^i$ ($i = a, b, c$), half-cell translation along *i*; \mathcal{M} , mirror plane.

twofold rotation along the *x* axis \mathcal{C}_{2x} , inversion \mathcal{I} , rotoinversion $\mathcal{S}_{6z} = \mathcal{C}_{3z}\mathcal{I}$, and mirror symmetry $\mathcal{M}_x = \mathcal{C}_{2x}\mathcal{I}$. At the (0001) surface of MnBi_2Te_4 , since \mathcal{C}_2 , \mathcal{I} , and \mathcal{S}_6 symmetries are broken, the point group is reduced to \mathcal{C}_{3v} . Therefore, when we take the local magnetic moment of Mn atoms into account, the symmetry preserved at this surface can only be \mathcal{C}_{3z} , \mathcal{M}_x , in-plane translation symmetry τ_{ab} , \mathcal{T} and their combinations, i.e., $\mathcal{C}_{3z}\mathcal{T}$, $\mathcal{M}_x\mathcal{T}$, and $\tau_{ab}\mathcal{T}$. We thus expect that the observed gapless surface Dirac cone is protected by one of these symmetries. Such a symmetry \mathcal{G} should fulfill $\mathcal{G}^2 = -1$ in our spin-1/2 systems for at least certain high-symmetry points in the *k* space, resulting in Kramers degeneracy and nontrivial topological classification. While high-order topology and gapless hinge or edge states can be protected by symmetry operations like threefold axis [56], $\mathcal{M}_x\mathcal{T}$, \mathcal{C}_{3z} , and $\mathcal{C}_{3z}\mathcal{T}$ are excluded in our following analysis because they do not support gapless

TABLE I. Properties of MnBi_2Te_4 with different magnetic configurations considered in our work, including the calculated total energy with respect to the magnetic structure of ground state, i.e., A-type AFM (z) configuration, the gap size of surface states (E_g), the topological classification, and the corresponding symmetry. The number in parentheses is the square of the symmetry operation. NM, nonmagnetic; MCN, mirror Chern number.

Phase	Energy (meV/Mn)	Surface E_g (meV)	Topological classification	Symmetry
A-type AFM (z)	0.00	62	\mathbb{Z}_2	$\mathcal{S}^c (-e^{-2ik\tau_{1/2}^c})$
A-type AFM (y)	0.41	0.3
A-type AFM (x)	0.41	0	MCN	$\mathcal{M}_x (-1)$
G-type AFM	8.34	0	\mathbb{Z}_2	$\mathcal{S}^a (-e^{-2ik\tau_{1/2}^a})$
C-type AFM	8.38	0	\mathbb{Z}_2	$\mathcal{S}^a (-e^{-2ik\tau_{1/2}^a})$
PM	5.73	0	\mathbb{Z}_2	$\mathcal{T} (-1)$
NM	4.12×10^3	0	\mathbb{Z}_2	$\mathcal{T} (-1)$

surface states [57]. Hence, the remaining symmetry operations are \mathcal{T} , \mathcal{M}_x , and $\tau_{ab}\mathcal{T}$.

The first possibility is that the ordered spin in the bulk state may show fragility at the surface layers, leading to a lower transition temperature and a PM state with spin disorder. In this case, the electron hopping and magnetic moment decouple with each other and \mathcal{T} symmetry is restored, leading to a gapless surface Dirac cone from a 3D \mathcal{T} -preserved TI. To obtain the total energy of such a PM state, we use a 4×4 supercell with special quasirandom structures to simulate the spin disorder effect [58]. Such an approach provides the best choice of randomness for a finite-size supercell in guaranteeing the best match of correlation functions of the infinite alloy, and thus can be applied in both cases of composition disorder and spin disorder. The total energy of such a magnetic configuration is found to be 5.7 meV/Mn compared with the ground state.

Without ordered magnetization, the model Hamiltonian for a single surface of MnBi_2Te_4 can be written up to the third order as $H = H_1 + H_3$. The first term H_1 is the well-known surface Rashba term,

$$H_1 = \alpha_1(k_x\sigma_y - k_y\sigma_x), \quad (1)$$

where σ is the Pauli matrix for spin degree of freedom. H_3 is the cubic- k term written as

$$H_3 = \alpha_2[(k_x^2 + k_y^2)k_x\sigma_y - (k_y^2 + k_x^2)k_y\sigma_x] + \alpha_3(k_x^2 - 3k_y^2)k_x\sigma_z, \quad (2)$$

which is derived from the $k \cdot p$ perturbation by considering all the possible k -polynomial terms that respect the crystal symmetry [59]. The basis used for this $k \cdot p$ model is the $m_j = \pm 1/2$ states belonging to the representation $E_{1/2}$ [60], because the bulk bands near the Fermi level are mainly contributed by Te- p_z and Bi- p_z orbitals with $l = 1$ and $m_l = 0$. The Hamiltonian H apparently supports a

gapless Dirac cone at the $\bar{\Gamma}$ point. Figure 4(b) shows the gapless surface Dirac cone of nonmagnetic MnBi_2Te_4 calculated by DFT as an approximation of the PM state, indicating a 3D \mathcal{T} -preserved TI. A careful comparison between ARPES data and DFT calculation reveals good consistency for the spin disorder scenario [38], which also explains the observed almost unchanged band structure with the temperature across the transition point of 24 K, and the robustness of the surface Dirac cone against severe degradation.

The second possible type of symmetry that can protect the gapless surface state is the mirror symmetry. In this case, we begin with A-type AFM with in-plane magnetic moment that is perpendicular to one mirror plane \mathcal{M}_x [because of \mathcal{C}_{3z} , there are three equivalent mirror planes at the (0001) surface]. Such a configuration needs to overcome only a small magnetic anisotropy energy compared with the magnetic ground state, i.e., 0.4 meV/Mn. In this case, MnBi_2Te_4 is calculated to be an AFM TI and an \mathcal{M}_x -protected AFM topological crystalline insulator (TCI) with nontrivial mirror Chern number (MCN)—in other words, a dual AFM TI. This is analogous to Bi_2Se_3 as a nonmagnetic dual TI [61]. As a result, the TCI phase gives rise to a gapless Dirac cone slightly off the $\bar{\Gamma}$ point, as shown in Fig. 4(c). In MnBi_2Te_4 the shift is 0.005 \AA^{-1} along the k_y direction that is perpendicular to the magnetic moment. Note that if this is realized at the surface, and the sizes of the magnetic domains having opposite magnetic moments are smaller than the size of the ARPES incident beam ($\sim 10 \mu\text{m}$ for laser ARPES), we would expect a doubling of the Dirac cone surface states with momentum separation 0.01 \AA^{-1} , which is marginally detectable under the momentum resolution of our ARPES data. The fact that this is not observed in our dataset would indicate either the absence of in-plane A-type AFM at the surface or magnetic domains that are significantly larger than $\sim 10 \mu\text{m}$.

We next consider the magnetic moment along a more general in-plane direction. Without the protection of mirror

symmetry, we can expect a gap opening at the (0001) surface. This can be understood by adding a magnetization-induced Zeeman term $H_{\text{mag}} = g\mathbf{B} \cdot \boldsymbol{\sigma}$ with in-plane magnetic field to the nonmagnetic Hamiltonian H [see Eqs. (1)–(2)]. If H_3 is omitted, $H_1 + H_{\text{mag}}$ will lead to the shift of the Dirac point perpendicular to the direction of the magnetic moment without a gap opening. On the other hand, adding H_{mag} to $H = H_1 + H_3$ will open a gap at the Dirac cone because the inclusion of the high-order term H_3 introduces a hexagonal warping term σ_z that tilts the spin out of the plane [59,61]. Only if \mathbf{B} is perpendicular to one of the mirror planes ($k_x = 0$ or $k_x = \pm\sqrt{3}k_y$), the σ_z term vanishes at the shifted Dirac point and the gapless Dirac cone retains. As shown in Table I, the features of the surface band gaps with different in-plane magnetic moment derived from the model Hamiltonian are consistent with our DFT calculation. However, our DFT calculation reveals that the size of the gap induced by the high-order term H_3 is as small as ~ 0.3 meV, which is negligible within the resolution of ARPES. Hence, a general A-type AFM configuration with in-plane magnetic moment is also compatible with our experimental observation. Since the total energies for A-type AFM with different in-plane spin orientations are almost the same, we suggest that the surface layers of real samples probably consist of magnetic domains with different in-plane FM spin moments.

The third type of symmetry is the combination of \mathcal{T} and translation symmetry τ_{ab} . This type of symmetry requires intralayer AFM spin configuration, exemplified by the G-type AFM where both intralayer and interlayer alignment of magnetic moments are AFM, as shown in Fig. 4(d). In such a magnetic configuration there exist $S^i = \mathcal{T}\tau_{1/2}^i$ symmetries along all the three lattice vectors $i = a, b, c$ that correspond to two independent elements S^a and S^c in the magnetic space group (S^a and S^b are equivalent elements). The square of S^i equals to -1 at certain time-reversal invariant momenta that meet the requirement $k\tau_{1/2}^i = n\pi$, leading to two \mathbb{Z}_2 invariants in this system. Since the only band inversion occurs at the Γ point in G-type AFM MnBi_2Te_4 , all three topological invariants are nontrivial, giving rise to a gapless Dirac cone at the (0001) surface because S^a remains invariant at this surface. Similarly, some other magnetic configurations with in-plane AFM alignment, such as C-type AFM, also host a gapless (0001) surface state protected by S^a symmetry with in-plane fractional translation. However, our DFT calculations show that forming intralayer AFM alignment in the surface layers needs to overcome the favored intralayer FM exchange coupling in the bulk, leading to a large energy cost of about 8.3 meV/Mn [38]. Furthermore, if the intralayer AFM is realized at the surface, the in-plane Fermi surface should exhibit a band folding effect, which is not observed by our ARPES measurements. Overall, to obtain the direct evidence for addressing the origin of the gapless feature, it is

crucial to involve surface-sensitive detection, such as x-ray magnetic circular dichroism and the NV center technique, to determine the surface magnetic structure of such intrinsic magnetic TI in the future.

V. DISCUSSION AND CONCLUSION

Apart from the possible origins of the gapless surface Dirac cone due to surface spin reorientation in ideal MnBi_2Te_4 single crystals, we briefly discuss the possibility of structural deformation owing to the sample imperfection that could also hint at the deviation of the electronic structure between ARPES measurements and the theoretical calculations based on A-type AFM magnetic configuration. For example, the MnBi_2Te_4 thin film could be grown by coevaporating Mn and Te elements onto a Bi_2Te_3 surface, corresponding to the coverage of a MnTe layer [21]. Although the Mn^{2+} ion is energetically favorable to intercalate into the central layer of a MnBi_2Te_4 SL, the growing condition determines the existence of cation mixing between Mn and Bi, or antisite defects [20]. Such an occasion would lead to disordered Mn distribution when approaching the surface layers as well as magnetic disorder. In addition, it is reported that the synthetic MnBi_2Te_4 tends to experience a decomposition into Bi_2Te_3 and MnTe_2 phases at a higher temperature [35]. Taking into account the surface potential, the surface MnBi_2Te_4 layer might also suffer structural reconstruction or dislocation, such as decaying to a Bi_2Te_3 layer, rendering different band dispersions compared with an ideal MnBi_2Te_4 surface. Finally, the imperfect crystal could lead to a number of ferromagnetic domains of which the moments point to different directions, contributing different values of the Zeeman term $H_{\text{mag}} = g\mathbf{B} \cdot \boldsymbol{\sigma}$. As a result, the measurable topological surface states could be compensated by the synergetic effect of different domains.

In summary, we demonstrate unambiguously by systematic ARPES measurements that MnBi_2Te_4 is not an ideal AFM TI. A gapless surface Dirac cone exists experimentally in single crystal MnBi_2Te_4 , hosting massless Dirac quasiparticles. The Dirac cone is found to be quasi-2D and stable under massive surface absorbents; the bulk and surface electronic structures show no observable change across the bulk magnetic transition temperature. Our first principles calculation further identifies several magnetic configurations that could yield such a gapless topological state. It is important to note that such reconstruction might not be limited only in MnBi_2Te_4 , but in a group of other intrinsic magnetic topological materials, because several competing phases with different structural or magnetic orders could have small energy differences and thus are sensitive to surrounding environments and the presence of surface termination. Therefore, our research also sheds light on other magnetic topological materials, revealing that nature deals with AFM TIs in a more intricate way than previously thought. Motivated by our results, the theme of

future works should be finding a way to overcome such surface reconstruction in favor of the long-sought axion insulators, or make use of such reconstruction to build devices with novel transport phenomena. Taken collectively, our discovery of the unexpected massless Dirac quasiparticles in an AFM TI indicates a space-varying magnetic structure more complex than previously assigned in these materials, brings about a more complete description of magnetic topological systems, and paves the way for the exploration of the interplay of massive and massless Dirac particles in a single material platform.

ACKNOWLEDGMENTS

We thank Jieming Sheng, Yue Zhao, Haizhou Lu, Jianpeng Liu, Weiqiang Chen, and Dapeng Yu for helpful discussions. ARPES experiments were performed with the approval of the Hiroshima Synchrotron Radiation Center (HSRC), Hiroshima, Japan under Proposals No. 19AG014 and No. 19AG004. Work at SUSTech was supported by the National Natural Science Foundation of China (NSFC) (No. 11504159, No. 11674149, and No. 11874195), NSFC Guangdong (No. 2016A030313650), the Guangdong Innovative and Entrepreneurial Research Team Program (No. 2016ZT06D348 and No. 2017ZT07C062), the Guangdong Provincial Key Laboratory of Computational Science and Material Design (Grant No. 2019B030301001), the Shenzhen Key Laboratory (Grant No. ZDSYS20170303165926217), and the Technology and Innovation Commission of Shenzhen Municipality (Grants No. JCYJ20150630145302240 and No. KYTDP20181011104202253). Work at UCLA was supported by the U.S. Department of Energy (DOE), Office of Science, Office of Basic Energy Sciences under Award No. DE-SC0011978.

Y.-J. H., P. L., and Y. F. contributed equally to this work.

Note added.—Recently, we became aware of similar studies [62–64] reporting gapless Dirac topological surface states in MnBi_2Te_4 .

-
- [1] Y. L. Chen *et al.*, *Massive Dirac Fermion on the Surface of a Magnetically Doped Topological Insulator*, *Science* **329**, 659 (2010).
 - [2] S.-Y. Xu *et al.*, *Hedgehog Spin Texture and Berry's Phase Tuning in a Magnetic Topological Insulator*, *Nat. Phys.* **8**, 616 (2012).
 - [3] Y. Tokura, K. Yasuda, and A. Tsukazaki, *Magnetic Topological Insulators*, *Nat. Rev. Phys.* **1**, 126 (2019).
 - [4] N. P. Armitage and L. Wu, *On the Matter of Topological Insulators as Magnetoelectrics*, *SciPost Phys.* **6**, 046 (2019).
 - [5] N. Regnault and B. A. Bernevig, *Fractional Chern Insulator*, *Phys. Rev. X* **1**, 021014 (2011).
 - [6] X.-L. Qi, T. L. Hughes, and S.-C. Zhang, *Topological Field Theory of Time-Reversal Invariant Insulators*, *Phys. Rev. B* **78**, 195424 (2008); *Erratum*, *Phys. Rev. B* **81**, 159901(E) (2010).
 - [7] R. Yu, W. Zhang, H.-J. Zhang, S.-C. Zhang, X. Dai, and Z. Fang, *Quantized Anomalous Hall Effect in Magnetic Topological Insulators*, *Science* **329**, 61 (2010).
 - [8] C. Fang, M. J. Gilbert, and B. A. Bernevig, *Bulk Topological Invariants in Noninteracting Point Group Symmetric Insulators*, *Phys. Rev. B* **86**, 115112 (2012).
 - [9] C.-Z. Chang *et al.*, *Experimental Observation of the Quantum Anomalous Hall Effect in a Magnetic Topological Insulator*, *Science* **340**, 167 (2013).
 - [10] D. Xiao *et al.*, *Realization of the Axion Insulator State in Quantum Anomalous Hall Sandwich Heterostructures*, *Phys. Rev. Lett.* **120**, 056801 (2018).
 - [11] J. G. Checkelsky, R. Yoshimi, A. Tsukazaki, K. S. Takahashi, Y. Kozuka, J. Falson, M. Kawasaki, and Y. Tokura, *Trajectory of the Anomalous Hall Effect towards the Quantized State in a Ferromagnetic Topological Insulator*, *Nat. Phys.* **10**, 731 (2014).
 - [12] X. Kou *et al.*, *Scale-Invariant Quantum Anomalous Hall Effect in Magnetic Topological Insulators beyond the Two-Dimensional Limit*, *Phys. Rev. Lett.* **113**, 137201 (2014); *Erratum* **113**, 199901 (2014).
 - [13] C.-Z. Chang, W. Zhao, D. Y. Kim, H. Zhang, B. A. Assaf, D. Heiman, S.-C. Zhang, C. Liu, M. H. W. Chan, and J. S. Moodera, *High-Precision Realization of Robust Quantum Anomalous Hall State in a Hard Ferromagnetic Topological Insulator*, *Nat. Mater.* **14**, 473 (2015).
 - [14] R. S. K. Mong, A. M. Essin, and J. E. Moore, *Antiferromagnetic Topological Insulators*, *Phys. Rev. B* **81**, 245209 (2010).
 - [15] B. Huang *et al.*, *Layer-Dependent Ferromagnetism in a van der Waals Crystal Down to the Monolayer Limit*, *Nature (London)* **546**, 270 (2017).
 - [16] Z. S. Aliev *et al.*, *Novel Ternary Layered Manganese Bismuth Tellurides of the $\text{MnTe-Bi}_2\text{Te}_3$ System: Synthesis and Crystal Structure*, *J. Alloys Compd.* **789**, 443 (2019).
 - [17] H. Sun, B. Xia, Z. Chen, Y. Zhang, P. Liu, Q. Yao, H. Tang, Y. Zhao, H. Xu, and Q. Liu, *Rational Design Principles of Quantum Anomalous Hall Effect from Superlattice-like Magnetic Topological Insulators*, *Phys. Rev. Lett.* **123**, 096401 (2019).
 - [18] S. H. Lee *et al.*, *Spin Scattering and Noncollinear Spin Structure-Induced Intrinsic Anomalous Hall Effect in Antiferromagnetic Topological Insulator MnBi_2Te_4* , *Phys. Rev. Res.* **1**, 012011 (2019).
 - [19] M. M. Otrokov *et al.*, *Prediction and Observation of the First Antiferromagnetic Topological Insulator*, *arXiv:1809.07389*.
 - [20] A. Zeugner *et al.*, *Chemical Aspects of the Candidate Antiferromagnetic Topological Insulator MnBi_2Te_4* , *Chem. Mater.* **31**, 2795 (2019).
 - [21] Y. Gong *et al.*, *Experimental Realization of an Intrinsic Magnetic Topological Insulator*, *Chin. Phys. Lett.* **36**, 076801 (2019).
 - [22] J. Li, C. Wang, Z. Zhang, B. L. Gu, W. Duan, and Y. Xu, *Magnetically Controllable Topological Quantum Phase*

- Transitions in the Antiferromagnetic Topological Insulator MnBi₂Te₄*, *Phys. Rev. B* **100**, 121103(R) (2019).
- [23] M. M. Otrokov, I. P. Rusinov, M. Blanco-Rey, M. Hoffmann, A. Yu. Vyazovskaya, S. V. Eremin, A. Ernst, P. M. Echenique, A. Arnau, and E. V. Chulkov, *Unique Thickness-Dependent Properties of the van der Waals Interlayer Antiferromagnet MnBi₂Te₄ Films*, *Phys. Rev. Lett.* **122**, 107202 (2019).
- [24] J.-Q. Yan, Q. Zhang, T. Heitmann, Z. Huang, K. Y. Chen, J.-G. Cheng, W. Wu, D. Vaknin, B. C. Sales, and R. J. McQueeney, *Crystal Growth and Magnetic Structure of MnBi₂Te₄*, *Phys. Rev. Mater.* **3**, 064202 (2019).
- [25] Y.-J. Deng *et al.*, *Magnetic-Field-Induced Quantized Anomalous Hall Effect in Intrinsic Magnetic Topological Insulator MnBi₂Te₄*, *arXiv:1904.11468*.
- [26] C. Liu *et al.*, *Quantum Phase Transition from Axion Insulator to Chern Insulator in MnBi₂Te₄*, *arXiv:1905.00715*.
- [27] J. Ge *et al.*, *High-Chern-Number and High-Temperature Quantum Hall Effect without Landau Levels*, *arXiv:1907.09947*.
- [28] R. C. Vidal, H. Bentmann, T. R. F. Peixoto, A. Zeugner, S. Moser, C. H. Min, S. Schatz, K. Kissner, M. Unzelmann, C. I. Fornari *et al.*, *Surface States and Rashba-Type Spin Polarization in Antiferromagnetic MnBi₂Te₄*, *Phys. Rev. B* **100**, 121104(R) (2019).
- [29] J.-Q. Yan, S. Okamoto, M. A. McGuire, A. F. May, R. J. McQueeney, and B. C. Sales, *Evolution of Structural, Magnetic and Transport Properties in MnBi_{2-x}Sb_xTe₄*, *Phys. Rev. B* **100**, 104409 (2019).
- [30] C.-W. Hu *et al.*, *A van der Waals Antiferromagnetic Topological Insulator with Weak Interlayer Magnetic Coupling*, *arXiv:1905.02154*.
- [31] B. Chen *et al.*, *Intrinsic Magnetic Topological Insulator Phases in the Sb Doped MnBi₂Te₄ Bulks and Thin Flakes*, *Nat. Commun.* **10**, 4469 (2019).
- [32] J. Cui, M. Shi, H. Wang, F. Yu, T. Wu, X. Luo, J. Ying, and X. Chen, *Transport Properties of Thin Flakes of the Antiferromagnetic Topological Insulator MnBi₂Te₄*, *Phys. Rev. B* **99**, 155125 (2019).
- [33] D. Zhang, M. Shi, T. Zhu, D. Xing, H. Zhang, and J. Wang, *Topological Axion States in Magnetic Insulator MnBi₂Te₄ with the Quantized Magnetoelectric Effect*, *Phys. Rev. Lett.* **122**, 206401 (2019).
- [34] J.-H. Li, Y. Li, S. Du, Z. Wang, B.-L. Gu, S.-C. Zhang, K. He, W. Duan, and Y. Xu, *Intrinsic Magnetic Topological Insulators in van der Waals Layered MnBi₂Te₄-Family Materials*, *Sci. Adv.* **5**, eaaw5685 (2019).
- [35] D. S. Lee, T.-H. Kim, C.-H. Park, C.-Y. Chung, Y. S. Lim, W.-S. Seo, and H.-H. Park, *Crystal Structure, Properties and Nanostructuring of a New Layered Chalcogenide Semiconductor, Bi₂MnTe₄*, *CrystEngComm* **15**, 5532 (2013).
- [36] J.-Z. Wu *et al.*, *Natural van der Waals Heterostructures with Tunable Magnetic and Topological States*, *arXiv:1905.02385*.
- [37] H. Iwasawa, E. F. Schwier, M. Arita, A. Ino, H. Namatame, M. Taniguchi, Y. Aiura, and K. Shimada, *Development of Laser-Based Scanning μ -ARPES System with Ultimate Energy and Momentum Resolutions*, *Ultramicroscopy* **182**, 85 (2017).
- [38] See Supplemental Material at <http://link.aps.org/supplemental/10.1103/PhysRevX.9.041038> for details, which includes Refs. [17–19,23,27,30,39–49].
- [39] G. Kresse and D. Joubert, *From Ultrasoft Pseudopotentials to the Projector Augmented-Wave Method*, *Phys. Rev. B* **59**, 1758 (1999).
- [40] J. P. Perdew, K. Burke, and M. Ernzerhof, *Generalized Gradient Approximation Made Simple*, *Phys. Rev. Lett.* **77**, 3865 (1996) Erratum **78**, 1396 (1997).
- [41] V. I. Anisimov, J. Zaanen, and O. K. Andersen, *Band Theory and Mott Insulators: Hubbard U Instead of Stoner I.*, *Phys. Rev. B* **44**, 943 (1991).
- [42] S. L. Dudarev, G. A. Botton, S. Y. Savrasov, C. J. Humphreys, and A. P. Sutton, *Electron-Energy-Loss Spectra and the Structural Stability of Nickel Oxide: An LSDA + U Study*, *Phys. Rev. B* **57**, 1505 (1998).
- [43] G. Kresse and J. Furthmüller, *Efficiency of Ab initio Total Energy Calculations for Metals and Semiconductors Using a Plane-Wave Basis Set*, *Comput. Mater. Sci.* **6**, 15 (1996).
- [44] M. M. Otrokov *et al.*, *Highly-Ordered Wide Bandgap Materials for Quantized Anomalous Hall and Magneto-electric Effects*, *2D Mater.* **4**, 025082 (2017).
- [45] A. A. Mostofi, J. R. Yates, G. Pizzi, Y.-S. Lee, I. Souza, D. Vanderbilt, and N. Marzari, *An Updated Version of wannier90: A Tool for Obtaining Maximally-Localised Wannier Functions*, *Comput. Phys. Commun.* **185**, 2309 (2014).
- [46] N. Marzari and D. Vanderbilt, *Maximally Localized Generalized Wannier Functions for Composite Energy Bands*, *Phys. Rev. B* **56**, 12847 (1997).
- [47] Q. Wu, S. Zhang, H.-F. Song, M. Troyer, and A. A. Soluyanov, *WannierTools: An Open-Source Software Package for Novel Topological Materials*, *Phys. Chem. Comm.* **224**, 405 (2018).
- [48] A. Takayama, T. Sato, S. Souma, T. Oguchi, and T. Takahashi, *One-Dimensional Edge States with Giant Spin Splitting in a Bismuth Thin Film*, *Phys. Rev. Lett.* **114**, 066402 (2015).
- [49] L. Miao *et al.*, *Quasiparticle Dynamics in Reshaped Helical Dirac Cone of Topological Insulators*, *Proc. Natl. Acad. Sci. U.S.A.* **110**, 2758 (2013).
- [50] Note that the Dirac point binding energy is ~ 290 meV for the sample used in Fig. 2(a) (Ref. [38], Sec. C), ~ 269 meV for that used in Figs. 2(b)–2(e) (Ref. [38], Sec. D), and ~ 280 meV for that used in Fig. 3(a). This difference is understandable as the carrier concentration is slightly different in each crystal.
- [51] C. Chen *et al.*, *Robustness of Topological Order and Formation of Quantum Well States in Topological Insulators Exposed to Ambient Environment*, *Proc. Natl. Acad. Sci. U.S.A.* **109**, 3694 (2012).
- [52] L. A. Wray, S.-Y. Xu, Y. Xia, D. Hsieh, A. V. Fedorov, Y. S. Hor, R. J. Cava, A. Bansil, H. Lin, and M. Z. Hasan, *A Topological Insulator Surface under Strong Coulomb, Magnetic and Disorder Perturbations*, *Nat. Phys.* **7**, 32 (2011).
- [53] Q. Liu, C. X. Liu, C. Xu, X. L. Qi, and S. C. Zhang, *Magnetic Impurities on the Surface of a Topological Insulator*, *Phys. Rev. Lett.* **102**, 156603 (2009).
- [54] J.-J. Zhu, D. X. Yao, S. C. Zhang, and K. Chang, *Electrically Controllable Surface Magnetism on the Surface of*

- Topological Insulators*, *Phys. Rev. Lett.* **106**, 097201 (2011).
- [55] G. Rosenberg and M. Franz, *Surface Magnetic Ordering in Topological Insulators with Bulk Magnetic Dopants*, *Phys. Rev. B* **85**, 195119 (2012).
- [56] F. Schindler *et al.*, *Higher-Order Topology in Bismuth*, *Nat. Phys.* **14**, 918 (2018).
- [57] R.-X. Zhang and C.-X. Liu, *Topological Magnetic Crystalline Insulators and Corepresentation Theory.*, *Phys. Rev. B* **91**, 115317 (2015).
- [58] A. Zunger, S. H. Wei, L. G. Ferreira, and J. E. Bernard, *Special Quasirandom Structures*, *Phys. Rev. Lett.* **65**, 353 (1990).
- [59] L. Fu, *Hexagonal Warping Effects in the Surface States of the Topological Insulator Bi₂Te₃*, *Phys. Rev. Lett.* **103**, 266801 (2009).
- [60] S. L. Altmann and P. Herzig, *Point-Group Theory Tables* (Clarendon Press, Oxford, 1994).
- [61] T. Rauch, M. Flieger, J. Henk, I. Mertig, and A. Ernst, *Dual Topological Character of Chalcogenides: Theory for Bi₂Te₃*, *Phys. Rev. Lett.* **112**, 016802 (2014).
- [62] Y. J. Chen *et al.*, this issue, *Topological Electronic Structure and Its Temperature Evolution in Antiferromagnetic Topological Insulator MnBi₂Te₄*, *Phys. Rev. X* **9**, 041040 (2019).
- [63] H. Li *et al.*, following paper, *Dirac Surface States in Intrinsic Magnetic Topological Insulators EuSn₂As₂ and MnBi₂Te₄*, *Phys. Rev. X* **9**, 041039 (2019).
- [64] P. Swatek, Y. Wu, L.-L. Wang, K. Lee, B. Schrunck, J. Yan, and A. Kaminski, *Gapless Dirac Surface States in the Antiferromagnetic Topological Insulator MnBi₂Te₄*, arXiv:1907.09596.

Te-Vacancy-Induced Surface Collapse and Reconstruction in Antiferromagnetic Topological Insulator MnBi_2Te_4

Fuchen Hou,[#] Qiushi Yao,[#] Chun-Sheng Zhou, Xiao-Ming Ma, Mengjiao Han, Yu-Jie Hao, Xuefeng Wu, Yu Zhang, Hongyi Sun, Chang Liu, Yue Zhao,* Qihang Liu,* and Junhao Lin*



Cite This: *ACS Nano* 2020, 14, 11262–11272



Read Online

ACCESS |



Metrics & More



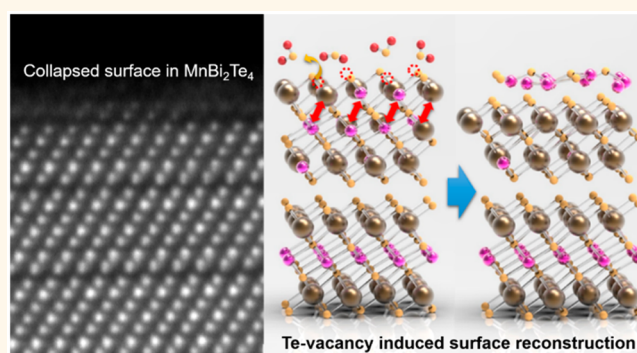
Article Recommendations



Supporting Information

ABSTRACT: MnBi_2Te_4 is an antiferromagnetic topological insulator that has stimulated intense interest due to its exotic quantum phenomena and promising device applications. The surface structure is a determinant factor to understand the magnetic and topological behavior of MnBi_2Te_4 , yet its precise atomic structure remains elusive. Here we discovered a surface collapse and reconstruction of few-layer MnBi_2Te_4 exfoliated under delicate protection. Instead of the ideal septuple-layer structure in the bulk, the collapsed surface is shown to reconstruct as a Mn-doped Bi_2Te_3 quintuple layer and a $\text{Mn}_x\text{Bi}_y\text{Te}$ double layer with a clear van der Waals gap in between. Combined with first-principles calculations, such surface collapse is attributed to the abundant intrinsic Mn–Bi antisite defects and the tellurium vacancy in the exfoliated surface, which is further supported by *in situ* annealing and electron irradiation experiments. Our results shed light on the understanding of the intricate surface-bulk correspondence of MnBi_2Te_4 and provide an insightful perspective on the surface-related quantum measurements in MnBi_2Te_4 few-layer devices.

KEYWORDS: surface reconstruction, MnBi_2Te_4 , magnetic topological insulator, antisite defects, tellurium vacancy, *in situ* surface dynamics



Magnetic topological quantum materials have stimulated intense research interest due to the interplay between magnetism and topology that results in an emerging quantum phenomenon.^{1–4} Examples include the quantum anomalous Hall effect (QAHE),^{3–5} Weyl semimetallic states,^{6,7} topological axion states,⁸ Majorana fermions,^{2,9} and so on, enabling potential applications in dissipationless electronic and quantum computing.¹⁰ In the early research, a magnetic topological insulator (TI) was achieved by magnetically doping a TI thin film to study the QAHE.^{3–5} However, the random distribution of magnetic dopants introduces impurity scattering together with the ferromagnetic ordering, limiting the temperature for the realization of the QAHE. Very recently, the tetradymite-type MnBi_2Te_4 compound was discovered as an intrinsic antiferromagnetic (AFM) TI in the A-type AFM ground state with out-of-plane magnetic moments.^{11–19} Although the existence of long-range magnetic order explicitly breaks the time-reversal symmetry, which is nevertheless preserved in conventional Z_2 TI,^{1,2} another type of Z_2 invariant can be defined in MnBi_2Te_4 as long as a combined symmetry between the time reversal and the fractional translation is preserved.^{11,20,21} As a result,

MnBi_2Te_4 provides an ideal platform for magnetic TI to realize the QAHE, the axion insulator state,^{15,17,22} and so on.

On the contrary, there are still discrepancies between theoretical expectations and experimental facts in MnBi_2Te_4 . For instance, theoretical predictions and some experimental observations declared a sizable magnetic gap at the surface of bulk MnBi_2Te_4 ,^{11–15} whereas a recent report shows an unambiguously gapless Dirac cone at the (001) surface of MnBi_2Te_4 crystal by using the high-resolution angle-resolved photoemission spectroscopy (ARPES).^{16,23,24} Such inconsistency implies that the surface structure is a key factor requiring precise measurements, which may affect many of the corresponding magnetic and topological behaviors in MnBi_2Te_4 , such as the QAHE in odd layers and the zero

Received: April 14, 2020

Accepted: August 19, 2020

Published: August 19, 2020



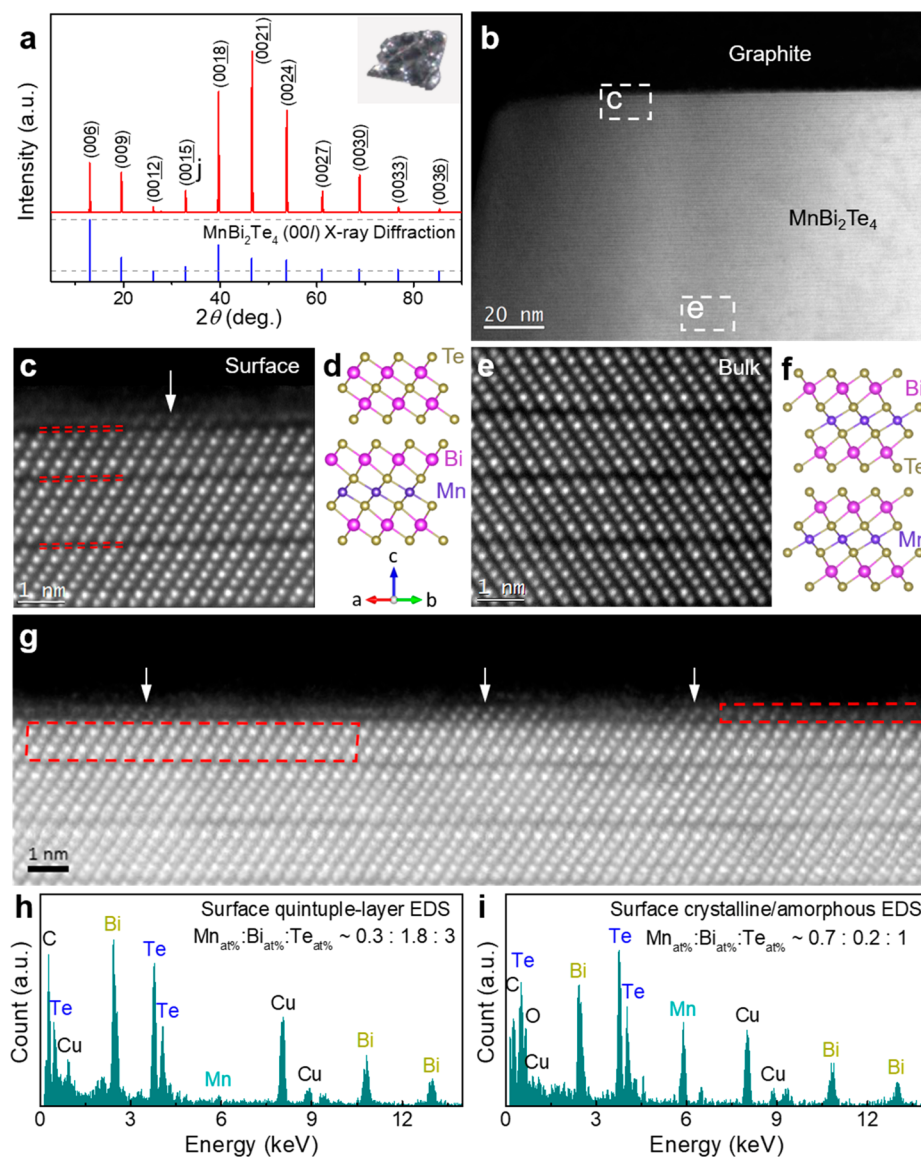


Figure 1. Atomic characterizations of the MnBi₂Te₄ surface structure. (a) X-ray diffraction (XRD) pattern (red) and the referenced (00l) peaks (blue) from standard PDF file of the parent single MnBi₂Te₄ crystal. (b) Large-scale high-angle annular dark-field scanning transmission electron microscopy (HAADF-STEM) image of the cross section of the layered MnBi₂Te₄ crystal viewed along the [110] direction, with the overlaid graphite as surface protection. (c–e) Zoom-in atomic-resolution HAADF-STEM images of the surface and bulk highlighted in panel b, respectively. A quintuple layer (QL) with a double-layer (DL) crystalline/amorphous structure, instead of the ideal septuple-layer (SL) MnBi₂Te₄, is seen at the surface. The arrows highlight the crystalline DL islands on the surface. (d,f) Corresponding atomic models from the images, respectively. (g) Large-scale atomic structure of the MnBi₂Te₄ surface showing the omnipresent crystalline DL islands indicated by arrows. (h,i) Corresponding energy-dispersive spectrum (EDS) maps for the surface QL and DL crystalline/amorphous structures, respectively. Cu and C come from the grid and substrate.

Hall plateau as an indicator of the axion state in even layers.^{11,17,18} Apparently, most of the previous results consider the surface structure using the ideal septuple-layer (SL) MnBi₂Te₄ lattice,^{11–19} which, on the contrary, lacks direct proof to connect the bridge between theory and experiments.

Because the surface-bulk correspondence is the kernel of the topological properties, in this Article, we systematically studied the atomic structure of the surface in MnBi₂Te₄ few-layer devices with intended surface protection. Using cross-sectional scanning transmission electron microscopy (STEM) imaging, atomic electron energy loss spectroscopy (EELS), and energy-dispersive spectroscopy (EDS), we unambiguously determined the surface of few-layer MnBi₂Te₄ to be a Mn-doped Bi₂Te₃ quintuple layer (QL) decorated with a crystalline/amorphous

Mn_xBi_yTe double layer (DL) rather than the ideal SL-layered structure; that is, a surface collapse and reconstruction occurred during the mechanical exfoliation. Such surface collapse is highly reproducible in all samples we measured. We further discovered that Bi–Mn antisite defects were omnipresent in bulk MnBi₂Te₄. Combining the density functional theory (DFT) calculations, we unveiled the origin of the surface collapse in few-layer MnBi₂Te₄ to be a result of the synergistic interaction between the Bi–Mn antisite defects and the surface tellurium vacancies. Our result shows that such defects are inevitable, even in an inert gas environment, due to trace oxygen, which makes the as-observed reconstructed surface preferential in the energy landscape. Similar surface collapse and reconstruction can be reproduced by heating the

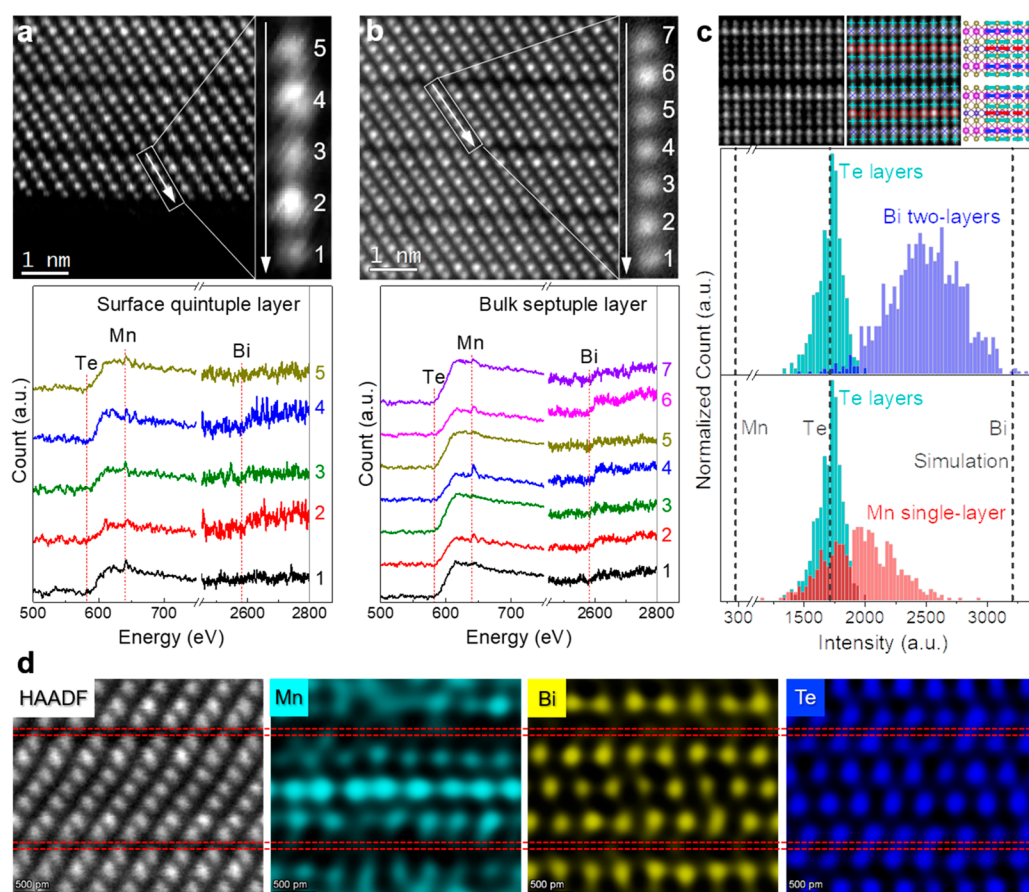


Figure 2. Chemical analysis of the exchange Mn–Bi defects at the surface and bulk. (a,b) Atomic-resolution cross-sectional HAADF images of the single-crystal MnBi₂Te₄, with the arrow indicating the position and direction of the electron energy loss spectrometry (EELS) linescan acquisition. The corresponding background-subtracted atom-by-atom EELS data for the (a) surface QL and (b) bulk SL are shown below. The numbers mark the different atomic columns corresponding to the labeled EELS data. The onset energies of Te ($M_{4,5}$ edge at 572 eV), Mn ($L_{2,3}$ edge at 640 eV), and Bi ($M_{4,5}$ edge at 2580 eV) are highlighted by dashed lines as a guide to the eye. (c) Histogram of the intensity distribution mapped from the Te (cyanine), Bi (blue), and Mn (red) atomic columns in bulk MnBi₂Te₄, respectively. The HAADF image shows the location of different atomic columns marked by corresponding colors, viewed from the $[110]$ direction. The dark-gray dashed lines represent the normalized intensities of Te, Mn, and Bi columns from the simulation without any Mn–Bi exchange defect. (d) Atomic-resolution HAADF image of the SL structure in MnBi₂Te₄ with corresponding EDS mapping for individual elements of Mn, Bi, and Te. The red dashed lines highlight an individual SL.

intact SL surface exfoliated in an ultrahigh vacuum (UHV) and probing by atomic scanning tunneling microscopy (STM) and by electron irradiation in STEM, which simultaneously monitor the dynamical surface collapse and reconstruction process atom-by-atom. These experiments further verified that the surface collapse and reconstruction that occurred in a well-controlled inert gas environment were indeed induced by the surface Te vacancy. Our findings of the vacancy-induced surface collapse and reconstruction in exfoliated MnBi₂Te₄ under a well-controlled inert gas environment not only shed light on the fabrication of MnBi₂Te₄ few-layer devices but also bring valuable insights into understanding the discrepancies and controversial arguments from many laboratories that are dedicated to MnBi₂Te₄ research, such as the discrepancies in the surface electronic structure in previous investigations.^{11–16,23,24}

RESULTS AND DISCUSSION

Atomic Structure of the Collapsed Surface in Exfoliated MnBi₂Te₄ Few-Layer Devices. The MnBi₂Te₄ single crystal is a member of the van der Waals (VDW) layered materials. A single VDW layer of MnBi₂Te₄ consists of

alternating Bi–Mn–Bi layer intercalated by Te, forming an SL structure. Its antiferromagnetism originates from the middle Mn cations with a superexchanged interlayer interaction between adjacent Mn layers. Figure 1a shows the X-ray diffraction (XRD) measurement of the parent MnBi₂Te₄ crystal with sharp and intense peaks that follow the $(00l)$, $l = 3n$, diffraction rule, which quantitatively agree with those in the standard PDF files. In addition, the X-ray photoelectron spectroscopy (XPS) characterization of the MnBi₂Te₄ single crystal reveals the core-level peaks of Mn 2p, Bi 4f, and Te 3d (Figure S1) without any impurity signal from other crystalline phases and elements, indicating the high quality of the parent single crystal. The fresh cleaved surface of the MnBi₂Te₄ crystal was initially investigated by high-resolution atomic force microscopy (AFM) operated in the same inert gas environment. A rough surface was seen with steps ranging from 2 to 6 Å (one to three atomic layers) (Figure S2), suggesting a possible disordered surface structure. We then performed a cross-section study to obtain atomic information on the surface. The surface was intentionally protected by graphite, which merely serves as a protective layer on the MnBi₂Te₄ surface, ensuring minimum surface degradation during cross-

section sample fabrication. (See the [Materials and Methods](#) for more details.)

Figure 1b shows a low-magnified high-angle annular dark-field (HAADF) STEM image of the as-prepared MnBi_2Te_4 few-layer cross-section, taken from the $[110]$ direction. The graphite appears in dark contrast due to its relative light atomic weight in the STEM image. Zoom-in images with the atomic resolution of the surface and bulk are exhibited in Figure 1c,e, respectively. A comparison of the two readily shows an apparent deviation of the surface structure: It is a five-atom layer instead of seven, similar to the atomic structure of $\text{TI Bi}_2\text{Te}_3$ (Te-Bi-Te-Bi-Te) viewed along the c axis, known as the QL structure. (The atomic model is shown in Figure 1d.) In contrast, the atomic structure of the bulk MnBi_2Te_4 (Figure 1e) is consistent with the previous reports,^{11,12,14} showing an SL structure ($\text{Te1-Bi-Te2-Mn-Te2-Bi-Te1}$), as depicted by the atomic model in Figure 1f. Quantitative EDS mapping (see the [Methods](#)) further revealed the chemical composition of the surface to mainly consist of Bi and Te, with trivial Mn. The ratio of Mn, Bi, and Te at the surface QL layer, highlighted by the red dashed rectangle in Figure 1g, is estimated to be $\sim 0.3:1.8:3$ (Figure 1h), whereas it reaches the normal $1:2:4$ ratio below the surface (Figure S3).

Above the QL structure, an amorphous layer with brighter contrast than the nearby graphite protection layer is observed. This amorphous layer separated from the QL surface with a clear VDW gap, as highlighted by red dashed lines in Figure 1c. Moreover, the crystalline structure with a DL height was occasionally observed to be embedded in such an amorphous layer, which is highlighted by the white arrows. A larger view of the surface (Figure 1g) further manifested that these tiny crystalline structures are omnipresent above the surface yet gapped by amorphous layers in between. EDS results of such an amorphous layer and an embedded crystalline quantum island (highlighted by the red dashed rectangle in Figure 1g) clearly reveal that in contrast with the QL layer, the major elements are Mn and Te, with trivial Bi. The element ratio among Mn, Bi, and Te is $\sim 0.7:0.2:1$ (Figure 1i).

The cross-sectional results pointed to a critical finding that the surface of the as-prepared MnBi_2Te_4 few-layer sample underwent a surface collapse even with intentional surface protection during the mechanical exfoliation in an inert gas environment. Instead of the ideal SL model with the chemical composition Mn:Bi:Te of $1:2:4$, which is the case below the surface, as verified by quantitative EDS, the realistic surface layer splits into a Bi-rich QL plus a Mn-rich DL crystalline/amorphous layer, with a complementary elemental distribution of $0.3:1.8:3$ and $0.7:0.2:1$, respectively. Such surface collapse and reconstruction are highly reproducible in all of the samples we measured, even in a mild transfer without heating during the drop-down process of the protection graphite layer. Mn-doped QL Bi_2Te_3 is stable, as previously reported,¹³ but the DL Bi-doped MnTe is theoretically unstable (see [Supporting Information Section II](#) for more details) and has high reactivity. The existence of the island-like DL crystalline structure is presumably due to the VDW interaction from the underlying layers and the local chemical composition fluctuation during the surface reconstruction.

Detection of the Mn–Bi Exchange Antisite Defects by Atomic EELS, EDS, and Intensity Quantification Analysis. The unexpected surface collapse and reconstruction may be related to the superficial chemical stoichiometry variation or surface defects.²⁵ To further find out the cause of

the surface collapse, we carried out atom-by-atom EELS across the reconstructed surface. Figure 2a shows the EELS of each atomic column in the surface QL structure, with the simultaneously collected HAADF image shown on the right. The identity of Bi shown by the M_4 edge at 2688 eV shows up only at the second and fourth layers, corresponding to the two brightest spots, which is consistent with the expected STEM HAADF intensity due to its large atomic number. The atomic EELS and simulated STEM HAADF image (see Figure S5) suggest that the surface QL is an alternating Te-Bi-Te-Bi-Te QL, similar to the Bi_2Te_3 structure. However, it is surprising that a clear Mn signal, labeled by the $L_{2,3}$ edge at 640 eV, also shows up exactly in the Bi columns. This suggests that antisite defects, Bi_{Mn} or Mn_{Bi} , may have been present on the surface even before the surface collapse occurred.

To further confirm the scenario of Bi_{Mn} or Mn_{Bi} , we also collected atomic EELS and EDS maps from the bulk SL structure. Figure 2b shows the EELS across the SL structure. Surprisingly, we found that a clear Bi signal appeared in the Mn layer (fourth atomic column in Figure 2b), whereas a strong Mn signal appeared in both of the Bi layers (second and sixth layers), evidencing the presence of Bi_{Mn} and Mn_{Bi} . As a result, the Mn layer has much brighter intensity than the simulated STEM HAADF image, which used the ideal SL model (Figure S5), due to the inclusion of the heavier Bi atoms and vice versa. In contrast, Te layers showed no Mn or Bi signals, excluding the presence of other types of antisite defects. Such behavior was also shown by the atomic-resolution EDS mapping in the bulk SL structure, as shown in Figure 2d, where clear Bi and Mn intermixing signals are detected in all Bi and Mn atomic columns but not in the Te layers. However, the elemental distribution of an SL in the bulk was exactly $1:2:4$, as probed by EDS, which implied the occurrence of intralayer exchange between Bi and Mn atoms. Therefore, such Mn–Bi intralayer exchange results in an almost equal amount of Bi_{Mn} and Mn_{Bi} in both Mn and Bi layers.

To further investigate the Mn–Bi intralayer exchange effect quantitatively, we mapped the intensity of all atomic columns in the SL structure on a large scale using a peak intensity finding software²⁶ and performed the quantitative statistical analysis. Figure 2c shows the intensity histogram. Mn, Bi, and Te sites are mapped separately, as indicated by the markers shown on the representative STEM image. To quantitatively study the intralayer exchange between the Mn and Bi layers, we compared the experimental value to the simulations. The dark-gray dashed lines in Figure 2c are the simulated intensities of Mn, Bi, and Te columns using the ideal SL structure without any antisite defects, where the Te column is normalized to the experimental value for direct comparison. As expected, the intensity of all Mn columns is much higher than the simulated one, whereas the intensity of Bi is lower, and both had a wider distribution than Te, which is direct evidence of intralayer Mn–Bi intermixing. From the simulated intensity, when the concentration of Bi_{Mn} reaches 30% in the Mn layer, the intensity of the Mn atomic column is almost similar to that of Te. (See Figure S5c.) The average concentration of the antisite defects in both Mn and Bi layers can be qualitatively estimated by comparing the full width at half-maximum (fwhm) of the intensity distribution with the simulation. The Bi_{Mn} concentration in the Mn layer is found to be 40–50%, which is approximately twice the value of Mn_{Bi} concentration in Bi atomic layers. The atomic EDS analysis also supports such a high Mn–Bi interchangeable ratio, with the Bi_{Mn} concentration

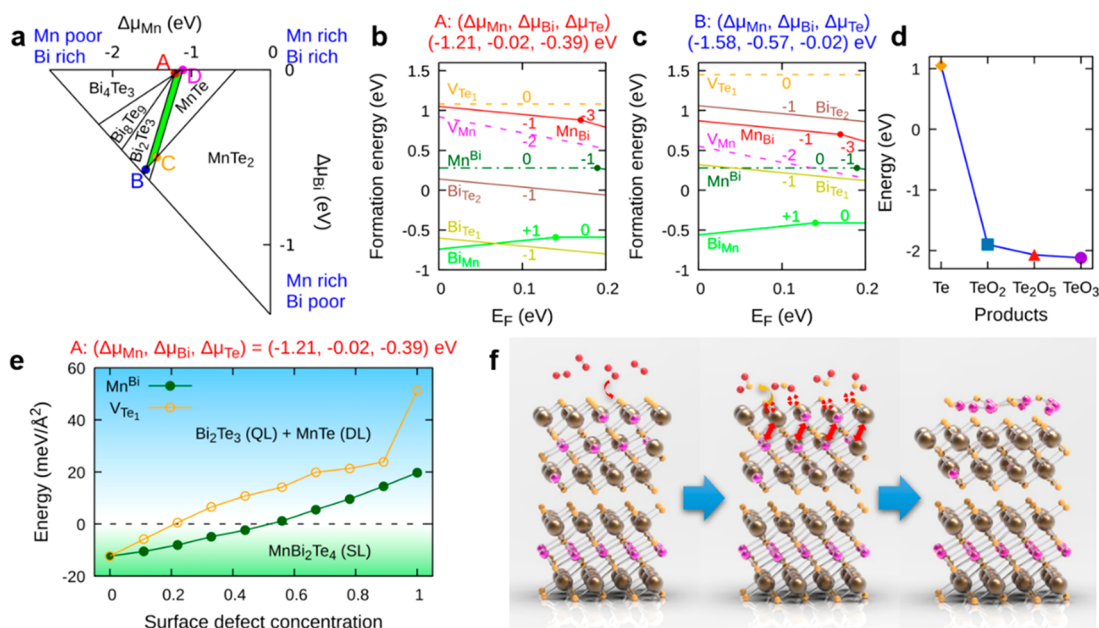


Figure 3. Physical origin of the surface collapse in MnBi_2Te_4 . (a) Allowed chemical potential domain (green area) for MnBi_2Te_4 shown in the $(\Delta\mu_{\text{Mn}}, \Delta\mu_{\text{Bi}})$ parameter space, which is sketched out by points A, B, C, and D. The other regions are excluded due to the formation of competing phases specified in the figure. (b,c) Formation energies of defects in MnBi_2Te_4 for chemical potential sets A and B shown in panel a. Formation energies at C and D are shown in the [Supporting Information](#). (d) Calculated formation energy of $V_{\text{Te}1}$ for different tellurium oxides. (e) Relative surface energy as a function of defect concentration under chemical potential set A. The dashed line indicates the energy of the surface terminating with Bi_2Te_3 and MnTe islands. (f) Schematic of the surface collapse and reconstruction in the MnBi_2Te_4 crystal induced by the formation of an oxygen-driven Te vacancy and the subsequent Mn–Bi exchange effect.

in the Mn layer being 40~50% and the Mn_{Bi} concentration in the Bi atomic layers being approximately 20~30%. These results are consistent with our previous analysis that the amount of Bi_{Mn} and Mn_{Bi} should be equal due to the intralayer exchange, whereas the amount of Bi is double the amount of Mn due to the 1:2:4 chemical stoichiometry.

Physical Origin of the Defect-Triggered Surface Collapse and Reconstruction. To uncover the physical origin of the observed surface reconstruction in MnBi_2Te_4 , we carried out comprehensive thermodynamic defect calculations by using the DFT. By far, our experiments evidenced that high concentrations of intrinsic antisite defects (Bi_{Mn} and Mn_{Bi}) are presented in the Mn and Bi layers, and thus we first examined the formation of antisite defects due to the Bi–Mn exchange in MnBi_2Te_4 . The chemical potential substantially affects the calculations of defect formation energy. Therefore, we determined the accessible range of the chemical potential, that is, the growth condition, of MnBi_2Te_4 in the $(\Delta\mu_{\text{Mn}}, \Delta\mu_{\text{Bi}})$ parameter space with the constraints imposed by competing binary compounds, as shown in the green area of [Figure 3a](#). In the unstable regions (white area), MnBi_2Te_4 tends to decompose to various competing phases. Therefore, the formation energies of native defects were calculated under merely two representative environments, that is, the Bi-rich condition ($\Delta\mu_{\text{Bi}} \approx 0$ eV) and the Te-rich condition ($\Delta\mu_{\text{Te}} \approx 0$ eV), denoted by the A and B points in [Figure 3a](#), respectively. More information about the defect calculations is provided in [Supporting Information Sections III–IV](#).

For the Bi-rich condition (see [Figure 3b](#)), Bi_{Mn} , having the lowest formation energy, is the dominant donor defect due to the excess valence electrons of Bi compared with Mn. On the contrary, the cation-to-cation antisite defect (Mn_{Bi}) has a much lower formation energy than the anion-to-cation antisite

defect (Te_{Bi}), even under Te-rich conditions ([Figure S7](#)), and thus Bi_{Mn} and Mn_{Bi} are two dominant defects in MnBi_2Te_4 . The combination of these two antisite defects creates a double defect of Mn–Bi exchange (Mn_{Bi}), with relatively small formation energies shown as the dark-green line of [Figure 3b,c](#). This explains the high concentration of the cation-to-cation antisite exchange defects observed in the STEM cross-section image. Note that to form Mn_{Bi} , no atom exchange between MnBi_2Te_4 and the reservoirs is required.

The physical origin of the ideal SL to the as-observed reconstructed surface (QL+DL structure) should be closely related to the defect landscape of MnBi_2Te_4 . First, we consider the total energy of MnBi_2Te_4 with Mn_{Bi} exchange defects at the surface and compare with the total energy of Bi_2Te_3 and MnTe islands under surface reconstruction. The latter is set to 0 as the reference, denoted by the dashed line in [Figure 3e](#). We find that the energy of the defective SL surface increases monotonically with the increasing Mn_{Bi} concentration, which is consistent with its positive defect formation energy from our calculation. (See [Supporting Information Section V](#) for calculation models and methods.) To pass the reference line and thus realize the collapse from SL to QL, the required concentration of Mn_{Bi} is extremely high (>50%). Such a high defect concentration is not observed in our experiments because the bulk still has a stable SL framework against reconstruction; only the surface did undergo such reconstruction. In other words, although Mn_{Bi} is the dominant defect under the equilibrium growth conditions, Mn_{Bi} alone can hardly promote the SL surface collapse into the QL. Therefore, the driving force of the surface collapse should be something else, most likely some defects that may form at the surface regardless of their relatively large formation energies in the bulk.

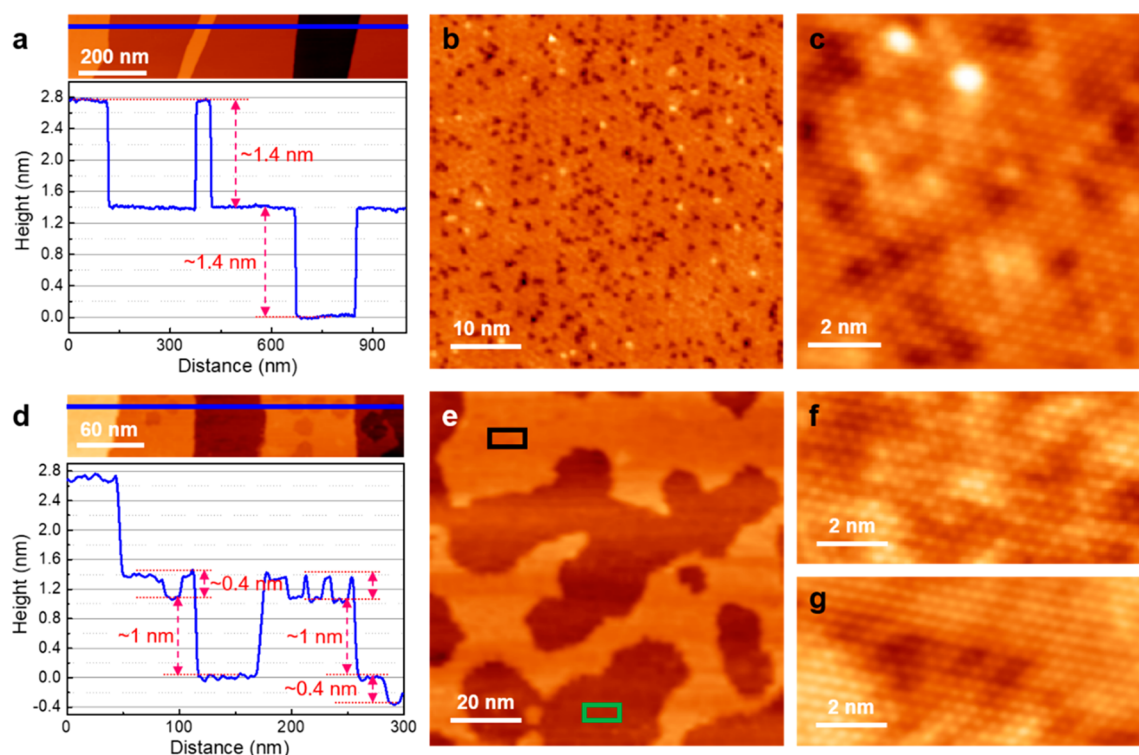


Figure 4. *In situ* heating of the exfoliated MnBi_2Te_4 surface in an ultrahigh vacuum. (a) Large-scale STM image of MnBi_2Te_4 (00l) surface exfoliated in an ultrahigh vacuum and the corresponding height line profile along the blue line. (b) Zoom-in STM image of the MnBi_2Te_4 (00l) surface with defects. (c) Atomic-resolution image of the MnBi_2Te_4 surface. The dark spots are concluded to be the Bi^{Mn} antisite defects under the Te layer. The SL height and the crystalline surface imply that the intact MnBi_2Te_4 surface can be preserved in an ultrahigh vacuum. (d) Large-scale STM image of the *in situ* heated MnBi_2Te_4 surface and the corresponding height line profile along the blue line. Holes with DL heights appear after heating. (e) Zoom-in image of the annealed surface. (f,g) Atomically resolved STM images of the annealed surface marked by black and green boxes in panel e, respectively. Tunneling parameters: (a) $V_{\text{bias}} = 1 \text{ V}$, $I_t = 200 \text{ pA}$; (b) $V_{\text{bias}} = 1 \text{ V}$, $I_t = 50 \text{ pA}$; (c) $V_{\text{bias}} = -1 \text{ V}$, $I_t = 3 \text{ nA}$; (d) $V_{\text{bias}} = 1.2 \text{ V}$, $I_t = 20 \text{ pA}$; (e) $V_{\text{bias}} = 1.5 \text{ V}$, $I_t = 1 \text{ nA}$; (f) $V_{\text{bias}} = -1 \text{ V}$, $I_t = 1 \text{ nA}$; (g) $V_{\text{bias}} = 0.2 \text{ V}$, $I_t = 500 \text{ pA}$.

From bulk to surface, the outermost layer (Te1 layer in MnBi_2Te_4) suffers the strongest environmental perturbation, such as unintentionally introduced atomic vacancies upon cleavage. It is known that tellurides like MnBi_2Te_4 are readily oxidized, which would break the equilibrium growth condition. Taking tellurium oxides into account, we reevaluated the formation energy of Te1 vacancy V_{Te1} . (See Supporting Information Section VI for calculation details.) As illustrated in Figure 3d, under equilibrium Te-poor conditions, the formation energy of V_{Te1} is $\sim 1.1 \text{ eV}$, indicating the relatively low V_{Te1} concentration in bulk. However, with the assistance of oxygen, instead of forming an elemental Te solid, Te forms tellurium oxides, with the V_{Te1} formation energy dramatically decreased. We consider three tellurium oxides, TeO_2 , Te_2O_3 , and TeO_3 . For all cases, the calculated V_{Te1} formation energies are about -2 eV , indicating an exothermal reaction. The total energy of MnBi_2Te_4 with V_{Te1} defects at the surface quickly increases with the increase in V_{Te1} concentration, as shown in Figure 3e. To realize the SL to QL collapse, the required surface V_{Te1} concentration is $\sim 20\%$ under the Bi-rich condition. With the assistance of Mn^{Bi} , the surface collapse may take place at an even lower V_{Te1} concentration. Overall, as illustrated by the schematic in Figure 3f, oxygen at the surface reacts with the Te1 sublayer, leaving tellurium vacancies. Such surface V_{Te1} serves as the dominant driving force to trigger the surface collapse and QL+DL reconstruction in the original SL MnBi_2Te_4 structure by accelerating the Bi–Mn exchange, which leads to the depletion of Mn in the QL, consistent with

the EDS results in Figure 1h. The exchange barrier between the Bi and Mn atoms in the lattice is quite small (0.28 eV , Figure 3b), and the depletion of Mn is essential to form a QL (Bi_2Te_3) + DL (MnTe) reconstructed structure, which is energetically more favorable than the defective SL MnBi_2Te_4 structure with a Te vacancy, as shown in Figure 3e. Indeed, we observed a small amount of oxygen signal at the interface between the QL structure and the graphite, as detected by both EELS and EDS (see Figure S4 and Figure 1i) and also in the XPS measurement, which confirmed the contribution of oxygen to creating surface Te vacancies and the subsequent oxidation of the reconstructed outermost DL structure during the depletion of the Mn in the surface collapse process. Moreover, the theory also suggests that such surface reconstruction involves a kinetic thermal nonequilibrium. Such a process would result in an incomplete Bi–Mn exchange, which is also consistent with the chemical stoichiometry of the QL and the amorphous/crystalline DL structure, as probed by EDS. (See Figure 1h,i.)

Verifying the Defect-Induced Surface Collapse and Reconstruction by *In Situ* STM and STEM. To verify the scenario of the Te-vacancy-driven surface collapse suggested by theory, we first tried to exclude the presence of oxygen by investigating the *in situ* cleaved MnBi_2Te_4 surface using UHV STM. The operation pressure is better than $2 \times 10^{-10} \text{ Torr}$, where the oxygen concentration is multiple orders of magnitude lower than the inert gas environment in a glovebox. Figure 4a shows the STM image of a freshly exfoliated

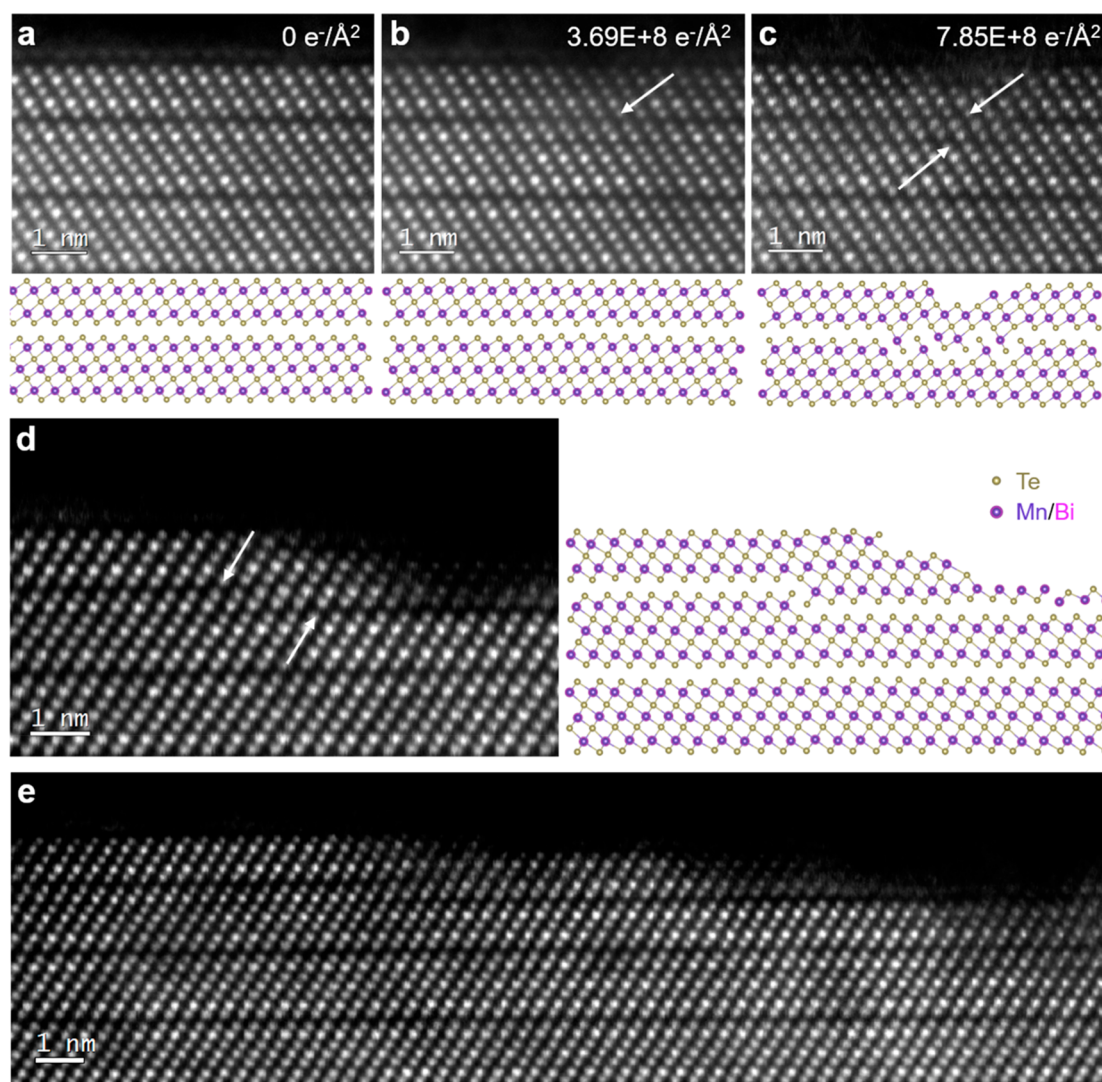


Figure 5. *In situ* observation of the dynamical surface collapse and reconstruction process induced by electron irradiation. (a–c) Evolution of the surface atomic structure as a function of electron dose: (a) 0, (b) 3.69×10^8 , and (c) 7.85×10^8 $\text{e}^-/\text{\AA}^2$. The corresponding atomic models are shown below where the Bi and Mn atoms are not discriminated due to the massive existence of Mn^{Bi} exchange defects. The arrows in panel c indicate the close of the original VDW gap due to the loss of Te atoms, with another VDW gap opening two layers down the collapsed and reconstructed region. (d) Atomic STEM image showing a discontinuous VDW gap along the surface after collapse and reconstruction. (e) STEM image showing a large scale of the surface structure after prolonged electron irradiation, where all surfaces were terminated by the QL or QL+DL structures. Note that the collapse and reconstruction process occurred under an ultrahigh vacuum.

MnBi_2Te_4 single crystal terminating with the (00 l) surface. Abrupt steps with a uniform height of ~ 1.4 nm (seven atomic layers, Figure 4a) were obtained. An enlarged STM image shows an atomic crystalline surface (Figure 4b,c) with randomly distributed dark spots. According to the bias-voltage-dependent STM images of these dark spots (see Figure S9), they are ascribed to the Bi^{Mn} antisite defects underneath the Te layer, which is consistent with our STEM results and the previous report.²⁷ This indeed confirmed that the ideal SL MnBi_2Te_4 surface can be preserved in a UHV.

To introduce Te vacancies at the surface, an *in situ* heating at 150 °C was then applied to the surface for ~ 41 h because Te is easily sublimated at an elevated temperature. An apparent structure collapse is observed, evidenced by the emergence of holes with a step height of ~ 0.4 nm (two atomic layers, Figure 4d) inside the originally flat surface. (See Figure 4e.) As a result, the height of the collapsed region, as shown by the dimmer contrast in Figure 4e, is ~ 1 nm (the height profile in

Figure 4d), corresponding to five atomic layers. The collapsed surface still shows a similar atomic crystalline structure with hexagonal patterns (Figure 4h,g) due to the surface similarity between MnBi_2Te_4 and Bi_2Te_3 .

The STM results point out that the elevated temperature can induce a similar surface collapse by sublimating surface Te atoms. Therefore, to rule out the heating effect from the high-energy Ga ions during the cross-sectional sample preparation in the focused ion beam (FIB), we carried out cryo-FIB to prepare the TEM sample in a high vacuum ($<10^{-6}$ mbar) and at liquid-nitrogen temperature (-140 °C). The surface of MnBi_2Te_4 still displays the same QL plus the DL amorphous/crystalline structure (Figure S10), which further certified that the surface reconstruction indeed occurred during the mechanical exfoliation in the inert gas environment.

The above results are in agreement with the surface collapse and reconstruction mechanism suggested by theory. We also attempted to capture the dynamical process of the collapsed

surface reconstruction directly. It is well known that the use of high-energy electrons in imaging also simultaneously transfers momentum and energy to the specimen, which can result in beam-induced defects.²⁸ Figure 5a–c shows sequential STEM images as a function of the electron dose, highlighting the dynamical surface collapse and reconstruction process on the MnBi_2Te_4 surface. As the electron dose accumulates, the atomic column intensity of the outermost layer (Te1 layer in the QL structure) is dimmed due to the loss of tellurium (Figure 5b). Meanwhile, the gap between the surface QL and the next SL, which is underneath the Te loss region, as highlighted by the arrow in Figure 5b, narrows from 2.6 to 2 Å. A significant split is seen in the first two atomic layers of the SL, a trend in the separation into a DL and a QL structure. Finally, as the two outermost atomic columns are eliminated by electron bombardment, the surface structure collapses and reconstructs from a QL+SL to double QLs (Figure 5c).

The dynamical collapse and reconstruction process indicates that the VDW gap can close and reopen during the formation of defects depending on the exact layer configurations. This indeed means that the VDW gap between layers can be discontinued in a reconstructed surface as long as the outermost surface is a QL structure, which is highlighted by the white arrows in Figure 5d. Moreover, once the surface QL got damaged by the electron irradiation, the SL structure underneath would also quickly reconstruct to form a stable QL, indicating the extreme instability of the SL structure under perturbation, which may not survive as the outermost surface. This is evidenced in Figure 5e, which shows a large view of the collapsed and reconstructed surface, including QL+SL, two QL, and DL+QL structures, all of which manifest the QL as the stable surface structure. The *in situ* dynamical imaging unambiguously confirmed that the formation of a Te vacancy leads to the surface collapse and reconstruction in the MnBi_2Te_4 single crystal.

Our results reveal that the surface structure of MnBi_2Te_4 is not as stable as previously thought, a condition that inevitably affects the surface electronic structure and thus the topological surface-bulk correspondence. Theoretically, when the surface inherits the crystal and magnetic structures of the bulk, a gapped Dirac cone with dozens of millielectronvolts is expected due to the intrinsic magnetism. However, high-resolution ARPES measurements unambiguously show a robust gapless Dirac cone at the MnBi_2Te_4 surface.^{16,23,24} One possibility is that the local moments of Mn atoms tend to distribute randomly, giving rise to the almost zero band gap with linear dispersion. However, direct experimental evidence, such as surface magnetic configurations, is still lacking to support this hypothesis. Here we suggest from our experimental results that the surface collapse leads to a significant absence of the magnetic atoms together with magnetic disorder, resulting in a vanishing surface gap. First of all, with the surface MnBi_2Te_4 SL collapsing to the Bi_2Te_3 QL, the origin of the Dirac gap opening is mainly the proximity effect from the ordered magnetic moments of the second topmost SL. Compared with the perfect SL surface, the proximity-induced gap is much smaller. To confirm this, we calculated by DFT the surface electronic structure with both terminations, that is, the perfect MnBi_2Te_4 SL and the collapsed Bi_2Te_3 QL. As shown in Figure S11, compared with the MnBi_2Te_4 termination without surface collapse and reconstruction, the surface band gap of MnBi_2Te_4 with the surface layers degraded to Bi_2Te_3 shows a significant reduction

(from 42 to 5 meV). In addition, residual MnTe DL islands on the Bi_2Te_3 QL surface tend to be antiferromagnetic with parallel Mn spins in the basal plane.^{29,30} Therefore, the floating Mn atoms in the DL atoms cannot help to open the surface Dirac gap either. Finally, our findings suggest that the device application of thin-film MnBi_2Te_4 , for example, the quantum anomalous Hall effect, may also suffer from the impact of the surface collapse and reconstruction, which calls for further exploration.

CONCLUSIONS

In summary, we have discovered that a vacancy-induced surface collapse and reconstruction in an exfoliated MnBi_2Te_4 single crystal occurs even under the protection of a well-controlled inert gas environment. Combining STEM imaging, STM experiments, and DFT calculations, we systematically show that such surface collapse results from the synergistic effect of the high-concentration intrinsic Mn–Bi exchange defects and the formation of a tellurium vacancy on the surface, which is induced by the trace of oxygen in the inert gas environment. The surface reconstruction and the existence of massive intrinsic defects bring a more comprehensive understanding of the antiferromagnetism and the anomalous quantum states of MnBi_2Te_4 few-layer devices. The discovery of such a sensitive surface not only provides an insightful perspective on all MnBi_2Te_4 few-layer devices fabricated in a non-UHV environment but also sheds light on understanding the surface-related measurements, the exploration of exotic quantum phenomena, and the device fabrication for applications based on the MnBi_2Te_4 crystal.

MATERIALS AND METHODS

Sample Fabrication. The few-layer MnBi_2Te_4 was exfoliated from bulk MnBi_2Te_4 through a Scotch-tape method in a glovebox filled with argon. The parent MnBi_2Te_4 bulk crystal was grown by the flux method.¹⁶ The fresh surface was exposed to an argon atmosphere and subsequently covered by graphite through a routine dry-transfer method in the glovebox to encapsulate the surface from being oxidized. To eliminate the possible impact of graphite, we prepared multiple samples of MnBi_2Te_4 covered by graphite with different thicknesses. The graphite layer was exfoliated and transferred to MnBi_2Te_4 immediately after a fresh cleavage. The same surface reconstruction was observed in all samples, proving that the graphite layer merely served as the surface protection against further oxidation. The cross-section STEM specimens were quickly prepared using a FIB and a cryo-FIB in a UHV ($<10^{-6}$ mbar) and under a liquid-nitrogen temperature (-140°C) environment after the sample was fetched from the glovebox, all of which ensured minimum surface degradation.

Characterizations. *X-ray Diffraction.* Single-crystal XRD was performed on a Rigaku MiniFlex diffractometer using Cu K α radiation at room temperature.

X-ray Photoelectron Spectroscopy. The XPS measurement on the freshly exfoliated surface of the MnBi_2Te_4 crystal was performed on a PHI 5000 Versaprobe III apparatus. The spectrum was analyzed by the PHI-MultiPak software.

Atomic Force Microscopy. The AFM measurement was carried out using the Asylum Research Cypher S system placed in an inert gas environment. To minimize the oxidation of MnBi_2Te_4 , the exfoliation of the MnBi_2Te_4 crystal and AFM measurements were performed one after another in the same glovebox.

Scanning Tunneling Microscopy. The STM experiments were carried out with a low-temperature STM (UNISOKU, USM1500) under UHV conditions. The MnBi_2Te_4 single crystal was cleaved along the (001) crystal plane in the STM chamber with a base pressure of 2×10^{-10} mbar. The freshly cleaved sample was immediately

transferred to the STM chamber for further measurements at 78 K (or 5 K). The sample was baked at 150 °C for 41 h to introduce surface reconstruction. The tungsten tip was prepared by electrochemical etching and subsequent e-beam heating and Ar⁺ sputtering. We trained the tip apex on a clean Cu (111) surface prior to all measurements. STM topography images were processed by WSxM.³¹

Scanning Transmission Electron Microscopy. STEM imaging and EDS and EELS analysis of the MnBi₂Te₄ crystal were performed on an FEI Titan Themis apparatus with an X-FEG electron gun and a DCOR aberration corrector operating at 300 kV. The inner and outer collection angles for the STEM images (β_1 and β_2) were 48 and 200 mrad, respectively. The convergence semiangle of the probe was 25 mrad. The beam current was ~100 pA for high-angle annular dark-field imaging and the EDS and EELS chemical analyses. All imaging was performed at room temperature. The ratios between Mn, Bi, and Te were normalized based on the bulk MnBi₂Te₄ crystal. Thereinto, in the electronic irradiation experiment, the electron dose (D) was calculated by $D = I \times T/A$ using the beam current (I), beam illuminating area (A), and the irradiation time (T).

Density Functional Theory Calculations. First-principles calculations were carried out using the Vienna *ab initio* simulation package (VASP)³² within the framework of the DFT.³³ The exchange-correlation functional was described by the generalized gradient approximation with the Perdew–Burke–Ernzerhof (PBE) formalism.³⁴ The electron–ion interaction was treated by projector-augmented-wave (PAW) potentials³⁵ with a planewave-basis cutoff of 500 eV. The whole Brillouin zone was sampled by the Monkhorst–Pack grid³⁶ for all models. Because of the correlation effects of 3d electrons in Mn atoms, we employed the GGA+U approach within the Dudarev scheme and set the U to be 5 eV, which was investigated by a previous work.¹⁶ All atoms were fully relaxed until the force on each atom was <0.01 eV/Å and the total energy minimization was performed with a tolerance of 10^{-5} eV. Freely available software VASPKIT³⁷ was used to deal with VASP output files. The calculation process is detailed in Supporting Information Sections II–VI.

ASSOCIATED CONTENT

Supporting Information

The Supporting Information is available free of charge at <https://pubs.acs.org/doi/10.1021/acsnano.0c03149>.

Further experimental and theoretical details, including XPS chemical analysis and AFM characterizations of the MnBi₂Te₄ single crystal at the cleaved surface, more cross-sectional STEM images of the MnBi₂Te₄ surface and the corresponding EDS and EELS mapping, the statistical intensity variation in STEM images with different concentrations of exchange Mn–Bi defects, phonon dispersion of the MnTe DL structure, the formation energies of various defects in MnBi₂Te₄ under different chemical environments, relative surface energy with different defect concentrations, and DFT-calculated surface band structures of MnBi₂Te₄ SL and Bi₂Te₃ QL terminations (PDF)

AUTHOR INFORMATION

Corresponding Authors

Junhao Lin – Department of Physics and Shenzhen Key Laboratory of for Advanced Quantum Functional Materials and Devices, Southern University of Science and Technology, Shenzhen 518055, Guangdong, P. R. China; orcid.org/0000-0002-2195-2823; Email: linjh@sustech.edu.cn

Qihang Liu – Department of Physics, Shenzhen Institute for Quantum Science and Engineering, Guangdong Provincial Key Laboratory for Computational Science and Material Design, and Shenzhen Key Laboratory of for Advanced Quantum Functional Materials and Devices, Southern University of

Science and Technology, Shenzhen 518055, Guangdong, P. R. China; Email: liuqh@sustech.edu.cn

Yue Zhao – Department of Physics and Shenzhen Institute for Quantum Science and Engineering, Southern University of Science and Technology, Shenzhen 518055, Guangdong, P. R. China; orcid.org/0000-0002-9174-0519; Email: zhaoy@sustech.edu.cn

Authors

Fuchen Hou – Department of Physics and Shenzhen Key Laboratory of for Advanced Quantum Functional Materials and Devices, Southern University of Science and Technology, Shenzhen 518055, Guangdong, P. R. China

Qishi Yao – Department of Physics, Southern University of Science and Technology, Shenzhen 518055, Guangdong, P. R. China

Chun-Sheng Zhou – Department of Physics, Southern University of Science and Technology, Shenzhen 518055, Guangdong, P. R. China

Xiao-Ming Ma – Department of Physics, Southern University of Science and Technology, Shenzhen 518055, Guangdong, P. R. China

Mengjiao Han – Department of Physics and Shenzhen Key Laboratory of for Advanced Quantum Functional Materials and Devices, Southern University of Science and Technology, Shenzhen 518055, Guangdong, P. R. China

Yu-Jie Hao – Department of Physics, Southern University of Science and Technology, Shenzhen 518055, Guangdong, P. R. China

Xuefeng Wu – Department of Physics, Southern University of Science and Technology, Shenzhen 518055, Guangdong, P. R. China

Yu Zhang – Department of Physics, Southern University of Science and Technology, Shenzhen 518055, Guangdong, P. R. China; Department of Physics, University of Hong Kong, Hong Kong, P. R. China

Hongyi Sun – Department of Physics, Southern University of Science and Technology, Shenzhen 518055, Guangdong, P. R. China

Chang Liu – Department of Physics and Shenzhen Institute for Quantum Science and Engineering, Southern University of Science and Technology, Shenzhen 518055, Guangdong, P. R. China

Complete contact information is available at: <https://pubs.acs.org/doi/10.1021/acsnano.0c03149>

Author Contributions

[#]F.H. and Q.Y. contributed equally to this work. J.L. conceived the project. F.H. and J.L. made the TEM samples and performed AFM measurements and STEM-related experiments, analysis, and simulations. DFT calculations were done by Q.Y., H.S., and Q.L. Sample growth and X-ray analysis was done by X.-M.M., Y.-J.H., and C.L. STM measurements were carried out by C.-S.Z., X.W., Y. Zhang, and Y. Zhao. J.L. constructed the schematic of the MnBi₂Te₄ surface collapse and reconstruction. M.H. participated in parts of the STEM experiments. The work was coordinated by J.L., Q.L. and Y.Z. The manuscript was written by J.L., F.H., Q.L., and Q.Y. with input from all authors. All authors commented on the manuscript.

Notes

The authors declare no competing financial interest.

This work was previously submitted to a preprint server: Hou, F. C.; Yao, Q. S.; Zhou, C. S.; Ma, X. M.; Han, M. J.; Hao, Y. J.; Wu, X. F.; Zhang, Y.; Sun, H.Y.; Liu, C.; Zhao, Y.; Liu, Q. H.; Lin, J. H. Spontaneous Surface Collapse and Reconstruction in Antiferromagnetic Topological Insulator MnBi_2Te_4 . 2020, arXiv:2004.08138. arXiv.org-Print archive. <https://arxiv.org/abs/2004.08138> (accessed April 17, 2020)..

ACKNOWLEDGMENTS

We thank J. Zhang for the support of XPS measurements. We acknowledge the support from the National Natural Science Foundation of China (grant no. 11974156, 11874195, 11674149 and 11674150), the Guangdong International Science Collaboration Project (grant no. 2019A050510001 and 2017ZT07C062), the National Key Research and Development Program (grant no. 2019YFA0704901), the Guangdong Provincial Key Laboratory of Computational Science and Material Design (grant no. 2019B030301001), the Key-Area Research and Development Program of Guangdong Province (2019B010931001), the Guangdong Innovative and Entrepreneurial Research Team Program (grant no. 2016ZT06D348, 2017ZT07C062, and 2019ZT08C044), the Highlight Project (No. PHYS-HL-2020-1) of the College of Science, SUSTech, and the Science, Technology and Innovation Commission of Shenzhen Municipality (nos. ZDSYS20190902092905285 and KQTD20190929173815000) and also the assistance of the SUSTech Core Research Facilities, in particular, the technical support from the Cryo-EM Center and the Pico-Centre, which receives support from the Presidential Fund and Development and Reform Commission of Shenzhen Municipality. First-principles calculations were also supported by the Center for Computational Science and Engineering at SUSTech.

REFERENCES

- (1) Hasan, M. Z.; Kane, C. L. Colloquium: Topological Insulators. *Rev. Mod. Phys.* **2010**, *82*, 3045–3067.
- (2) Qi, X.-L.; Zhang, S.-C. Topological Insulators and Superconductors. *Rev. Mod. Phys.* **2011**, *83*, 1057–1110.
- (3) Yu, R.; Zhang, W.; Zhang, H. J.; Zhang, S. C.; Dai, X.; Fang, Z. Quantized Anomalous Hall Effect in Magnetic Topological Insulators. *Science* **2010**, *329*, 61–64.
- (4) Chang, C. Z.; Zhang, J.; Feng, X.; Shen, J.; Zhang, Z.; Guo, M.; Li, K.; Ou, Y.; Wei, P.; Wang, L. L.; Ji, Z. Q.; Feng, Y.; Ji, S.; Chen, X.; Jia, J.; Dai, X.; Fang, Z.; Zhang, S. C.; He, K.; Wang, Y.; et al. Experimental Observation of the Quantum Anomalous Hall Effect in a Magnetic Topological Insulator. *Science* **2013**, *340*, 167–170.
- (5) Chang, C. Z.; Zhao, W.; Kim, D. Y.; Zhang, H.; Assaf, B. A.; Heiman, D.; Zhang, S. C.; Liu, C.; Chan, M. H. W.; Moodera, J. S. High-Precision Realization of Robust Quantum Anomalous Hall State in a Hard Ferromagnetic Topological Insulator. *Nat. Mater.* **2015**, *14*, 473–477.
- (6) Soluyanov, A. A.; Gresch, D.; Wang, Z.; Wu, Q.; Troyer, M.; Dai, X.; Bernevig, B. A. Type-II Weyl Semimetals. *Nature* **2015**, *527*, 495–498.
- (7) Tang, P.; Zhou, Q.; Xu, G.; Zhang, S.-C. Dirac Fermions in an Antiferromagnetic Semimetal. *Nat. Phys.* **2016**, *12*, 1100–1104.
- (8) Mogi, M.; Kawamura, M.; Yoshimi, R.; Tsukazaki, A.; Kozuka, Y.; Shirakawa, N.; Takahashi, K. S.; Kawasaki, M.; Tokura, Y. A Magnetic Heterostructure of Topological Insulators as a Candidate for an Axion Insulator. *Nat. Mater.* **2017**, *16*, 516–521.
- (9) He, Q. L.; Pan, L.; Stern, A. L.; Burks, E. C.; Che, X.; Yin, G.; Wang, J.; Lian, B.; Zhou, Q.; Choi, E. S.; Murata, K.; Kou, X.; Chen, Z.; Nie, T.; Shao, Q.; Fan, Y.; Zhang, S.-C.; Liu, K.; Xia, J.; Wang, K. L. Chiral Majorana Fermion Modes in a Quantum Anomalous Hall Insulator-Superconductor Structure. *Science* **2017**, *357*, 294–299.
- (10) Tokura, Y.; Yasuda, K.; Tsukazaki, A. Magnetic Topological Insulators. *Nat. Rev. Phys.* **2019**, *1*, 126–143.
- (11) Li, J.; Li, Y.; Du, S.; Wang, Z.; Gu, B.-L.; Zhang, S.-C.; He, K.; Duan, W.; Xu, Y. Intrinsic Magnetic Topological Insulators in van der Waals Layered MnBi_2Te_4 -Family Materials. *Sci. Adv.* **2019**, *5*, No. eaaw5685.
- (12) Li, H.; Liu, S.; Liu, C.; Zhang, J.; Xu, Y.; Yu, R.; Wu, Y.; Zhang, Y.; Fan, S. Antiferromagnetic Topological Insulator MnBi_2Te_4 : Synthesis and Magnetic Properties. *Phys. Chem. Chem. Phys.* **2020**, *22*, 556.
- (13) Rienks, E. D. L.; Wimmer, S.; Sánchez-Barriga, J.; Caha, O.; Mandal, P. S.; Ružička, J.; Ney, A.; Steiner, H.; Volobuev, V. V.; Groiss, H.; Albu, M.; Kothleitner, G.; Michalička, J.; Khan, S. A.; Minár, J.; Ebert, H.; Bauer, G.; Freyse, F.; Varykhalov, A.; Rader, O.; et al. Large Magnetic Gap at the Dirac Point in $\text{Bi}_2\text{Te}_3/\text{MnBi}_2\text{Te}_4$ Heterostructures. *Nature* **2019**, *576*, 423–428.
- (14) Gong, Y.; Guo, J.; Li, J.; Zhu, K.; Liao, M.; Liu, X.; Zhang, Q.; Gu, L.; Tang, L.; Feng, X.; Zhang, D.; Li, W.; Song, C.; Wang, L.; Yu, P.; Chen, X.; Wang, Y.; Yao, H.; Duan, W.; Xu, Y.; et al. Experimental Realization of an Intrinsic Magnetic Topological Insulator. *Chin. Phys. Lett.* **2019**, *36*, 076801.
- (15) Liu, C.; Wang, Y.; Li, H.; Wu, Y.; Li, Y.; Li, J.; He, K.; Xu, Y.; Zhang, J.; Wang, Y. Robust Axion Insulator and Chern Insulator Phases in a Two-Dimensional Antiferromagnetic Topological Insulator. *Nat. Mater.* **2020**, *19*, 522–527.
- (16) Hao, Y.-J.; Liu, P.; Feng, Y.; Ma, X.-M.; Schwier, E. F.; Arita, M.; Kumar, S.; Hu, C.; Lu, R.; Zeng, M.; Wang, Y.; Hao, Z.; Sun, H.; Zhang, K.; Mei, J.; Ni, N.; Wu, L.; Shimada, K.; Chen, C.; Liu, Q.; et al. Gapless Surface Dirac Cone in Antiferromagnetic Topological Insulator MnBi_2Te_4 . *Phys. Rev. X* **2019**, *9*, 041038.
- (17) Ge, J.; Liu, Y.; Li, J.; Li, H.; Luo, T.; Wu, Y.; Xu, Y.; Wang, J. High-Chern-Number and High-Temperature Quantum Hall Effect without Landau Levels. *Natl. Sci. Rev.* **2020**, *7*, No. 1280.
- (18) Otrokov, M. M.; Rusinov, I. P.; Blanco-Rey, M.; Hoffmann, M.; Vyazovskaya, A. Y.; Ereemeev, S. V.; Ernst, A.; Echenique, P. M.; Arnau, A.; Chulkov, E. V. Unique Thickness-Dependent Properties of the van der Waals Interlayer Antiferromagnet MnBi_2Te_4 Films. *Phys. Rev. Lett.* **2019**, *122*, 107202.
- (19) Otrokov, M. M.; Klimovskikh, I. I.; Bentmann, H.; Estyunin, D.; Zeugner, A.; Aliev, Z. S.; Gaß, S.; Wolter, A. U. B.; Koroleva, A. V.; Shikin, A. M.; Blanco-Rey, M.; Hoffmann, M.; Rusinov, I. P.; Vyazovskaya, A. Y.; Ereemeev, S. V.; Koroteev, Y. M.; Kuznetsov, V. M.; Freyse, F.; Sánchez-Barriga, J.; Amiraslanov, I. R.; et al. Prediction and Observation of an Antiferromagnetic Topological Insulator. *Nature* **2019**, *576*, 416–422.
- (20) Mong, R. S. K.; Essin, A. M.; Moore, J. E. Antiferromagnetic Topological Insulators. *Phys. Rev. B: Condens. Matter Mater. Phys.* **2010**, *81*, 245209.
- (21) Zhang, D.; Shi, M.; Zhu, T.; Xing, D.; Zhang, H.; Wang, J. Topological Axion States in the Magnetic Insulator MnBi_2Te_4 with the Quantized Magnetoelectric Effect. *Phys. Rev. Lett.* **2019**, *122*, 206401.
- (22) Deng, Y.; Yu, Y.; Shi, M. Z.; Guo, Z.; Xu, Z.; Wang, J.; Chen, X. H.; Zhang, Y. Quantum Anomalous Hall Effect in Intrinsic Magnetic Topological Insulator MnBi_2Te_4 . *Science* **2020**, *367*, 895–900.
- (23) Chen, Y. J.; Xu, L. X.; Li, J. H.; Li, Y. W.; Wang, H. Y.; Zhang, C. F.; Li, H.; Wu, Y.; Liang, A. J.; Chen, C.; Jung, S. W.; Cacho, C.; Mao, Y. H.; Liu, S.; Wang, M. X.; Guo, Y. F.; Xu, Y.; Liu, Z. K.; Yang, L. X.; Chen, Y. L. Topological Electronic Structure and Its Temperature Evolution in Antiferromagnetic Topological Insulator MnBi_2Te_4 . *Phys. Rev. X* **2019**, *9*, 041040.
- (24) Li, H.; Gao, S.-Y.; Duan, S.-F.; Xu, Y.-F.; Zhu, K.-J.; Tian, S.-J.; Gao, J.-C.; Fan, W.-H.; Rao, Z.-C.; Huang, J.-R.; Li, J.-J.; Yan, D.-Y.; Liu, Z.-T.; Liu, W.-L.; Huang, Y.-B.; Li, Y.-L.; Liu, Y.; Zhang, G.-B.; Zhang, P.; Kondo, T.; Shin, S.; Lei, H.-C.; Shi, Y.-G.; Zhang, W.-T.; Weng, H.-M.; Qian, T.; Ding, H. Dirac Surface States in Intrinsic

Magnetic Topological Insulators EuSn_2As_2 and $\text{MnBi}_{2n}\text{Te}_{3n+1}$. *Phys. Rev. X* **2019**, *9*, 041039.

(25) Lin, J.; Zuluaga, S.; Yu, P.; Liu, Z.; Pantelides, S. T.; Suenaga, K. Novel Pd_2Se_3 Two-Dimensional Phase Driven by Interlayer Fusion in Layered PdSe_2 . *Phys. Rev. Lett.* **2017**, *119*, 016101.

(26) Zhang, Q.; Zhang, L. Y.; Jin, C. H.; Wang, Y. M.; Lin, F. CalAtom: A Software for Quantitatively Analysing Atomic Columns in a Transmission Electron Microscope Image. *Ultramicroscopy* **2019**, *202*, 114–120.

(27) Yan, J.-Q.; Zhang, Q.; Heitmann, T.; Huang, Z.; Chen, K. Y.; Cheng, J.-G.; Wu, W.; Vaknin, D.; Sales, B. C.; McQueeney, R. J. Crystal Growth and Magnetic Structure of MnBi_2Te_4 . *Phys. Rev. Mater.* **2019**, *3*, 064202.

(28) Hong, J.; Pan, Y.; Hu, Z.; Lv, D.; Jin, C.; Ji, W.; Yuan, J.; Zhang, Z. Direct Imaging of Kinetic Pathways of Atomic Diffusion in Monolayer Molybdenum Disulfide. *Nano Lett.* **2017**, *17*, 3383–3390.

(29) Kriegner, D.; Výborný, K.; Olejník, K.; Reichlová, H.; Novák, V.; Marti, X.; Gazquez, J.; Saidl, V.; Němec, P.; Volobuev, V. V.; Springholz, G.; Holý, V.; Jungwirth, T. Multiple-Stable Anisotropic Magnetoresistance Memory in Antiferromagnetic MnTe . *Nat. Commun.* **2016**, *7*, 11623.

(30) He, Q. L.; Yin, G.; Grutter, A. J.; Pan, L.; Che, X.; Yu, G.; Gilbert, D. A.; Disseler, S. M.; Liu, Y.; Shafer, P.; Zhang, B.; Wu, Y.; Kirby, B. J.; Arenholz, E.; Lake, R. K.; Han, X.; Wang, K. L. Exchange-Biasing Topological Charges by Antiferromagnetism. *Nat. Commun.* **2018**, *9*, 2767.

(31) Horcas, I.; Fernández, R.; Gómez-Rodríguez, J. M.; Colchero, J.; Gómez-Herrero, J.; Baro, A. M. WSXM: A Software for Scanning Probe Microscopy and a Tool for Nanotechnology. *Rev. Sci. Instrum.* **2007**, *78*, 013705.

(32) Kresse, G.; Furthmüller, J. Efficient Iterative Schemes for *Ab Initio* Total-Energy Calculations Using a Plane-Wave Basis Set. *Phys. Rev. B* **1996**, *54*, 11169–11186.

(33) Hohenberg, P.; Kohn, W. Inhomogeneous Electron Gas. *Phys. Rev.* **1964**, *136*, B864–B871.

(34) Kohn, W.; Sham, L. J. Self-Consistent Equations Including Exchange and Correlation Effects. *Phys. Rev.* **1965**, *140*, A1133–A1138.

(35) Kresse, G.; Joubert, D. From Ultrasoft Pseudopotentials to the Projector Augmented-Wave Method. *Phys. Rev. B* **1999**, *59*, 1758–1775.

(36) Pack, J. D.; Monkhorst, H. J. Special Points for Brillouin-Zone Integrations. *Phys. Rev. B* **1977**, *16*, 1746–1747.

(37) Wang, V.; Xu, N.; Liu, J. C. VASPKIT: A Pre- and Post-Processing Program for VASP Code. 2020, arXiv:1908.08269 [cond-mat.mtrl-sci]. arXiv.org e-Print archive. <https://arxiv.org/abs/1908.08269> (accessed February 22, 2020).

Fermi Velocity Reduction of Dirac Fermions around the Brillouin Zone Center in In_2Se_3 -Bilayer Graphene Heterostructures

Zhenyu Wang,* Zhanyang Hao, Yayun Yu, Yuan Wang, Shiv Kumar, Xiangnan Xie, Mingyu Tong, Ke Deng, Yu-Jie Hao, Xiao-Ming Ma, Ke Zhang, Cai Liu, Mingxiang Ma, Jiawei Mei, Guang Wang, Eike F. Schwier, Kenya Shimada, Fufang Xu, Chang Liu, Wen Huang, Jianfeng Wang,* Tian Jiang, and Chaoyu Chen*

Emergent phenomena such as unconventional superconductivity, Mott-like insulators, and the peculiar quantum Hall effect in graphene-based heterostructures are proposed to stem from the superlattice-induced renormalization of (moiré) Dirac fermions at the graphene Brillouin zone corners. Understanding the corresponding band structure commonly demands photoemission spectroscopy with both sub-meV resolution and large-momentum coverage, beyond the capability of the current state-of-the-art. Here the realization of moiré Dirac cones around the Brillouin zone center in monolayer In_2Se_3 /bilayer graphene heterostructure is reported. The renormalization is evidenced by reduced Fermi velocity ($\approx 23\%$) of the moiré Dirac cones and the reshaped Dirac point at the Γ point where they intersect. While there have been many theoretical predictions and much indirect experimental evidence, the findings here are the first direct observation of Fermi velocity reduction of the moiré Dirac cones. These features suggest strong In_2Se_3 /graphene interlayer coupling, which is comparable with that in twisted bilayer graphene. The strategy expands the choice of materials in the heterostructure design and stimulates subsequent broad investigations of emergent physics at the sub-meV energy scale.

Hall state^[3a] and quantum fractal.^[3b] The underlying physics is derived from low-energy Dirac fermions renormalized by the superlattice potential. The key point to realize these emergent phenomena is to employ graphene/moiré superlattice potential as a way of modulation to bring closer the Dirac cones in reciprocal space, which are originally far apart in monolayer graphene. One of the effective approaches is to stack two atomic layers with identical or similar lattices to form long-range periodic moiré patterns. The resultant moiré Dirac cones are located in the extended (moiré) Brillouin zone (BZ) corners. For example, in TBG, the moiré Dirac cones appear at the corners of reciprocal hexagonal BZ defined by the two Dirac points of the bottom and top graphene layers which are rotated against each other.

In a generic tight-binding description,^[10] the appearance of moiré Dirac cones in graphene based heterostructure satisfies the generalized Umklapp scattering condition:

$$\bar{\mathbf{K}} + \bar{\mathbf{G}} = \bar{\mathbf{K}}' + \bar{\mathbf{G}}' \quad (1)$$

where $\bar{\mathbf{K}}$ and $\bar{\mathbf{K}}'$ are the in-plane wave vector of the original graphene Dirac cone and moiré Dirac cone, while the $\bar{\mathbf{G}}$ and $\bar{\mathbf{G}}'$ are

Recently, graphene-based heterostructures and twisted bilayer graphene (TBG) have been studied intensively due to their novel physics and promising properties such as strong light-matter interaction,^[1–8] quantum phase transition,^[9] correlated insulator,^[2] unconventional superconductivity,^[1] fractional quantum

Dr. Z. Wang, Dr. Y. Yu, Dr. M. Ma, Dr. F. Xu
National Innovation Institute of Defense Technology
Academy of Military Sciences PLA China
Beijing 100010, China
E-mail: wangzy@baqis.ac.cn

Dr. Z. Wang, Dr. X. Xie, Dr. M. Tong, Dr. G. Wang, Dr. T. Jiang
National University of Defense Technology
Changsha 410073, China

Dr. Z. Wang
Beijing Academy of Quantum Information Sciences
Beijing 100084, China

The ORCID identification number(s) for the author(s) of this article can be found under <https://doi.org/10.1002/adma.202007503>.

DOI: 10.1002/adma.202007503

Dr. Z. Hao, Dr. Y. Wang, Dr. K. Deng, Dr. Y.-J. Hao, Dr. X.-M. Ma, Dr. C. Liu, Dr. J. Mei, Dr. C. Liu, Dr. W. Huang, Dr. C. Chen
Shenzhen Institute for Quantum Science and Engineering (SIQSE)
and Department of Physics
Southern University of Science and Technology (SUSTech)
Shenzhen 518055, China
E-mail: chency@sustech.edu.cn

Dr. S. Kumar, Dr. K. Zhang, Dr. E. F. Schwier, Prof. K. Shimada
Hiroshima Synchrotron Radiation Center
Hiroshima University
Higashi-Hiroshima, Hiroshima 739-0046, Japan

Dr. J. Wang
Beijing Computational Science Research Center
Beijing 100193, China
E-mail: wangjf@csrc.ac.cn

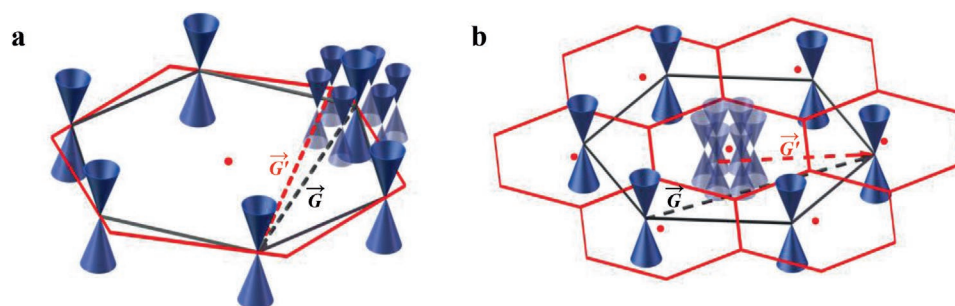


Figure 1. Schematic of moiré Dirac cones created in monolayer graphene-based heterostructures. Black (red) hexagons represent the BZs of monolayer graphene (its counterpart). The black (red) dashed arrows represent the reciprocal vectors of monolayer graphene (its counterpart). a) Graphene and hBN reciprocal vectors are slightly different. The moiré Dirac cones are surrounding graphene K-points. b) If the reciprocal vectors have larger mismatch, the moiré Dirac cones locate closer to the center of the BZ.

the reciprocal vector of graphene and its counterpart. As schematically shown in **Figure 1a**, we use a monolayer graphene/hBN heterostructure as a simple example to illustrate the moiré Dirac cone distribution in reciprocal space. The dashed arrows represent the reciprocal vector of graphene (\vec{G} , black) and hBN (\vec{G}' , red). Because \vec{G} and \vec{G}' are only slightly different (in both magnitude and direction) in graphene/hBN, the moiré-generated Dirac cone vector \vec{K} is also only slightly different from the original graphene Dirac cone vector \vec{K} . Consequently, the moiré Dirac cones mainly locate around the graphene hexagonal BZ corners (K points) as shown in **Figure 1a**.

The large-momentum location of moiré Dirac cones in graphene-based heterostructures and TBG imposes certain constraints on exploring their fine electronic structure in momentum-resolved experiment. In particular, the correlated insulator and unconventional superconducting phase in TBG involve band structure change in millielectronvolt (meV) scale^[1–2] around graphene K points ($k \approx 1.7 \text{ \AA}^{-1}$), a challenge for current angle-resolved photoemission spectroscopy (ARPES) measurement. Although ARPES with vacuum ultraviolet (VUV) laser is capable of achieving sub-meV resolution,^[5] its low excitation energy makes it impossible to cover the large-momentum space where those moiré Dirac cones are located. This fact leaves the fine electronic structure of magic-angle TBG^[1–2] unexplored, despite many theoretical speculations on the origin of the related exotic phenomena (for a review, see ref. [11]).

To investigate the detailed band structure and ultrafast dynamics of the renormalized moiré Dirac cones using ARPES and time-resolved ARPES, extreme-ultraviolet laser excitation would be needed,^[12] with energy-momentum resolution and signal-to-noise ratio being severely compromised. To break the impasse, we have taken an approach to create moiré Dirac cones around the BZ center (Γ -point). This is realized by engineering a heterostructure using components with larger lattice constant/reciprocal vector mismatch. As schematically shown in **Figure 1b**, the black hexagon represents the monolayer graphene BZ with its reciprocal vector $|\vec{G}| = 2.95 \text{ \AA}^{-1}$ and six Dirac cones occupying the BZ corners. The red hexagons represent the BZs of monolayer In_2Se_3 selected as its counterpart, with a reciprocal vector $|\vec{G}'| = 1.80 \text{ \AA}^{-1}$ which is rotated by $\approx 30^\circ$ with respect to graphene. The fact that $|\vec{G}'|$ is much smaller than $|\vec{G}|$ and close to $|\vec{K}| = |\vec{G}|/\sqrt{3}$ results in vanishing $|\vec{K}'|$. In this way, the moiré Dirac cones are located close to the Γ point.

We have grown monolayer In_2Se_3 /AB-stacking bilayer graphene (BLG) heterostructure by molecular-beam epitaxy (MBE). AB-stacking BLG shares the same lattice constant and reciprocal vector with monolayer graphene. Although BLG is $\approx 0.1 \text{ eV}$ gapped at the Dirac point, its lower Dirac cone in the range of 0–2 eV (the range considered in this work) with respect to the neutral point can still be approximated as a linear band with almost the same Fermi velocity as that of monolayer graphene.^[13] The low-energy electron diffraction (LEED) spots have indicated that monolayer In_2Se_3 is rotated $\approx 28^\circ$ with respect to BLG. Furthermore, the moiré superlattice of $\approx 3.6 \text{ nm}$ has been directly observed by scanning tunneling microscopy (STM), much smaller than that of graphene/hBN heterostructure^[7c] ($\approx 14 \text{ nm}$), in agreement with our expectation of the lattice registry. ARPES has directly revealed that the moiré Dirac cones are actually surrounding Γ point while the original graphene Dirac cones at the K-points. From the ARPES spectra we directly observe an $\approx 23\%$ reduction of the moiré Dirac cone Fermi velocity ($v_F \approx 5.8 \text{ eV \AA}$) compared to the original Dirac cones of BLG at K points ($v_F^0 \approx 7.5 \text{ eV \AA}$). This is the first direct confirmation of the Fermi velocity reduction of moiré Dirac cone despite the fact that there have been many theoretical predictions^[6] and indirect experimental evidence.^[2,7] Besides the Fermi velocity reduction, another evidence of moiré Dirac fermion renormalization is the elongated Dirac point formed at the Γ point where those moiré Dirac cones intersect each other. Our work not only effectively broadens the option of materials for van der Waals heterostructure engineering, to explore emerging phenomena such as superconductivity and strong correlation, but also paves the path to unveil the underlying physics in sub-meV energy scale with desired efficiency.

Monolayer In_2Se_3 samples were grown by MBE on BLG-terminated 6H-SiC(0001) substrates (**Figure 2a**), and preliminarily characterized by reflection high-energy electron diffraction (RHEED), LEED and STM. **Figure 2b–c** present typical RHEED patterns while **Figure 2d–e** present LEED patterns of substrate BLG and epitaxial In_2Se_3 . Sharp RHEED and LEED patterns indicate high-quality surfaces. Co-existence of BLG and In_2Se_3 patterns are observed in both RHEED and LEED of as-grown films, indicating the epitaxial In_2Se_3 is sub-monolayer. From the sharp RHEED/LEED streaks/spots one can estimate the corresponding in-plane lattice constant according to their distance. Using BLG as a standard reference with in-plan lattice

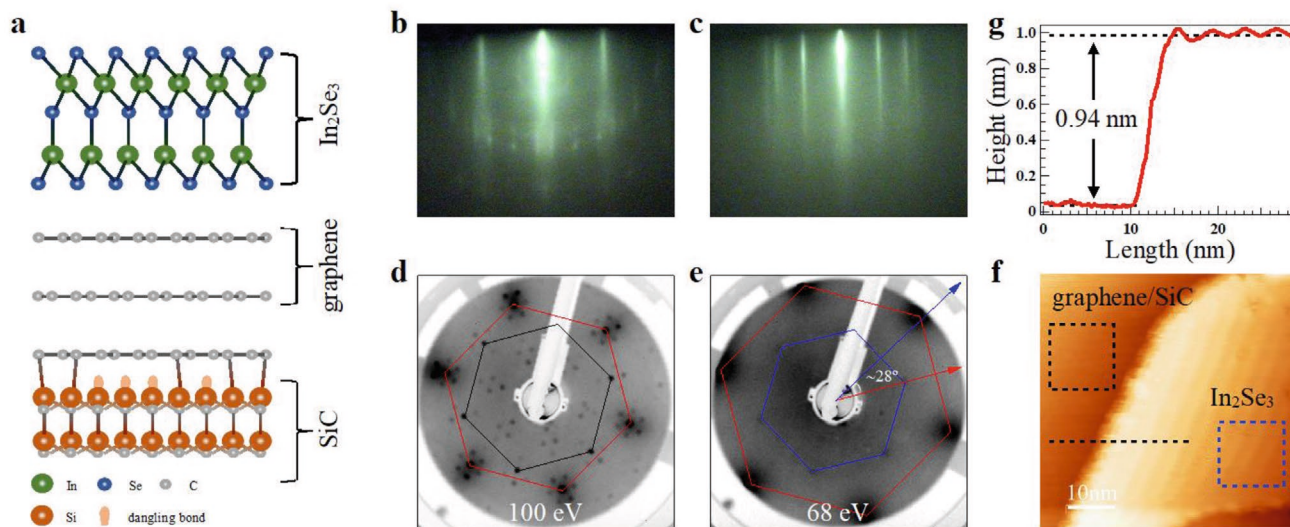


Figure 2. Materials growth and characterization. a) Side view of monolayer In_2Se_3 on BLG grown on 6H-SiC(0001). b,c) RHEED patterns of BLG/SiC substrate (b) and a sub-monolayer In_2Se_3 film grown on the BLG substrate (c). d,e) LEED patterns of the BLG (d) measured at electron energy 100 eV and epitaxial In_2Se_3 (e) measured at electron energy of 68 eV. The red lines indicate the diffraction pattern of graphene, while black lines correspond to SiC and blue to In_2Se_3 . f) STM morphology of epitaxial In_2Se_3 on BLG/SiC(0001), scanning parameters: $V = 100$ mV, $I = 0.1$ nA. g) The height profile along black dashed line in (f) shows ≈ 1.0 nm edge step, indicating that the In_2Se_3 island is of monolayer height. The black and blue dashed squares mark areas where atomic-resolution STM images of graphene (Figure 3c) and In_2Se_3 (Figure 3a,e) were acquired, respectively.

constant $a = 2.46$ Å, we found that the In_2Se_3 monolayer is rotated by $28^\circ \pm 1^\circ$ with respect to graphene lattice. The in-plane lattice constant of In_2Se_3 is estimated as $b = 4.0 \pm 0.1$ Å. Typical terrace-and-step morphology is observed by STM, as shown in Figure 2f. The height profile shows an edge step of 0.94 ± 0.02 nm, indicating an atomically sharp monolayer In_2Se_3 /BLG interface.^[14] All the RHEED, LEED and STM characterizations reveal the high crystalline quality of the as-grown In_2Se_3 monolayer.

To reveal the superlattice registry, we perform atomically resolved STM measurements, as shown in Figure 3. The substrate BLG surface (Figure 3c) exhibits a graphene like unit cell (BLG-UC) with a lattice constant $a = 2.46 \pm 0.01$ Å. As BLG is Bernal stacked, there is no BLG superlattice cell. The periodic structure with a length of 18.5 ± 0.1 Å observed in Figure 3c corresponds to the 6×6 corrugation of the interface carbon layer.^[15] The atoms of the In_2Se_3 surface (Figure 3a,e) show an unit cell (IS-UC) with a lattice constant $b = 4.02 \pm 0.01$ Å, which agrees well with the reported lattice constant of bulk In_2Se_3 , indicating strain-free epitaxial growth.^[14] The superlattice visible on the In_2Se_3 surface (IS-SC) has a lattice constant of $\lambda = 36.2 \pm 0.1$ Å. From both STM atomic structure and fast-Fourier transform (FFT) patterns, we found that the IS-SC is almost aligned with the IS-UC and both of them are rotated $\phi = 28^\circ \pm 1^\circ$ with respect to the BLG-UC. The lattice constant and orientation of monolayer In_2Se_3 extracted from STM agree well with those from LEED.

The lattice constants and alignment of In_2Se_3 and BLG indicate the possible presence of a commensurate moiré superlattice which should match the IS-SC periodicity. If we define the rhombohedra lattice vectors of BLG as \vec{a}_1 and \vec{a}_2 , In_2Se_3 as \vec{b}_1 and \vec{b}_2 , the moiré superlattice as \vec{c}_1 and \vec{c}_2 , the commensurability requires $\vec{c} = m_1 \vec{a}_1 + m_2 \vec{a}_2 = n_1 \vec{b}_1 + n_2 \vec{b}_2$. Using the STM

measured unit cell lattice constants as input, we found that $\frac{|\vec{c}|^2}{|\vec{a}|^2} = m_1^2 + m_1 m_2 + m_2^2 \approx 217$ and $\frac{|\vec{c}|^2}{|\vec{b}|^2} = n_1^2 + n_1 n_2 + n_2^2 \approx 81$. Solving these equations, we have extracted the commensurate moiré superlattice vector as $\vec{c} = 9\vec{a}_1 + 8\vec{a}_2 = 9\vec{b}_1$. The angle between BLG-UC and IS-SC would then be $\phi = \langle \vec{c}, \vec{a}_1 \rangle = \langle \vec{a}_1, \vec{b}_1 \rangle \approx 28^\circ$. Both length and angle of the calculated moiré match the experimentally determined IS-SC. In Figure 3g this commensurate configuration is strictly simulated and the moiré superlattice appears with the period as expected.

Having established a commensurate moiré superlattice, we proceed to explore its modulation imposed on the electronic structure. Figure 4a,b present the reciprocal BZs of the heterostructure components with their reciprocal vectors and orientation determined by LEED and STM. The red hexagons represent BLG BZ (with respect to BLG-UC) and K-points are their corners where the electronic Dirac cones locate. The blue hexagons represent the In_2Se_3 BZ related to the IS-UC. It is rotated by 28° with respect to the graphene BZ. The blue arrow indicates the reciprocal vector \vec{G}' of In_2Se_3 , whose magnitude and orientation are close to the BLG \vec{K} . In fact, we found that $|\vec{G}'| = 1.80$ Å⁻¹ and $|\vec{K}| = 1.70$ Å⁻¹ with a relative rotation of $\phi' = \langle \vec{G}', \vec{K} \rangle \approx 2^\circ$. In a simple picture, the Dirac cones at the BLG K-points are back-folded by the In_2Se_3 reciprocal vectors \vec{G}' to the central region of the heterostructure BZ, as shown in Figure 4b. In the inset of Figure 4a,b, we zoom in the BZ center and highlight the moiré superlattice BZ (related to IS-SC) in white. The scattered Dirac cones should locate at the moiré superlattice BZ corners.

To measure the electronic structure of graphene, a photon energy of 90 eV is used to cover the K points of its first BZ. In Figure 4c, one can see six point-like FSs at the K-points of the BLG BZ. The ARPES intensity map in Figure 4d shows linear

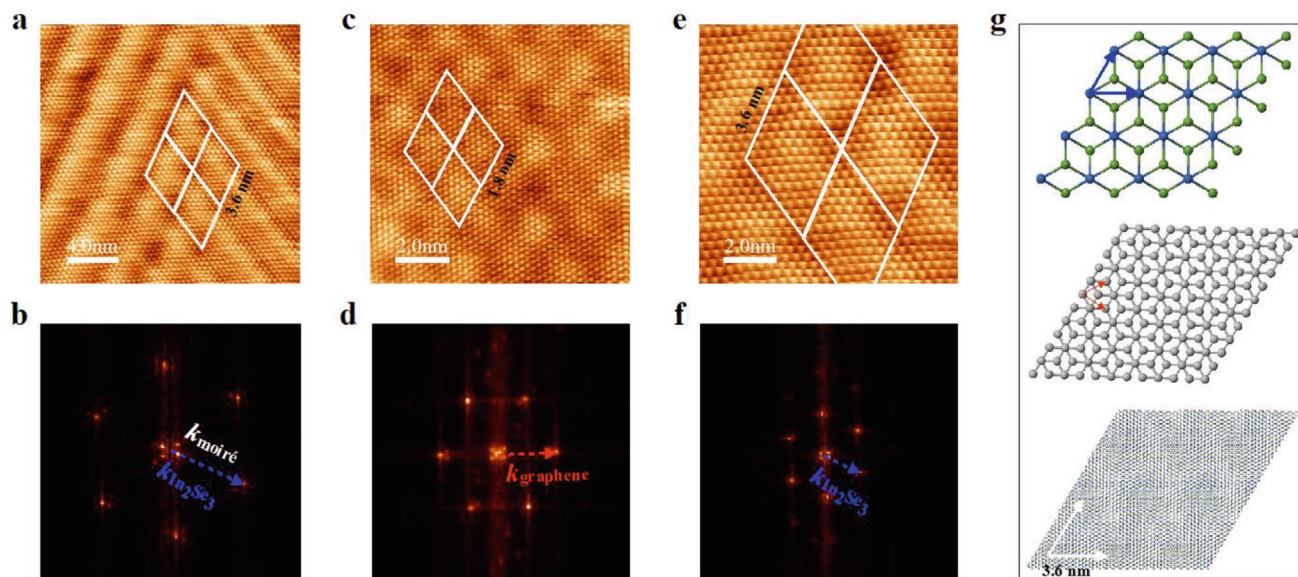


Figure 3. Atomically resolved moiré commensurate superlattices of BLG and $\text{In}_2\text{Se}_3/\text{BLG}$ heterostructures. a) High-resolution STM image of $\text{In}_2\text{Se}_3/\text{BLG}$ with a moiré pattern of $36.2 \pm 0.1 \text{ \AA}$. Scanning parameters: $V = 100 \text{ mV}$, $I = 1 \text{ nA}$. b) Fast-Fourier transform (FFT) of (a), showing that the lattice orientations of moiré pattern and In_2Se_3 are approximately the same. c, e) Zoomed-in STM images of BLG/SiC(0001) substrate (c) and epitaxial In_2Se_3 film (e), with topmost C and Se atoms resolved, respectively. Scanning parameters: c) $V = 100 \text{ mV}$, $I = 1 \text{ nA}$; e) $V = 50 \text{ mV}$, $I = 3 \text{ nA}$. The measured lattice constant of In_2Se_3 is $b = 4.02 \pm 0.01 \text{ \AA}$, indicating that the epitaxial layers are strain-free. d, f) Corresponding FFT maps of (c, e). Both the STM and FFT maps suggest that the In_2Se_3 lattice is rotated by $\approx 28^\circ$ with respect to graphene. g) Crystal structure of monolayer In_2Se_3 , BLG, and their superlattice moiré pattern in ball-and-stick model. The green, blue and gray balls represent In, Se, and C atoms, respectively. When the BLG and In_2Se_3 lattice are overlaid with a relative angle of 28° , a $36.2 \text{ \AA} \times 36.2 \text{ \AA}$ superlattice is formed.

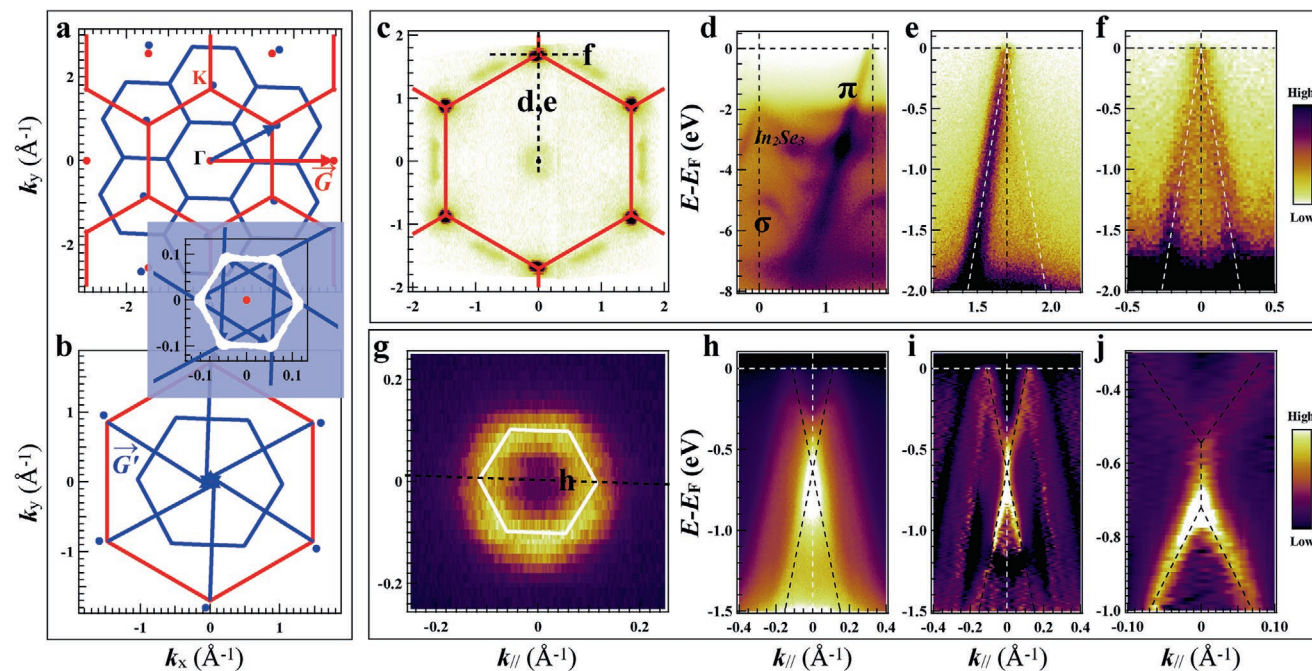


Figure 4. Γ point moiré Dirac cones and Fermi velocity reduction of $\text{In}_2\text{Se}_3/\text{BLG}$ heterostructures. a, b) Schematic BZs, reciprocal vectors and moiré Dirac cone positions. Red lines, arrows and points indicate graphene BZ, reciprocal vector, and Γ points while blue for In_2Se_3 . The inset zooms in the BZ center of (b) and the white hexagon indicate the moiré superlattice BZ. c–f) BLG Dirac cone Fermi surface (c) and dispersions (d–f). The black dashed lines in (c) indicate the momentum cuts where dispersions in (d–f) are taken. e) Magnification of (d) around the Dirac point. g–j) Moiré Dirac cone Fermi surface (g) and dispersions (h–j). The black dashed lines in (g) indicate the momentum cut where dispersion in (h) is taken. i) The 2D curvature of (h). j) The magnification of (i) at the Γ point.

band dispersion to the Fermi level, corresponding to the Dirac cone of underlying BLG. Figure 4e,f present the Dirac cone dispersions parallel and perpendicular to the $\bar{\Gamma}-\bar{K}$ directions. For both directions, the fitted dispersions (white dashed lines) yield a slope of $\approx 7.5 \text{ eV } \text{\AA}^{-1}$, corresponding to a Fermi velocity of $\approx 1.1 \times 10^6 \text{ ms}^{-1}$, in agreement with the reported results for quasi-free standing epitaxial graphene.^[13,16] It is worthy to note here that, while BLG is expected to have two Dirac cones and a small gap close to the Dirac point, here we can only distinguish mainly one linear Dirac cone without clear signature of gap opening. We believe that this is due to the broadening of the Dirac band observed here. The observed momentum width of the Dirac band ($\approx 0.1 \text{ \AA}^{-1}$) is comparable to the Dirac cone splitting in BLG ($\approx 0.1 \text{ \AA}^{-1}$),^[13] rendering generally single gapless Dirac cone.

The hole-like band locating $\approx 5 \text{ eV}$ below the Fermi level at the Γ point is the BLG-derived σ band. Furthermore, the hole-like bands in the energy range of $1.5\text{--}4 \text{ eV}$ below the Fermi level are assigned to the valence bands of monolayer In_2Se_3 , which's dispersion is also in agreement with theoretical expectation.^[17] From the Fermi surface (Figure 4c) one can find weak features besides the K-point Dirac cones. The weak features between adjacent K-points are attributed to Dirac cones of misoriented BLG which grew under a different ration with respect to the SiC substrate. The weak features around the Γ point suggest the existence of moiré Dirac cones as expected in Figure 4a,b and cannot be explained by a parasitic phase of BLG grown on 6H-SiC.

To clearly measure the moiré Dirac cones at the Γ point, we chose a photon energy of 21.2 eV for better momentum resolution. The corresponding electronic structures are shown in Figure 4g–j. Indeed, we found the expected moiré Dirac cones around the Γ point, with momentum $\approx 0.11 \text{ \AA}^{-1}$, matching well the expected moiré BZ as shown in Figure 4g. We note that these moiré Dirac cones form a continuous circle, instead of six discrete points, surrounding the Γ point, most likely due to the broadening of the dispersion and the misorientation of the substrate BLG. The latter has been discussed in the above paragraph, leaving the misoriented moiré Dirac cones filling the gap between adjacent K points of the moiré BZ. The individual cut (Figure 4h) contains two Dirac cones distributed symmetrically and centered on the Γ point. Even at the first glance one can notice the abrupt increase of the spectral intensity at the merging point (Γ point), reflecting much enhanced density of states. In order to better resolve the dispersion of the moiré Dirac cones, 2D curvature is employed to highlight the spectra weight peak position, as shown in Figure 4i,j.

Fermi velocity reduction is predicted in TBG^[6a–c] and graphene-based heterostructures^[6d] due to interlayer interaction. However, to the best of our knowledge, only negative^[7e,f] or indirect^[2,7a–d] experimental evidence has been reported so far. The moiré Dirac cones around Γ point allow us to resolve this conflict directly from the ARPES spectra. As show in Figure 4h,i, the moiré Dirac cone dispersion is tracked by profile peak locating and approximated with linear black dashed lines. In this linear approximation, the Fermi velocity of the moiré Dirac cones is estimated as $v_F \approx 5.8 \text{ eV } \text{\AA}^{-1}$ or $\approx 8.8 \times 10^5 \text{ ms}^{-1}$. This suggests a velocity reduction as much as $\approx 23\%$ with respect to the velocity of the Dirac cone of BLG at the K-point. According

to theoretical calculation,^[6d] this magnitude of reduction in the weak potential limit can be treated as:

$$v_F / v_F^0 = 1 - \frac{6V_0^2}{\hbar^2 v_F^0 \bar{G}^2} \quad (2)$$

where v_F^0 and v_F are the original and renormalized Fermi velocity of Dirac cones, V_0 is the strength of interlayer interaction induced by the substrate charges, and $\bar{G} = \bar{G} - \bar{G}'$ is the moiré superlattice reciprocal vector. From our experimental results, $v_F^0 \approx 7.5 \text{ eV } \text{\AA}^{-1}$ and $|\bar{G}| = 0.2 \text{ \AA}^{-1}$. The $\approx 23\%$ Fermi velocity reduction from our ARPES result corresponds to an interlayer coupling strength $V_0 = 0.3 \text{ eV}$, comparable with that in TBG.^[6a,b,7e]

Beside the Fermi velocity reduction, another distinct feature of the Dirac fermion renormalization is the elongated Dirac point. As shown in Figure 4j, magnification of the merging point of the moiré Dirac cone at the Γ point clearly presents deviation of band structure from the standard “X”-shaped crossing. In fact, the Dirac cone looks elongated and becomes nondispersive in an energy range of $\approx 0.17 \text{ eV}$, as schematically shown by the black dashed line in Figure 4j as a guide to the eye. One possibility of this Dirac point deformation is many-body effects^[18] such as electron–electron interaction or electron–plasmon interaction, which is strengthened by the much enhanced density of state. Due to the limited quasiparticle lifetime or ARPES resolution, the exact nature of the many-body effect remains unclear and deserves further investigation with optimized energy and momentum resolution as well as tuning of photon energy. Another possible explanation is a massless gap opening scenario,^[19] which accounts for the linear dispersion of the upper and lower Dirac cones (Figure 4j) and suggests a massless gap of $2\Delta \approx 0.17 \text{ eV}$. Both possibilities point to the presence of strong interactions between moiré Dirac cones. This, together with the reduced Fermi velocity, enables us to draw a conclusion on the emergence of renormalized moiré Dirac cones around the BZ center of $\text{In}_2\text{Se}_3/\text{BLG}$ heterostructure.

We have performed the first-principles calculations on the $\text{In}_2\text{Se}_3/\text{BLG}$ heterostructure. As shown in Figure 5a, the $\text{In}_2\text{Se}_3/\text{BLG}$ moiré superlattice is constructed by (9×9) monolayer In_2Se_3 and $(\sqrt{217} \times \sqrt{217})$ BLG with $\bar{c}_1 = 9\bar{a}_1 + 8\bar{a}_2 = 9\bar{b}_1$, $\bar{c}_2 = -8\bar{a}_1 + 17\bar{a}_2 = 9\bar{b}_2$, where \bar{a}_1 and \bar{a}_2 , \bar{b}_1 and \bar{b}_2 , \bar{c}_1 and \bar{c}_2 are the rhombohedra lattice vectors of BLG, In_2Se_3 and moiré superlattice respectively. The interlayer distance of BLG is 3.44 \AA , and the relaxed distance between BLG and In_2Se_3 is 3.45 \AA .

Unfolded bands are calculated to compare with the experimental ARPES in the BZ of graphene, as shown in Figure 5b. By projecting to different atoms, we can identify the contributions of graphene and In_2Se_3 . It is seen that the calculated π bands of graphene or BLG exactly coincide with the ARPES observations, while the energies of calculated σ bands are higher than the experimental measurements. The bands contributed by In_2Se_3 are also roughly consistent with the observations. Importantly, from the nearly linear π band (highlighted by green line in the right panel of Figure 5b), the Fermi velocity is calculated as $6.86 \text{ eV } \text{\AA}^{-1}$, consistent with the measurement.

To check the emerging Dirac cone at the Γ point, we calculate the band structure in the BZ of moiré superlattice, and project

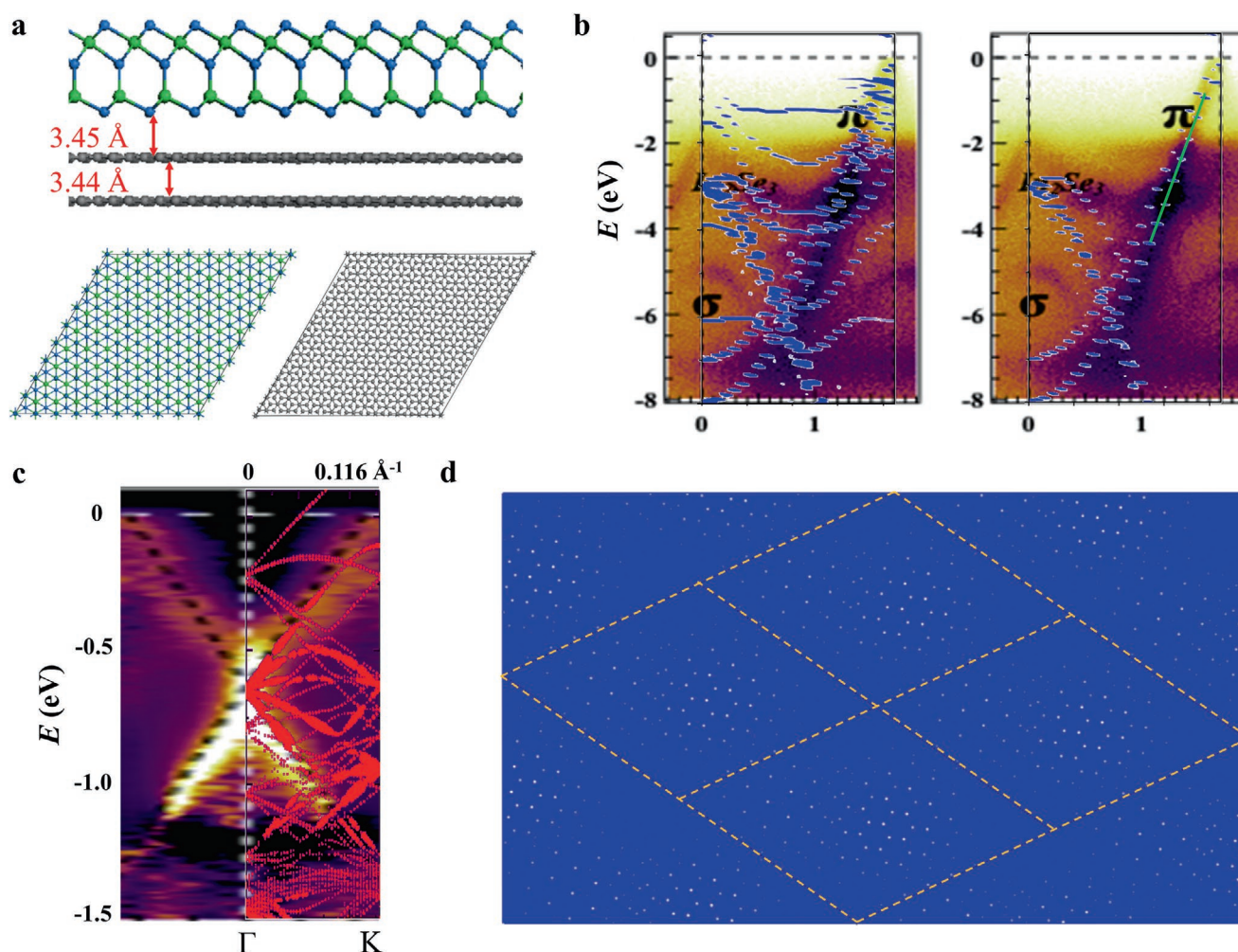


Figure 5. Results from the first-principles calculations. a) Adopted structure of $\text{In}_2\text{Se}_3/\text{BLG}$ for calculations. Top (bottom): Side (top) view of the structure. b) Unfolded bands along ΓK in the BZ of graphene and comparison with the experimental ARPES. Left: unfolded bands projected to all atoms of $\text{In}_2\text{Se}_3/\text{BLG}$. Right: unfolded bands projected to the top-layer graphene. c) Band structure projected to the top-layer graphene of BLG along $\Gamma\text{--K}$ in the BZ of the moiré superlattice, and the comparison with experiments. d) Charge distribution (white point) of the emerging Dirac state at the Γ point.

it to the top-layer graphene, as shown in Figure 5c. An energy shift of 0.2 eV is implemented to better match the experiment, which corresponds to the case of hole doping. Remarkably, an “elongated” Dirac point is formed at the Γ point, in good agreement with the ARPES observation. Based on our calculations, the observed “elongation” of Dirac point actually arises from the gap opening (≈ 50 meV) of Dirac cone at Γ , indicating an interaction between In_2Se_3 and graphene in the moiré superlattice. The calculated Fermi velocity is 5.47 eV \AA ; $\approx 20\%$ reduction compared to the unfolded π band of graphene, also consistent with the experimental measurement. In Figure 5d, we plot the charge distribution of “elongated” Dirac point. Instead of the uniform distribution in graphene, a moiré pattern of charge density is formed, which further confirms the moiré Dirac fermion renormalization and interactions.

We have realized for the first time a practical strategy to construct moiré Dirac cone around the BZ center by folding graphene Dirac cones through van der Waals heterostructure engineering. From comprehensive microscopic and spectroscopic characterization, this strategy has been demonstrated to be feasible in

monolayer $\text{In}_2\text{Se}_3/\text{BLG}$ heterostructures. By combining the first-principles calculations, the Fermi velocity reduction and the elongated Dirac point at Γ have been verified. From the charge distribution of the elongated Dirac point, a moiré pattern of charge density is formed, which further confirms the moiré Dirac fermion renormalization and interactions. More exotic physics and properties, such as Kekulé textures,^[20] strong electron correlation, unconventional superconductivity, or strong light-matter interaction, are expected to emerge by material engineering. The location of the moiré Dirac cone around the BZ center allows direct band structure measurement with sub-meV energy resolution and ultrafast electronic dynamics study combining hundreds-of-femtosecond time resolution and tens-of-meV energy resolution. These advantages pave the way to understand the exotic physics triggered by the moiré Dirac fermion renormalization in the underlying electronic structure. Furthermore, this strategy will stimulate broad investigation in graphene-based heterostructure engineering, namely, quantum transport and electronic structure study using In_2Se_3 -like materials such as InSe family, topological Bi_2Se_3 family, and antiferromagnetic topological MnBi_2Te_4 family of materials.

Experimental Section

Sample Preparation: Epitaxial growth of In_2Se_3 samples was performed in an MBE chamber with a base pressure of 1×10^{-10} mbar. Prior to growth, the 6H-SiC(0001) substrates were treated by flash heating to ≈ 1400 °C to form BLG. After cooling down, the substrate temperature was kept between 250 and 300 °C to perform MBE growth. The elemental In (99.999%) and Se (99.999%) sources were simultaneously evaporated from independent Knudsen cells with temperature set to 700 and 140 °C, respectively. Such Se-rich conditions ensured the crystallinity and stoichiometry of epitaxial In_2Se_3 . The growth process was real-time monitored by RHEED operated at 25 kV.

ARPES and STM Measurements: In situ measurements were performed in an ultrahigh vacuum system including MBE, STM (SPECS), and ARPES (VG-Scienta R4000). STM measurements were carried out at room temperature with platinum–iridium tips. Helium-lamp-based ARPES measurements were carried out at 80 K with unpolarized He-I α photons (21.2 eV) generated by a Gammadata discharge lamp.

Ex situ ARPES measurements were performed at the Beamline 1 of Hiroshima Synchrotron Radiation Center (HSRC)^[21] Hiroshima, Japan with a VG Scienta R4000 electron analyzer and a photon energy of 30–90 eV. The beam was linearly polarized with its polarization lying in the measurement and incidence plane. The energy and angular resolution were better than 20 meV and less than 0.1°, respectively. Samples were measured under ultrahigh vacuum conditions with pressure better than 5×10^{-11} mbar and temperatures below 25 K. Amorphous Se capping and decapping were employed to retain the clean surface of as-grown samples.

Supporting Information

Supporting Information is available from the Wiley Online Library or from the author.

Acknowledgements

Z.W., Z.H., and Y.Y. contributed equally to this work. Z.W. is supported by the General Program of Beijing Academy of Quantum Information Sciences (Project Y18G17), the National Natural Science Foundation of China (NSFC) (Grant No. 12004434), and the Opening Foundation of State Key Laboratory of High-Performance Computing (Grant No. 201601-02). C.C. is supported by NSFC (Grant No. 12074163), the Shenzhen High-Level Special Fund (Grant Nos. G02206304, G02206404), the Guangdong Innovative and Entrepreneurial Research Team Program (Grant No. 2019ZT08C044), Shenzhen Science and Technology Program (Grant No. KQTD20190929173815000), and the University Innovative Team in Guangdong Province (Grant No. 2020KCXTD001). J.W. acknowledges the support from NSFC (Grant No. 12004030). ARPES measurements were performed with the approval of the Proposal Assessing Committee of the Hiroshima Synchrotron Radiation Center (Proposal Nos. 19BU002, 19BU005, 19BG044, 19BG006). The authors thank Prof. Qihang Liu for helpful discussions.

Conflict of Interest

The authors declare no conflict of interest.

Data Availability Statement

The data that support the findings of this study are available from the corresponding author upon reasonable request.

Keywords

“elongated” Dirac points, Fermi velocity reduction, In_2Se_3 /bilayer graphene heterostructures, interlayer coupling, moiré Dirac cones

Received: November 2, 2020

Revised: January 24, 2021

Published online: March 19, 2021

- [1] a) Y. Cao, V. Fatemi, S. Fang, K. Watanabe, T. Taniguchi, E. Kaxiras, P. Jarillo-Herrero, *Nature* **2018**, 556, 43; b) A. Kerelsky, L. J. McGilly, D. M. Kennes, L. Xian, M. Yankowitz, S. Chen, K. Watanabe, T. Taniguchi, J. Hone, C. Dean, A. Rubio, A. N. Pasupathy, *Nature* **2019**, 572, 95; c) M. Yankowitz, S. Chen, H. Polshyn, Y. Zhang, K. Watanabe, T. Taniguchi, D. Graf, A. F. Young, C. R. Dean, *Science* **2019**, 363, 1059.
- [2] Y. Cao, V. Fatemi, A. Demir, S. Fang, S. L. Tomarken, J. Y. Luo, J. D. Sanchez-Yamagishi, K. Watanabe, T. Taniguchi, E. Kaxiras, R. C. Ashoori, P. Jarillo-Herrero, *Nature* **2018**, 556, 80.
- [3] a) B. Hunt, J. D. Sanchez-Yamagishi, A. F. Young, M. Yankowitz, B. J. LeRoy, K. Watanabe, T. Taniguchi, P. Moon, M. Koshino, P. Jarillo-Herrero, R. C. Ashoori, *Science* **2013**, 340, 1427; b) C. R. Dean, L. Wang, P. Maher, C. Forsythe, F. Ghahari, Y. Gao, J. Katoch, M. Ishigami, P. Moon, M. Koshino, T. Taniguchi, K. Watanabe, K. L. Shepard, J. Hone, P. Kim, *Nature* **2013**, 497, 598.
- [4] a) H. Isobe, N. F. Q. Yuan, L. Fu, *Phys. Rev. X* **2018**, 8, 041041; b) J. Gonzalez, T. Stauber, *Phys. Rev. Lett.* **2019**, 122, 026801; c) N. F. Q. Yuan, H. Isobe, L. Fu, *Nat. Commun.* **2019**, 10, 5769; d) Y. Choi, J. Kemmer, Y. Peng, A. Thomson, H. Arora, R. Polski, Y. Zhang, H. Ren, J. Alicea, G. Refael, F. von Oppen, K. Watanabe, T. Taniguchi, S. Nadj-Perge, *Nat. Phys.* **2019**, 15, 1174; e) G. Li, A. Luican, J. M. B. Lopes dos Santos, A. H. Castro Neto, A. Reina, J. Kong, E. Y. Andrei, *Nat. Phys.* **2009**, 6, 109; f) L. A. Ponomarenko, R. V. Gorbachev, G. L. Yu, D. C. Elias, R. Jalil, A. A. Patel, A. Mishchenko, A. S. Mayorov, C. R. Woods, J. R. Wallbank, M. Mucha-Kruczynski, B. A. Piot, M. Potemski, I. V. Grigorieva, K. S. Novoselov, F. Guinea, V. I. Fal'ko, A. K. Geim, *Nature* **2013**, 497, 594.
- [5] a) H. Iwasawa, E. F. Schwier, M. Arita, A. Ino, H. Namatame, M. Taniguchi, Y. Aiura, K. Shimada, *Ultramicroscopy* **2017**, 182, 85; b) G. D. Liu, G. L. Wang, Y. Zhu, H. B. Zhang, G. C. Zhang, X. Y. Wang, Y. Zhou, W. T. Zhang, H. Y. Liu, L. Zhao, J. Q. Meng, X. L. Dong, C. T. Chen, Z. Y. Xu, X. J. Zhou, *Rev. Sci. Instrum.* **2008**, 79, 023105.
- [6] a) J. M. Lopes Dos Santos, N. M. Peres, A. H. Castro Neto, *Phys. Rev. Lett.* **2007**, 99, 256802; b) G. Trambly de Laissardiere, D. Mayou, L. Magaud, *Nano Lett.* **2010**, 10, 804; c) R. Bistritzer, A. H. MacDonald, *Proc. Natl. Acad. Sci. USA* **2011**, 108, 12233; d) C. Ortix, L. Yang, J. van den Brink, *Phys. Rev. B* **2012**, 86, 081405.
- [7] a) Z. Ni, Y. Wang, T. Yu, Y. You, Z. Shen, *Phys. Rev. B* **2008**, 77, 235403; b) A. Luican, G. Li, A. Reina, J. Kong, R. R. Nair, K. S. Novoselov, A. K. Geim, E. Y. Andrei, *Phys. Rev. Lett.* **2011**, 106, 126802; c) M. Yankowitz, J. Xue, D. Cormode, J. D. Sanchez-Yamagishi, K. Watanabe, T. Taniguchi, P. Jarillo-Herrero, P. Jacquod, B. J. LeRoy, *Nat. Phys.* **2012**, 8, 382; d) L.-J. Yin, J.-B. Qiao, W.-X. Wang, W.-J. Zuo, W. Yan, R. Xu, R.-F. Dou, J.-C. Nie, L. He, *Phys. Rev. B* **2015**, 92, 201408; e) J. Hicks, M. Sprinkle, K. Shepperd, F. Wang, A. Tejeda, A. Taleb-Ibrahimi, F. Bertran, P. Le Fèvre, W. A. de Heer, C. Berger, E. H. Conrad, *Phys. Rev. B* **2011**, 83, 205403; f) S. J. Ahn, P. Moon, T.-H. Kim, H.-W. Kim, H.-C. Shin, E. H. Kim, H. W. Cha, S.-J. Kahng, P. Kim, M. Koshino, *Science* **2018**, 361, 782.
- [8] L. Britnell, R. Ribeiro, A. Eckmann, R. Jalil, B. Belle, A. Mishchenko, Y.-J. Kim, R. Gorbachev, T. Georgiou, S. Morozov, *Science* **2013**, 340, 1311.
- [9] Y. Kim, P. Herlinger, P. Moon, M. Koshino, T. Taniguchi, K. Watanabe, J. H. Smet, *Nano Lett.* **2016**, 16, 5053.

- [10] M. Koshino, *New J. Phys.* **2015**, *17*, 015014.
- [11] A. Nimbalkar, H. Kim, *Nano-Micro Lett.* **2020**, *12*, 126.
- [12] I. Gierz, J. C. Petersen, M. Mitrano, C. Cacho, I. C. Turcu, E. Springate, A. Stohr, A. Kohler, U. Starke, A. Cavalleri, *Nat. Mater.* **2013**, *12*, 1119.
- [13] T. Ohta, A. Bostwick, J. L. McChesney, T. Seyller, K. Horn, E. Rotenberg, *Phys. Rev. Lett.* **2007**, *98*, 206802.
- [14] S. Popović, B. Čelustka, D. Bidjin, *Phys. Status Solidi A* **1971**, *6*, 301.
- [15] C. Riedl, C. Coletti, U. Starke, *J. Phys. D: Appl. Phys.* **2010**, *43*, 374009.
- [16] S. Forti, K. V. Emtsev, C. Coletti, A. A. Zakharov, C. Riedl, U. Starke, *Phys. Rev. B* **2011**, *84*, 125449.
- [17] W. Ding, J. Zhu, Z. Wang, Y. Gao, D. Xiao, Y. Gu, Z. Zhang, W. Zhu, *Nat. Commun.* **2017**, *8*, 14956.
- [18] L. Miao, Z. F. Wang, W. Ming, M. Y. Yao, M. Wang, F. Yang, Y. R. Song, F. Zhu, A. V. Fedorov, Z. Sun, C. L. Gao, C. Liu, Q. K. Xue, C. X. Liu, F. Liu, D. Qian, J. F. Jia, *Proc. Natl. Acad. Sci. USA* **2013**, *110*, 2758.
- [19] L. Benfatto, E. Cappelluti, *Phys. Rev. B* **2008**, *78*, 115434.
- [20] G. Giovannetti, M. Capone, J. van den Brink, C. Ortix, *Phys. Rev. B* **2015**, *91*, 121417.
- [21] H. Iwasawa, K. Shimada, E. F. Schwier, M. Zheng, Y. Kojima, H. Hayashi, J. Jiang, M. Higashiguchi, Y. Aiura, H. Namatame, M. Taniguchi, *J. Synchrotron Radiat.* **2017**, *24*, 836.

Distinct Topological Surface States on the Two Terminations of MnBi_4Te_7

Xuefeng Wu,^{1,*} Jiayu Li^{1,*}, Xiao-Ming Ma^{1,*}, Yu Zhang^{1,2,*}, Yuntian Liu,¹ Chun-Sheng Zhou,¹ Jifeng Shao,¹ Qiaoming Wang,¹ Yu-Jie Hao,¹ Yue Feng,¹ Eike F. Schwier,³ Shiv Kumar,³ Hongyi Sun,¹ Pengfei Liu,¹ Kenya Shimada³, Koji Miyamoto,³ Taichi Okuda,³ Kedong Wang,¹ Maohai Xie², Chaoyu Chen¹, Qihang Liu^{1,4,†}, Chang Liu^{1,‡} and Yue Zhao^{1,§}

¹*Shenzhen Institute for Quantum Science and Engineering and Department of Physics, Southern University of Science and Technology, Shenzhen 518055, China*

²*Department of Physics, The University of Hong Kong, Hong Kong, China*

³*Hiroshima Synchrotron Radiation Center, Hiroshima University, 2-313 Kagamiyama, Higashi-Hiroshima 739-0046, Japan*

⁴*Guangdong Provincial Key Laboratory for Computational Science and Material Design, Southern University of Science and Technology, Shenzhen 518055, China*



(Received 6 February 2020; revised 15 April 2020; accepted 5 May 2020; published 16 July 2020)

The recently discovered intrinsic magnetic topological insulator MnBi_2Te_4 has been met with unusual success in hosting emergent phenomena such as the quantum anomalous Hall effect and the axion insulator states. However, the surface-bulk correspondence of the Mn-Bi-Te family, composed by the superlatticelike $\text{MnBi}_2\text{Te}_4/(\text{Bi}_2\text{Te}_3)_n$ ($n = 0, 1, 2, 3, \dots$) layered structure, remains intriguing but elusive. Here, by using scanning tunneling microscopy and angle-resolved photoemission spectroscopy techniques, we unambiguously assign the two distinct surface states of MnBi_4Te_7 ($n = 1$) to the quintuple-layer (QL) Bi_2Te_3 termination and the septuple-layer (SL) MnBi_2Te_4 termination, respectively. A comparison of the experimental observations with theoretical calculations reveals diverging topological behaviors, especially the hybridization effect between the QL and SL, on the two terminations. We identify a gap on the QL termination, originating from the hybridization between the topological surface states of the QL and the bands of the SL beneath, and a gapless Dirac-cone band structure on the SL termination with time-reversal symmetry. The quasiparticle interference patterns further confirm the topological nature of the surface states for both terminations, continuing far above the Fermi energy. The QL termination carries a spin-helical Dirac state with hexagonal warping, while at the SL termination, a strongly canted helical state from the surface lies between a pair of Rashba-like splitting bands from its neighboring layer. Our work elucidates an unprecedented hybridization effect between the building blocks of the topological surface states and also reveals the termination-dependent time-reversal symmetry breaking in a magnetic topological insulator.

DOI: [10.1103/PhysRevX.10.031013](https://doi.org/10.1103/PhysRevX.10.031013)

Subject Areas: Condensed Matter Physics, Magnetism, Topological Insulators

I. INTRODUCTION

The recent discovery of the intrinsic magnetic topological insulator MnBi_2Te_4 and its derivatives $\text{MnBi}_2\text{Te}_4/(\text{Bi}_2\text{Te}_3)_n$ ($n = 1, 2, \dots$), comprising alternating

layers of MnBi_2Te_4 and nonmagnetic topological insulator (TI) Bi_2Te_3 , has boosted exciting possibilities of producing exotic quantum phenomena by engineering topology and magnetism at the atomic scale [1–10]. Specifically, MnBi_2Te_4 , having antiferromagnetic (AFM) order and, thus, broken time-reversal symmetry, holds the potential for realizing both a quantum anomalous Hall insulator and an axion insulator [11–13]. When subjected to an external magnetic field of around 5–10 T, few-layer MnBi_2Te_4 turns to a ferromagnetic (FM) quantum anomalous Hall insulator [11,12]. On the other hand, a zero Hall plateau is observed in even-layer MnBi_2Te_4 as an indicator for the axion insulator [13]. However, recent angle-resolved photoemission spectroscopy (ARPES) measurements show a robust surface Dirac cone, indicating that time-reversal symmetry is preserved at the surface of MnBi_2Te_4 [14–17]. Other members in van der Waals $\text{MnBi}_2\text{Te}_4/(\text{Bi}_2\text{Te}_3)_n$, with

*These authors contributed equally to this work.

†To whom correspondence should be addressed. liuqh@sustech.edu.cn.

‡To whom correspondence should be addressed. liuc@sustech.edu.cn

§To whom correspondence should be addressed. zhaoy@sustech.edu.cn

Published by the American Physical Society under the terms of the [Creative Commons Attribution 4.0 International license](https://creativecommons.org/licenses/by/4.0/). Further distribution of this work must maintain attribution to the author(s) and the published article's title, journal citation, and DOI.

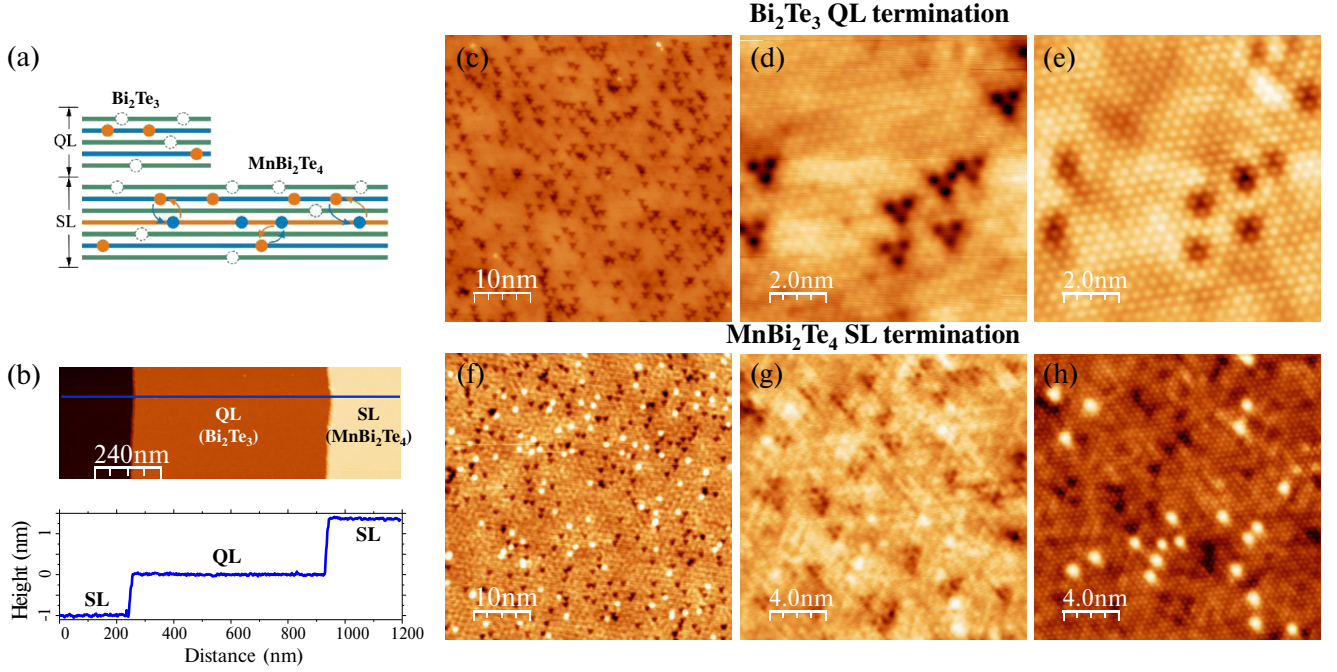


FIG. 1. STM topographic images of the MnBi₄Te₇ surface. (a) Schematic diagram of two terminations—the QL termination of Bi₂Te₃ and the SL termination of MnBi₂Te₄—with atomic defects. (b) A large area topographic image of MnBi₄Te₇ surface showing two kinds of terrace steps. The lower part of (b) shows a line profile with step heights of 1.01 and 1.35 nm along the blue line, for the QL termination of Bi₂Te₃ and the SL termination of MnBi₂Te₄, respectively. A considerable number of defects can be found in the enlarged views of the QL (c) and SL (f) terminations. (d), (e) and (g), (h) are the atomic resolution images of the same areas at different biases on the QL and SL terminations, respectively. The dark defects are found on both QL and SL terminations. For the SL, an additional type of defect is observed as a bright dot at both positive and negative biases. Tunneling parameters: (b) $V_{\text{bias}} = 1.2$ V, and $I_t = 20$ pA; (c), (f) $V_{\text{bias}} = 1.0$ V and $I_t = 20$ pA; (d) $V_{\text{bias}} = 0.5$ V and $I_t = 1$ nA; (e) $V_{\text{bias}} = -1$ V and $I_t = 1$ nA; (g) $V_{\text{bias}} = 0.5$ V and $I_t = 200$ pA; (h) $V_{\text{bias}} = -1$ V and $I_t = 200$ pA.

tunable interlayer magnetic exchange coupling, also exhibit controversially a gap or gapless feature at different terminations [18–25], highlighting the complication of the interplay between magnetism and topology and the crucial role of defects and disorder in such a material system.

Surface-bulk correspondence is generally considered to be the unifying feature relating the topology of the bulk bands to the surface states in topological materials [26]. However, this correspondence is intriguing in the superlattice-like MnBi₂Te₄/(Bi₂Te₃)_n layered structure for $n \geq 1$, where the hybrid structure creates distinct electronic structures on separate terminations due to the interplay of topology and magnetism at the interfaces of magnetic TI (MnBi₂Te₄) and nonmagnetic TI (Bi₂Te₃) layers. Local probe approaches to the scattering processes [27–29] on different terminations of the van der Waals heterostructure are crucial to determine the spin configuration of the topological surface states and advance the theoretical understanding of heterostructure engineering. Moreover, despite the evidence of the band structure in MnBi₂Te₄/(Bi₂Te₃)_n series from ARPES and transport studies, so far there has been little experimental work on probing the robustness of these states against scattering

[30,31], which is one of the key properties toward the application of topological devices.

Here, we present the first local probe scanning tunneling microscopy (STM) measurements of MnBi₄Te₇ ($n = 1$) in both the real and momentum spaces. Combined with the observed ARPES band dispersion, we unambiguously assign the observed electronic band structures to the MnBi₂Te₄ septuple-layer (SL) and Bi₂Te₃ quintuple-layer (QL) terminations. Together with the input of ARPES (both regular and spin-resolved) and theoretical calculations, further investigation on the scattering process by quasiparticle interference (QPI) patterns unveils the spin configuration of their topological surface states. Unlike the surface state of a conventional TI (e.g., Bi₂Se₃) that is simply localized at the surface layer with attenuation into the bulk, the surface states of MnBi₄Te₇ show strong hybridization between the SL and QL at both terminations. For QL termination, a gap is formed due to the hybridization between the topological surface bands of the topmost QL and the bands from the neighboring SL. For SL termination, our results suggest a restoration of time-reversal symmetry, possibly due to the magnetically disordered surface. The spin texture of the topological surface

bands shows a pair of Rashba-like splitting bands from the QL underneath and a strongly warped band from the SL, the hybridization of which contributes to the flower-shaped QPI patterns. Our findings of such diverging topological behaviors on the two terminations of MnBi_4Te_7 strongly rely on the hybridization of bands from different building blocks of magnetic TI and nonmagnetic TI, providing new insights into the surface-bulk correspondence of magnetic TIs and guidance to heterostructure engineering in the emerging intrinsic magnetic topological systems.

II. SURFACE TOPOGRAPHY

Figure 1 illustrates the topographic images obtained by STM, where the two terminations are identified unambiguously. As shown in Fig. 1(b), the crystal naturally cleaves at the QL termination of Bi_2Te_3 and the SL termination of MnBi_2Te_4 with step heights of 1.01 and 1.35 nm, respectively. Comparing the enlarged views of the QL [Fig. 1(c)] and SL [Fig. 1(f)] terminations, many more surface defects can be found on the SL termination. Even on the surface defect-free area, QL termination shows less corrugation, indicating lower bulk defect beneath the topmost layer (Fig. S2 [32]). Two types of major defects are found on the SL surface, categorized as bright and dark spots, the former of which is almost absent on the QL surface. We then obtain the atomic resolution images of the Te-terminated QL [Figs. 1(d) and 1(e)] and SL [Figs. 1(g) and 1(h)] surfaces at different bias voltages. Similar bright spots are also found in the STM study of MnBi_2Te_4 [33]. On both terminations, the dark defects merge from triangularly placed holes to one triangular dark spot when the bias voltage is shifted from 0.5 to -1 V, while the atoms from the topmost layer remain intact. Right on top of the dark defects on both terminations, as shown in Fig. S2 [32], there is a slight rightward shift (approximately 10 meV) of dI/dV spectra compared with the defect-free area, indicating a local p -type doping from this local defect. Such topographic and spectroscopic behaviors were previously seen on the surface of Mn-doped Bi_2Te_3 [34,35], where it is attributed to be substitutional Mn atoms close to the sample surface. This similarity, especially on the QL with limited types of surface defects, implies the possibility of magnetic atom migration from the designed sites in the middle of the SL. The density of such defects is about 3.0% on the QL termination and 2.1% on the SL termination. Note that these results are for the topmost and the second atomic layer, as STM is surface sensitive. The possibility of Mn migration may induce complicated surface magnetic order or disorder on both terminations, especially for the QL, as stated in previous studies that such an amount of magnetic dopant is sufficient enough to induce long-range ferromagnetic order in magnetically doped topological insulators [28,36,37].

III. ELECTRONIC STRUCTURES

We now focus on the defect-free regions to obtain our averaged dI/dV spectra by scanning tunneling spectroscopy (STS). The results, as shown in Fig. 2(a), reveal a great suppression of density of states (DOS) from approximately -285 to -350 meV on the QL termination, differing from the V-shaped, Dirac-like suppression of the DOS near approximately -285 meV on the SL termination. The SL surface holds a higher density of states above -285 meV, while, on the other side (below approximately -400 meV), the QL surface hosts higher DOS. Although it is not straightforward to determine gaps or positions of bands solely from the STS spectra, we can compare with our ARPES data to gain a better understanding of the states. Figures 2(c) and 2(d) are two representative laser- μ -ARPES spectra obtained from the same batch of crystals [38], representing the electronic structure on the two surface terminations of MnBi_4Te_7 . In Fig. 2(c), the outer electron pocket at $\bar{\Gamma}$ is seen to have a relatively flat bottom, where an apparent gaplike suppression of spectral weight is observed between $E = -270$ to -320 meV, in agreement with the STS at the QL termination [marked by the purple and the red arrows in Figs. 2(a) and 2(c)]. Much higher ARPES intensity is observed for the bands below $E = -400$ meV, which is also reproduced by the high DOS below -400 meV bias voltage in the STS. We thus conclude that Fig. 2(c) shows the band structure of the QL termination. Similar analysis also reveals that Fig. 2(d) depicts the bands of the SL termination, where a high DOS is observed from E_F to $E = -0.3$ eV. In this energy region, the bottom of one of the conduction bands at $E = -150$ meV can be identified in the STS by a DOS peak [brown arrows in Figs. 2(a) and 2(d)]. Moreover, the X-shaped, Dirac-like linear dispersion and the gapless crossing point at $E = -285$ meV [red arrow in Fig. 2(d)] is endorsed by a V-shaped dip at the SL STS whose minimum locates at approximately -280 meV [red arrow in Fig. 2(a)]. Therefore, by comparing with the STS spectra, we experimentally ascertain the assignment of the QL and SL terminations in the ARPES measurements for the first time, which is also confirmed by our surface-dependent DOS calculations from density functional theory (DFT) [see Fig. 2(a)].

We also perform DFT calculations of the band dispersion for MnBi_4Te_7 slabs to advance our understanding of the two terminations. For the QL termination, we assume that the local moment of the SLs near the surface remains the same as that in the bulk, i.e., A-type AFM with out-of-plane spin orientation confirmed by neutron diffraction measurements [39]. The resulting band structure in Fig. 2(e) shows that the Dirac cone of the surface states is gapped by the magnetic proximity from the second SL, merging into the valence band at approximately 400 meV below the Fermi level [see the green box in Fig. 2(e)]. More importantly, an indirect gap near the Dirac point energy occurs. The layer

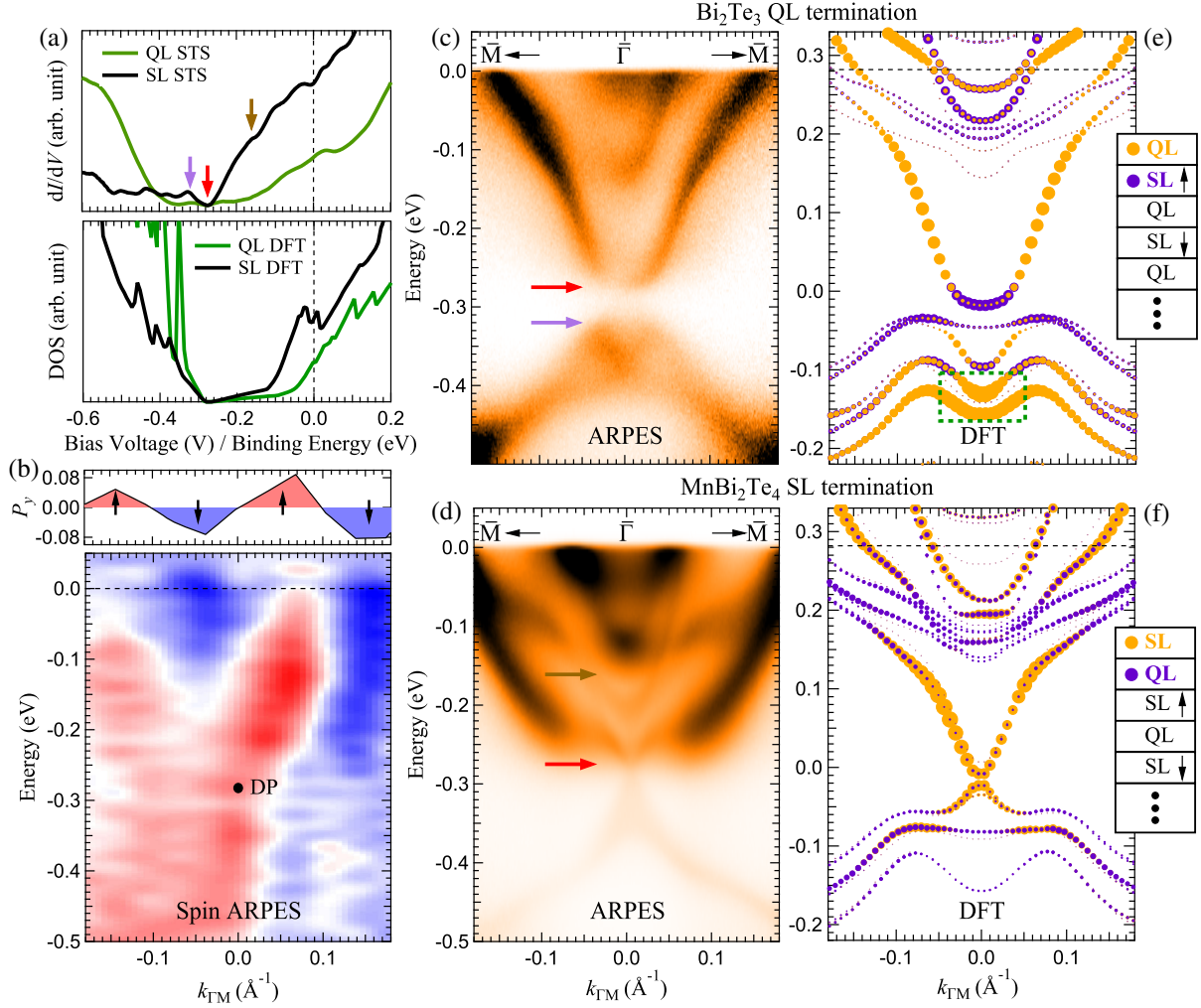


FIG. 2. Electronic structure of the two terminations of MnBi₄Te₇. (a) Top: Averaged dI/dV spectra of a series of STS spectra obtained at defect-free areas of the QL (green) and SL (black) terminations. Tunneling parameters: $V_{\text{bias}} = 0.5$ V and $I_t = 500$ pA. The arrows mark the hybridization gap opening on the QL termination (red and purple), the Dirac point (red), and the onset of the inner Rashba-like splitting band on the SL termination (brown), in good agreement with the ARPES measurement. Bottom: DFT-calculated surface-dependent DOS for both terminations. The surface projections include the top two surface layers, containing one SL and one QL. The calculated DOS plots are offset to -285 meV to match the Dirac point of SL termination. The dashed line marks the Fermi level. (b) Spin-polarized ARPES map for both terminations of MnBi₄Te₇, with a line cut at $E_B = 0.08$ eV showing the antiparallel helicity of the two bands. (c) and (d) are the ARPES intensity maps of the QL and SL terminations at the $\bar{\Gamma} - \bar{M}$ direction, respectively. Arrows highlight important STS features in (a). (e) and (f) show the results from density functional theory calculations for the QL and SL terminations, respectively. The slab model assumes a nonmagnetic SL termination for (f), while for (e) an A-type AFM spin configuration is used with the assumption that the magnetic order of the second SL is protected by the topmost QL. The green dashed box in (e) marks the gapped Dirac cone of the surface states.

projection of the Bloch wave functions clearly shows that there is a band inversion between the conduction and valence bands, which is dominated by the topmost QL and the second SL, respectively [see Fig. S3(a) [32]]. Therefore, the indirect gap is caused by the hybridization effect between these two layers. This result is in sharp contrast to the conventional TI or magnetic-doped TI, where the surface states around the Fermi level are governed by the surface layer, with attenuation into the bulk. It is also worth noting that other ARPES studies on the QL termination reveal a Λ -shaped intensity within the

above mentioned hybridization gap [21,22]. With the assumption of an A-type AFM spin configuration, such an in-gap state can be interpreted as a hybridization effect between different orbitals contributed by the surface QL and its neighboring SL, respectively.

For the MnBi₂Te₄ SL termination [Fig. 2(f)], the experimental A-type AFM order with an out-of-plane moment will inevitably open a sizable gap of around 60 meV at the surface state [Fig. S4(a) [32]], inconsistent with our ARPES observation showing a gapless Dirac cone. In real materials, surface magnetism can be different

from the bulk due to various reasons including surface reconstruction, disorder, or spin canting, etc., [40–42], which essentially affects the magnetic-related topological behaviors. In MnBi_4Te_7 , a considerable number of defects, as spotted on both terminations, may further complicate the surface magnetism. In principle, several possible magnetic orders on the surface, such as in-plane ferromagnetism or disordered local moments, could lead to a vanishing surface gap [see Figs. S4(b) and S4(c) [32]] [14]. Without loss of generality, we suggest a topmost nonmagnetic SL with disordered spin to be the scenario, giving rise to a restoration of the time-reversal symmetry on the SL termination. As shown in Fig. 2(f), by assuming a non-magnetic SL surface layer, our DFT calculations obtain almost linear dispersion with a negligibly gapped Dirac cone (gap size less than 10 meV), originating from the proximity effect of the third MnBi_2Te_4 layer, in good agreement with our ARPES results [Fig. 2(d)]. Unlike the QL termination, the projection onto layers shows that the linear Dirac bands are mainly contributed by the surface SL [Fig. S3(b) [32]].

IV. SPIN-SELECTIVE QUASIPARTICLE INTERFERENCE

Having established the distinct band dispersion at the two terminations, now we carry out Fourier transform scanning tunneling spectroscopy (FT STS) at various energies to further investigate the topological surface states. The disorder scattering mixes the states with different moments (\mathbf{k}_1 and \mathbf{k}_2) at the same contour of constant energy (CCE) for the surface bands, resulting in a standing wave with wave vector $(\mathbf{k}_1 - \mathbf{k}_2)/2$. Such interference patterns can be probed as a local DOS modulation in the real space with wavelength $\lambda = 2\pi/q$, where $\mathbf{q} = \mathbf{k}_1 - \mathbf{k}_2$ [43,44]. In the simplest approach, the quasiparticle interference patterns should match the joint density of states (JDOS) as a function of momentum differences (\mathbf{q}) between the two scattering states, $\text{JDOS}(\mathbf{q}, E) = \int I(\mathbf{k}, E) I(\mathbf{k} + \mathbf{q}, E) d^2\mathbf{k}$, where $I(\mathbf{k})$ can be experimentally determined from CCEs in the ARPES measurement. Figures 3(c) and 3(d) show typical CCEs of ARPES data for the QL and SL terminations, respectively, at approximately -50 meV. Comparing with the calculated JDOS patterns from ARPES CCE maps [Figs. 3(e) and 3(f)], the FT STS maps [Figs. 3(i) and 3(j)] display clear suppression of scattering intensity along $\bar{\Gamma} - \bar{K}$ directions. Previous FT STS studies on topological insulators suggest that the scattering process can be greatly affected by the spin texture of the topological surface states, as helicity allows interference to occur only when there is a finite spin overlap between the two scattering states [27,28,35,45]. On the QL termination, a hexagonally warped shape of surface band structure is observed [Fig. 3(c)], accompanied by suppressed $\bar{\Gamma} - \bar{K}$ scattering in the QPI pattern. This scattering resembles the warping-induced attenuation of $\bar{\Gamma} - \bar{K}$ scattering in

Bi_2Te_3 , where an out-of-plane spin component can be introduced in between the warped corners, suggesting that the spin texture on QL termination can be understood in a similar manner.

Compared with the case of the QL termination, the QPI pattern of the SL is more intricate. We first look into the results from spin-resolved ARPES for possible spin texture guidance at the SL termination. Figure 2(b) represents a spin resolved ARPES map of MnBi_4Te_7 along the $\bar{\Gamma} - \bar{M}$ direction measured with a high-efficiency very low energy electron diffraction (VLEED) spin detector [46], showing the spin component along the tangential direction of the CCE band contours. The data are a mixed result of both the SL and QL terminations due to the millimeter-sized spatial resolution of the spin ARPES device. Interestingly, the electronic states of MnBi_4Te_7 show an up-down-up-down spin configuration above the Dirac point energy ($-280 < E < 0$ meV), resembling a typical Rashba-like spin splitting. We conclude such a spin pattern comes from the SL termination for the following reasons: (i) The k -space locations of the spin-polarized bands in Fig. 2(b) match those for the SL termination [Fig. 2(d)] to a better degree than those for the QL termination [Fig. 2(c)]. Specifically, the spin pattern at moderate binding energies (i.e., $E_b \sim 0.2$ eV) spreads to a wider range of $k_{\Gamma M}$ than the QL bands do [dashed curves in Figs. 2(b) and 2(d)]. (ii) The inner ring in the QL termination [Fig. 3(c)] is assigned as a bulk electronic state [15], where spin polarization is assumed to be far less polarized than that of surface states. Therefore, our spin-resolved ARPES results suggest a pair of Rashba-like splitting bands on the SL termination, which could originate from the potential gradient of the confining electrostatic potential in the surface space-charge regions [47].

Taking the above-mentioned experimental observations and DFT calculations into account, we construct a uniform surface $k \cdot p$ model Hamiltonian to extract the central information of the electronic structures of both terminations, including Dirac bands, Rashba bands, hexagonal warping [48], hybridization between the SL and QL, and the exchange field due to the proximity effect from the bulk magnetism. It reads in the following:

$$H_k = \tau_+ H_k^1 + \tau_- H_k^2 + \Delta \tau_x. \quad (1)$$

In Eq. (1), $H_k^1 = \epsilon_k^D + v_F^D(\boldsymbol{\sigma} \times \mathbf{k})_z + (\lambda/2)(k_+^3 + k_-^3)\sigma_z$ describes a gapless, warped Dirac cone representing both the topmost Bi_2Te_3 layer for the QL termination and the topmost MnBi_2Te_4 layer with a disordered local moment for the SL termination ($k_{\pm} = k_x \pm ik_y$). $H_k^2 = \epsilon_k^R + v_F^R(\boldsymbol{\sigma} \times \mathbf{k})_z + m_z^R \sigma_z$ describes a pair of Rashba bands with possible proximity-induced exchange field m_z^R capturing the dispersion from the second topmost layers for both terminations. $\epsilon_k^{D/R}$ and $v_F^{D/R}$ denote the parabolic dispersion and Fermi velocity of Dirac and Rashba bands, respectively, with λ and Δ the parameters of hexagonal warping and

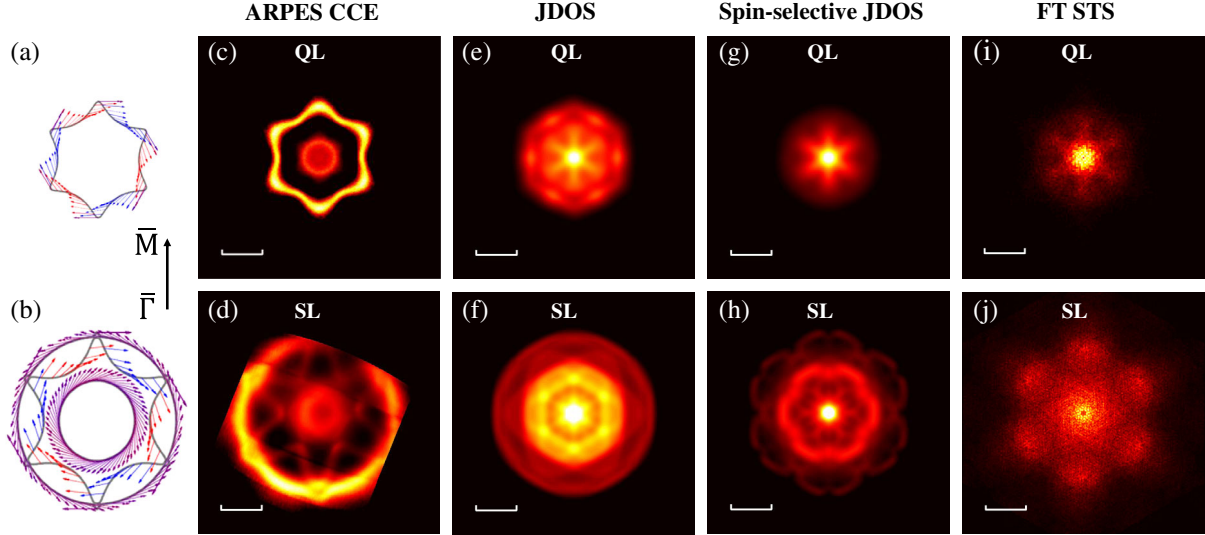


FIG. 3. ARPES contours of constant energy, JDOS, and spin-selective JDOS calculated from ARPES data and FT STS maps at -50 meV of the two terminations. (a) and (b) are the schematics of the spin texture derived from the $k \cdot p$ Hamiltonian for the QL (a) and SL (b) terminations. Arrows and colors of the vectors represent the in-plane (purple) and out-of-plane (red, $+z$; blue, $-z$) components of spin at the contour maps of the Fermi energy, respectively. The black arrow indicates the $\bar{\Gamma} - \bar{M}$ direction for all the maps. For QL termination, the hexagonal warping effect causes a canted spin at the z direction. For SL termination, a pair of Rashba-like splitting bands contribute antiparallel helicity for the inner and outer rings in the CCE map. A strong warping effect is observed as a flower-shaped band in between the rings. (c),(d) CCE maps from ARPES measurements at 50 meV below Fermi level for QL (c) and SL (d) terminations. (e),(f) JDOS calculated from the intensity of the CCE map are shown for QL (e) and SL (f) terminations. For the calculation on the SL, idealized bands with an experimentally determined adjusted intensity ratio are used. The JDOS maps show unexpected scattering intensity at $\bar{\Gamma} - \bar{K}$ directions. (g),(h) Taking into account the spin-selective joint density of states, the scattering maps are (g) for QL and (h) SL terminations. For both simulations, the scattering at $\bar{\Gamma} - \bar{K}$ directions are greatly suppressed. (i) and (j) are the Fourier transformation on the dI/dV maps (FT STS) at $V_{\text{bias}} = -50$ mV, $I_t = 500$ pA, image size 100×100 nm², showing good agreement with the spin-selective JDOS maps. The scale bars are 0.1 \AA^{-1} in CCE maps and 0.2 \AA^{-1} in the rest maps. FT STS maps are rotationally symmetrized.

hybridization strength between the top two layers, while τ and σ are Pauli matrices with $\tau_{\pm} = (1 \pm \tau_z)/2$. The corresponding surface band dispersions of both terminations, calculated from Eq. (1), reproduce a direct gap in the QL termination due to the combined effect of the hybridization Δ and the exchange field m_z^R , as well as a gapless Dirac cone beneath the Rashba bands [see Figs. S12 (a) and S12(c) [32]]. We next use the obtained spin textures to calculate the spin-selective JDOS and compare with the observed QPI.

The spin configurations derived from the $k \cdot p$ model near the Fermi level are summarized in Figs. 3(a) and 3(b). We find that (i) the QL termination carries a spin-helical Dirac state with hexagonal warping, which gives rise to the canted spin texture along the z direction; (ii) on the SL termination, a Rashba-like splitting state comprises a pair of concentric circular bands with antiparallel spin helicity, between which lies another strongly canted helical state whose spin is antiparallel to the outer ring. The spin-selective JDOS can be estimated by adding a spin scattering matrix to the JDOS calculation via $\text{SSJDOS}(\mathbf{q}, E) = \int I(\mathbf{k}, E) T(\mathbf{q}, \mathbf{k}, E) I(\mathbf{k} + \mathbf{q}, E) d^2\mathbf{k}$, where $T(\mathbf{q}, \mathbf{k}, E) = |\langle S(\mathbf{k}, E) | S(\mathbf{k} + \mathbf{q}, E) \rangle|^2$ [27] describes the scattering

matrix where only the states with overlapped spin can be scattered. By assigning the above-mentioned spin configuration [Figs. 3(a) and 3(b)] to the CCE maps of ARPES [Figs. 3(c) and 3(d)], the spin-selective JDOS maps at $E = -50$ meV are calculated in Figs. 3(g) and 3(h). For the QL termination, there is a remarkable similarity between the QPI map [Fig. 3(i)] and spin-selective JDOS [Fig. 3(g)]. Compared with the JDOS map [Fig. 3(e)], the scattering intensity along $\bar{\Gamma} - \bar{K}$ directions is greatly suppressed, confirming the previously discussed hexagonal warping effect. For the SL termination, the QPI map is with a six-petal flower shape. Similar to the QL termination, there is clear attenuation of $\bar{\Gamma} - \bar{K}$ scattering, while the $\bar{\Gamma} - \bar{M}$ scattering is preserved, if we compare the QPI map [Fig. 3(j)] with the JDOS map [Fig. 3(f)]. The decreased scattering intensity along $\bar{\Gamma} - \bar{K}$ directions is well captured by the spin-selective JDOS map in Fig. 3(h), caused by the helicity assignment in the Rashba-like splitting bands (inner and outer rings) and the strongly warped band. Moreover, it is worth noting that, in the ARPES CCE map on the SL [Fig. 3(d)], a small hybridization gap appears near the Fermi level when the strongly warped band and the outer circular band intersect along $\bar{\Gamma} - \bar{M}$ directions. Such spin texture

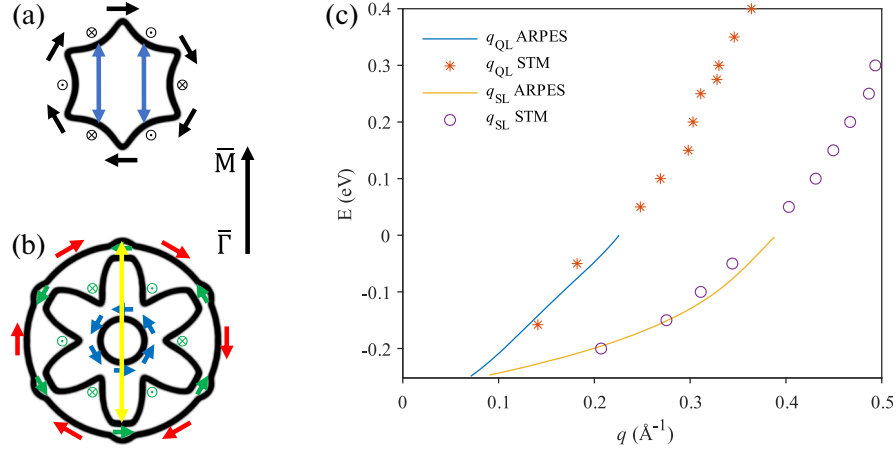


FIG. 4. Dispersion of $\Gamma - M$ scattering edges from ARPES and FT STS. (a),(b) Schematic of CCEs resulting in the edges of q vectors observed in the FT STS maps along the $\bar{\Gamma} - \bar{M}$ direction; arrows mark the spin orientation on these topological surface states: on the QL termination (a), the circular shape surface band is slightly warped for $E > -100$ meV, causing a canted spin along z , thus resulting in q_{QL} marked by the blue arrows; on the SL termination (b), for $E > -150$ meV, Rashba-like spin splitting contributes antiparallel helicity for the inner and outer rings in the CCE map (marked as blue and red arrows), where the outer ring hybridizes with a strongly warped surface band sandwiched in between. The middle warped band has the same helicity as the inner circular bands to fit the intensity along the $\bar{\Gamma} - \bar{M}$ direction in the QPI map, leading to q_{SL} marked by the yellow arrow. (c) Dispersion of the q vectors calculated from the ARPES data (solid lines) on the QL (blue) and SL (yellow) terminations and the q vectors obtained from the FT STS data (orange stars for QL and purple circles for SL). The original FT STS and CCE maps are shown in Figs. S6–S9 [32], respectively.

from the hybridization allows scattering around $\bar{\Gamma} - \bar{M}$ directions with the largest wave vectors [see the yellow arrow in Fig. 4(b)], preserving the scattering intensity along the curved edges of the petals, as seen in Fig. 3(h). On the other hand, the calculated spin-selective JDOS map show little intensity inside the petals compared with the QPI map. The rearranged spin texture near hybridization between the outer circular band and the strongly warped band could be more complicated than the simplified model we use for the simulation, which could result in redistributed scattering intensity at the six petals. Scattering from other energy cuts may also play a role. However, despite the inevitable discrepancy resulting from a simplified model, the strong correlation between the QPI and spin-selective JDOS confirms the topological nature of the surface bands as well as the spin configurations on the two distinct terminations of MnBi_4Te_7 , highlighting the hybridization between the strongly canted helical state from the surface SL and the Rashba-like splitting states from its neighboring QL.

Consequently, as illustrated by Figs. 4(a) and 4(b), the major scattering channel forming the edge of the petals in the QPI pattern can be originated only from q_{SL} along $\bar{\Gamma} - \bar{M}$ with aligned spins for the SL termination, while for QL termination, the majority of allowed scattering occurs for wave vector q_{QL} . We then overlay the dispersion of the wave vectors q_{QL} and q_{SL} obtained in the QPI patterns (Figs. S6, S7, and S11 [32]) with the energy dispersion expected in the spin-selective JDOS calculated from ARPES data (Figs. S8 and S9 [32]). The plot [Fig. 4(c)] shows good agreement between QPI and ARPES below the Fermi level

for both terminations, reassuring the topological nature of these bands. The dispersion for both vectors remains at the high-energy regime up to 400 meV (about 685 meV above the Dirac point), showing robust surface states.

V. CONCLUSION

In summary, we have studied the distinct topological surface states of the two terminations of MnBi_4Te_7 by ARPES and STM. Compared with theoretical calculations, a gapless Dirac electronic structure is observed on the SL termination, whereas the QL termination is found to be gapped because of the hybridization between different orbitals of the neighboring TI building blocks, implying different surface magnetism on the two terminations. Despite the microscopic defects related to the magnetic atoms, the scattering process on both terminations can be understood by the topological surface states and the newly discovered spin configurations. The robust topological surface states remain present up to an energy regime far above the Fermi energy on both terminations, showing great tolerance to disorders. Our results provide insight not only to the impact of surface magnetism on the topological surface states, but also the potential of the hybridization effect in the heterostructure engineering in magnetic TI systems. Further surface-sensitive magnetic measurements or quantum transport study may be able to directly probe the detailed surface magnetic ordering on the two terminations and the related exotic quantum states.

ACKNOWLEDGMENTS

The research was supported by National Natural Science Foundation of China under Projects No. 11674150, No. 11674149, No. 11874195, and No. 11804402, the Key-Area Research and Development Program of Guangdong Province (2019B010931001), Guangdong Innovative and Entrepreneurial Research Team Program (2016ZT06D348 and 2017ZT07C062), the Guangdong Provincial Key Laboratory of Computational Science and Material Design (Grant No. 2019B030301001), the Science, Technology, and Innovation Commission of Shenzhen Municipality (JCYJ20150630145302240, G02206304, and G02206404), and Center for Computational Science and Engineering at SUSTech. M.X. acknowledges the financial support from a Collaborative Research Fund (C7036-17W) from the Research Grant Council, Hong Kong Special Administrative Region. C.L. acknowledges support from the Highlight Project (No. PHYS-HL-2020-1) of the College of Science, SUSTech. ARPES experiments were performed with the approval of the Hiroshima Synchrotron Radiation Center (HSRC), Hiroshima, Japan under Proposals No. 19AU004, No. 19AU015, and No. 19AG002. We thank Jianpeng Liu, Haizhou Lu, and Junhao Lin for valuable discussions.

APPENDIX: METHODS

Single crystals of MnBi_4Te_7 are prepared by the flux growth method and confirmed by single crystal x-ray diffraction data and the subsequent magnetic and transport measurements. The crystal has an AFM ground state with $T_N \sim 12$ K and a critical field of the spin-flop transition of $B_c = 0.2$ T, as shown in Fig. S1 [32]. The STM measurements are performed on *in situ* cleaved surfaces of MnBi_4Te_7 using commercialized STM (Unisoku 1500) operating at approximately 4.5 K with a base pressure better than 1×10^{-10} mbar. Tungsten tips are modified *in situ* by scanning on copper when needed. The dI/dV spectroscopy is obtained by a standard lock-in technique with frequency 687.2 Hz and an ac modulation of 5 mV. The spatial resolution for the FT STS maps is 0.17 nm. For the QL termination, the JDOS data are calculated by the self-convolution of raw CCE from ARPES, and a scattering matrix taking into account of the spin texture derived from the $k \cdot p$ model (Fig. S12 [32]) is used for the spin-selective JDOS. For the SL termination, an idealized CCE constructed based on the ARPES CCE is used for the JDOS and spin-selective JDOS calculation because of the complexity of the spin configuration in the topological bands. Details can be found in Supplemental Material [32].

ARPES measurements are performed at the Hiroshima Synchrotron Radiation Center (HiSOR). The spin-integrated spectra are obtained with an offline ARPES setup under 6.36 eV laser light, while the spin-resolved ARPES map

[Fig. 2(d)] is obtained at Beam line 9B of HiSOR, using a VLEED spin detector and 18 eV incident light.

The surface band structures of both terminations are calculated by density functional theory. We use the projector-augmented wave (PAW) pseudopotentials [49] with the exchange correlation of Perdew-Burke-Ernzerhof (PBE) form [50] and GGA + U approach within the Dudarev scheme [51] as implemented in the Vienna *Ab Initio* Simulation Package [52,53]. The energy cutoff is chosen 1.5 times as large as the values recommended in relevant pseudopotentials. The U value is set to be 5 eV. The k -points-resolved value of BZ sampling is $0.02 \times 2\pi \text{ \AA}^{-1}$. The total energy minimization is performed with a tolerance of 10^{-6} eV. Spin-orbit coupling is included self-consistently throughout the calculations. The surface band structures of QL and SL terminations are obtained from slab calculations with the thickness of 9 and 7 van der Waals layers, respectively.

-
- [1] Y. Tokura, K. Yasuda, and A. Tsukazaki, *Magnetic Topological Insulators*, *Nat. Rev. Phys.* **1**, 126 (2019).
 - [2] C.-Z. Chang *et al.*, *Experimental Observation of the Quantum Anomalous Hall Effect in a Magnetic Topological Insulator*, *Science* **340**, 167 (2013).
 - [3] R. Yu, W. Zhang, H.-J. Zhang, S.-C. Zhang, X. Dai, and Z. Fang, *Quantized Anomalous Hall Effect in Magnetic Topological Insulators*, *Science* **329**, 61 (2010).
 - [4] Y. Gong *et al.*, *Experimental Realization of an Intrinsic Magnetic Topological Insulator*, *Chin. Phys. Lett.* **36**, 076801 (2019).
 - [5] J. Li, Y. Li, S. Du, Z. Wang, B.-L. Gu, S.-C. Zhang, K. He, W. Duan, and Y. Xu, *Intrinsic Magnetic Topological Insulators in van der Waals Layered MnBi_2Te_4 -Family Materials*, *Sci. Adv.* **5**, eaaw5685 (2019).
 - [6] D. Zhang, M. Shi, T. Zhu, D. Xing, H. Zhang, and J. Wang, *Topological Axion States in the Magnetic Insulator MnBi_2Te_4 with the Quantized Magnetoelectric Effect*, *Phys. Rev. Lett.* **122**, 206401 (2019).
 - [7] M. M. Otrokov *et al.*, *Prediction and Observation of an Antiferromagnetic Topological Insulator*, *Nature (London)* **576**, 416 (2019).
 - [8] E. D. L. Rienks *et al.*, *Large Magnetic Gap at the Dirac Point in $\text{Bi}_2\text{Te}_3/\text{MnBi}_2\text{Te}_4$ heterostructures*, *Nature (London)* **576**, 423 (2019).
 - [9] M. M. Otrokov, I. P. Rusinov, M. Blanco-Rey, M. Hoffmann, A. Yu. Vyazovskaya, S. V. Eremeev, A. Ernst, P. M. Echenique, A. Arnau, and E. V. Chulkov, *Unique Thickness-Dependent Properties of the van der Waals Interlayer Antiferromagnet MnBi_2Te_4 Films*, *Phys. Rev. Lett.* **122**, 107202 (2019).
 - [10] H. Sun, B. Xia, Z. Chen, Y. Zhang, P. Liu, Q. Yao, H. Tang, Y. Zhao, H. Xu, and Q. Liu, *Rational Design Principles of the Quantum Anomalous Hall Effect in Superlattice-like Magnetic Topological Insulators*, *Phys. Rev. Lett.* **123**, 096401 (2019).
 - [11] Y. Deng, Y. Yu, M. Z. Shi, Z. Guo, Z. Xu, J. Wang, X. H. Chen, and Y. Zhang, *Quantum Anomalous Hall Effect in*

- Intrinsic Magnetic Topological Insulator* MnBi_2Te_4 , *Science* **367**, 895 (2020).
- [12] J. Ge *et al.*, *High-Chern-Number and High-Temperature Quantum Hall Effect without Landau Levels*, [arXiv:1907.09947](#) [Nat. Sci. Rev. (to be published)].
- [13] C. Liu, Y. Wang, H. Li, Y. Wu, Y. Li, J. Li, K. He, Y. Xu, J. Zhang, and Y. Wang, *Robust Axion Insulator and Chern Insulator Phases in a Two-Dimensional Antiferromagnetic Topological Insulator*, *Nat. Mater.* **19**, 522 (2020).
- [14] Y.-J. Hao *et al.*, *Gapless Surface Dirac Cone in Antiferromagnetic Topological Insulator* MnBi_2Te_4 , *Phys. Rev. X* **9**, 041038 (2019).
- [15] H. Li *et al.*, *Dirac Surface States in Intrinsic Magnetic Topological Insulators* EuSn_2As_2 and $\text{MnBi}_{2n}\text{Te}_{3n+1}$, *Phys. Rev. X* **9**, 041039 (2019).
- [16] Y. J. Chen *et al.*, *Topological Electronic Structure and Its Temperature Evolution in Antiferromagnetic Topological Insulator* MnBi_2Te_4 , *Phys. Rev. X* **9**, 041040 (2019).
- [17] P. Swatek, Y. Wu, L.-L. Wang, K. Lee, B. Schrunck, J. Yan, and A. Kaminski, *Gapless Dirac Surface States in the Antiferromagnetic Topological Insulator* MnBi_2Te_4 , *Phys. Rev. B* **101**, 161109 (2020).
- [18] R. C. Vidal *et al.*, *Topological Electronic Structure and Intrinsic Magnetization in* MnBi_4Te_7 : A Bi_2Te_3 Derivative with a Periodic Mn Sublattice, *Phys. Rev. X* **9**, 041065 (2019).
- [19] J. Wu *et al.*, *Natural van der Waals Heterostructural Single Crystals with Both Magnetic and Topological Properties*, *Sci. Adv.* **5**, eaax9989 (2019).
- [20] X.-M. Ma *et al.*, *Hybridization-Induced Gapped and Gapless States on the Surfaces of Magnetic Topological Insulators*, [arXiv:1912.13237](#).
- [21] Y. Hu *et al.*, *Universal Gapless Dirac Cone and Tunable Topological States in* $(\text{MnBi}_2\text{Te}_4)_m(\text{Bi}_2\text{Te}_3)_n$ Heterostructures, *Phys. Rev. B* **101**, 161113 (2020).
- [22] L. X. Xu *et al.*, *Persistent Gapless Surface States in* $\text{MnBi}_2\text{Te}_4/\text{Bi}_2\text{Te}_3$ Superlattice Antiferromagnetic Topological Insulator, [arXiv:1910.11014](#).
- [23] C. Hu *et al.*, *A van der Waals Antiferromagnetic Topological Insulator with Weak Interlayer Magnetic Coupling*, *Nat. Commun.* **11**, 97 (2020).
- [24] C. Hu *et al.*, *Realization of an Intrinsic, Ferromagnetic Axion Insulator in* $\text{MnBi}_8\text{Te}_{13}$, [arXiv:1910.12847](#).
- [25] K. N. Gordon *et al.*, *Strongly Gapped Topological Surface States on Protected Surfaces of Antiferromagnetic* MnBi_4Te_7 and $\text{MnBi}_6\text{Te}_{10}$, [arXiv:1910.13943](#).
- [26] M. Z. Hasan and C. L. Kane, *Colloquium: Topological Insulators*, *Rev. Mod. Phys.* **82**, 3045 (2010).
- [27] P. Roushan, J. Seo, C. V. Parker, Y. S. Hor, D. Hsieh, D. Qian, A. Richardella, M. Z. Hasan, R. J. Cava, and A. Yazdani, *Topological Surface States Protected from Backscattering by Chiral Spin Texture*, *Nature (London)* **460**, 1106 (2009).
- [28] Y. Okada *et al.*, *Direct Observation of Broken Time-Reversal Symmetry on the Surface of a Magnetically Doped Topological Insulator*, *Phys. Rev. Lett.* **106**, 206805 (2011).
- [29] T. Zhang *et al.*, *Experimental Demonstration of Topological Surface States Protected by Time-Reversal Symmetry*, *Phys. Rev. Lett.* **103**, 266803 (2009).
- [30] Y. Yuan *et al.*, *Electronic States and Magnetic Response of* MnBi_2Te_4 *by Scanning Tunneling Microscopy and Spectroscopy*, [arXiv:2001.00462v1](#).
- [31] Z. Liang *et al.*, *Mapping the Dirac Fermions in Intrinsic Antiferromagnetic Topological Insulators* $(\text{MnBi}_2\text{Te}_4)(\text{Bi}_2\text{Te}_3)_n$ ($n = 0, 1$), [arXiv:2001.00866v1](#).
- [32] See Supplemental Material at <http://link.aps.org/supplemental/10.1103/PhysRevX.10.031013> for Supplemental Figures and the algorithm for calculating JDOS and spin-selective JDOS maps.
- [33] J.-Q. Yan, Q. Zhang, T. Heitmann, Z. Huang, K. Y. Chen, J.-G. Cheng, W. Wu, D. Vaknin, B. C. Sales, and R. J. McQueeney, *Crystal Growth and Magnetic Structure of* MnBi_2Te_4 , *Phys. Rev. Mater.* **3**, 064202 (2019).
- [34] Y. S. Hor *et al.*, *Development of Ferromagnetism in the Doped Topological Insulator* $\text{Bi}_{2-x}\text{Mn}_x\text{Te}_3$, *Phys. Rev. B* **81**, 195203 (2010).
- [35] H. Beidenkopf, P. Roushan, J. Seo, L. Gorman, I. Drozdov, Y. S. Hor, R. J. Cava, and A. Yazdani, *Spatial Fluctuations of Helical Dirac Fermions on the Surface of Topological Insulators*, *Nat. Phys.* **7**, 939 (2011).
- [36] Y. L. Chen *et al.*, *Massive Dirac Fermion on the Surface of a Magnetically Doped Topological Insulator*, *Science* **329**, 659 (2010).
- [37] I. Lee *et al.*, *Imaging Dirac-Mass Disorder from Magnetic Dopant Atoms in the Ferromagnetic Topological Insulator* $\text{Cr}_x(\text{Bi}_{0.1}\text{Sb}_{0.9})_{2-x}\text{Te}_3$, *Proc. Natl. Acad. Sci. U.S.A.* **112**, 1316 (2015).
- [38] H. Iwasawa, E. F. Schwier, M. Arita, A. Ino, H. Namatame, M. Taniguchi, Y. Aiura, and K. Shimada, *Development of Laser-Based Scanning μ -ARPES System with Ultimate Energy and Momentum Resolutions*, *Ultramicroscopy* **182**, 85 (2017).
- [39] J.-Q. Yan *et al.*, *A-type Antiferromagnetic Order in* MnBi_4Te_7 and $\text{MnBi}_6\text{Te}_{10}$ Single Crystals, *Phys. Rev. Mater.* **4**, 054202 (2020).
- [40] B. Niu *et al.*, *Coexistence of Magnetic Orders in Two-Dimensional Magnet* CrI_3 , *Nano Lett.* **20**, 553 (2020).
- [41] F. Yang, Y. R. Song, H. Li, K. F. Zhang, X. Yao, C. Liu, D. Qian, C. L. Gao, and J.-F. Jia, *Identifying Magnetic Anisotropy of the Topological Surface State of* $\text{Cr}_{0.05}\text{Sb}_{1.95}\text{Te}_3$ *with Spin-Polarized STM*, *Phys. Rev. Lett.* **111**, 176802 (2013).
- [42] A. Chikina *et al.*, *Strong Ferromagnetism at the Surface of an Antiferromagnet Caused by Buried Magnetic Moments*, *Nat. Commun.* **5**, 3171 (2014).
- [43] M. F. Crommie, C. P. Lutz, and D. M. Eigler, *Imaging Standing Waves in a Two-Dimensional Electron Gas*, *Nature (London)* **363**, 524 (1993).
- [44] J. E. Hoffman, K. McElroy, D.-H. Lee, K. M. Lang, H. Eisaki, S. Uchida, and J. C. Davis, *Imaging Quasiparticle Interference in* $\text{Bi}_2\text{Sr}_2\text{CaCu}_2\text{O}_{8+\delta}$, *Science* **297**, 1148 (2002).
- [45] Z. Alpichshev, J. G. Analytis, J.-H. Chu, I. R. Fisher, Y. L. Chen, Z. X. Shen, A. Fang, and A. Kapitulnik, *STM Imaging of Electronic Waves on the Surface of* Bi_2Te_3 : *Topologically Protected Surface States and Hexagonal Warping Effects*, *Phys. Rev. Lett.* **104**, 016401 (2010).

- [46] T. Okuda, K. Miyamoto, A. Kimura, H. Namatame, and M. Taniguchi, *A Double VLEED Spin Detector for High-Resolution Three Dimensional Spin Vectorial Analysis of Anisotropic Rashba Spin Splitting*, *J. Electron Spectrosc. Relat. Phenom.* **201**, 23 (2015).
- [47] M. S. Bahramy *et al.*, *Emergent Quantum Confinement at Topological Insulator Surfaces*, *Nat. Commun.* **3**, 1159 (2012).
- [48] L. Fu, *Hexagonal Warping Effects in the Surface States of the Topological Insulator Bi₂Te₃*, *Phys. Rev. Lett.* **103**, 266801 (2009).
- [49] G. Kresse and D. Joubert, *From Ultrasoft Pseudopotentials to the Projector Augmented-Wave Method*, *Phys. Rev. B* **59**, 1758 (1999).
- [50] J. P. Perdew, K. Burke, and M. Ernzerhof, *Generalized Gradient Approximation Made Simple*, *Phys. Rev. Lett.* **77**, 3865 (1996).
- [51] S. L. Dudarev, G. A. Botton, S. Y. Savrasov, C. J. Humphreys, and A. P. Sutton, *Electron-Energy-Loss Spectra and the Structural Stability of Nickel Oxide: An LSDA + *U* study*, *Phys. Rev. B* **57**, 1505 (1998).
- [52] G. Kresse and J. Furthmüller, *Efficiency of Ab-Initio Total Energy Calculations for Metals and Semiconductors Using a Plane-Wave Basis Set*, *Comput. Mater. Sci.* **6**, 15 (1996).
- [53] G. Kresse and J. Furthmüller, *Efficient Iterative Schemes for Ab Initio Total-Energy Calculations Using a Plane-Wave Basis Set*, *Phys. Rev. B* **54**, 11169 (1996).

Hybridization-induced gapped and gapless states on the surface of magnetic topological insulators

Xiao-Ming Ma¹, Zhongjia Chen¹, Eike F. Schwier², Yang Zhang³, Yu-Jie Hao¹, Shiv Kumar², Ruie Lu¹, Jifeng Shao¹, Yuanjun Jin¹, Meng Zeng¹, Xiang-Rui Liu¹, Zhanyang Hao¹, Ke Zhang², Wumiti Mansuer², Chunyao Song⁴, Yuan Wang¹, Boyan Zhao¹, Cai Liu¹, Ke Deng¹, Jiawei Mei¹, Kenya Shimada², Yue Zhao¹, Xingjiang Zhou⁴, Bing Shen^{1,3,*}, Wen Huang^{1,†}, Chang Liu¹, Hu Xu¹ and Chaoyu Chen^{1,‡}

¹Shenzhen Institute for Quantum Science and Engineering (SIQSE) and Department of Physics, Southern University of Science and Technology (SUSTech), Shenzhen 518055, China

²Hiroshima Synchrotron Radiation Center, Hiroshima University, Higashi-Hiroshima, Hiroshima 739-0046, Japan

³School of Physics, Sun Yat-Sen University, Guangzhou 510275, China

⁴Institute of Physics and Beijing National Laboratory for Condensed Matter Physics, Chinese Academy of Sciences, Beijing 100190, China



(Received 7 February 2020; accepted 18 November 2020; published 22 December 2020)

The layered $\text{MnBi}_{2n}\text{Te}_{3n+1}$ family represents the first intrinsic antiferromagnetic (AFM) topological insulator (protected by a combination symmetry S) ever discovered, providing an ideal platform to explore novel areas of physics such as the quantum anomalous Hall effect at elevated temperature and axion electrodynamics. Some of the recent angle-resolved photoemission spectroscopy (ARPES) experiments on this family have revealed that all terminations exhibit (nearly) gapless topological surface states (TSSs) in the AFM state. The gapless behavior is inconsistent with the theoretical expectation, as the surfaces being studied are S -breaking and shall therefore open a gap. Here we explain this curious paradox using a surface-bulk band hybridization picture. Combining circular dichroism ARPES and first-principles calculations on $\text{MnBi}_6\text{Te}_{10}$, we prove that gaplike features are induced through hybridization between TSSs and certain bulk bands with Rashba character. The observed (nearly) gapless features are consistently reproduced by tight-binding simulations where TSSs are coupled to a pair of Rashba-split bands (RSBs). The Dirac-cone-like spectral features actually originate from the RSBs. Our findings highlight the role of band hybridization, superior to magnetism in this case, in shaping the general surface band structure in this family of magnetic topological materials.

DOI: [10.1103/PhysRevB.102.245136](https://doi.org/10.1103/PhysRevB.102.245136)

I. INTRODUCTION

The discovery of topological insulators (TIs) in two-dimensional (2D) and three-dimensional (3D) material systems has triggered a paradigmatic evolution in condensed matter physics, in which the phase of matter and novel properties of quantum materials are explored based on the topology of electronic structure in reciprocal space [1–3]. The combination of the electronic topology and other degrees of freedom may lead to a variety of exotic phases of matter and physical responses such as axionic excitation [4–6], the Majorana state, and topological superconductivity [2,7]. More specifically, the interplay between magnetism and topology could generate various quantum states, such as antiferromagnetic TIs (AFM TIs) [8], the quantum anomalous Hall (QAH) state [9,10] hosting dissipationless chiral edge modes [11,12], the axion insulator displaying quantized magnetoelectric effects [4–6], and the magnetic Weyl and nodal-line semimetals [13,14], which harbor Fermi arc surface states and chiral anomalies [13].

The realization of magnetic TIs [15] requires crystalline materials with both magnetic order and electronic topology. Previous efforts were devoted to magnetically doped TIs and magnetic topological heterostructures [11,12,16–19], whose fabrication, measurement, and property optimization are quite challenging. Recently, MnBi_2Te_4 has emerged as the first AFM TI [20–26] with periodically ordered Mn atoms on well-defined crystallographic sites, hosting possible axion electrodynamics in condensed matter. The interlayer AFM with intralayer ferromagnetic (FM) order (c -axis A-type AFM) occurs below a Néel temperature of about $T_N = 24.6$ K [27–34]. In particular, in the presence of a high field that fully polarizes the magnetic moments, the quantized Hall effect indicative of a Chern insulating state and the transition from axion to Chern insulator have been demonstrated in MnBi_2Te_4 in the 2D limit [35–38].

Considering its topology, AFM TI MnBi_2Te_4 can be classified by a topological \mathbb{Z}_2 invariant [8], protected by a combination symmetry $S = \Theta T_{1/2}$, where Θ is time-reversal symmetry and $T_{1/2}$ is a lattice translation symmetry of the “primitive” lattice, both broken by the AFM order but their combination preserved. At the natural cleavage (001) surface of MnBi_2Te_4 , S is broken, generating a sizable surface state gap, which has been reported by works on angle-resolved photoemission spectroscopy (ARPES) [21,30,34,39]. This surface gap opening is crucial to realize the half-quantum Hall effect,

*shenbingdy@mail.sysu.edu

†huangw3@sustech.edu.cn

‡chency@sustech.edu.cn

which may aid experimental confirmation of $\theta = \pi$ quantized magnetoelectric coupling [8]. However, there also exist systematic ARPES measurements that clearly resolved a (nearly) gapless topological surface state (TSS) Dirac cone at the (001) surface of MnBi_2Te_4 [40–43]. This gapless feature remains intact in both paramagnetic (PM) and AFM phases, and it is even robust against severe surface degradation [40,44], indicating additional topological protection from magnetic, structural, or electronic complication. This may explain the necessity of a high field for the observation of the quantized Hall effect, even in thin films with an odd number of layers [35,36].

In fact, MnBi_2Te_4 belongs to the ternary van der Waals compound series $(\text{MnBi}_2\text{Te}_4)_m(\text{Bi}_2\text{Te}_3)_n$ with [Te-Bi-Te-Mn-Te-Bi-Te] septuple (S) layers ($[\text{MnBi}_2\text{Te}_4]$, SLs) and [Te-Bi-Te-Bi-Te] quintuple (Q) layers ($[\text{Bi}_2\text{Te}_3]$, QLs) alternately stacking along the c axis [45,46]. While MnBi_2Te_4 has been extensively studied recently, its sister compounds with a higher n number, such as MnBi_4Te_7 ($n = 1$) and $\text{MnBi}_6\text{Te}_{10}$ ($n = 2$), remain less explored [47–58]. Structurally, the FM SLs are more separated in space as n increases, reducing the interlayer AFM exchange coupling. Indeed, MnBi_4Te_7 and $\text{MnBi}_6\text{Te}_{10}$ both exhibit lower magnetic transition temperatures (~ 13 and ~ 11 K, respectively) compared to MnBi_2Te_4 . A much smaller magnetic field is needed to generate a spin-flip transition. Importantly, FM hysteresis, a prerequisite for realizing the intrinsic QAH effect, was observed at low temperatures. However, similar to the situation for MnBi_2Te_4 , controversial ARPES results exist regarding the TSSs gap in the $n = 1$ and 2 compounds. On the surface terminated by the SL (S-termination), both gapped [50,57] and gapless [48,54–56] TSSs have been reported in both PM and AFM phases. Likewise, on the Q-termination (SQ- and SQQ-terminations), both gapped [48–50,55] and (nearly) gapless [54,56–58] TSSs were observed. The presence of gapless TSSs at the S -breaking terminations would be ostentatiously at odds with the theoretical expectation for these AFT TI compounds. Thus, it is of critical importance to determine the underlying mechanism for this puzzling observation.

In this work, combining ARPES, density functional theory (DFT), and tight-binding (TB) analysis, we study $\text{MnBi}_6\text{Te}_{10}$ as an example to unveil the nature of the TSSs gap at different terminations. Using ARPES with a focused laser spot ($\sim 5 \mu\text{m}$) and superior energy and momentum resolution (μ -laser-ARPES [59]), four types of surface-driven band structures are spatially resolved, corresponding to the three terminations of $\text{MnBi}_6\text{Te}_{10}$, i.e., S -termination, SQ-termination, SQQ-termination, and one additional SQQQ-termination resulting from either vertical stacking disorder or degradation of the topmost SLs. This assignment is well supported by the DFT slab calculations based on different surface stacking configurations. For both Q- and S -terminations, DFT calculations reveal a hybridization between the TSSs and certain bulk states. Circular dichroism (CD) ARPES further resolves spin helicity for all these states, suggesting that these bulk states also acquire Rashba splitting. To further account for certain key features of the ARPES spectra, we utilize an effective TB model where the TSSs hybridize with a pair of Rashba-split bands (RSBs) near the surface and demonstrate how such hybridization may satisfactorily reproduce

those features. In particular, in the nonmagnetic phase, a new Dirac cone may overtake the original TI Dirac cone at the Γ point. The new Dirac cone is actually of bulk origin, which is not necessarily sensitive to the S -breaking at the surfaces of the AFM phase. Our finding, therefore, has the potential to provide a self-consistent picture to explain the (nearly) gapless behavior of the TSSs at the surfaces of MnBi_4Te_7 and $\text{MnBi}_6\text{Te}_{10}$ [48,54–58]. Our study suggests a significant role of the band hybridization, in addition to other driving forces such as magnetism, in shaping the intriguing surface band structure in the $(\text{MnBi}_2\text{Te}_4)_m(\text{Bi}_2\text{Te}_3)_n$ family.

II. RESULTS

$\text{MnBi}_6\text{Te}_{10}$ has a trigonal structure with a space group of $R\bar{3}m$. The lattice of $\text{MnBi}_6\text{Te}_{10}$ consists of one septuple MnBi_2Te_4 layer and two quintuple Bi_2Te_3 layers alternately stacking along the c axis [Fig. 1(a)]. These SLs or QLs are coupled through weak van der Waals forces. Cleaving the single crystal perpendicular to the c axis could have three possible terminations, i.e., S -termination, Q-termination, and QQ-termination. The crystallinity was examined by x-ray diffraction (XRD). As shown in Fig. 1(b), all peaks in the XRD pattern can be well indexed by the $(00l)$ reflections of $\text{MnBi}_6\text{Te}_{10}$.

The zero-field in-plane longitudinal resistivity $\rho_{xx}(T)$ [Fig. 1(c)] shows a monotonic decrease with decreasing temperature for $20 < T < 300$ K, suggesting a metallic phase, which is confirmed by the following ARPES data. Around 10.7 K, the resistivity shows a weak upturn with decreasing temperature, likely from the enhanced electron scattering by magnetic fluctuation close to the AFM transition. Upon further cooling, the resistivity decreases again, indicating a gradual FM ordering of the spins in the ab plane.

The magnetic susceptibility measurement [Fig. 1(d)] establishes a long-range AFM order below $T_N = 10.7$ K. A sharp cusp around T_N for $H//c$, in contrast to the saturating plateau for $H//ab$, suggests that the magnetization-easy axis is the c direction. All these behaviors are consistent with an A-type AFM configuration (intralayer FM and interlayer AFM) along the c -axis. Fitting the PM regime (150 – 300 K) with the Curie-Weiss formula $\chi(T) = \chi_0 + C/(T - \theta_{CW})$ gives an effective moment $\mu_{\text{eff}} \approx 5.4 \mu_B/\text{Mn}$ and $5.1 \mu_B/\text{Mn}$ for $H//c$ and $H//ab$, respectively, confirming the high spin states of Mn^{2+} . The Curie-Weiss temperature is fitted as $\theta_{CW} = 9$ and 23 K for $H//c$ and $H//ab$, respectively, suggesting the existence of an additional FM interaction induced by an external magnetic field. The additional FM interaction is further confirmed by the loop shape of the field-dependent magnetization $[M(H)]$ results at 2 K [given in Fig. 1(e)]. Compared to $H//c$, a much higher field is needed to fully polarize the spins with $H//ab$, indicating that the magnetization-easy axis is the c -axis. For the c direction, the spin-flip transition occurs at 0.2 T and the magnetic moments are fully polarized. This spin-flip field is much smaller than that in MnBi_2Te_4 (~ 3.5 T) [32]. These features indicate that $\text{MnBi}_6\text{Te}_{10}$ is more suitable for exploring the intrinsic QAH effect.

All the above structural, magnetic, and transport characterizations agree well with other works on the same materials

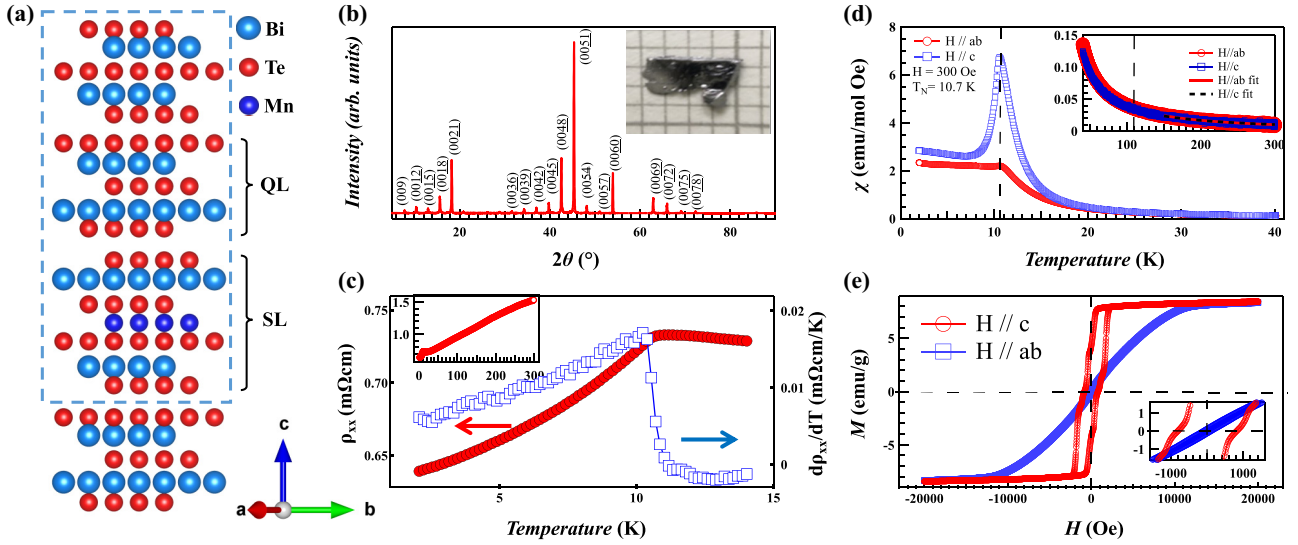


FIG. 1. Lattice structure and characterization of $\text{MnBi}_6\text{Te}_{10}$ single crystals. (a) Schematic lattice structure. (b) Single-crystal XRD result and peak index result. The inset shows a typical single crystal on a millimeter grid. (c) Zero-field in-plane longitudinal resistivity vs temperature. The inset shows the results up to 300 K. (d) Magnetic susceptibility vs temperature for magnetic field (300 Oe) parallel to the ab plane (red) and the c axis (blue). The inset shows the Curie-Weiss fitting for temperatures ranging from 150 to 300 K. (e) Magnetization hysteresis at 2 K. The inset highlights the coercive fields.

[53,58]. Throughout this work, the ARPES spectra presented at the main text were measured at 20 K, i.e., the PM phase. In addition, in Sec. 1 of the Supplemental Material [60] we also present temperature-dependent ARPES measurements down to 6.5 K (AFM phase) for both S- and Q-terminations. No observable difference can be detected within instrumental resolution [59].

To probe the intrinsic band structure of $\text{MnBi}_6\text{Te}_{10}$ at different surface terminations, we employ a μ -laser-ARPES system [59] with a focused laser with spot size $\sim 5 \mu\text{m}$ to measure the cleaved $\text{MnBi}_6\text{Te}_{10}$ surface at 20 K. Figure 2 shows four distinct types of ARPES spectra that can be identified for the cleaved surfaces. Also shown are the corresponding schematics of the surface termination, the 2D curvature spectra [61], and the DFT band structures. Note that in the DFT calculations, the slabs are in AFM phase, hence a gap opening is in principle expected. The corresponding Fermi surface mapping and the dispersion along high symmetry directions are shown in Sec. 1 of the Supplemental Material [60]. The assignment of the measured ARPES spectra to the corresponding terminations is based on the comparison with the DFT-calculated band structure on various slab configurations (shown in the schematics). From the ARPES spectra, each termination has a characteristic band dispersion. Specifically, the S-termination shows a cordial glass-shaped conduction-band minimum (CBM) and gapless linear surface states with the Dirac point located at $\sim 300 \text{ meV}$ below the Fermi level [Fig. 2(a)]. The Q-termination exhibits a gaplike feature of $\sim 80 \text{ meV}$ centered at $\sim 320 \text{ meV}$ below the Fermi level and an M-shaped valence-band maximum (VBM) [Fig. 2(b)]. The band structure of the QQ-termination is similar to that of the Q-termination but with a much smaller gap (a few meVs) [Fig. 2(c)]. Finally, there exists another termination with a band structure resembling that on the QQ-termination, which appears to be less electron-doped and features a gapless

TSSs [Fig. 2(d)]. Its band structure can be well reproduced by a QQQ-terminated DFT slab calculation. This termination likely originates from either the vertical stacking disorder or the degradation of the topmost SLs. It is worth noting that this termination differs from the Bi_2Te_3 single crystal in the sense that, for the latter the group velocity of TSS is $\sim 3 \text{ eV \AA}$ [62] while for the former it is only $\sim 2 \text{ eV \AA}$.

Our PM ARPES spectra for S- and Q-terminations are quantitatively similar to the AFM ARPES spectra reported in Sec. 1 of the Supplemental Material [60] and in Refs [54,57,58]. This behavior is consistent with previous works on MnBi_2Te_4 , which show that the TSSs exhibit no observable change across the bulk Néel temperature within the experimental resolution [40–43]. We also calculate the total energies of several slabs with different magnetic structures (Sec. 2 of the Supplemental Material [60]). The total energy differences between AFM and FM states are very small ($\sim 2 \text{ meV/Mn}$), suggesting that magnetic fluctuation may be essential in determining the macroscopic behavior [27,29,33,34]. This indicates that the underlying magnetic structure plays an insignificant role in determining the general band structure on the surfaces of this family of materials. The absence of an unambiguous gap opening in the AFM phase stands in sharp contrast to the recent ARPES results reported in, e.g., Refs. [21,22]. We note here that there are mainly three factors one needs to be aware of in order to resolve the gapless TSSs using ARPES in this material family. The first one is micrometer-scale spatial resolution, to resolve the termination-dependent band structure for $n = 1$ and 2 compounds; the second one is angular resolution, since the momentum window for the gapless features is as narrow as about $\pm 0.05 \text{ \AA}^{-1}$; the last but most important one is the tuning of the excitation photon energy, as sharp TSSs are only observable at a certain low energy range [40]. The corresponding physics will be addressed in Sec. III.

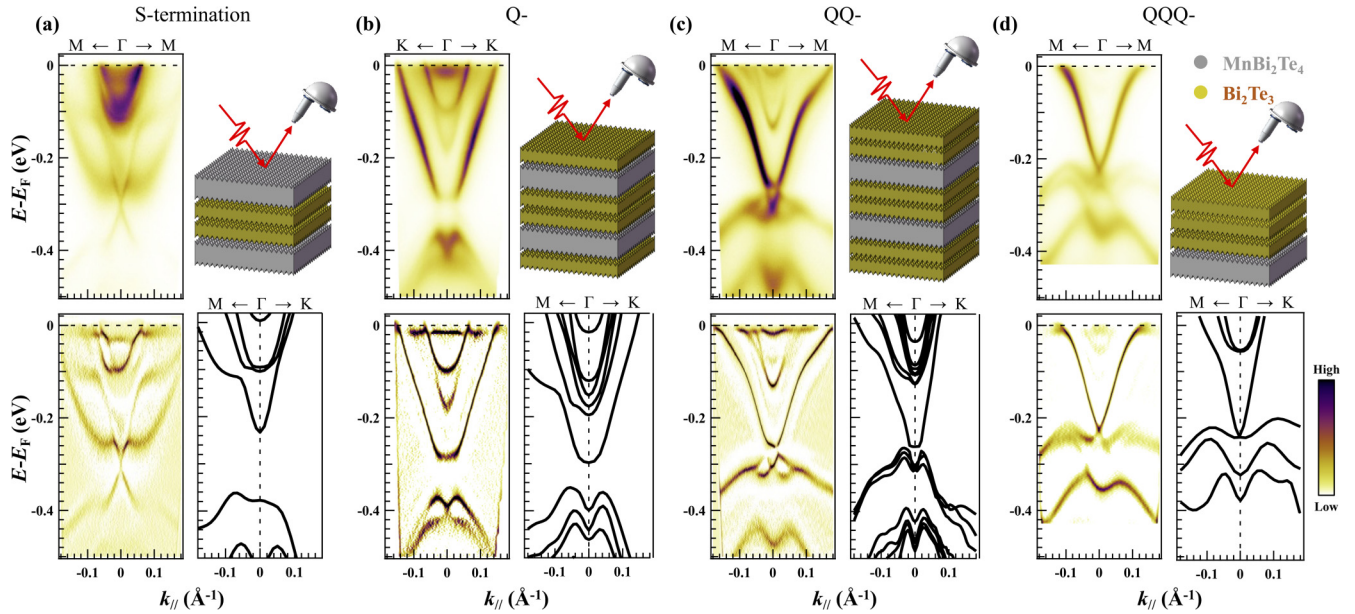


FIG. 2. Termination-dependent electronic structure of $\text{MnBi}_6\text{Te}_{10}$ single crystals. Parts (a)–(d) correspond to the results of S-, Q-, QQ-, and QQQ-terminations, respectively. For each section, the top-left panel shows the raw ARPES spectra, while the bottom-left panel shows the 2D curvature spectra [61]. The top-right panel shows the schematic structural configuration while the bottom-right panel presents the respective calculated band structure.

From Fig. 2, the ARPES spectra and the DFT slab band structure show general agreement regarding the shape of the CBM and the VBM as well as the gap size between them, especially for the Q-, QQ-, and QQQ-terminations. However, DFT fails to capture some key elements in the spectra, such as the gapless Dirac-cone-like feature at S- and Q-terminations, as we describe in detail below. Resolving this puzzle, therefore, constitutes the main objective of the present study.

Figures 3(a)–3(d) highlight the discrepancy between the experimental ARPES spectra and the DFT slab simulation for the Q-termination. On the one hand, the emergence of one Λ -shaped in-gap band V1 [indicated by black arrows in Fig. 3(d)] makes this termination gapless since the cusp of band V1 touches the CBM. A similar observation has been reported by other groups at the Q-terminations in MnBi_4Te_7 [54,56] and $\text{MnBi}_6\text{Te}_{10}$ [54,57]. On the other hand, DFT predicts an M-shape, instead of a Λ -shape, for this V1 band and generally gapped behavior for Q-termination [Figs. 3(b) and 3(c)]. Such a discrepancy between ARPES and DFT results concerning the shape of the V1 band is also present for S-termination, as shown in Figs. 3(f)–3(i).

We first analyze the band structure on the Q-termination. Around the Γ point at -0.4 eV, V2 and V3 form a Dirac-cone-like feature in both ARPES [Fig. 3(d)] and DFT [Fig. 3(b)]. The general shape of C1 and this Dirac-cone-like feature is indicative of an upper Dirac cone intersecting and hybridizing with a pair of additional bands. Some traces of this hybridization can indeed be identified from DFT projection analysis. As shown in Figs. 3(a)–3(c), the lowest conduction band C1 is mainly surface-originated, although with surface domination decreasing with decreasing wave vector. And at the Γ point, the conduction band C1 is instead mainly derived from states located away from the topmost layer. For the valence bands V2 and V3, the opposite occurs: the surface weight dominates

around Γ , and the bulk contribution increases with increasing wave vector. Again, such hybridization features can be observed for S-termination from DFT [Figs. 3(f)–3(h)]. This time the TSS Dirac cone with surface domination [enlarged blue circles in Fig. 3(g)] is intersected by bulk-dominated conduction bands C2 and C3 [enlarged red circles in Fig. 3(h)]. For both cases of Q- and S-terminations, the V2/V3 and C2/C3 bands compose Rashba-like features as indicated in Figs. 3(e) and 3(j) by the red and blue solid lines.

In principle, surface band dispersions other than the TSSs may originate from bulk states that gain surface character due to a confining electrostatic environment in the surface region [63,64]. We note that such quantum confinement could be associated with realistic microscopic surface conditions such as lattice relaxation/distortion and is thus not necessarily captured by the DFT calculations, which assume ideal lattice structure. These bands naturally acquire Rashba-like spin-orbit coupling due to surface confinement [63,64], hence the name RSBs. Notably, similar states have been widely reported on the surfaces of the prototypical TI Bi_2Se_3 family [44,65–70]. More importantly, recent experiments on MnBi_2Te_4 and MnBi_4Te_7 have also provided compelling evidence for the existence of such RSBs [39,71,72] in Mn-Bi-Te compounds. For $\text{MnBi}_6\text{Te}_{10}$, the signatures of such bands can indeed be identified from the CD ARPES spectra. CD ARPES has proved to be powerful in indirectly revealing the helical spin structure of TSS and RSBs in both the Bi_2Se_3 family [70,73–75] and the Mn-Bi-Te family [71] of materials. As shown in Fig. 3(e) [3(j)], in addition to the opposite spin polarization/chirality at opposite momenta for C1 in Fig. 3(d) and C1, V1 in Fig. 3(i), as expected for the TSS Dirac cone spin texture, V2 and V3 (C2 and C3) also exhibit opposite spin polarization/chirality at opposite momenta, forming the well-recognized Rashba-type band splitting at Q- (S-) termination.

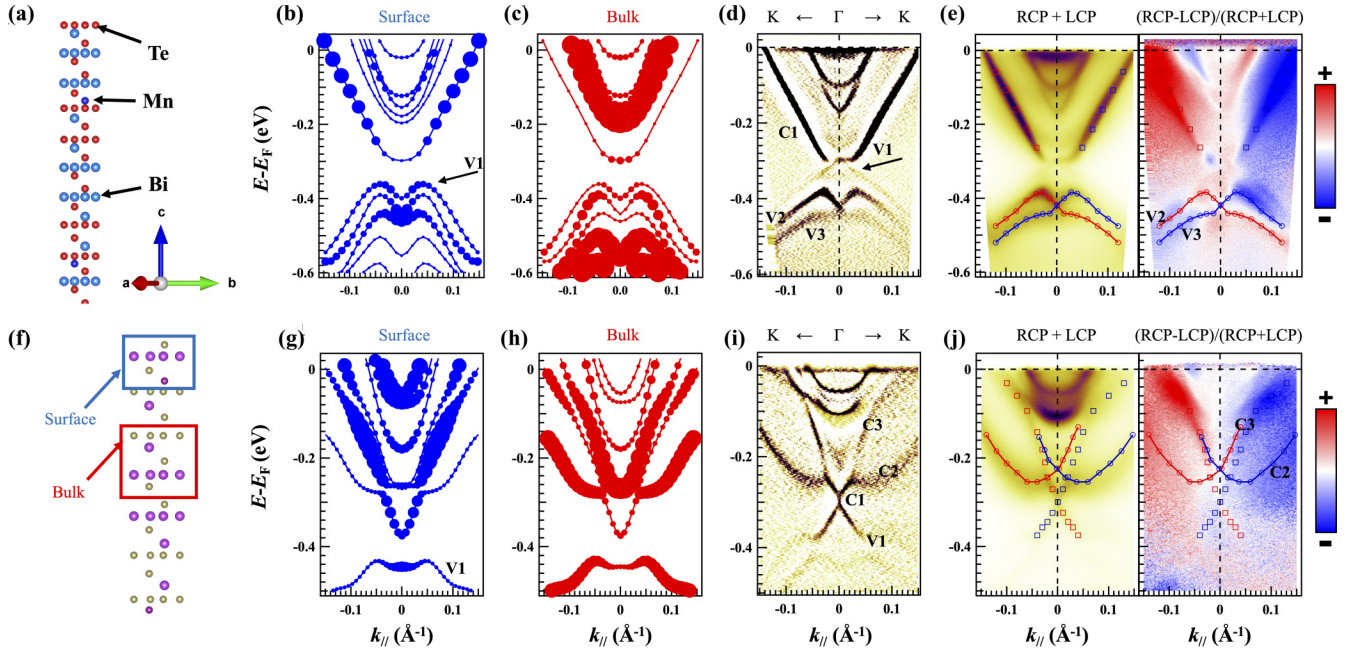


FIG. 3. Evidence of TSS-RSBs hybridization at Q- and S-terminations of $\text{MnBi}_6\text{Te}_{10}$. (a)–(e) ARPES and DFT results for Q-termination. (a)–(c) AFM DFT band structure with the fatted bands projected onto corresponding layers as indicated by the blue (b) and red (c) boxes in (a). (d) ARPES spectra in 2D curvature. Bands around the Dirac points are labeled as C1, V1, V2, and V3, respectively. The black arrow indicates the weak in-gap V1 band. (e) Left: ARPES spectra from the sum of right circular polarization (RCP) and left circular polarization (LCP) light (RCP+LCP); right: circular dichroism (CD) ARPES spectra from the polarization (RCP-LCP)/(RCP+LCP). Red and blue squares indicate the TSS Dirac cone dispersion. Red and blue filled circles indicate the RSBs dispersion. (f)–(j) Similar analysis for S-termination.

We now employ a tight-binding model analysis to demonstrate how a hybridization between the TSSs and the RSBs may describe the complicated electronic band structure as observed by ARPES. For simplicity, we consider the scenario in which the TSS Dirac cone hybridizes with a pair of quasi-two-dimensional RSBs. Note that these RSBs are not intrinsically related to the underlying topological insulating phase. The band dispersions of the TSSs and the RSBs are empirically inferred from the ARPES spectra shown in Figs. 3(e) and 3(j). More details are available in Sec. 3 of the Supplemental Material [60].

As schematically drawn in Fig. 4(a), the TI is modeled by a 3D stacking of bilayers of p_z -like Wannier orbitals, which has been shown to be appropriate for this series of TIs [23]. The RSBs may originate from either certain additional p_z orbitals, or certain p_x/p_y -like Wannier orbitals that lie close in energy. In our simplified model, we consider spin-orbit coupled $(p_x + ip_y) \uparrow$ and $(p_x - ip_y) \downarrow$ Wannier orbitals in a fictitious layer. Note that they are the only p -wave states that could be distinguished from the TI p_z -orbitals under the C_3 symmetry at the surface of the TI. Nevertheless, the results are qualitatively similar if the RSBs come from p_z -like orbitals instead, as we shall mention later. The RSB orbitals couple with the topmost bilayer of the TI, and the effective Hamiltonian reads

$$H = H_{\text{TI}} + H_{\text{RSB}} + H_{\text{hyb}}.$$

In order, the three terms stand for the Hamiltonian of the TI, the RSBs, and the hybridization. While more details are provided in Sec. 3 of the Supplemental Material [60], the

hybridization term deserves special attention. Expanded around the Γ -point, it reads

$$H_{\text{hyb}} = V \sum_{m,k} (-1)^m [(k_x - ik_y) c_{0m\uparrow}^\dagger d_{k\uparrow} + (k_x + ik_y) c_{0m\downarrow}^\dagger d_{k\downarrow}] + \text{H.c.},$$

where V denotes the strength of the hybridization, c_{0m}^\dagger and c_{0m} represent the creation and annihilation of p_z -orbitals on the top TI bilayer where $m = 0, 1$ index its two sublayers, and $d_{k(\uparrow)}^\dagger$ and $d_{k(\downarrow)}^\dagger$ create and annihilate the respective $(p_x + ip_y) \uparrow$ and $(p_x - ip_y) \downarrow$ orbitals of the RSBs. It is important to note that the time-reversal and C_3 symmetry ensure that the hybridization vanishes at the Γ point, meaning that the Dirac crossings of the RSBs and that of the TSSs remain intact. Due to the finite hybridization away from the Γ point, the two Dirac crossings switch designations, i.e., the original RSB crossing becomes the crossing of the new Dirac cone that connects the conduction and valence bands, and vice versa. In this manner, the essential topological properties of the hybrid system are unaltered from the original TI. As a side remark, had we considered RSBs originating from other orbitals, such as one with p_z -symmetry, the hybridization between the two Dirac crossings at the Γ point would have become finite, shifting their relative energy. However, this hybridization does not lift the degeneracy of the individual crossings so long as time-reversal symmetry is preserved. Hence, as in the above case, the two crossings switch designations and the overall topology remains.

In Fig. 4(c), we present the results of TB simulations of the Q-termination within the PM state, in which only the

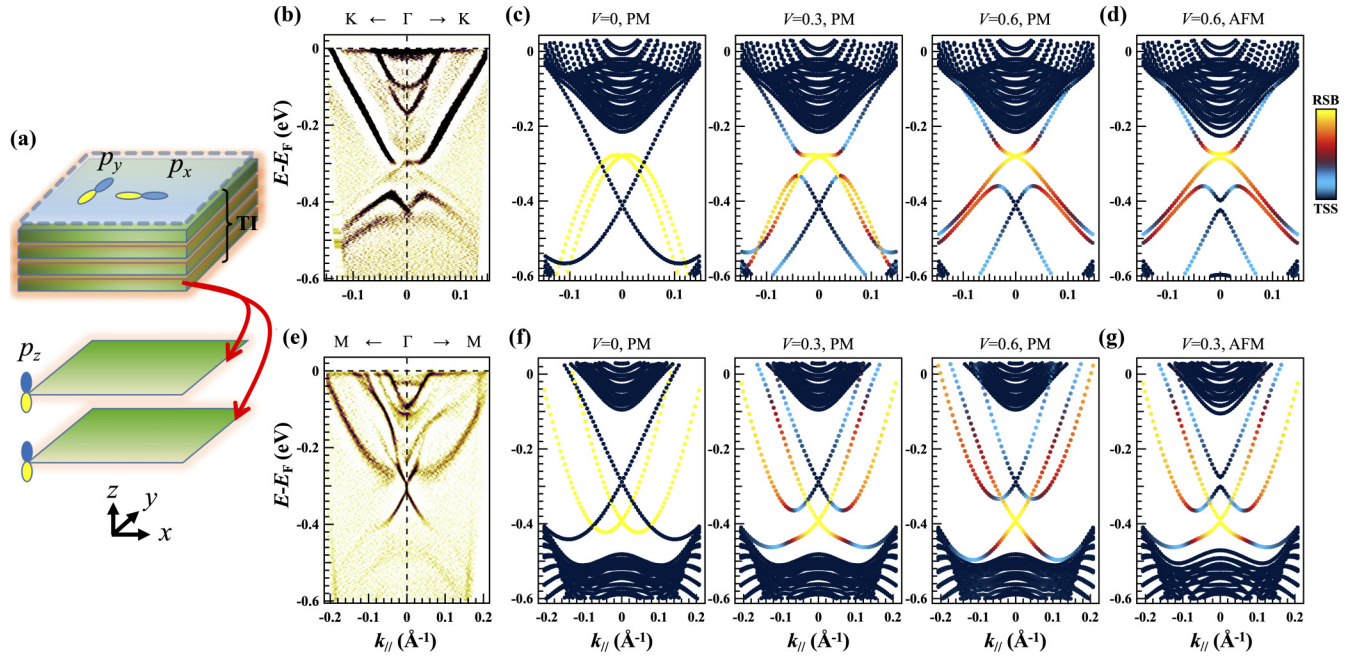


FIG. 4. TB simulation on the TSS-RSBs hybridization. (a) Schematic of the TB model. (b)–(d) TB simulation for Q-termination band structure. (b) ARPES spectra in 2D curvature. (c) TB model simulated band structure and its evolution with increasing hybridization at the PM state. The color bar indicates the contribution from TSS and RSB for the hybridized bands, excluding the ordinary bulk conduction and valence band. (d) TB simulated bands at AFM order. (e)–(g) Similar results for S-termination.

hybridization strength V is varied. Note that both the Rashba SOC and the coupling strength V are determined by realistic surface conditions and are hence expected to be different between the two types of surface termination, as shown in Figs. 3(e) and 3(j). Here, we aim to qualitatively explain the key features of the ARPES spectra using the simplest model, without trying to fully reproduce the observed band structure. For $V = 0$, the TSSs (blue) and RSBs (red) remain intact. With increasing V ($V = 0.6$), the main features of the experimental spectra are readily reproduced, including not only the M-shaped VBM and the gaplike structure already presented in the DFT calculation, but also the Λ -shaped in-gap band, which is absent in the DFT calculation. Further inclusion of AFM order [Fig. 4(d)] opens gaps at both the original TSS Dirac point and the crossing of the RSBs at the Γ point. The magnitude of these two gaps depends on the effective exchange fields that TSS and RSB wave functions experience in the real material.

Within this picture, those intriguing features found in the experimental spectra of Q-terminations [Fig. 3(d)] can now be understood. The M-shaped VBM consists of the original TSS Dirac cone and RSBs; the gaplike feature appears in the upper Dirac cone region due to the surface-bulk hybridization; the gaplessness comes from the symmetry-protected touching of the gapped TSSs and Λ -shaped in-gap band at the Γ point. With AFM order, gaps are opened at both the original TSS Dirac cone and the new touching point, but the gap size could be so small that extrinsic factors can smear it easily.

This TB hybridization model is also applicable to the S-termination shown in Fig. 4(f). The main difference is that RSBs are hole-type in Q-termination but electron-type in S-termination, as presented in Figs. 3(e) and 3(j). With appropriate SOC and increasing V , the cordial glass-shaped CBM

and gapless linear Dirac cones start to manifest. The $V = 0.3$ panel matches the experimental spectra the most. The resultant (nearly) gapless features at S-termination thus come from the original RSB Dirac cone. The original TSS Dirac cone gains broadness due to its hybridization with bulk states, and its tiny gap at the AFM state may be smeared. We note that small gaps are observed by ARPES in Q- and S-terminations with AFM order by others [57], which may be captured by our TB model if we appropriately choose small exchange fields [Fig. 4(g)]. We stress that, since the effective exchange fields are expected to depend crucially on the microscopic details of the surface magnetism and on the wave function of the RSBs and TSSs, the exact prediction of these exchange fields, and consequently the exact gap size of TSSs at AFM phase, are not the focus of our study.

III. DISCUSSION

We have demonstrated the applicability of a surface-bulk hybridization model to account for the band structure at the S- and Q-terminations of $\text{MnBi}_6\text{Te}_{10}$. Built on the DFT orbital projection and CD ARPES spectral analyses, this model is well-grounded and provides a unique physical picture to explain the intriguing band structure observed on the surfaces of these magnetic TI compounds. Within this description, the Dirac cones identified by ARPES are of bulk origin, with wave functions extending deeper into the crystal than the nonhybridized ones. This means that the impact of S symmetry breaking at the surface on these spectral features could be smaller than expected for the perfectly surface localized TSS. Given the similarity in the lattice and band structures, the universal (nearly) gapless behavior on the surfaces of the

magnetic TI family of $(\text{MnBi}_2\text{Te}_4)_m(\text{Bi}_2\text{Te}_3)_n$ can be potentially understood within this picture.

Ideally, spin-resolved ARPES (SpinARPES) would be the right tool to directly prove the existence of RSBs. Unfortunately, SpinARPES with μm spatial resolution is not an available technique, leaving CD ARPES the only choice to gain insights into the spin texture of $\text{MnBi}_6\text{Te}_{10}$. Similar weak CD signals were also observed on the bulk states in Bi_2Te_3 with specific photon energy [70]. One may also raise a concern about the final state effect as the photon energy we use is very low. Systematic photon-energy-dependent μ -ARPES measurement is expected to clarify this issue, which, unfortunately again, is constrained by the limited photon energy range due to the accessibility of the TSS Dirac cone in this family of materials, as discussed below.

The bulk origin of the effective TSS Dirac cones suggests that their accessibility depends on the bulk sensitivity of probes employed. In the ultraviolet photoemission process, the increase of bulk sensitivity (mean free path of photoelectrons) with decreasing energy follows the “universal curve” [76]. The accessibility of the TSS Dirac cone in this material family is much improved in ARPES measurement using a laser (6–7 eV) [40–43,54,56–58] than that using higher photon energies (tens of eV) [21,22,30,34,39,48–50]. This explains the controversial ARPES observations concerning the gapless/gapped nature of TSS Dirac cone, providing insightful guidance to improve the TSS addressability from both experimental and theoretical approaches, but it limits the available photon energy range to clarify the final state effect.

IV. MATERIALS AND METHODS

A. Sample growth and characterization

High-quality $\text{MnBi}_6\text{Te}_{10}$ single crystals were grown by the conventional high-temperature solution method with Bi_2Te_3 as the flux. Mn (purity 99.98%), Bi (purity 99.999%), and Te (99.999%) blocks were placed in an alumina crucible with a molar ratio of Mn : Bi : Te = 1 : 11.3 : 18. Then the alumina crucible was sealed in a quartz tube under the argon environment. The assembly was first heated up in a box furnace to 950 °C, held for 10 h, then subsequently cooled down to 700 °C over 10 h and further cooled down slowly to 575 °C over 100 h. After this heating procedure, the quartz tube was taken out quickly and then decanted into the centrifuge to remove the excess flux from the single crystals.

Resistivity measurements were performed by a Quantum Design (QD) Physical Properties Measurement System (PPMS) with a standard six-probe method. The driven current is 10 mA and flows in the *ab* plane. Magnetic measurements were performed using the QD PPMS with the Vibrating Sample Magnetometer (VSM) mode. Temperature-dependent magnetization results were collected with an external magnetic field of 300 Oe, both along and perpendicular to the *c*-axis direction of the sample.

B. ARPES measurement

μ -laser-ARPES measurements were performed at the Hiroshima Synchrotron Radiation Center (HSRC), Hiroshima,

Japan, with a VG Scienta R4000 electron analyzer and a photon energy of 6.3 eV [59]. The energy and angular resolution were better than 3 meV and less than 0.05°, respectively. Samples were cleaved *in situ* along the (001) crystal plane under ultrahigh-vacuum conditions with pressure better than 5×10^{-11} mbar and temperatures below 25 K.

C. DFT calculation method

First-principles calculations were performed using the Vienna *ab initio* simulation package (VASP) [77,78] within the framework of density-functional theory [79,80]. The generalized gradient approximation (GGA) with the Perdew-Burke-Ernzerhof (PBE) formalism was chosen for the exchange-correlation functional [81]. The projector augmented wave (PAW) method was implemented to treat core-valence interactions with a cutoff energy of 400 eV for the plane-wave expansion [82,83]. The full Brillouin zone was sampled by an $8 \times 8 \times 1$ Monkhorst-Pack grid [84]. The slab structures (including both lattice and fractional coordinates) were fully relaxed until the forces on each atom were less than 0.01 eV/Å. Considering the strongly correlated nature of 3d electrons in Mn, we introduced on-site Coulomb repulsion by employing GGA+U calculations [85] and set the correlation energy to be 5 eV, which worked well in previous work [19].

D. Tight-binding simulation method

We construct a model to effectively simulate the hybridization between the TI surface states and a pair of Rashba-split bands. Since we are only concerned with the physics around the Γ -point, it is sufficient to build the model on a lattice with tetragonal symmetry to keep the expressions in their simplest forms. No essential feature of the hybridization in question is lost due to this simplification. We generalize a standard $k \cdot p$ theory of the TI [86] to a 3D lattice model, which is formed by a stacking of bilayers with each sublayer featuring a p_z -orbital. Regarding the hybridization to bulk states, we consider that the topmost bilayer of the TI is coupled to an extra band with Rashba SOC, whose band top (or bottom) overlaps with the TSSs in momentum space. More details can be found in Sec. 3 of the Supplemental Material [60].

Note added: Recently, we became aware of several scanning tunneling microscopy studies [72,87,88] that reveal that defect states at the Dirac energy could potentially hinder the detection of magnetic gaps at the surface of these AFM TIs. While defect states may influence the resolution of ARPES spectra, they are unlikely to be the origin of the well-resolved dispersive in-gap bands observed in our study. Indeed, the quasiparticle interference patterns indicate that the topological surface states may be embedded in deeper layers beneath the topmost surface [87], in qualitative agreement with our findings here. Furthermore, similar surface-bulk band hybridization has been discussed on the Q-termination of MnBi_4Te_7 from DFT calculation [72].

ACKNOWLEDGMENTS

We thank Prof. Qihang Liu, Junhao Lin, Haizhou Lu, and Zhongbo Yan for helpful discussions. This work

is supported by the National Natural Science Foundation of China (NSFC) (Grant Nos. 12074163, 12074161, 11888101, 11904155 and 12004159), NSFC Guangdong (No. 2016A030313650), the Shenzhen High-level Special Fund (Grant Nos. G02206304, G02206404), the Guangdong Innovative and Entrepreneurial Research Team Program (Grant Nos. 2019ZT08C044, 2016ZT06D348), the Peacock Team Program supported by the Science, Technology and Innovation Commission of Shenzhen Municipality (Grant No. KQTD20190929173815000), the University Innovative Team in Guangdong Province (No. 2020KCXTD001). X.J.Z. is also supported by the National Key Research and Development Program of China (Grant No. 2016YFA0300300 and 2017YFA0302900). H.X. is supported by Center for Computational Science and Engineering at Southern University of

Science and Technology. Ch.L. acknowledges support from the Highlight Project (No. PHYS-HL-2020-1) of the College of Science, SUSTech. B.S. acknowledges support from the Fundamental Research Funds for the Central Universities (Grant No. 19lgpy260). K.D. acknowledges the support from the Youth Project of Guangdong NSF Regional Joint Foundation under Contract No. 2019A1515110712. J.F.S. is supported by the National Foundation for Young Scientists of China (NFYSC) (Grant No. 11804402). R.L. is supported by the NFYSC (Grant No. 11804144). The ARPES measurements were performed with the approval of the Proposal Assessing Committee of the Hiroshima Synchrotron Radiation Center (Proposal Numbers: 19AU002, 19AU007 and 19BG006).

X-M.M., Z.C., E.F.S., and Y.Z. contributed equally to this work.

- [1] M. Z. Hasan and C. L. Kane, Colloquium: topological insulators, *Rev. Mod. Phys.* **82**, 3045 (2010).
- [2] X.-L. Qi and S.-C. Zhang, Topological insulators and superconductors, *Rev. Mod. Phys.* **83**, 1057 (2011).
- [3] Y. Ando and L. Fu, Topological crystalline insulators and topological superconductors: from concepts to materials, *Annu. Rev. Condens. Matter Phys.* **6**, 361 (2015).
- [4] N. P. Armitage and L. Wu, On the matter of topological insulators as magnetoelectrics, *SciPost Phys.* **6**, 46 (2019).
- [5] D. Xiao, J. Jiang, J.-H. Shin, W. Wang, F. Wang, Y.-F. Zhao, C. Liu, W. Wu, M. H. W. Chan, N. Samarth, and C.-Z. Chang, Realization of the Axion Insulator State in Quantum Anomalous Hall Sandwich Heterostructures, *Phys. Rev. Lett.* **120**, 056801 (2018).
- [6] J. Wang, B. Lian, X.-L. Qi, and S.-C. Zhang, Quantized topological magnetoelectric effect of the zero-plateau quantum anomalous Hall state, *Phys. Rev. B* **92**, 081107(R) (2015).
- [7] L. Fu and C. L. Kane, Superconducting Proximity Effect and Majorana Fermions at the Surface of a Topological Insulator, *Phys. Rev. Lett.* **100**, 096407 (2008).
- [8] R. S. K. Mong, A. M. Essin, and J. E. Moore, Antiferromagnetic topological insulators, *Phys. Rev. B* **81**, 245209 (2010).
- [9] F. D. M. Haldane, Model for a Quantum Hall Effect Without Landau Levels: Condensed-Matter Realization of the “Parity Anomaly,” *Phys. Rev. Lett.* **61**, 2015 (1988).
- [10] R. Yu, W. Zhang, H.-J. Zhang, S.-C. Zhang, X. Dai, and Z. Fang, Quantized anomalous Hall effect in magnetic topological insulators, *Science* **329**, 61 (2010).
- [11] C. Z. Chang, J. Zhang, X. Feng, J. Shen, Z. Zhang, M. Guo, K. Li, Y. Ou, P. Wei, L.-L. Wang, Z.-Q. Ji, Y. Feng, S. Ji, X. Chen, J. Jia, X. Dai, Z. Fang, S.-C. Zhang, K. He, Y. Wang, L. Lu, X.-C. Ma, and Q.-K. Xue, Experimental observation of the quantum anomalous Hall effect in a magnetic topological insulator, *Science* **340**, 167 (2013).
- [12] C.-Z. Chang, W. Zhao, D. Y. Kim, H. Zhang, B. A. Assaf, D. Heiman, S.-C. Zhang, C. Liu, M. H. W. Chan, and J. S. Moodera, High-precision realization of robust quantum anomalous Hall state in a hard ferromagnetic topological insulator, *Nat. Mater.* **14**, 473 (2015).
- [13] N. P. Armitage, E. J. Mele, and A. Vishwanath, Weyl and Dirac semimetals in three-dimensional solids, *Rev. Mod. Phys.* **90**, 015001 (2018).
- [14] K. Kim, J. Seo, E. Lee, K.-T. Ko, B. S. Kim, B. G. Jang, J. M. Ok, J. Lee, Y. J. Jo, W. Kang, J. H. Shim, C. Kim, H. W. Yeom, B. I. Min, B.-J. Yang, and J. S. Kim, Large anomalous Hall current induced by topological nodal lines in a ferromagnetic van der Waals semimetal, *Nat. Mater.* **17**, 794 (2018).
- [15] Y. Tokura, K. Yasuda, and A. Tsukazaki, Magnetic topological insulators, *Nat. Rev. Phys.* **1**, 126 (2019).
- [16] F. Katmis, V. Lauter, F. S. Nogueira, B. A. Assaf, M. E. Jamer, P. Wei, B. Satpati, J. W. Freeland, I. Eremin, D. Heiman, P. Jarillo-Herrero, and J. S. Moodera, A high-temperature ferromagnetic topological insulating phase by proximity coupling, *Nature (London)* **533**, 513 (2016).
- [17] M. Mogi, M. Kawamura, R. Yoshimi, A. Tsukazaki, Y. Kozuka, N. Shirakawa, K. S. Takahashi, M. Kawasaki, and Y. Tokura, A magnetic heterostructure of topological insulators as a candidate for an axion insulator, *Nat. Mater.* **16**, 516 (2017).
- [18] M. M. Otrokov, T. V. Menshchikova, I. P. Rusinov, M. G. Vergniory, V. M. Kuznetsov, and E. V. Chulkov, Magnetic extension as an efficient method for realizing the quantum anomalous Hall state in topological insulators, *JETP Lett.* **105**, 297 (2017).
- [19] M. M. Otrokov, T. V. Menshchikova, M. G. Vergniory, I. P. Rusinov, A. Yu. Vyazovskaya, Yu. M. Koroteev, G. Bihlmayer, A. Ernst, P. M. Echenique, A. Arnau, and E. V. Chulkov, Highly-ordered wide bandgap materials for quantized anomalous Hall and magnetoelectric effects, *2D Mater.* **4**, aa6bec (2017).
- [20] R. S. K. Mong and J. E. Moore, Magnetic and topological order united in a crystal, *Nature (London)* **576**, 390 (2019).
- [21] M. M. Otrokov, I. I. Klimovskikh, H. Bentmann, D. Estyunin, A. Zeugner, Z. S. Aliev, S. Gaß, A. U. B. Wolter, A. V. Koroleva, A. M. Shikin, M. Blanco-Rey, M. Hoffmann, I. P. Rusinov, A. Yu. Vyazovskaya, S. V. Eremeev, Yu. M. Koroteev, V. M. Kuznetsov, F. Freyse, J. Sánchez-Barriga, I. R. Amiraslanov, M. B. Babanly, N. T. Mamedov, N. A. Abdullayev, V. N. Zverev, A. Alfonsov, V. Kataev, B. Büchner, E. F. Schwier, S. Kumar, A. Kimura, L. Petaccia, G. Di Santo, R. C. Vida, S. Schatz, K. Kißner, M. Ünzelmänn, C. H. Min, Simon Moser, T. R. F. Peixoto, F. Reinert, A. Ernst, P. M. Echenique, A. Isaeva, and E. V. Chulkov, Prediction and observation of an antiferromagnetic topological insulator, *Nature (London)* **576**, 416 (2019).

- [22] E. D. L. Rienks, S. Wimmer, J. Sánchez-Barriga, O. Caha, P. S. Mandal, J. Rrmůžička, A. Ney, H. Steiner, V. V. Volobuev, H. Groiss, M. Albu, G. Kothleitner, J. Michalička, S. A. Khan, J. Minár, H. Ebert, G. Bauer, F. Freyse, A. Varykhalov, O. Rader, and G. Springholz, Large magnetic map at the Dirac point in $\text{Bi}_2\text{Te}_3/\text{MnBi}_2\text{Te}_4$ heterostructures, *Nature (London)* **576**, 423 (2019).
- [23] J. Li, Y. Li, S. Du, Z. Wang, B.-L. Gu, S.-C. Zhang, K. He, W. Duan, and Y. Xu, Intrinsic magnetic topological insulators in van der waals layered MnBi_2Te_4 -family materials, *Sci. Adv.* **5**, eaaw5685 (2019).
- [24] J. Li, C. Wang, Z. Zhang, B.-L. Gu, W. Duan, and Y. Xu, Magnetically controllable topological quantum phase transitions in the antiferromagnetic topological insulator MnBi_2Te_4 , *Phys. Rev. B* **100**, 121103(R) (2019).
- [25] M. M. Otrokov, I. P. Rusinov, M. Blanco-Rey, M. Hoffmann, A. Yu. Vyazovskaya, S. V. Eremeev, A. Ernst, P. M. Echenique, A. Arnau, and E. V. Chulkov, Unique Thickness-Dependent Properties of the Van Der Waals Interlayer Antiferromagnet MnBi_2Te_4 Films, *Phys. Rev. Lett.* **122**, 107202 (2019).
- [26] D. Zhang, M. Shi, T. Zhu, D. Xing, H. Zhang, and J. Wang, Topological Axion States in the Magnetic Insulator MnBi_2Te_4 with the Quantized Magnetoelectric Effect, *Phys. Rev. Lett.* **122**, 206401 (2019).
- [27] K. Y. Chen, B. S. Wang, J.-Q. Yan, D. S. Parker, J.-S. Zhou, Y. Uwatoko, and J.-G. Cheng, Suppression of the antiferromagnetic metallic state in the pressurized MnBi_2Te_4 single crystal, *Phys. Rev. Mater.* **3**, 094201 (2019).
- [28] J. Cui, M. Shi, H. Wang, F. Yu, T. Wu, X. Luo, J. Ying, and X. Chen, Transport properties of thin flakes of the antiferromagnetic topological insulator MnBi_2Te_4 , *Phys. Rev. B* **99**, 155125 (2019).
- [29] J.-Q. Yan, S. Okamoto, M. A. McGuire, A. F. May, R. J. McQueeney, and B. C. Sales, Evolution of structural, magnetic, and transport properties in $\text{MnBi}_{2-x}\text{Sb}_x\text{Te}_4$, *Phys. Rev. B* **100**, 104409 (2019).
- [30] A. Zeugner, F. Nietschke, A. U. B. Wolter, S. Gaß, R. C. Vidal, T. R. F. Peixoto, D. Pohl, C. Damm, A. Lubk, R. Hentrich, S. K. Moser, C. Fornari, C. H. Min, S. Schatz, K. Kißner, M. Ünzelmänn, M. Kaiser, F. Scaravaggi, B. Rellinghaus, K. Nielsch, C. Hess, B. Büchner, F. Reinert, H. Bentmann, O. Oeckler, T. Doert, M. Ruck, and A. Isaeva, Chemical aspects of the candidate antiferromagnetic topological insulator MnBi_2Te_4 , *Chem. Mater.* **31**, 2795 (2019).
- [31] H. Li, S. Liu, C. Liu, J. Zhang, Y. Xu, R. Yu, Y. Wu, Y. Zhang, and S. Fan, Antiferromagnetic topological insulator mnbite : synthesis and magnetic properties, *Phys. Chem. Chem. Phys.* **22**, 556 (2019).
- [32] J.-Q. Yan, Q. Zhang, T. Heitmann, Z. Huang, K. Y. Chen, J.-G. Cheng, W. Wu, D. Vaknin, B. C. Sales, and R. J. McQueeney, Crystal growth and magnetic structure of MnBi_2Te_4 , *Phys. Rev. Mater.* **3**, 064202 (2019).
- [33] B. Li, J.-Q. Yan, D. M. Pajerowski, E. Gordon, A.-M. Nedić, Y. Sizyuk, L. Ke, P. P. Orth, D. Vaknin, and R. J. McQueeney, Competing Magnetic Interactions in the Antiferromagnetic Topological Insulator MnBi_2Te_4 , *Phys. Rev. Lett.* **124**, 167204 (2020).
- [34] S. H. Lee, Y. Zhu, Y. Wang, L. Miao, T. Pillsbury, H. Yi, S. Kempinger, J. Hu, C. A. Heikes, P. Quarterman, W. Ratchliff, J. A. Borchers, H. Zhang, X. Ke, D. Graf, N. Alem, C.-Z. Chang, N. Samarth, and Z. Mao, Spin scattering and noncollinear spin structure-induced intrinsic anomalous Hall effect in antiferromagnetic topological insulator MnBi_2Te_4 , *Phys. Rev. Res.* **1**, 012011(R) (2019).
- [35] Y. Deng, Y. Yu, M. Z. Shi, Z. Guo, Z. Xu, J. Wang, X. H. Chen, and Y. Zhang, Quantum anomalous Hall effect in intrinsic magnetic topological insulator MnBi_2Te_4 , *Science* **367**, 895 (2020).
- [36] J. Ge, Y. Liu, J. Li, H. Li, T. Luo, Y. Wu, Y. Xu, and J. Wang, High-Chern-number and high-temperature quantum Hall effect without Landau levels, *Natl. Sci. Rev.* **7**, 1280 (2020).
- [37] C. Liu, Y. Wang, H. Li, Y. Wu, Y. Li, J. Li, K. He, Y. Xu, J. Zhang, and Y. Wang, Robust axion insulator and Chern insulator phases in a two-dimensional antiferromagnetic topological insulator, *Nat. Mater.* **19**, 522 (2020).
- [38] Y. Gong, J. Guo, J. Li, K. Zhu, M. Liao, X. Liu, Q. Zhang, L. Gu, L. Tang, X. Feng, D. Zhang, W. Li, C. Song, L. Wang, P. Yu, X. Chen, Y. Wang, H. Yao, W. Duan, Y. Xu, S.-C. Zhang, X. Ma, Q.-K. Xue, and K. He, Experimental realization of an intrinsic magnetic topological insulator, *Chin. Phys. Lett.* **36**, 076801 (2019).
- [39] R. C. Vidal, H. Bentmann, T. R. F. Peixoto, A. Zeugner, S. Moser, C.-H. Min, S. Schatz, K. Kißner, M. Ünzelmänn, C. I. Fornari, H. B. Vasili, M. Valvidares, K. Sakamoto, D. Mondal, J. Fujii, I. Vobornik, S. Jung, C. Cacho, T. K. Kim, R. J. Koch, C. Jozwiak, A. Bostwick, J. D. Denlinger, E. Rotenberg, J. Buck, M. Hoesch, F. Diekmann, S. Rohlf, M. Kalläne, K. Rossnagel, M. M. Otrokov, E. V. Chulkov, M. Ruck, A. Isaeva, and F. Reinert, Surface states and Rashba-type spin polarization in antiferromagnetic MnBi_2Te_4 (0001), *Phys. Rev. B* **100**, 121104(R) (2019).
- [40] Y.-J. Hao, P. Liu, Y. Feng, X.-M. Ma, E. F. Schwier, M. Arita, S. Kumar, C. Hu, R. Lu, M. Zeng, Y. Wang, Z. Hao, H.-Y. Sun, K. Zhang, J. Mei, N. Ni, L. Wu, K. Shimada, C. Chen, Q. Liu, and C. Liu, Gapless Surface Dirac Cone in Antiferromagnetic Topological Insulator MnBi_2Te_4 , *Phys. Rev. X* **9**, 041038 (2019).
- [41] H. Li, S.-Y. Gao, S.-F. Duan, Y.-F. Xu, K.-J. Zhu, S.-J. Tian, J.-C. Gao, W.-H. Fan, Z.-C. Rao, J.-R. Huang, J.-J. Li, D.-Y. Yan, Z.-T. Liu, W.-L. Liu, Y.-B. Huang, Y.-L. Li, Y. Liu, G.-B. Zhang, P. Zhang, T. Kondo, S. Shin, H.-C. Lei, Y.-G. Shi, W.-T. Zhang, H.-M. Weng, T. Qian, and H. Ding, Dirac Surface States in Intrinsic Magnetic Topological Insulators EuSn_2As_2 and $\text{MnBi}_{2n}\text{Te}_{3n+1}$, *Phys. Rev. X* **9**, 041039 (2019).
- [42] P. Swatek, Y. Wu, L.-L. Wang, K. Lee, B. Schrunk, J. Yan, and A. Kaminski, Gapless Dirac surface states in the antiferromagnetic topological insulator MnBi_2Te_4 , *Phys. Rev. B* **101**, 161109(R) (2020).
- [43] Y. J. Chen, L. X. Xu, J. H. Li, Y. W. Li, H. Y. Wang, C. F. Zhang, H. Li, Y. Wu, A. J. Liang, C. Chen, S. W. Jung, C. Cacho, Y. H. Mao, S. Liu, M. X. Wang, Y. F. Guo, Y. Xu, Z. K. Liu, L. X. Yang, and Y. L. Chen, Topological Electronic Structure and its Temperature Evolution in Antiferromagnetic Topological Insulator MnBi_2Te_4 , *Phys. Rev. X* **9**, 041040 (2019).
- [44] C. Chen, S. He, H. Weng, W. Zhang, L. Zhao, H. Liu, X. Jia, D. Mou, S. Liu, J. He, Y. Peng, Y. Feng, Z. Xie, G. Liu, X. Dong, J. Zhang, X. Wang, Q. Peng, Z. Wang, S. Zhang, F. Yang, C. Chen, Z. Xu, Xi Dai, Z. Fang, and X. J. Zhou, Robustness of topological order and formation of quantum well states in topological insulators exposed to ambient environment, *Proc. Natl. Acad. Sci. (U.S.A.)* **109**, 3694 (2012).

- [45] Z. S. Aliev, I. R. Amiraslanov, D. I. Nasonova, A. V. Shevelkov, N. A. Abdullayev, Z. A. Jahangirli, E. N. Orujlu, M. M. Otrokov, N. T. Mamedov, M. B. Babanly, and E. V. Chulkov, Novel ternary layered manganese bismuth tellurides of the MnTe-Bi₂Te₃ system: synthesis and crystal structure, *J. Alloy. Comp.* **789**, 443 (2019).
- [46] D. Souchay, M. Nentwig, D. Günther, S. Keilholz, J. d. Boor, A. Zeugner, A. Isaeva, M. Ruck, A. U. B. Wolter, B. Büchner, and O. Oeckler, Layered manganese bismuth tellurides with GeBi₄Te₇- and GeBi₆Te₁₀-type structures: towards multifunctional materials, *J. Mater. Chem. C* **7**, 9939 (2019).
- [47] H. Sun, B. Xia, Z. Chen, Y. Zhang, P. Liu, Q. Yao, H. Tang, Y. Zhao, H. Xu, and Q. Liu, Rational Design Principles of the Quantum Anomalous Hall Effect in Superlattice-like Magnetic Topological Insulators, *Phys. Rev. Lett.* **123**, 096401 (2019).
- [48] C. Hu, K. N. Gordon, P. Liu, J. Liu, X. Zhou, P. Hao, D. Narayan, E. Emmanouilidou, H. Sun, Y. Liu, H. Brawer, A. P. Ramirez, L. Ding, H. Cao, Q. Liu, D. Dessau, and N. Ni, A van der Waals antiferromagnetic topological insulator with weak interlayer magnetic coupling, *Nat. Commun.* **11**, 97 (2020).
- [49] J. Wu, F. Liu, M. Sasase, K. Ienaga, Y. Obata, R. Yukawa, K. Horiba, H. Kumigashira, S. Okuma, T. Inoshita, and H. Hosono, Natural van der Waals heterostructural single crystals with both magnetic and topological properties, *Sci. Adv.* **5**, eaax9989 (2019).
- [50] R. C. Vidal, A. Zeugner, J. I. Facio, R. Ray, M. H. Haghighi, A. U. B. Wolter, L. T. C. Bohorquez, F. Caglieris, S. Moser, T. Figgemeier, T. R. F. Peixoto, H. B. Vasili, M. Valvidares, S. Jung, C. Cacho, A. Alfonsov, K. Mehawat, V. Kataev, C. Hess, M. Richter, B. Bchner, J. V. D. Brink, M. Ruck, F. Reinert, H. Bentmann, and A. Isaeva, Topological Electronic Structure and Intrinsic Magnetization in MnBi₄Te₇: A Bi₂Te₃-Derivative with a Periodic Mn Sublattice, *Phys. Rev. X* **9**, 041065 (2019).
- [51] L. Ding, C. Hu, F. Ye, E. Feng, N. Ni, and H. Cao, Crystal and magnetic structures of magnetic topological insulators MnBi₂Te₄ and MnBi₄Te₇, *Phys. Rev. B* **101**, 020412(R) (2020).
- [52] J.-Q. Yan, Y. H. Liu, D. S. Parker, Y. Wu, A. A. Aczel, M. Matsuda, M. A. McGuire, and B. C. Sales, A-type antiferromagnetic order in MnBi₄Te₇ and MnBi₆Te₁₀ single crystals, *Phys. Rev. Mater.* **4**, 054202 (2020).
- [53] M. Z. Shi, B. Lei, C. S. Zhu, D. H. Ma, J. H. Cui, Z. L. Sun, J. J. Ying, and X. H. Chen, Magnetic and transport properties in the magnetic topological insulators MnBi₂Te₄(Bi₂Te₃)_n (*n* = 1, 2), *Phys. Rev. B* **100**, 155144 (2019).
- [54] Y. Hu, L. Xu, M. Shi, A. Luo, S. Peng, Z. Y. Wang, J. J. Ying, T. Wu, Z. K. Liu, C. F. Zhang, Y. L. Chen, G. Xu, X.-H. Chen, and J.-F. He, Universal gapless Dirac cone and tunable topological states in (MnBi₂Te₄)_m(Bi₂Te₃)_n heterostructures, *Phys. Rev. B* **101**, 161113(R) (2020).
- [55] K. N. Gordon, H. Sun, C. Hu, A. G. Linn, H. Li, Y. Liu, P. Liu, S. Mackey, Q. Liu, N. Ni, and D. Dessau, Strongly gapped topological surface states on protected surfaces of antiferromagnetic MnBi₄Te₇ and MnBi₆Te₁₀, [arXiv:1910.13943](https://arxiv.org/abs/1910.13943).
- [56] L. X. Xu, Y. H. Mao, H. Y. Wang, J. H. Li, Y. J. Chen, Y. Y. Xia, Y. W. Li, J. Zhang, H. J. Zheng, K. Huang, C. F. Zhang, S. T. Cui, A. J. Liang, W. Xia, H. Su, S. W. Jung, C. Cacho, M. X. Wang, G. Li, Y. Xu, Y. F. Guo, L. X. Yang, Z. K. Liu, and Y. L. Chen, Persistent gapless surface states in MnBi₂Te₄/Bi₂Te₃ superlattice antiferromagnetic topological insulator, [arXiv:1910.11014](https://arxiv.org/abs/1910.11014).
- [57] N. H. Jo, L.-L. Wang, R.-J. Slager, J. Yan, Y. Wu, K. Lee, B. Schunk, A. Vishwanath, and A. Kaminski, Intrinsic axion insulating behavior in antiferromagnetic MnBi₆Te₁₀, *Phys. Rev. B* **102**, 045130 (2020).
- [58] S. Tian, S. Gao, S. Nie, Y. Qian, C. Gong, Y. Fu, H. Li, W. Fan, P. Zhang, T. Kondo, S. Shin, J. Adell, H. Fedderwitz, H. Ding, Z. Wang, T. Qian, and H. Lei, Magnetic topological insulator in MnBi₆Te₁₀ with zero-field ferromagnetic state, *Phys. Rev. B* **102**, 035144 (2020).
- [59] H. Iwasawa, E. F. Schwier, M. Arita, A. Ino, H. Namatame, M. Taniguchi, Y. Aiura, and K. Shimada, Development of laser-based scanning micro-arpes system with ultimate energy and momentum resolutions, *Ultramicroscopy* **182**, 85 (2017).
- [60] See Supplemental Material at <http://link.aps.org/supplemental/10.1103/PhysRevB.102.245136> for additional material on the experimental details, calculation method and further interpretation on the validity of the Rashba assumption [89–94].
- [61] P. Zhang, P. Richard, T. Qian, Y.-M. Xu, X. Dai, and H. Ding, A precise method for visualizing dispersive features in image plots, *Rev. Sci. Instrum.* **82**, 043712 (2011).
- [62] C. Chen, Z. Xie, Y. Feng, H. Yi, A. Liang, S. He, D. Mou, J. He, Y. Peng, X. Liu, Y. Liu, L. Zhao, G. Liu, X. Dong, J. Zhang, L. Yu, X. Wang, Q. Peng, Z. Wang, S. Zhang, F. Yang, C. Chen, Z. Xu, and X. J. Zhou, Tunable Dirac fermion dynamics in topological insulators, *Sci. Rep.* **3**, 2411 (2013).
- [63] A. Kimura, E. E. Krasovskii, R. Nishimura, K. Miyamoto, T. Kadono, K. Kanomaru, E. V. Chulkov, G. Bihlmayer, K. Shimada, H. Namatame, and M. Taniguchi, Strong Rashba-Type Spin Polarization of the Photocurrent from Bulk Continuum States: Experiment and Theory for Bi(111), *Phys. Rev. Lett.* **105**, 076804 (2010).
- [64] E. E. Krasovskii and E. V. Chulkov, Rashba polarization of bulk continuum states, *Phys. Rev. B* **83**, 155401 (2011).
- [65] M. Bianchi, D. Guan, S. Bao, J. Mi, B. B. Iversen, P. D. C. King, and P. Hofmann, Coexistence of the topological state and a two-dimensional electron gas on the surface of Bi₂Se₃, *Nat. Commun.* **1**, 128 (2010).
- [66] H. M. Benia, C. Lin, K. Kern, and C. R. Ast, Reactive Chemical Doping of the Bi₂Se₃ Topological Insulator, *Phys. Rev. Lett.* **107**, 177602 (2011).
- [67] M. Bianchi, R. C. Hatch, J. Mi, B. B. Iversen, and P. Hofmann, Simultaneous Quantization of Bulk Conduction and Valence States Through Adsorption of Nonmagnetic Impurities on Bi₂Se₃, *Phys. Rev. Lett.* **107**, 086802 (2011).
- [68] P. D. C. King, R. C. Hatch, M. Bianchi, R. Ovsyannikov, C. Lupulescu, G. Landolt, B. Slomski, J. H. Dil, D. Guan, J. L. Mi, E. D. L. Rienks, J. Fink, A. Lindblad, S. Svensson, S. Bao, G. Balakrishnan, B. B. Iversen, J. Osterwalder, W. Eberhardt, F. Baumberger, and P. Hofmann, Large Tunable Rashba Spin Splitting of a Two-Dimensional Electron Gas in Bi₂Se₃, *Phys. Rev. Lett.* **107**, 096802 (2011).
- [69] Z.-H. Zhu, G. Levy, B. Ludbrook, C. N. Veenstra, J. A. Rosen, R. Comin, D. Wong, P. Dosanjh, A. Ubaldini, P. Syers, N. P. Butch, J. Paglione, I. S. Elfimov, and A. Damascelli, Rashba Spin-Splitting Control at the Surface of the Topological Insulator Bi₂Se₃, *Phys. Rev. Lett.* **107**, 186405 (2011).

- [70] M. S. Bahramy, P. D. C. King, A. D. L. Torre, J. Chang, M. Shi, L. Patthey, G. Balakrishnan, P. Hofmann, R. Arita, N. Nagaosa, and F. Baumberger, Emergent quantum confinement at topological insulator surfaces, *Nat. Commun.* **3**, 1159 (2012).
- [71] D. Nevola, H. X. Li, J.-Q. Yan, R. G. Moore, H.-N. Lee, H. Miao, and P. D. Johnson, Coexistence of Surface Ferromagnetism and Gapless Topological State in MnBi_2Te_4 , *Phys. Rev. Lett.* **125**, 117205 (2020).
- [72] X. Wu, J. Li, X.-M. Ma, Y. Zhang, Y. Liu, C.-S. Zhou, J. Shao, Q. Wang, Y.-J. Hao, Y. Feng, E. F. Schwier, S. Kumar, H. Sun, P. Liu, K. Shimada, K. Miyamoto, T. Okuda, K. Wang, M. Xie, C. Chen, Q. Liu, C. Liu, and Y. Zhao, Distinct Topological Surface States on the Two Terminations of MnBi_4Te_7 , *Phys. Rev. X* **10**, 031013 (2020).
- [73] S. R. Park, J. Han, C. Kim, Y. Y. Koh, C. Kim, H. Lee, H. J. Choi, J. H. Han, K. D. Lee, N. J. Hur, M. Arita, K. Shimada, H. Namatame, and M. Taniguchi, Chiral Orbital-Angular Momentum in the Surface States of Bi_2Se_3 , *Phys. Rev. Lett.* **108**, 046805 (2012).
- [74] Y. H. Wang, D. Hsieh, D. Pilon, L. Fu, D. R. Gardner, Y. S. Lee, and N. Gedik, Observation of a Warped Helical Spin Texture in Bi_2Se_3 from Circular Dichroism Angle-Resolved Photoemission Spectroscopy, *Phys. Rev. Lett.* **107**, 207602 (2011).
- [75] S. R. Park, C. H. Kim, J. Yu, J. H. Han, and C. Kim, Orbital-Angular-Momentum Based Origin of Rashba-Type Surface Band Splitting, *Phys. Rev. Lett.* **107**, 156803 (2011).
- [76] C. J. Powell, A. Jablonski, I. S. Tilinin, S. Tanuma, and D. R. Penn, Surface sensitivity of Auger-electron spectroscopy and x-ray photoelectron spectroscopy, *J. Electron Spectrosc. Relat. Phenom.* **98–99**, 1 (1999).
- [77] G. Kresse and J. Furthmüller, Efficient iterative schemes for ab initio total-energy calculations using a plane-wave basis set, *Phys. Rev. B* **54**, 11169 (1996).
- [78] G. Kresse and J. Furthmüller, Efficiency of ab-initio total energy calculations for metals and semiconductors using a plane-wave basis set, *Comput. Mater. Sci.* **6**, 15 (1996).
- [79] W. Kohn and L. J. Sham, Self-consistent equations including exchange and correlation effects, *Phys. Rev.* **140**, A1133 (1965).
- [80] P. Hohenberg and W. Kohn, Inhomogeneous electron gas, *Phys. Rev.* **136**, B864 (1964).
- [81] J. P. Perdew, K. Burke, and M. Ernzerhof, Generalized Gradient Approximation Made Simple, *Phys. Rev. Lett.* **77**, 3865 (1996).
- [82] P. E. Blöchl, Projector augmented-wave method, *Phys. Rev. B* **50**, 17953 (1994).
- [83] G. Kresse and D. Joubert, From ultrasoft pseudopotentials to the projector augmented-wave method, *Phys. Rev. B* **59**, 1758 (1999).
- [84] H. J. Monkhorst and J. D. Pack, Special points for Brillouin-zone integrations, *Phys. Rev. B* **13**, 5188 (1976).
- [85] A. I. Liechtenstein, V. I. Anisimov, and J. Zaanen, Density-functional theory and strong interactions: Orbital ordering in Mott-Hubbard insulators, *Phys. Rev. B* **52**, R5467 (1995).
- [86] L. Fu and E. Berg, Odd-Parity Topological Superconductors: Theory and Application to $\text{Cu}_x\text{Bi}_2\text{Se}_3$, *Phys. Rev. Lett.* **105**, 097001 (2010).
- [87] Y. Yuan, X. Wang, H. Li, J. Li, Y. Ji, Z. Hao, Y. Wu, K. He, Y. Wang, Y. Xu, W. Duan, W. Li, and Q.-K. Xue, Electronic states and magnetic response of MnBi_2Te_4 by scanning tunneling microscopy and spectroscopy, *Nano. Lett.* **20**, 3271 (2020).
- [88] Z. Liang, A. Luo, M. Shi, Q. Zhang, S. Nie, J.-J. Ying, J.-F. He, T. Wu, Z. Wang, G. Xu, Z.-Y. Wang, and X.-H. Chen, Mapping the Dirac fermions in intrinsic antiferromagnetic topological insulators $(\text{MnBi}_2\text{Te}_4)(\text{Bi}_2\text{Te}_3)_n$ ($n = 0, 1$), *Phys. Rev. B* **102**, 161115(R) (2020).
- [89] P. V. C. Medeiros, S. Stafström, and J. Björk, Effects of extrinsic and intrinsic perturbations on the electronic structure of graphene: Retaining an effective primitive cell band structure by band unfolding, *Phys. Rev. B* **89**, 041407(R) (2014).
- [90] P. V. C. Medeiros, S. S. Tsirkin, S. Stafström, and J. Björk, Unfolding spinor wave functions and expectation values of general operators: Introducing the unfolding-density operator, *Phys. Rev. B* **91**, 041116(R) (2015).
- [91] I. I. Klimovskikh, M. M. Otrokov, D. Estyunin, S. V. Ereemeev, S. O. Filnov, A. Koroleva, E. Shevchenko, V. Voroshnin, I. P. Rusinov, M. Blanco-Rey, M. Hoffmann, Z. S. Aliev, M. B. Babanly, I. R. Amiraslanov, N. A. Abdullayev, V. N. Zverev, A. Kimura, O. E. Tereshchenko, K. A. Kokh, L. Petaccia, G. Di Santo, A. Ernst, P. M. Echenique, N. T. Mamedov, A. M. Shikin, and E. V. Chulkov, Variety of magnetic topological phases in the $(\text{MnBi}_2\text{Te}_4)(\text{Bi}_2\text{Te}_3)_m$ family, *npj Quantum Mater.* **5**, 54 (2020).
- [92] F. Hou, Q. Yao, C.-S. Zhou, X.-M. Ma, M. Han, Y.-J. Hao, X. Wu, Y. Zhang, H. Sun, C. Liu, Y. Zhao, Q. Liu, and J. Lin, Te-vacancy-induced surface collapse and reconstruction in antiferromagnetic topological insulator MnBi_2Te_4 , *ACS Nano* **14**, 11262 (2020).
- [93] V. V. Volobuev, S. Mandal, M. Galicka, O. Caha, J. Sánchez-Barriga, D. D. Sante, A. Varykhalov, A. Khier, S. Picozzi, G. Bauer, P. Kacman, R. Buczko, O. Rader, and G. Springholz, Giant Rashba splitting in $\text{Pb}_{1-x}\text{Sn}_x\text{Te}$ (111) topological crystalline insulator films controlled by bi doping in the bulk, *Adv. Mater.* **29**, 1604185 (2017).
- [94] K. Ishizaka, M. S. Bahramy, H. Murakawa, M. Sakano, T. Shimojima, T. Sonobe, K. Koizumi, S. Shin, H. Miyahara, A. Kimura, K. Miyamoto, T. Okuda, H. Namatame, M. Taniguchi, R. Arita, N. Nagaosa, K. Kobayashi, Y. Murakami, R. Kumai, Y. Kaneko, Y. Onose, and Y. Tokura, Giant Rashba-type spin splitting in bulk BiTeI , *Nat. Mater.* **10**, 521 (2011).

Evidence of Weyl fermions in α -RuCl₃

Yuan Wang^{1,*}, Yuanjun Jin^{1,*}, Le Wang¹, Zhanyang Hao¹, Cai Liu¹, Yu-Jie Hao¹, Xiao-Ming Ma¹, Shiv Kumar², Eike F. Schwier², Kenya Shimada², Chang Liu¹, Jiawei Mei^{1,3}, Hu Xu^{1,†}, and Chaoyu Chen^{1,‡}

¹*Shenzhen Institute for Quantum Science and Engineering (SIQSE) and Department of Physics, Southern University of Science and Technology (SUSTech), Shenzhen 518055, China*

²*Hiroshima Synchrotron Radiation Centre, Hiroshima University, Higashi-Hiroshima, Hiroshima 739-0046, Japan*

³*Shenzhen Key Laboratory of Advanced Quantum Functional Materials and Devices, Southern University of Science and Technology, Shenzhen 518055, China*



(Received 29 October 2020; accepted 8 January 2021; published 29 January 2021)

Layered honeycomb lattice antiferromagnetic α -RuCl₃ has been studied intensively recently as a Kitaev spin liquid candidate. Here we present strong evidence that this material host realistic Weyl fermions derived from Cl 2*p* electrons. Our theoretical analysis suggests the existence of quadratic Weyl fermions without spin-orbit coupling and linear Weyl fermion with spin-orbit coupling. Angle-resolved photoemission spectroscopy with systematic photon energy-dependent measurements demonstrates that this Weyl cone possesses linear dispersion at bulk Brillouin zone center along all the three reciprocal directions and hyperbolic dispersion off center. Our work reveals the rich topological physics lying in the band structure of Kitaev QSL candidates and will stimulate further investigation not only limited to α -RuCl₃ but also honeycomb iridate family of materials.

DOI: [10.1103/PhysRevB.103.035150](https://doi.org/10.1103/PhysRevB.103.035150)

I. INTRODUCTION

Exploring novel elementary particles represented by electronic excitations based on topological quantum materials has been a central topic in current condensed matter physics. The existence of Dirac and Weyl fermions in condensed-matter systems has been confirmed experimentally in various families of materials such as the two-dimensional (2D) surfaces of three-dimensional (3D) topological insulators [1,2], semimetallic Na₃Bi [3–5], Cd₃As₂ [6–8], TaAs family [9–13], WTe₂ family [14,15], ZrSiS family [16–20], and Co-based magnets [21–23]. The signature of Majorana fermions has also been allocated by various experiments [24–28]. Recently, exotic fermionic excitations beyond the Dirac-Weyl-Majorana category have been discovered in condensed matter, as they are constrained by the symmetries of the 230 crystal space groups rather than by Poincaré invariance [29–37]. In general, these topological quasiparticles are characterized by their degeneracy, order of dispersion and topological charge of band crossing points in momentum space. In material systems with time-reversal symmetry, the degeneracy of multiband crossings in momentum space could be 2, 3, 4, 6, and 8, of which twofold degeneracy corresponds to Weyl points and fourfold being Dirac points. In Weyl-type crossings, the in-plane dispersion power n equals its Chern number, corresponding to a degeneracy of n conventional Weyl fermions (left- or right-handed), all with the same chirality [38,39]. Thus far, topological quasiparticles with twofold [40–45], threefold [29,37,46], fourfold [47–49], sixfold [29], and eightfold

[29,50] degeneracy have been theoretically explored based on a wide range of materials, with some of them being experimentally confirmed [3–16,30,31,51–53].

In parallel to this ever-evolving field of topological band materials, another type of topological phase of matter, termed the quantum spin liquid (QSL), has been intensively studied since the concept was proposed [54] in 1973 by P.W. Anderson. QSL exhibits rich physics and exotic properties such as long-range entanglement and fractional elementary excitations, holding potential for quantum communication and computation [55–59]. Among many others, the Kitaev model [60], based on $S = 1/2$ spin model on a 2D honeycomb lattice, represents the only exactly soluble QSL model. The material realization of Kitaev QSL has been focused on the iridate family of materials and α -RuCl₃. Compared with iridates such as (Li, Na)₂IrO₃ [57,59], more convincing signatures of QSL have been reported in α -RuCl₃ since its van der Waals layered structure is a better approximation of exact Kitaev honeycomb lattice [61–72].

Concerning α -RuCl₃, it is a $J_{\text{eff}} = 1/2$ spin-orbit Mott insulator with a localized moment magnetism. While extensive experimental efforts have been devoted to study its thermal [61–63], magnetic/structural [70–72], optical properties [73–75], and elementary excitations [64–70], much less is known about its band structure. Up to now, studies on the electronic properties of α -RuCl₃ (say, via angle-resolved photoemission spectroscopy (ARPES)), have been hindered by the lack of systematic band structure measurement and the poor agreement between measured and calculated band structure [76–78]. Previous studies have merely focused on the qualitative comparison of bands calculated by DFT and measured by ARPES with few random photon energies, leaving its band dispersion along k_z direction unknown. Although α -RuCl₃ is traditionally considered as a more proximate 2D

*These authors contributed equally to this work.

[†]xuh@sustech.edu.cn

[‡]chency@sustech.edu.cn

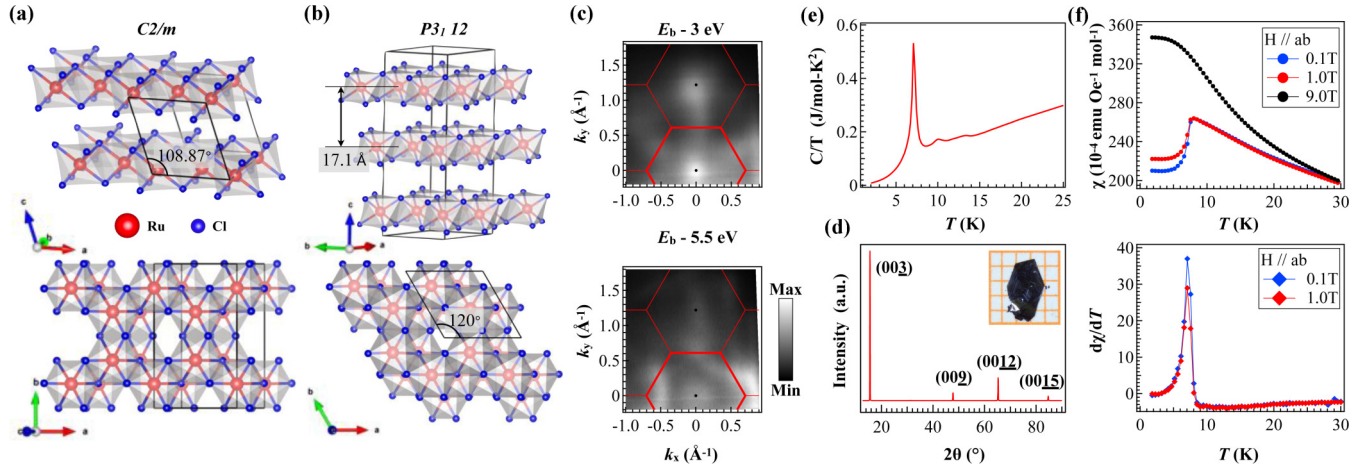


FIG. 1. Crystal structure and magnetic, electronic properties of α - RuCl_3 . (a) The crystal structure of α - RuCl_3 with a space group of $C2/m$, $\beta \approx 108.8^\circ$. (b) Crystal structure of α - RuCl_3 with a space group of $P3_112$. (c) Constant energy contours (CECs) at binding energy $E_B = 3$ eV and 5.5 eV measure by ARPES at 300 K. Red lines indicate the 2D BZ. (d) Single-crystal x-ray diffraction result taken at 300 K. The inset shows a typical single-crystal photo on a millimeter grid. (e) Low-temperature specific heat C/T without magnetic field. (f) The magnetic susceptibility (χ) vs. temperature (T) and the corresponding differential for $H // ab$ at various magnetic fields $H = 0.1$ T, 1.0 T, and 9.0 T, respectively.

Kitaev honeycomb lattice with neglectable interlayer interaction, here we point out that its k_z dispersion is nonignorable, composing potential evidence for its nontrivial band topology.

In this work, we present systematic photon-energy-dependent ARPES measurement and theoretical calculation on α - RuCl_3 to fully uncover its band structure in 3D Brillouin zone (BZ). It is found that, while the topmost valence bands consisting of Ru 4d electrons are almost completely 2D dispersed, the deeper valence bands consisting of Cl 3p electrons show clear k_z dispersion. More surprisingly, in the Cl 3p valence band region, we discovered a 3D conelike band structure centered at the bulk BZ center (Γ point). Around the band crossing point, the band shows linear dispersion. Our low-energy effective Hamiltonian analysis supports its nontrivial band topology with Chern number $C = \pm 2$ and the existence of quadratic Weyl fermions in this system without spin-orbit coupling (SOC). When SOC is included, this Weyl cone is linearly dispersed with $C = \pm 1$, which is directly confirmed by k_z -dependent ARPES spectra. Our work reveals the rich topological physics lying in the band structure of Kitaev QSL candidates and will stimulate further exploration on the electronic properties of other types of QSL materials.

II. RESULTS AND DISCUSSION

A. Crystal structure and magnetic properties of α - RuCl_3

The exact space group of the crystal structure of α - RuCl_3 is still a controversy. While some experimental results show that it is a monoclinic crystal structure with the $C2/m$ space group [72,79] and a monoclinic angle of $\beta \approx 108.8^\circ$ [Fig. 1(a)], there are also reports showing that it is a trigonal crystal structure with the $P3_112$ space group [Fig. 1(b)] [75,80]. Detailed magnetic and microscopic studies even reveal a temperature-dependent space group change [71,81] from $C2/m$ to $P3_112$ at 150 K upon cooling. In fact, both structural models share very close in-plane honeycomb lattice and the interlayer stacking difference is so small that stacking disorder makes them

experimentally indistinguishable. Throughout this work, we will adopt the $P3_112$ notation with a simple hexagonal 3D BZ [Fig. 2(b)], which has been widely used for this material in neutron studies [66,70,82] and ARPES studies [76–78].

Figure 1(c) shows ARPES measured CECs in reciprocal space at different energies (i.e., $E - E_F = -3$ eV and -5.5 eV). The periodicity of as-measured spectral intensity can be well described by the hexagonal 2D BZ based on an in-plane hexagonal lattice constant $a = 5.96$ Å. The crystallinity of as-grown α - RuCl_3 single crystals was examined by x-ray diffraction (XRD). As shown in Fig. 1(d), all the diffraction peaks can be well indexed by the $(00l)$ reflections with lattice parameter $c^* = 17.1 \pm 0.2$ Å. Figure 1(e) presents temperature-dependent specific heat (C/T) measured without external magnetic field. A sharp peak is observed at $T_N \approx 7$ K, corresponding to the antiferromagnetic (AFM) transition [81]. The temperature dependence of the magnetic susceptibility (χ for $H // ab$) measured at various magnetic fields is shown in Fig. 1(f). The AFM transition is also revealed around 7 K for $H = 0.1$ T, 1.0 T, and is suppressed at $H = 9.0$ T, in agreement with previous report [61]. In the lower panel of Fig. 1(f), the differential plots of χ ($d\chi/dT$) clearly show that this 7 K transition is the only present transition at the current temperature range. Previous works report coexisting 7 and 14 K transitions due to stacking disorder [79,81–83]. The existence of only one low temperature transition in our susceptibility indicates the high stacking homogeneity of the as-grown single crystal. Furthermore, this 7 K transition was shown by inelastic neutron scattering to correspond to AB-CABC stacking [70], justifying our choice of space group $P3_112$.

B. General valence band structure

The general valence band structure covering the full 3D BZ is presented in Fig. 2. We firstly performed photon-energy-dependent ARPES measurement to trace its valence band

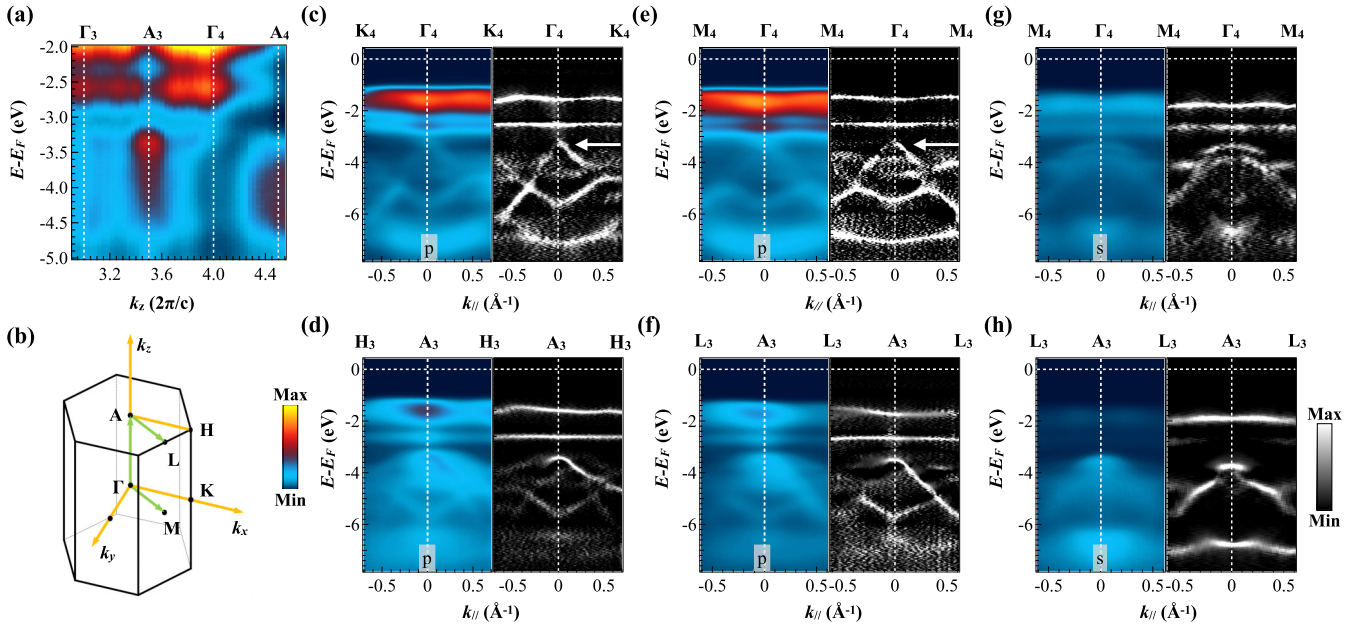


FIG. 2. General valence band structure of α -RuCl₃ measured at 300 K. (a) Photon energy-dependent ARPES measured spectra along k_z . (b) The 3D Brillouin zone of α -RuCl₃ corresponding to the space group of $P3_112$. (c–h) ARPES spectra (left panels) and corresponding 2D curvature spectra (right panels) along different high symmetry lines. The measurement geometry is p -polarization for (c–f) and s -polarization for (g–h).

dispersion along the k_z direction. As shown in Fig. 2(a), the dispersion and intensity oscillation indeed show a periodic pattern and help us to identify the high symmetry points along k_z by assuming an inner potential $V_0 = 18$ eV and effective out-of-plane lattice constant $c = c^*/3$. It is found that the Γ_4 point corresponds to a photon energy of 63 eV and A_3 point 46 eV. With this information, the valence bands along in-plane high symmetry cuts of 3D BZ are shown in Figs. 2(c)–2(h). Several key characters of the valence bands are obtained. First of all, the valence band maximum is nearly dispersionless along all the in-plane (k_x and k_y) and out-of-plane (k_z) directions. The band edge locates around 1.2 eV below the Fermi level, corresponding to a charge gap of ~ 2.4 eV assuming a neutral Mott phase (Fig. S1 [92]). Second, the valence bands locating above -3 eV, presumably from Ru $4d$ t_{2g} states [77], are nearly flat along all the three directions, too. In contrast, valence bands below -3 eV, presumably from Cl $2p$ orbitals, show clear in-plane dispersion. In particular, the topmost Cl-derivate valence band, as indicated by white arrows in Figs. 2(c) and 2(e), show conelike dispersion at bulk Γ point and disperse with k_z . Last but not least, this conelike band is present in measurement with p -polarization geometry but absent with s -polarization geometry, suggesting its origin from either in-plane p_x or out-of-plane p_z orbitals, see Fig. S2 [92] for details of geometry.

We have performed first-principles calculations based on density functional theory (DFT) coded in Vienna *ab initio* package (VASP) [84,85]. The GGA+U scheme is employed to describe the correlation effect of Ru $4d$ electrons [86]. We have also performed band structure calculation based on a slab model constructed by stacking seven monolayer RuCl₃ with a $1 \times \sqrt{3}$ supercell. The paramagnetic state sets random magnetic moments for the Ru atoms. Then the unfolding

effective band structure in the unit cell is obtained by performing the BandUP code [87,88]. Figure S3 [92] presents DFT calculated comprehensive band structure along high symmetry lines through the full 3D BZ. Comparing DFT results with the ARPES results shown in Fig. 2 and here in Figs. 3(a) and 3(b), one can find agreement regarding the general band shape and gap size. The main discrepancy arises for the Ru $3d$ bands above -3 eV while two manifolds are resolved by ARPES, DFT has given five manifolds below the Fermi level, suggesting that single electron picture is not suitable for strongly correlated Ru $4d$ electrons. Nevertheless, The DFT calculated Cl $2p$ -derived bands (below -3 eV) match the ARPES spectra well. In particular, from the slab calculation, the Cl p_x projected bands shown in Fig. 3(c) resemble the ARPES observed conelike structure near -3.2 eV at Γ , in consistent with the above polarization analysis. It is worthy to note that in Figs. 3(b) and 3(c), the conelike structure from ARPES measurement and slab calculation show agreement on the details related to the shape of the flat upper cone and dispersed linear lower cone, as indicated by the white arrows. Furthermore, in Fig. 3(d), the enlarged drawing of the DFT energy dispersion, corresponding to this crossing node at Γ near -3.2 eV in Figs. 3(a)–3(c), also show general agreement with ARPES observation on the shape of this conelike structure.

Symmetry arguments and low-energy effective Hamiltonian are performed to uncover the property of the twofold degeneracy at Γ . As the space group $P3_112$ has a point group D_3 , the Γ point always possesses essential twofold degeneracy enforced by threefold rotational axis along the z axis C_{3z} and time reversal symmetry T [89]. In the absence of SOC, the energy band exhibits quadratic dispersion relation near Γ within the $k_x - k_y$ plane. The Wilson loop [90,91] method shows that the two bands have Chern number C of ± 2 , suggesting the

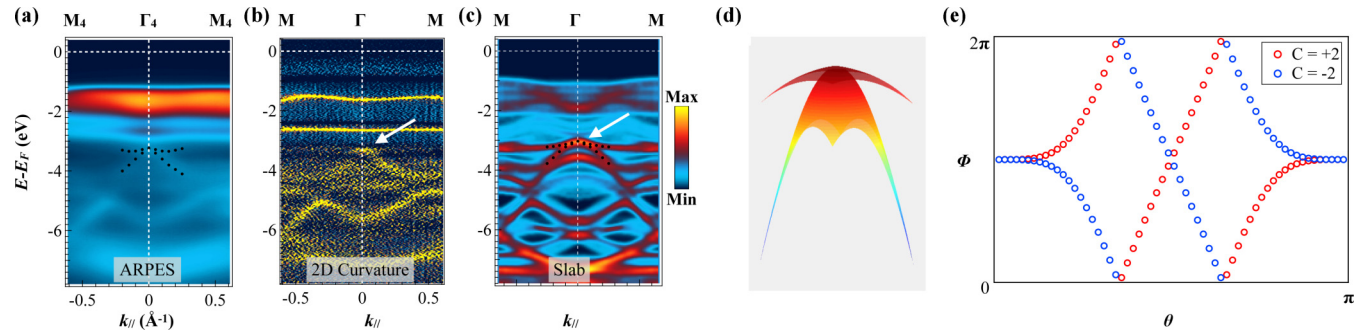


FIG. 3. Comparison of band structure from ARPES and slab calculation. (a) ARPES spectra. (b) 2D curvature plot of ARPES spectra. (c) Calculated dispersion based on a slab of 7 monolayer RuCl_3 with the false color representing its projection on $\text{Cl } p_x$ orbital. (d) The 3D representation of the energy dispersion near the Weyl point within the $k_x - k_y$ plane, which is extracted from the DFT results. (e) The Wilson loop obtained by Eq. (S3) [92], where the Φ ranges from 0 to 2π and θ varies from 0 to π to enclose a crossing point. Filled black circles in panels (a) and (c) are guide for the eye.

existence of quadratic Weyl fermions; see Fig. 3(d). When SOC is included, the crossing node evolves into spin-1/2 Weyl point with linear dispersion [92].

In Fig. 4 we prove that the Weyl cone from the top $\text{Cl } 2p$ orbitals predicted by DFT is indeed observed by ARPES measurement. The k_z -dependent band structure of this Weyl cone is measured by ARPES using the corresponding photon energies and presented in Fig. 4(a). Since the upper flat cone is very weak in intensity and dispersion, here we only focus on the lower cone. ARPES spectra, with respective k_z values expanding more than half of the BZ, show successive evolution of this hole type band for k_z varying from $A_3 = 3.5 \times 2\pi/c$ to $\Gamma_4 = 4.0 \times 2\pi/c$. First of all, all the dispersion in

Fig. 4(a) with different k_z values, except the one at Γ_4 , can be fitted with hyperparabolic line shape (yellow dashed line). Secondly, the maximums of these parabolic bands present linear shift in energy with k_z . As summarized in the left panel of Fig. 4(c), the hole band maximum evolution with k_z follows a linear trend centered at Γ_4 . Most importantly, at $\Gamma_4 = 4.0 \times 2\pi/c$ where the hole type band reaches its maximum, its dispersion can be well fitted with linear line shape along all the three reciprocal directions, suggesting a linear cone centered at the Γ point of the 3D BZ. Fig. 4(c) summarized the line shape of this cone along all the three reciprocal axes. While this linear cone is nearly isotropic in $k_x - k_y$ plane with similar band group velocity, its dispersion

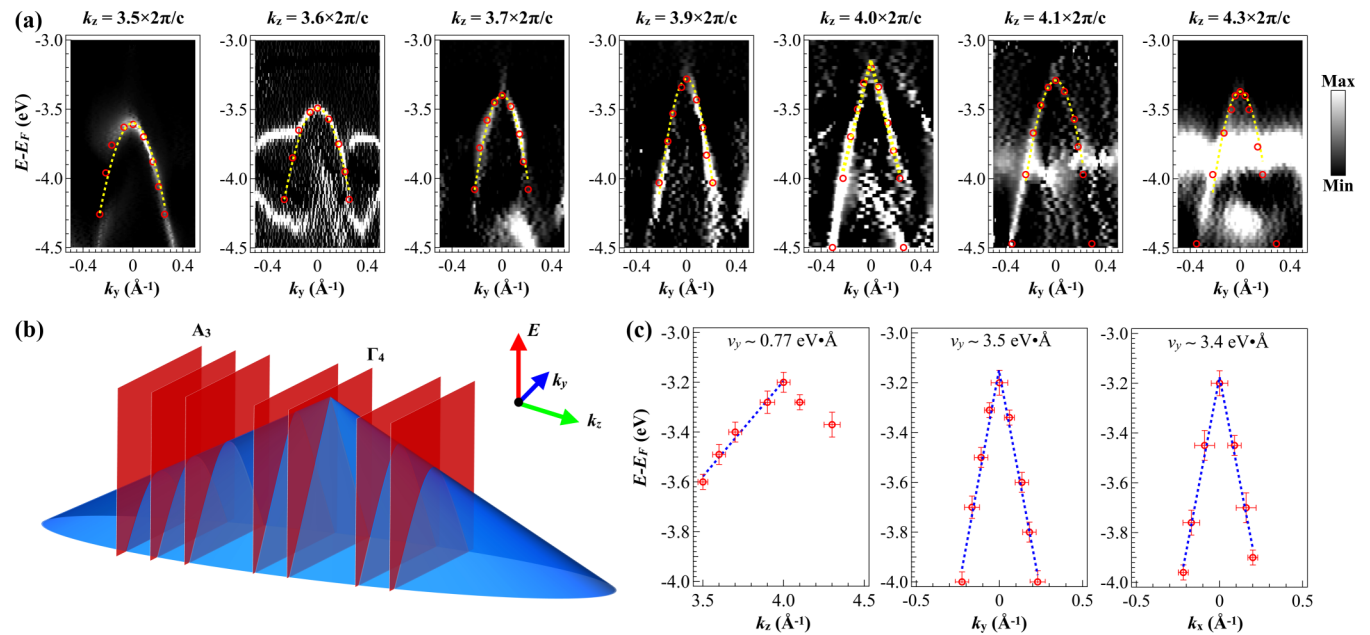


FIG. 4. Evidence of linear Weyl cone. (a) $\text{Cl } 2p$ top valence bands (2D curvature) measured with different photon energies, corresponding to different k_z values. Red circles indicate the band peak positions while yellow dashed lines are the fitted dispersions using linear and hyperbolic line shape. (b) Schematic of the Weyl cone in $E - k_z - k_y$ space. Red planes indicate the photoemission measurement planes corresponding to the spectra in panel (a). (c) Fitted dispersion along k_x , k_y and k_z directions. Left panel: the hole band maximum evolution with k_z , with the red circles represent the band maximum shown in panels of panel (a). Middle panel: hole band dispersion along k_y , corresponding to the spectra shown in panel (a) with $k_z = 4.0 \times 2\pi/c$. Right panel: hole band dispersion along k_x , corresponding to the spectra shown in Fig. 2(c).

along k_z is much flatter with a velocity much lower than the in-plane ones, consistent with the quasi-2D nature of the lattice structure. It is worthy to note that here we have only analyzed the lower Weyl cone experimentally, as the upper one is too flat and weak in spectral weight.

Combining systematic photon energy-dependent ARPES measurement, first-principles calculations, and low-energy effective Hamiltonian analysis, we have demonstrated the emergence of linear Weyl cone derived from $Cl\ 2p_x$ orbitals in α - $RuCl_3$. As this material is insulating and severe charging effect occurs when measured by ARPES at low temperature, we envision further efforts to overcome this issue by thinning the sample or grounding the surface, to explore the interplay of band topology and magnetic order below 7 K by ARPES. The finding of a Weyl cone in α - $RuCl_3$ also suggests possible nontrivial band topology in other van der Waals ferromagnetic insulators [93,94] (such as VI_3 and CrI_3) and Kitaev iridates, as they all share similar in-plane honeycomb lattice.

III. METHODS

A. Sample growth and characterization

Single crystals of α - $RuCl_3$ were grown by vacuum sublimation from commercial $RuCl_3$ powder. The quality of the crystals was checked by single-crystal x-ray diffraction with $Cu\ K\alpha$ radiation at room temperature using a Rigaku MiniFlex diffractometer. Specific heat measurement was performed using a quantum design physical property measurement system (PPMS). The specific heat was measured in the range from 2 to 30 K. Magnetic measurements were performed using a quantum design magnetic property measurement system (MPMS) with the vibrating sample magnetometer (VSM) mode. The magnetization results are collected at room temperature with varied magnetic field parallel to the ab plane of the sample.

B. ARPES measurement:

ARPES measurements were performed at Beamline 1 of Hiroshima Synchrotron Radiation Center (HSRC), Hiroshima University, Japan, with a VG Scienta R4000 electron analyzer [95]. For synchrotron based ARPES measurements, we used linearly polarized lights of 30–80 eV. The beam was linearly

polarized with its polarization lying in the plane of incidence as well as photoelectron detection plane. The energy and angular resolutions were set at 20 meV and 0.1° , respectively. Samples were cleaved at 300 K and measured at 300 K, both at vacuum better than 7×10^{-10} mbar. A shiny mirrorlike surface was obtained after cleaving, confirming its high quality.

C. First-principles calculations:

The first-principles calculations based on density functional theory (DFT) coded in Vienna *ab initio* package (VASP) [84,85] are performed to examine the band dispersion. The projector augmented wave (PAW) [96] method is adopted to treat the core-valence electron interactions. The exchange correlation is chosen within the Perdew-Berke-Ernzerhof (PBE) [97] schemes with a cutoff energy 500 eV. The GGA+U method is employed to describe the correlation effect of Ru $4d$ electrons and the on-site Coulomb energy U is set to be 3 eV [86]. The band structures are calculated by stacking 7 monolayer $RuCl_3$ with a $1 \times \sqrt{3}$ supercell. Then the unfolding effective band structure in the unit cell is obtained by performing the BandUP code [87,88]. The paramagnetic state sets random-magnetic moments for the Ru atoms with the values of $4\ \mu_B$.

ACKNOWLEDGEMENTS

This work is supported by the National Natural Science Foundation of China (NSFC) (Grant No. 12074163), the Shenzhen High-level Special Fund (Grants No. G02206304 and No. G02206404), the Guangdong Innovative and Entrepreneurial Research Team Program (Grants No. 2019ZT08C044 and No. 2017ZT07C062), Shenzhen Science and Technology Program (Grant No. KQTD20190929173815000), the University Innovative Team in Guangdong Province (Grant No. 2020KCXTD001), Shenzhen Key Laboratory of Advanced Quantum Functional Materials and Devices (Grant No. ZDSYS20190902092905285), and the Center for Computational Science and Engineering at Southern University of Science and Technology. ARPES measurements were performed with the approval of the Proposal Assessing Committee of the Hiroshima Synchrotron Radiation Center (Proposal No. 19AG004).

-
- [1] M. Z. Hasan and C. L. Kane, Colloquium: Topological insulators, *Rev. Mod. Phys.* **82**, 3045 (2010).
 - [2] X.-L. Qi and S.-C. Zhang, Topological insulators and superconductors, *Rev. Mod. Phys.* **83**, 1057 (2011).
 - [3] S.-Y. Xu, C. Liu, S. K. Kushwaha, R. Sankar, J. W. Krizan, I. Belopolski, M. Neupane, G. Bian, N. Alidoust, T.-R. Chang, H.-T. Jeng, C.-Y. Huang, W.-F. Tsai, H. Lin, P. P. Shibayev, F.-C. Chou, R. J. Cava, and M. Z. Hasan, Observation of Fermi arc surface states in a topological metal, *Science* **347**, 294 (2015).
 - [4] Z. K. Liu, B. Zhou, Y. Zhang, Z. J. Wang, H. M. Weng, D. Prabhakaran, S. K. Mo, Z. X. Shen, Z. Fang, X. Dai, Z. Hussain, and Y. L. Chen, Discovery of a three-dimensional topological Dirac semimetal, Na_3Bi , *Science* **343**, 864 (2014).
 - [5] A. Liang, C. Chen, Z. Wang, Y. Shi, Y. Feng, H. Yi, Z. Xie, S. He, J. He, Y. Peng, Y. Liu, D. Liu, C. Hu, L. Zhao, G. Liu, X. Dong, J. Zhang, M. Nakatake, H. Iwasawa, K. Shimada, M. Arita, H. Namatame, M. Taniguchi, Z. Xu, C. Chen, H. Weng, X. Dai, Z. Fang, and X.-J. Zhou, Electronic structure, Dirac points and Fermi arc surface states in three-dimensional Dirac semimetal Na_3Bi from angle-resolved photoemission spectroscopy, *Chin. Phys. B* **25**, 077101 (2016).
 - [6] Z. K. Liu, J. Jiang, B. Zhou, Z. J. Wang, Y. Zhang, H. M. Weng, D. Prabhakaran, S. K. Mo, H. Peng, P. Dudin, T. Kim, M. Hoesch, Z. Fang, X. Dai, Z. X. Shen, D. L. Feng, Z. Hussain, and Y. L. Chen, A stable three-dimensional topological Dirac semimetal Cd_3As_2 , *Nat. Mater.* **13**, 677 (2014).

- [7] H. Yi, Z. Wang, C. Chen, Y. Shi, Y. Feng, A. Liang, Z. Xie, S. He, J. He, Y. Peng, X. Liu, Y. Liu, L. Zhao, G. Liu, X. Dong, J. Zhang, M. Nakatake, M. Arita, K. Shimada, H. Namatame, M. Taniguchi, Z. Xu, C. Chen, X. Dai, Z. Fang, and X. J. Zhou, Evidence of topological surface state in three-dimensional Dirac semimetal Cd_3As_2 , *Sci Rep.* **4**, 6106 (2014).
- [8] M. Neupane, S. Y. Xu, R. Sankar, N. Alidoust, G. Bian, C. Liu, I. Belopolski, T. R. Chang, H. T. Jeng, H. Lin, A. Bansil, F. Chou, and M. Z. Hasan, Observation of a three-dimensional topological Dirac semimetal phase in high-mobility Cd_3As_2 , *Nat. Commun.* **5**, 3786 (2014).
- [9] S.-Y. Xu, I. Belopolski, N. Alidoust, M. Neupane, G. Bian, C. Zhang, R. Sankar, G. Chang, Z. Yuan, C.-C. Lee, S.-M. Huang, H. Zheng, J. Ma, D. S. Sanchez, B. Wang, A. Bansil, F. Chou, P. P. Shibaev, H. Lin, S. Jia, and M. Z. Hasan, Discovery of a Weyl fermion semimetal and topological Fermi arcs, *Science* **349**, 613 (2015).
- [10] L. X. Yang, Z. K. Liu, Y. Sun, H. Peng, H. F. Yang, T. Zhang, B. Zhou, Y. Zhang, Y. F. Guo, M. Rahn, D. Prabhakaran, Z. Hussain, S. K. Mo, C. Felser, B. Yan, and Y. L. Chen, Weyl semimetal phase in the noncentrosymmetric compound TaAs, *Nat. Phys.* **11**, 728 (2015).
- [11] S.-Y. Xu, N. Alidoust, I. Belopolski, Z. Yuan, G. Bian, T.-R. Chang, H. Zheng, V. N. Strocov, D. S. Sanchez, G. Chang, C. Zhang, D. Mou, Y. Wu, L. Huang, C.-C. Lee, S.-M. Huang, B. Wang, A. Bansil, H.-T. Jeng, T. Neupert, A. Kaminski, H. Lin, S. Jia, and M. Zahid Hasan, Discovery of a Weyl fermion state with Fermi arcs in niobium arsenide, *Nat. Phys.* **11**, 748 (2015).
- [12] B. Q. Lv, N. Xu, H. M. Weng, J. Z. Ma, P. Richard, X. C. Huang, L. X. Zhao, G. F. Chen, C. E. Matt, F. Bisti, V. N. Strocov, J. Mesot, Z. Fang, X. Dai, T. Qian, M. Shi, and H. Ding, Observation of Weyl nodes in TaAs, *Nat. Phys.* **11**, 724 (2015).
- [13] Z. K. Liu, L. X. Yang, Y. Sun, T. Zhang, H. Peng, H. F. Yang, C. Chen, Y. Zhang, Y. F. Guo, D. Prabhakaran, M. Schmidt, Z. Hussain, S. K. Mo, C. Felser, B. Yan, and Y. L. Chen, Evolution of the Fermi surface of Weyl semimetals in the transition metal pnictide family, *Nat. Mater.* **15**, 27 (2016).
- [14] J. Jiang, Z. K. Liu, Y. Sun, H. F. Yang, C. R. Rajamathi, Y. P. Qi, L. X. Yang, C. Chen, H. Peng, C. C. Hwang, S. Z. Sun, S. K. Mo, I. Vobornik, J. Fujii, S. S. P. Parkin, C. Felser, B. H. Yan, and Y. L. Chen, Signature of type-II Weyl semimetal phase in MoTe_2 , *Nat. Commun.* **8**, 13973 (2017).
- [15] L. Huang, T. M. McCormick, M. Ochi, Z. Zhao, M.-T. Suzuki, R. Arita, Y. Wu, D. Mou, H. Cao, J. Yan, N. Trivedi, and A. Kaminski, Spectroscopic evidence for a type II Weyl semimetallic state in MoTe_2 , *Nat Mater* **15**, 1155 (2016).
- [16] M. Neupane, I. Belopolski, M. M. Hosen, D. S. Sanchez, R. Sankar, M. Szlowska, S.-Y. Xu, K. Dimitri, N. Dhakal, P. Maldonado, P. M. Oppeneer, D. Kaczorowski, F. Chou, M. Z. Hasan, and T. Durakiewicz, Observation of topological nodal fermion semimetal phase in ZrSiS , *Phys. Rev. B* **93**, 201104 (2016).
- [17] L. M. Schoop, M. N. Ali, C. Strasser, A. Topp, A. Varykhalov, D. Marchenko, V. Duppel, S. S. Parkin, B. V. Lotsch, and C. R. Ast, Dirac cone protected by nonsymmorphic symmetry and three-dimensional Dirac line node in ZrSiS , *Nat. Commun.* **7**, 11696 (2016).
- [18] D. Takane, Z. Wang, S. Souma, K. Nakayama, C. X. Trang, T. Sato, T. Takahashi, and Y. Ando, Dirac-node arc in the topological line-node semimetal HfSiS , *Phys. Rev. B* **94**, 121108 (2016).
- [19] A. Topp, J. M. Lippmann, A. Varykhalov, V. Duppel, B. V. Lotsch, C. R. Ast, and L. M. Schoop, Nonsymmorphic band degeneracy at the Fermi level in ZrSiTe , *New J. Phys.* **18**, 125014 (2016).
- [20] C. Chen, X. Xu, J. Jiang, S. C. Wu, Y. P. Qi, L. X. Yang, M. X. Wang, Y. Sun, N. B. M. Schröter, H. F. Yang, L. M. Schoop, Y. Y. Lv, J. Zhou, Y. B. Chen, S. H. Yao, M. H. Lu, Y. F. Chen, C. Felser, B. H. Yan, Z. K. Liu, and Y. L. Chen, Dirac line nodes and effect of spin-orbit coupling in the nonsymmorphic critical semimetals MSiS ($M = \text{Hf}, \text{Zr}$), *Phys. Rev. B* **95**, 125126 (2017).
- [21] I. Belopolski, K. Manna, D. S. Sanchez, G. Chang, B. Ernst, J. Yin, S. S. Zhang, T. Cochran, N. Shumiya, H. Zheng, B. Singh, G. Bian, D. Multer, M. Litskevich, X. Zhou, S.-M. Huang, B. Wang, T.-R. Chang, S.-Y. Xu, A. Bansil, C. Felser, H. Lin, and M. Z. Hasan, Discovery of topological Weyl fermion lines and drumhead surface states in a room temperature magnet, *Science* **365**, 1278 (2019).
- [22] D. F. Liu, A. J. Liang, E. K. Liu, Q. N. Xu, Y. W. Li, C. Chen, D. Pei, W. J. Shi, S. K. Mo, P. Dudin, T. Kim, C. Cacho, G. Li, Y. Sun, L. X. Yang, Z. K. Liu, S. S. P. Parkin, C. Felser, and Y. L. Chen, Magnetic Weyl semimetal phase in a Kagomé crystal, *Science* **365**, 1282 (2019).
- [23] N. Morali, R. Batabyal, P. K. Nag, E. Liu, Q. Xu, Y. Sun, B. Yan, C. Felser, N. Avraham, and H. Beidenkopf, Fermi-arc diversity on surface terminations of the magnetic Weyl semimetal $\text{Co}_3\text{Sn}_2\text{S}_2$, *Science* **365**, 1286 (2019).
- [24] V. Mourik, K. Zuo, S. M. Frolov, S. R. Plissard, E. P. a. M. Bakkers, and L. P. Kouwenhoven, Signatures of Majorana fermions in hybrid superconductor-semiconductor nanowire devices, *Science* **336**, 1003 (2012).
- [25] S. Nadj-Perge, I. K. Drozdov, J. Li, H. Chen, S. Jeon, J. Seo, A. H. Macdonald, B. A. Bernevig, and A. Yazdani, Observation of Majorana fermions in ferromagnetic atomic chains on a superconductor, *Science* **346**, 602 (2014).
- [26] D. Wang, L. Kong, P. Fan, H. Chen, S. Zhu, W. Liu, L. Cao, Y. Sun, S. Du, J. Schneeloch, R. Zhong, G. Gu, L. Fu, H. Ding, and H.-J. Gao, Evidence for Majorana bound states in an iron-based superconductor, *Science* **362**, 333 (2018).
- [27] Z. Wang, J. O. Rodriguez, L. Jiao, S. Howard, M. Graham, G. D. Gu, T. L. Hughes, D. K. Morr, and V. Madhavan, Evidence for dispersing 1D Majorana channels in an iron-based superconductor, *Science* **367**, 104 (2020).
- [28] H. Zhang, C. X. Liu, S. Gazibegovic, D. Xu, J. A. Logan, G. Wang, N. Van Loo, J. D. S. Bommer, M. W. A. De Moor, D. Car, R. L. M. Op Het Veld, P. J. Van Veldhoven, S. Koelling, M. A. Verheijen, M. Pendharkar, D. J. Pennachio, B. Shojaei, J. S. Lee, C. J. Palmstrom, E. Bakkers, S. D. Sarma, and L. P. Kouwenhoven, Quantized Majorana conductance, *Nature* **556**, 74 (2018).
- [29] B. Bradlyn, J. Cano, Z. Wang, M. G. Vergniory, C. Felser, R. J. Cava, and B. A. Bernevig, Beyond Dirac and Weyl fermions: Unconventional quasiparticles in conventional crystals, *Science* **353**, aaf5037 (2016).
- [30] B. Q. Lv, Z. L. Feng, Q. N. Xu, X. Gao, J. Z. Ma, L. Y. Kong, P. Richard, Y. B. Huang, V. N. Strocov, C. Fang, H. M. Weng, Y. G. Shi, T. Qian, and H. Ding, Observation of three-component

- fermions in the topological semimetal molybdenum phosphide, *Nature* **546**, 627 (2017).
- [31] J. Z. Ma, J. B. He, Y. F. Xu, B. Q. Lv, D. Chen, W. L. Zhu, S. Zhang, L. Y. Kong, X. Gao, L. Y. Rong, Y. B. Huang, P. Richard, C. Y. Xi, E. S. Choi, Y. Shao, Y. L. Wang, H. J. Gao, X. Dai, C. Fang, H. M. Weng, G. F. Chen, T. Qian, and H. Ding, Three-component fermions with surface Fermi arcs in tungsten carbide, *Nat. Phys.* **14**, 349 (2018).
- [32] D. Takane, Z. Wang, S. Souma, K. Nakayama, T. Nakamura, H. Oinuma, Y. Nakata, H. Iwasawa, C. Cacho, T. Kim, K. Horiba, H. Kumigashira, T. Takahashi, Y. Ando, and T. Sato, Observation of Chiral Fermions with a Large Topological Charge and Associated Fermi-Arc Surface States in CoSi, *Phys. Rev. Lett.* **122**, 076402 (2019).
- [33] N. B. M. Schröter, D. Pei, M. G. Vergniory, Y. Sun, K. Manna, F. De Juan, J. A. Krieger, V. Süß, M. Schmidt, P. Dudin, B. Bradlyn, T. K. Kim, T. Schmitt, C. Cacho, C. Felser, V. N. Strocov, and Y. Chen, Chiral topological semimetal with multifold band crossings and long Fermi arcs, *Nat. Phys.* **15**, 759 (2019).
- [34] D. S. Sanchez, I. Belopolski, T. A. Cochran, X. Xu, J. X. Yin, G. Chang, W. Xie, K. Manna, V. Süß, C. Y. Huang, N. Alidoust, D. Multer, S. S. Zhang, N. Shumiya, X. Wang, G. Q. Wang, T. R. Chang, C. Felser, S. Y. Xu, S. Jia, H. Lin, and M. Z. Hasan, Topological chiral crystals with helicoid-arc quantum states, *Nature* **567**, 500 (2019).
- [35] Z. Rao, H. Li, T. Zhang, S. Tian, C. Li, B. Fu, C. Tang, L. Wang, Z. Li, W. Fan, J. Li, Y. Huang, Z. Liu, Y. Long, C. Fang, H. Weng, Y. Shi, H. Lei, Y. Sun, T. Qian, and H. Ding, Observation of unconventional chiral fermions with long Fermi arcs in CoSi, *Nature* **567**, 496 (2019).
- [36] G. Chang, S. Y. Xu, B. J. Wieder, D. S. Sanchez, S. M. Huang, I. Belopolski, T. R. Chang, S. Zhang, A. Bansil, H. Lin, and M. Z. Hasan, Unconventional Chiral Fermions and Large Topological Fermi Arcs in RhSi, *Phys. Rev. Lett.* **119**, 206401 (2017).
- [37] Z. Zhu, G. W. Winkler, Q. Wu, J. Li, and A. A. Soluyanov, Triple Point Topological Metals, *Phys. Rev. X* **6**, 031003 (2016).
- [38] Q. Liu and A. Zunger, Predicted Realization of Cubic Dirac Fermion in Quasi-One-Dimensional Transition-Metal Monochalcogenides, *Phys. Rev. X* **7**, 021019 (2017).
- [39] C. Fang, M. J. Gilbert, X. Dai, and B. A. Bernevig, Multi-Weyl Topological Semimetals Stabilized by Point Group Symmetry, *Phys. Rev. Lett.* **108**, 266802 (2012).
- [40] X. G. Wan, A. M. Turner, A. Vishwanath, and S. Y. Savrasov, Topological semimetal and Fermi-arc surface states in the electronic structure of pyrochlore iridates, *Phys. Rev. B* **83**, 205101 (2011).
- [41] G. Xu, H. Weng, Z. Wang, X. Dai, and Z. Fang, Chern Semimetal and the Quantized Anomalous Hall Effect in HgCr_2Se_4 , *Phys. Rev. Lett.* **107**, 186806 (2011).
- [42] S. M. Huang, S. Y. Xu, I. Belopolski, C. C. Lee, G. Chang, B. Wang, N. Alidoust, G. Bian, M. Neupane, C. Zhang, S. Jia, A. Bansil, H. Lin, and M. Z. Hasan, A Weyl Fermion semimetal with surface Fermi arcs in the transition metal monophosphides TaAs class, *Nat. Commun.* **6**, 7373 (2015).
- [43] A. A. Soluyanov, D. Gresch, Z. Wang, Q. Wu, M. Troyer, X. Dai, and B. A. Bernevig, Type-II Weyl semimetals, *Nature* **527**, 495 (2015).
- [44] H. Weng, C. Fang, Z. Fang, B. A. Bernevig, and X. Dai, Weyl Semimetal Phase in Noncentrosymmetric Transition-Metal Monophosphides, *Phys. Rev. X* **5**, 011029 (2015).
- [45] S. M. Huang, S. Y. Xu, I. Belopolski, C. C. Lee, G. Chang, T. R. Chang, B. Wang, N. Alidoust, G. Bian, M. Neupane, D. Sanchez, H. Zheng, H. T. Jeng, A. Bansil, T. Neupert, H. Lin, and M. Z. Hasan, New type of Weyl semimetal with quadratic double Weyl fermions, *Proc. Natl. Acad. Sci. USA* **113**, 1180 (2016).
- [46] H. Weng, C. Fang, Z. Fang, and X. Dai, Topological semimetals with triply degenerate nodal points in θ -phase tantalum nitride, *Phys. Rev. B* **93**, 241202 (2016).
- [47] Z. Wang, Y. Sun, X.-Q. Chen, C. Franchini, G. Xu, H. Weng, X. Dai, and Z. Fang, Dirac semimetal and topological phase transitions in A_3Bi ($\text{A} = \text{Na}, \text{K}, \text{Rb}$), *Phys. Rev. B* **85**, 195320 (2012).
- [48] S. M. Young, S. Zaheer, J. C. Y. Teo, C. L. Kane, E. J. Mele, and A. M. Rappe, Dirac Semimetal in Three Dimensions, *Phys. Rev. Lett.* **108**, 140405 (2012).
- [49] Z. J. Wang, H. M. Weng, Q. S. Wu, X. Dai, and Z. Fang, Three-dimensional Dirac semimetal and quantum transport in Cd_3As_2 , *Phys. Rev. B* **88**, 125427 (2013).
- [50] B. J. Wieder, Y. Kim, A. M. Rappe, and C. L. Kane, Double Dirac Semimetals in Three Dimensions, *Phys. Rev. Lett.* **116**, 186402 (2016).
- [51] N. Kumar, M. Yao, J. Nayak, M. G. Vergniory, J. Bannier, Z. Wang, N. B. M. Schröter, V. N. Strocov, L. Muchler, W. Shi, E. D. L. Rienks, J. L. Manes, C. Shekhar, S. S. P. Parkin, J. Fink, G. H. Fecher, Y. Sun, B. A. Bernevig, and C. Felser, Signatures of sixfold degenerate exotic fermions in a superconducting metal PdSb_2 , *Adv. Mater.* **32**, 1906046 (2020).
- [52] Z. P. Sun, C. Q. Hua, X. L. Liu, Z. T. Liu, M. Ye, S. Qiao, Z. H. Liu, J. S. Liu, Y. F. Guo, Y. H. Lu, and D. W. Shen, Direct observation of sixfold exotic fermions in the pyrite-structured topological semimetal PdSb_2 , *Phys. Rev. B* **101**, 155114 (2020).
- [53] X. Yang, T. A. Cochran, R. Chapai, D. Tristant, J.-X. Yin, I. Belopolski, Z. Cheng, D. Multer, S. S. Zhang, N. Shumiya, M. Litskevich, Y. Jiang, G. Chang, Q. Zhang, I. Vekhter, W. A. Shelton, R. Jin, S.-Y. Xu, and M. Z. Hasan, Observation of sixfold degenerate fermions in PdSb_2 , *Phys. Rev. B* **101**, 201105 (2020).
- [54] P. W. Anderson, Resonating valence bonds: A new kind of insulator? *Mater. Res. Bull.* **8**, 153 (1973).
- [55] L. Savary and L. Balents, Quantum spin liquids: A review, *Rep. Prog. Phys.* **80**, 016502 (2017).
- [56] Y. Zhou, K. Kanoda, and T.-K. Ng, Quantum spin liquid states, *Rev. Mod. Phys.* **89**, 025003 (2017).
- [57] H. Takagi, T. Takayama, G. Jackeli, G. Khaliullin, and S. E. Nagler, Concept and realization of Kitaev quantum spin liquids, *Nat. Rev. Phys.* **1**, 264 (2019).
- [58] J. Wen, S.-L. Yu, S. Li, W. Yu, and J.-X. Li, Experimental identification of quantum spin liquids, *npj Quantum Mater.* **4**, 12 (2019).
- [59] S. M. Winter, A. A. Tsirlin, M. Daghofer, J. Van Den Brink, Y. Singh, P. Gegenwart, and R. Valenti, Models and materials for generalized Kitaev magnetism, *J. Phys.: Condens. Matter.* **29**, 493002 (2017).
- [60] A. Kitaev, Anyons in an exactly solved model and beyond, *Ann. Phys.* **321**, 2 (2006).

- [61] Y. J. Yu, Y. Xu, K. J. Ran, J. M. Ni, Y. Y. Huang, J. H. Wang, J. S. Wen, and S. Y. Li, Ultralow-Temperature Thermal Conductivity of the Kitaev Honeycomb Magnet α -RuCl₃ across the Field-Induced Phase Transition, *Phys. Rev. Lett.* **120**, 067202 (2018).
- [62] Y. Kasahara, T. Ohnishi, Y. Mizukami, O. Tanaka, S. Ma, K. Sugii, N. Kurita, H. Tanaka, J. Nasu, Y. Motome, T. Shibauchi, and Y. Matsuda, Majorana quantization and half-integer thermal quantum Hall effect in a Kitaev spin liquid, *Nature* **559**, 227 (2018).
- [63] R. Hentrich, A. U. B. Wolter, X. Zotos, W. Brenig, D. Nowak, A. Isaeva, T. Doert, A. Banerjee, P. Lampen-Kelley, D. G. Mandrus, S. E. Nagler, J. Sears, Y.-J. Kim, B. Büchner, and C. Hess, Unusual Phonon Heat Transport in α -RuCl₃: Strong Spin-Phonon Scattering and Field-Induced Spin Gap, *Phys. Rev. Lett.* **120**, 117204 (2018).
- [64] N. Janša, A. Zorko, M. Gomilšek, M. Pregelj, K. W. Krämer, D. Biner, A. Biffin, C. Rüegg, and M. Klanjšek, Observation of two types of fractional excitation in the Kitaev honeycomb magnet, *Nat. Phys.* **14**, 786 (2018).
- [65] J. Zheng, K. Ran, T. Li, J. Wang, P. Wang, B. Liu, Z. X. Liu, B. Normand, J. Wen, and W. Yu, Gapless Spin Excitations in the Field-Induced Quantum Spin Liquid Phase of α -RuCl₃, *Phys. Rev. Lett.* **119**, 227208 (2017).
- [66] K. Ran, J. Wang, W. Wang, Z.-Y. Dong, X. Ren, S. Bao, S. Li, Z. Ma, Y. Gan, Y. Zhang, J. T. Park, G. Deng, S. Danilkin, S.-L. Yu, J.-X. Li, and J. Wen, Spin-Wave Excitations Evidencing the Kitaev Interaction in Single Crystalline α -RuCl₃, *Phys. Rev. Lett.* **118**, 107203 (2017).
- [67] J. Nasu, J. Knolle, D. L. Kovrizhin, Y. Motome, and R. Moessner, Fermionic response from fractionalization in an insulating two-dimensional magnet, *Nat. Phys.* **12**, 912 (2016).
- [68] L. J. Sandilands, Y. Tian, K. W. Plumb, Y. J. Kim, and K. S. Burch, Scattering Continuum and Possible Fractionalized Excitations in α -RuCl₃, *Phys. Rev. Lett.* **114**, 147201 (2015).
- [69] A. Banerjee, J. Yan, J. Knolle, C. A. Bridges, M. B. Stone, M. D. Lumsden, D. G. Mandrus, D. A. Tennant, R. Moessner, and S. E. Nagler, Neutron scattering in the proximate quantum spin liquid α -RuCl₃, *Science* **356**, 1055 (2017).
- [70] A. Banerjee, C. A. Bridges, J. Q. Yan, A. A. Aczel, L. Li, M. B. Stone, G. E. Granroth, M. D. Lumsden, Y. Yiu, J. Knolle, S. Bhattacharjee, D. L. Kovrizhin, R. Moessner, D. A. Tennant, D. G. Mandrus, and S. E. Nagler, Proximate Kitaev quantum spin liquid behaviour in a honeycomb magnet, *Nat. Mater.* **15**, 733 (2016).
- [71] M. Ziatdinov, A. Banerjee, A. Maksov, T. Berlijn, W. Zhou, H. B. Cao, J. Q. Yan, C. A. Bridges, D. G. Mandrus, S. E. Nagler, A. P. Baddorf, and S. V. Kalinin, Atomic-scale observation of structural and electronic orders in the layered compound α -RuCl₃, *Nat. Commun.* **7**, 13774 (2016).
- [72] R. D. Johnson, S. C. Williams, A. A. Haghighirad, J. Singleton, V. Zapf, P. Manuel, I. I. Mazin, Y. Li, H. O. Jeschke, R. Valentí, and R. Coldea, Monoclinic crystal structure of α -RuCl₃ and the zigzag antiferromagnetic ground state, *Phys. Rev. B* **92**, 235119 (2015).
- [73] L. J. Sandilands, C. H. Sohn, H. J. Park, S. Y. Kim, K. W. Kim, J. A. Sears, Y.-J. Kim, and T. W. Noh, Optical probe of Heisenberg-Kitaev magnetism in α -RuCl₃, *Phys. Rev. B* **94**, 195156 (2016).
- [74] L. J. Sandilands, Y. Tian, A. A. Reijnders, H.-S. Kim, K. W. Plumb, Y.-J. Kim, H.-Y. Kee, and K. S. Burch, Spin-orbit excitations and electronic structure of the putative Kitaev magnet α -RuCl₃, *Phys. Rev. B* **93**, 075144 (2016).
- [75] K. W. Plumb, J. P. Clancy, L. J. Sandilands, V. V. Shankar, Y. F. Hu, K. S. Burch, H.-Y. Kee, and Y.-J. Kim, α -RuCl₃: A spin-orbit assisted Mott insulator on a honeycomb lattice, *Phys. Rev. B* **90**, 041112 (2014).
- [76] A. Koitzsch, C. Habenicht, E. Müller, M. Knupfer, B. Büchner, H. C. Kandpal, J. Van Den Brink, D. Nowak, A. Isaeva, and T. Doert, J_{eff} Description of the Honeycomb Mott Insulator α -RuCl₃, *Phys. Rev. Lett.* **117**, 126403 (2016).
- [77] S. Sinn, C. H. Kim, B. H. Kim, K. D. Lee, C. J. Won, J. S. Oh, M. Han, Y. J. Chang, N. Hur, H. Sato, B.-G. Park, C. Kim, H.-D. Kim, and T. W. Noh, Electronic structure of the Kitaev material α -RuCl₃ probed by photoemission and inverse photoemission spectroscopies, *Sci. Rep.* **6**, 39544 (2016).
- [78] X. Zhou, H. Li, J. A. Waugh, S. Parham, H.-S. Kim, J. A. Sears, A. Gomes, H.-Y. Kee, Y.-J. Kim, and D. S. Dessau, Angle-resolved photoemission study of the Kitaev candidate α -RuCl₃, *Phys. Rev. B* **94**, 161106 (2016).
- [79] H. B. Cao, A. Banerjee, J. Q. Yan, C. A. Bridges, M. D. Lumsden, D. G. Mandrus, D. A. Tennant, B. C. Chakoumakos, and S. E. Nagler, Low-temperature crystal and magnetic structure of α -RuCl₃, *Phys. Rev. B* **93**, 134423 (2016).
- [80] Z. Dai, J.-X. Yu, B. Zhou, S. A. Tenney, P. Lampen-Kelley, J. Yan, D. Mandrus, E. A. Henriksen, J. Zang, K. Pohl, and J. T. Sadowski, Crystal structure reconstruction in the surface monolayer of the quantum spin liquid candidate α -RuCl₃, *2D Mater.* **7**, 035004 (2020).
- [81] Y. Kubota, H. Tanaka, T. Ono, Y. Narumi, and K. Kindo, Successive magnetic phase transitions in α -RuCl₃: XY-like frustrated magnet on the honeycomb lattice, *Phys. Rev. B* **91**, 094422 (2015).
- [82] J. A. Sears, M. Songvilay, K. W. Plumb, J. P. Clancy, Y. Qiu, Y. Zhao, D. Parshall, and Y.-J. Kim, Magnetic order in α -RuCl₃: A honeycomb-lattice quantum magnet with strong spin-orbit coupling, *Phys. Rev. B* **91**, 144420 (2015).
- [83] M. Majumder, M. Schmidt, H. Rosner, A. A. Tsirlin, H. Yasuoka, and M. Baenitz, Anisotropic Ru³⁺ 4d⁵ magnetism in the α -RuCl₃ honeycomb system: Susceptibility, specific heat, and zero-field NMR, *Phys. Rev. B* **91**, 180401 (2015).
- [84] G. Kresse and J. Furthmüller, Efficient iterative schemes for *ab initio* total-energy calculations using a plane-wave basis set, *Phys. Rev. B* **54**, 11169 (1996).
- [85] G. Kresse and J. Hafner, *Ab initio* molecular-dynamics simulation of the liquid-metal-amorphous-semiconductor transition in germanium, *Phys. Rev. B* **49**, 14251 (1994).
- [86] A. I. Liechtenstein, V. I. Anisimov, and J. Zaanen, Density-functional theory and strong interactions: Orbital ordering in Mott-Hubbard insulators, *Phys. Rev. B* **52**, R5467 (1995).
- [87] P. V. C. Medeiros, S. Stafström, and J. Björk, Effects of extrinsic and intrinsic perturbations on the electronic structure of graphene: Retaining an effective primitive cell band structure by band unfolding, *Phys. Rev. B* **89**, 041407 (2014).
- [88] P. V. C. Medeiros, S. S. Tsirkin, S. Stafström, and J. Björk, Unfolding spinor wave functions and expectation values of general operators: Introducing the unfolding-density operator, *Phys. Rev. B* **91**, 041116 (2015).

- [89] C. Bradley and A. Cracknell, *The Mathematical Theory of Symmetry in Solids* (Clarendon, Oxford, 1972).
- [90] A. A. Soluyanov and D. Vanderbilt, Computing topological invariants without inversion symmetry, *Phys. Rev. B* **83**, 235401 (2011).
- [91] H. Weng, R. Yu, X. Hu, X. Dai, and Z. Fang, Quantum anomalous Hall effect and related topological electronic states, *Adv. Phys.* **64**, 227 (2015).
- [92] See Supplemental Material at <http://link.aps.org/supplemental/10.1103/PhysRevB.103.035150> for additional material on the details about experience and calculation method.
- [93] A. K. Kundu, Y. Liu, C. Petrovic, and T. Valla, Valence band electronic structure of the van der Waals ferromagnetic insulators: VI_3 and CrI_3 , *Sci. Rep.* **10**, 15602 (2020).
- [94] B. Huang, G. Clark, E. Navarro-Moratalla, D. R. Klein, R. Cheng, K. L. Seyler, D. Zhong, E. Schmidgall, M. A. McGuire, D. H. Cobden, W. Yao, D. Xiao, P. Jarillo-Herrero, and X. Xu, Layer-dependent ferromagnetism in a van der Waals crystal down to the monolayer limit, *Nature* **546**, 270 (2017).
- [95] H. Iwasawa, K. Shimada, E. F. Schwier, M. Zheng, Y. Kojima, H. Hayashi, J. Jiang, M. Higashiguchi, Y. Aiura, H. Namatame, and M. Taniguchi, Rotatable high-resolution ARPES system for tunable linear-polarization geometry, *J. Synchrotron. Radiat.* **24**, 836 (2017).
- [96] P. E. Blöchl, Projector augmented-wave method, *Phys. Rev. B* **50**, 17953 (1994).
- [97] J. P. Perdew, K. Burke, and M. Ernzerhof, Generalized Gradient Approximation Made Simple, *Phys. Rev. Lett.* **77**, 3865 (1996).

Realization of a tunable surface Dirac gap in Sb-doped MnBi_2Te_4

Xiao-Ming Ma^{1,*}, Yufei Zhao^{1,*}, Ke Zhang^{2,*}, Shiv Kumar^{3,*}, Ruie Lu¹, Jiayu Li¹, Qiushi Yao¹, Jifeng Shao¹, Fuchen Hou¹, Xuefeng Wu¹, Meng Zeng¹, Yu-Jie Hao¹, Zhanyang Hao¹, Yuan Wang¹, Xiang-Rui Liu¹, Huiwen Shen¹, Hongyi Sun¹, Jiawei Mei¹, Koji Miyamoto³, Taichi Okuda³, Masashi Arita³, Eike F. Schwier³, Kenya Shimada³, Ke Deng¹, Cai Liu¹, Junhao Lin¹, Yue Zhao¹, Chaoyu Chen^{1,†}, Qihang Liu^{1,4,‡}, and Chang Liu^{1,§}

¹Shenzhen Institute for Quantum Science and Engineering (SIQSE) and Department of Physics, Southern University of Science and Technology (SUSTech), Shenzhen, Guangdong 518055, China

²Department of Physical Science, Graduate School of Science, Hiroshima University, 2-313 Kagamiyama, Higashi-Hiroshima 739-0046, Japan

³Hiroshima Synchrotron Radiation Center, Hiroshima University, 2-313 Kagamiyama, Higashi-Hiroshima 739-0046, Japan

⁴Guangdong Provincial Key Laboratory for Computational Science and Material Design, Southern University of Science and Technology (SUSTech), Shenzhen, Guangdong 518055, China



(Received 1 July 2020; revised 19 February 2021; accepted 24 February 2021; published 17 March 2021)

Signatures of both the quantum anomalous Hall effect and axion electrodynamics have been recently observed to exist in thin films of MnBi_2Te_4 , a stoichiometric antiferromagnetic topological insulator. Direct evidence of the bulk topological magnetoelectric response in an axion insulator requires an energy gap at its topological surface state (TSS). However, independent spectroscopic experiments revealed that such a surface gap is much smaller than previously thought. Here we utilize angle resolved photoemission spectroscopy and density functional theory calculations to demonstrate that a sizable TSS gap unexpectedly exists in Sb-doped MnBi_2Te_4 where the bulk system remains topologically nontrivial. This gap is found to be insensitive to the bulk antiferromagnetic-paramagnetic transition, while it enlarges along with increasing Sb concentration, enabling simultaneous tunability of the Fermi level and the TSS gap size (up to >100 meV). Our work shows that Sb dopants in MnBi_2Te_4 can not only control the Fermi level but also induce a tunable surface gap, providing a potential platform to observe the key features of the high-temperature axion-insulator phase.

DOI: [10.1103/PhysRevB.103.L121112](https://doi.org/10.1103/PhysRevB.103.L121112)

Magnetic topological insulators (MTIs) are condensed matter systems that possess long-range magnetic order but remain topologically nontrivial [1–3]. Compared to nonmagnetic TIs whose topological surface states (TSSs) manifest a gapless Dirac cone that is protected by time reversal symmetry (\mathcal{T}), the TSSs of MTIs could open an energy gap if out-of-plane ferromagnetic (FM) order exists at the surface [4]. The presence of this gap in MTIs is of central importance to reveal the bulk topological magnetoelectric response in a so-called “axion insulator”, as each of these gapped surfaces hosts an anomalous Hall conductivity (AHC) that is quantized to a half of e^2/h [5–7]. Albeit much less explored than the quantum anomalous Hall state [8–10], axion insulators shed light on the fundamental understanding of topological insulators as bulk magnetoelectrics [2,11], and are potentially practical even in the astronomical search for the dark axions, quasiparticle candidates of the long-sought nonbaryonic dark matter [12].

The newly discovered van der Waals magnetic compounds $(\text{MnBi}_2\text{Te}_4)(\text{Bi}_2\text{Te}_3)_n$ ($n = 0, 1, 2, \dots$) are thus far the only stoichiometric material system that enables both the quantum anomalous Hall and the axion insulator states [13–19], whose Dirac surface state is first detected by angle-resolved

photoemission spectroscopy (ARPES) [20]. The ground-state magnetic orders of the $n < 2$ compounds are found to be A-type antiferromagnetic (AFM), with out-of-plane moments coming from the central Mn planes of the septuple-layer (SL) building blocks [16,21–27]. Along with strong band inversion, these compounds are predicted to be three-dimensional AFM TIs and strong candidates of axion insulators with TSS gaps at their natural cleaving planes [4,13,28]. Intriguingly, ARPES and scanning tunneling spectroscopy (STM) measurements uncovered near-vanishing surface state gaps in single crystals of the undoped “parent” compounds [29–37], raising the question of whether the impurities, defects, and possible surface structural and magnetic reconstruction plays a role in realizing the macroscopic quantum phases [29]. Above all, if a surface state gap exists in any of the Mn-Bi-Te family at all is still controversial [29–41].

Antimony is a convenient choice of nonmagnetic atomic dopant in the Bi-based topological materials. In $\text{Bi}_2(\text{Se},\text{Te})_3$, Sb is known to effectively introduce holes to the otherwise n doped system [42,43]. Meanwhile, it also drives the system towards the topologically trivial side continuously, while maintaining the Dirac cone before the topological phase transition because the \mathcal{T} symmetry is always preserved [44]. Here, we demonstrate via systematic ARPES measurements that the situation in MnBi_2Te_4 is fundamentally different. Besides the overall p -type doping behavior, a sizable global surface state gap opens in Sb-doped MnBi_2Te_4 single crystals. A relatively small concentration of Sb dopants was able to raise the gap

*These authors contributed equally to this work.

[†]chency@sustech.edu.cn

[‡]liuqh@sustech.edu.cn

[§]liuc@sustech.edu.cn

size up to >100 meV. This gap remains immune from the AFM ground state to the high temperature paramagnetic (PM) state, while it increases monotonically with the density of p dopants. Therefore, Sb dosage enables convenient control of the surface state gap in the AFM TI MnBi_2Te_4 within a wide range. Based on the modern theory of doping and alloying implemented to density functional theory (DFT) calculations, we identified the signature of the electronic structure during the magnetic phase transition, and confirmed the nontrivial topological nature of the bulk within the doping range studied. Possible origins of the anomalous surface gap are also discussed.

Physical and topological properties of Sb-doped MnBi_2Te_4 $\{\text{Mn}_{1-\alpha}(\text{Bi}_{1-x}\text{Sb}_x)_2\text{Te}_{4-\beta}\}$, See Section S2 in Ref. [45]] is a subject of intense recent study [65–69]. Our successful doping of Sb into MnBi_2Te_4 is first confirmed by atomic energy dispersive x-ray spectrum (EDX) mapping on a set of samples with nominal doping levels $0 \leq x_{\text{nominal}} \leq 0.1$ (Section S2 [45]). Together with cross-sectional scanning transmission electron microscopy (STEM) (Section S3 [45]), we found reasonably uniform distribution of Sb dopants over a microscopic region but considerable sample-to-sample variation of doping concentration. Topographic images, obtained by scanning tunneling microscopy, reveal no trace of surface atomic reconstruction and surface lattice constant change (Section S4 [45]). Variation of carrier concentration is also found via Hall measurements between growth batches with different nominal doping, as well as via different samples in the same growth batch (Section S5 [45]). We then distinguish the bulk and surface dispersion and demonstrate the existence of the surface state gap in Sb-doped MnBi_2Te_4 via systematic ARPES measurements. Figure 1 shows our ARPES data taken on a typical sample with $x_{\text{nominal}} = 0.075$ at $T = 10$ K (below $T_N \sim 23$ K). Figures 1(a)–1(c) present the raw and second derivative ARPES k - E maps along the $\bar{\Gamma}$ - \bar{M} high symmetry direction taken under three representative photon energies, corresponding to two consecutive bulk Γ points and a bulk Z point in between. Great care was taken in these measurements to ensure that the $\bar{\Gamma}$ points are reached very accurately (with uncertainty less than 0.2° for all photon energies), so that the sizes of the global gaps are measured precisely. A clear, sizable energy gap is observed with an identical value at the crossing point of the otherwise linear bands in three different photon energies. This is in drastic contrast to the case of undoped MnBi_2Te_4 , where the gap is close to diminishing at the Dirac point (see also Section S6 [45] for the existence of the gap in the k_x - k_y plane). From Fig. 1(d) we found that the gap is a global one, which opens under all photon energies measured, covering more than two out-of-plane Brillouin zones (BZs). There are five visible bands [defined in Fig. 1(b)] near the apparent gap (See Section S7 [45] for details of gap size determination). The bulk nature of the BV band is proven via its strong and periodic k_z dispersive behavior seen in Fig. 1(d). The SV and SC bands, on the other hand, exhibit no discernible dispersion across a k_z range of $\sim 5\pi/c$, endorsing their surface origin. We can therefore unambiguously conclude that the surface state of Sb-doped MnBi_2Te_4 is gapped.

In Fig. 2 we examine quantitatively the temperature evolution of the bulk and surface bands from the ARPES data on

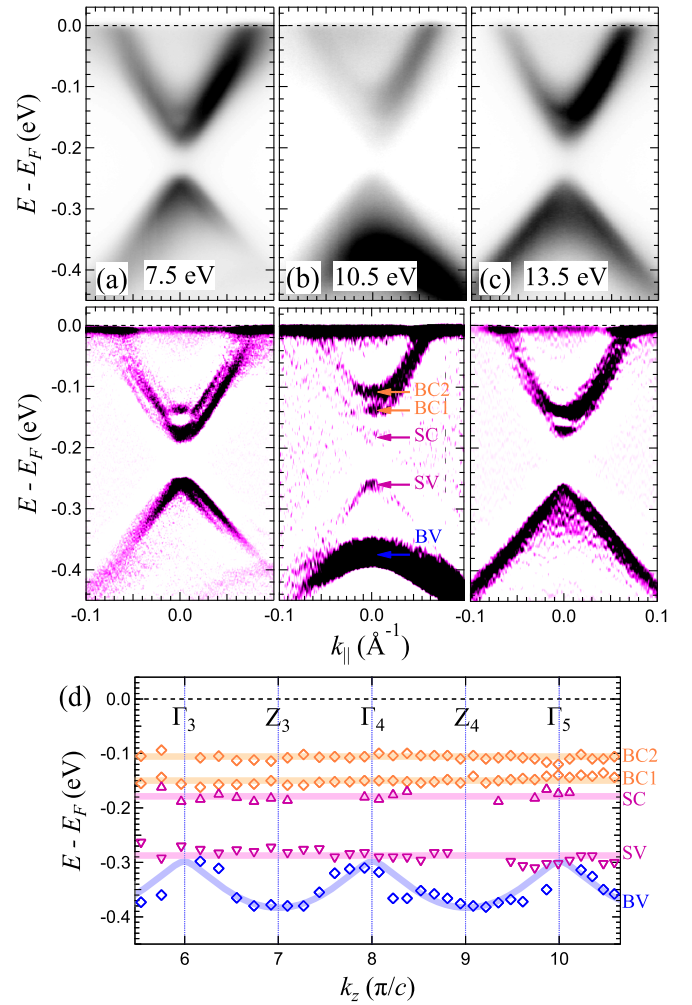


FIG. 1. Presence of the surface state gap in Sb-doped MnBi_2Te_4 . Data taken on a $x_{\text{nominal}} = 0.075$ sample at $T = 10$ K. (a)–(c) Raw (top) and second derivative (bottom) ARPES k - E maps on three representative photon energies, close to the bulk high-symmetry points (a) Γ_3 , (b) Z_3 , and (c) Γ_4 , respectively. BV: bulk valence band; SV/SC: surface valence/conduction band (bottom/top part of the gapped surface state); BC1/BC2: the two bulk conduction bands seen at $T < T_N$. The persistence of the surface state gap and the evolution of BV is seen clearly. (d) Extraction of k_z dispersion for the bands at $\bar{\Gamma}$. Photon energy ranges from 6.5 to 23 eV, corresponding to $\sim 5.5\pi/c < k_z < \sim 10.6\pi/c$. Colored lines are guides to the eye.

a prototypical Sb-doped sample [Sample S2, $x_{\text{nominal}} = 0.05$, Figs. 2(a)–2(d)], as well as the theoretical AFM and PM electronic structures of bulk $\text{Mn}(\text{Bi}_{1-x}\text{Sb}_x)_2\text{Te}_4$ at $x_{\text{cal}} = 0.056$ (1/18) calculated by DFT [Figs. 2(e)–2(h)]. To simulate the electronic structure of Sb doping and the PM phase with randomly distributed local moments, we apply DFT calculations using the Special Quasirandom Structures (SQS) method [70] that takes into account the local disorder effects. To directly compare with the ARPES spectral function, we unfold the resulting band structures obtained from the supercell approach [52,53] to the BZ of the primitive cell. As shown in Figs. 2(e)–2(h), while the slightly doped system for the AFM phase does not change much, the long wavevector spectral density away from E_F for the PM phase looks fuzzy,

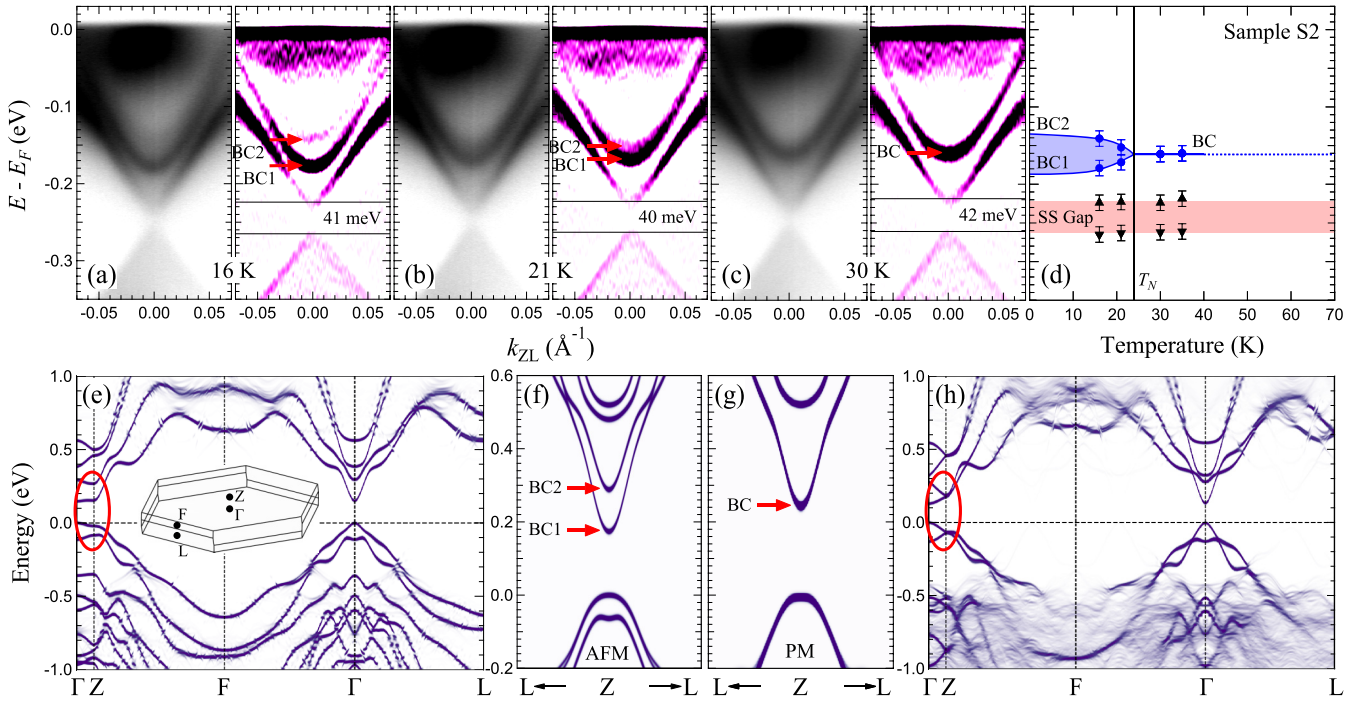


FIG. 2. Temperature independence of the bulk and surface state gap. (a)–(d) Temperature evolution of the bands of Sample S2 ($x_{\text{nominal}} = 0.05$). Data is taken with a 6.36-eV laser ARPES setup [i.e., at $k_z \sim 5\pi/c$ (Z_2)]. (a)–(c) Raw (left) and second derivative (right) ARPES k - E maps taken at three representative temperatures, below and above the bulk AFM-PM transition temperature $T_N \sim 23.5$ K. (d) Summary on the temperature evolution of BC1, BC2, and the surface state (SS) gap. While BC1 and BC2 merges into a single bulk conduction (BC) band around T_N , the SS gap remains essentially unchanged. (e)–(h) Effective band structure (EBS) calculation results for the AFM and PM state electronic structure on a $x = 1/18$ (0.056) system. (e)/(h) Overall band structure of the AFM/PM state. Inset: AFM Brillouin zone with high-symmetry points. Red ellipses highlight the merging of BC1 and BC2 at Z. (f)/(g) Focused band structure of the AFM/PM state along L - Z - L .

informing the extent to which the translational symmetry is retained. The most profound difference of the band dispersion between AFM and PM phases near E_F occurs at the Z point, where the BC1 and BC2 bands merge into a single BC band at the high-temperature PM phase. We note that such “Zeeman-like” band splitting and merging [Figs. 2(f)–2(g)] only happens at the BZ boundary such as the $Z(0, 0, 0.5)$ and $L(0, 0.5, 0.5)$ points. We attribute this phenomenon to the band folding effect due to the doubled primitive cell of the AFM phase with lower translational symmetry compared to the PM phase. Such a spectroscopy signature can be used to monitor the magnetic phase transition. Therefore, we perform ARPES measurements at a photon energy of 6.36 eV, focusing on the bulk Z_2 point ($k_z \sim 5\pi/c$). Indeed, we see in Figs. 2(a)–2(d) that the BC1 and BC2 bands come closer to each other as the temperature rises, merge into a single BC band around $T_N \sim 23.5$ K, and finally keep a constant binding energy for $T > T_N$. Therefore, the band evolution through the AFM-PM magnetic phase transition is unambiguously observed.

Surprisingly, the surface gap on the other hand remains essentially unchanged for all temperatures measured, across T_N from 16 K to 35 K [Fig. 2(d)]. In Fig. S7 [45] we graph the temperature evolution of this gap for two other samples with different x , reproducing again a constant-sized gap up to 150 K. These observations reveal an unexpected fact that the surface state gap of Sb-doped MnBi_2Te_4 is insensitive to

the change of temperature, regardless of its bulk magnetic phase. Another important feature about the gap is that it increases in samples (or regions) with higher p -type dopants. This behavior is elaborated in Fig. 3 where the sizes of both the SS and the bulk gap are compared at $T > T_N$ [71] for seven samples with different carrier densities, corresponding to $0 \leq x_{\text{nominal}} \leq 0.1$. Since the actual carrier concentration varies within the same growth batch and even the same sample (Sections S2 and S11 [45]), the doping levels are calibrated using the binding energies at the center of the SS gap (E_c) instead of x_{nominal} . This procedure is justified by the knowledge that Sb atoms are effective p dopants of the system, pushing the Fermi level downward in a rigid band shifting scenario except for the gap region. From Figs. 3(a)–3(e), we see that the gap size increases as E_c increases, from ~ 12 meV at Sample S1 ($x = 0$, $E_c = -272$ meV) [72] to 122 meV at Sample S5 ($E_c = -156.5$ meV). Local doping variation in a single sample gives different E_c values at different spatial positions, causing a synchronous change of the gap size (Section S11 [45]). Importantly, Fig. 3(f) and Fig. S10 show that the TSS gap and E_c values aligned nicely to a single linear relation. It did not matter if they were measured in different samples or within the same crystal [73].

So far we have demonstrated the presence and the anomalous temperature-doping dependence of a global energy gap in the TSS of Sb-doped MnBi_2Te_4 . This gap is nearly constant across a wide temperature range, insensitive to the bulk

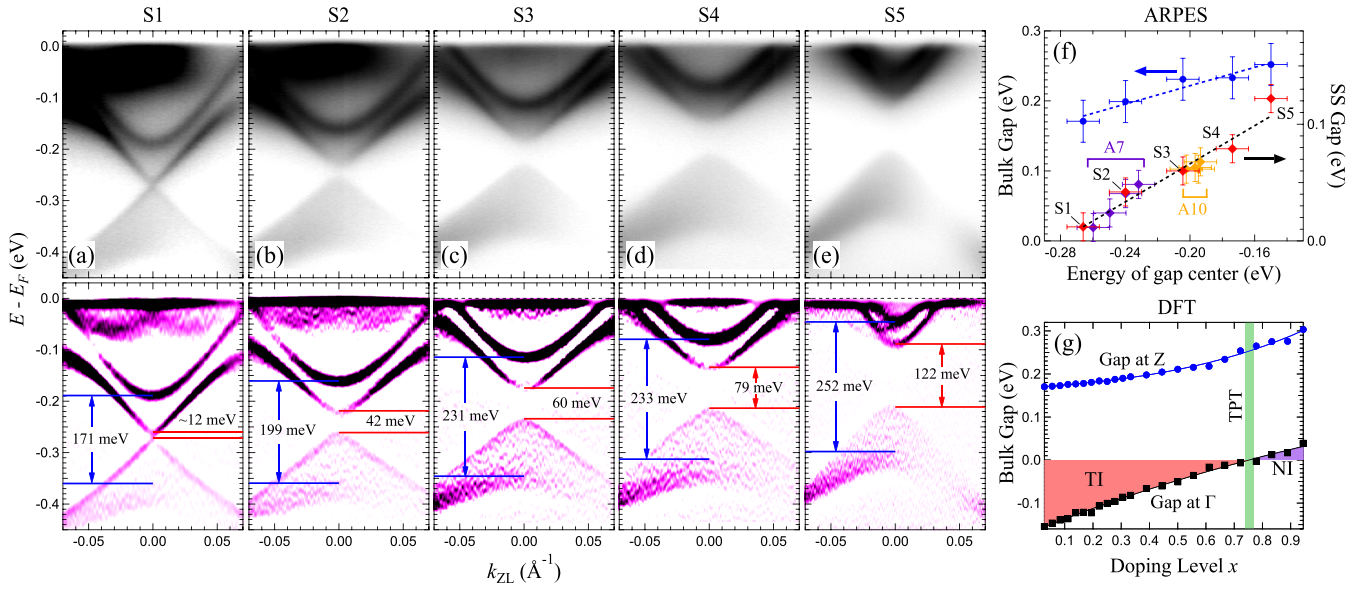


FIG. 3. Carrier concentration dependence of the SS gap and the bulk gap. Data is taken with a 6.36-eV laser ARPES setup at $T = 30\text{--}35\text{ K}$ (above T_N). (a)–(e) Raw (top) and second derivative (bottom) ARPES k - E maps for five samples with different carrier concentrations ordered by E_c . Red/blue lines: SS/bulk gap. (f) E_c dependence of the bulk gap at Z (blue, left), and the SS gap (black, right). Data taken with Samples A7 and A10 (Section S11 [45]) is also included. (g) Bulk gap at Γ (black) and Z (blue) calculated via supercell approach. Possible errors due to different Sb configuration are within symbol size. Solid lines are polynomial fits. TI: topological insulator; NI: normal insulator; TPT: topological phase transition.

magnetic transition, but enlarges monotonically with increasing p dopants. Before looking into the possible origins of these gapped phases, we first point out that the bulk system remains topologically nontrivial within the doping range studied. Experimentally, we notice that the size of the bulk gap between the BV and the BC bands is increasing with doping at the bulk Z point (Fig. 3), from 171 meV at Sample S1 to 252 meV at Sample S5 (See Section S8 [45] for details of gap size determination), while decreasing with doping at the bulk Γ point (Section S10 [45]). This proves that the bulk system evolves toward the topologically trivial side, but has not yet reached the topological phase transition. Theoretically, our DFT calculations using the SQS method show that the topological phase transition (TPT) in $\text{Mn}(\text{Bi}_{1-x}\text{Sb}_x)_2\text{Te}_4$ occurs at a much larger x . Figure 3(g) marks the TPT by displaying the calculated band gap evolution at Γ and Z. Both the growing gap at Z and the decreasing gap at Γ with increasing x is consistent with our ARPES results. The gap at Γ closes at $x_c \simeq 0.75$, where the system undergoes a transition to the normal-insulator state. Similar calculation results using the virtual crystal approximation (VCA) [64] are shown in Section S14 [45], in which x_c is found to be about 0.65. Therefore, for $0 \leq x \leq 0.1$, the system stays in the topological regime.

We note that the TSS of the $x = 0$ parent compound has a near-vanishing gap that is much smaller than DFT prediction (Figs. 2, 3 and Refs. [29–32]). Although a comprehensive explanation on the intact Dirac cone of MnBi_2Te_4 is not reached, these results point to the possibility that the structural and/or magnetic structure on the surface of the system is fundamentally different from that in the bulk [29]. Thus, it is natural to speculate that Sb doping in MnBi_2Te_4 suppresses the surface spin reorientation and somehow restore the surface

FM, which is supported by the ferrimagnetic state recently found by transport measurements in Sb-doped samples [74]. However, this argument is not consistent with our ARPES results in the PM phase, because a magnetic gap arising from this mechanism is supposed to vanish at $T > T_N$. Similarly, previous work proposed that the Dirac electronic states could couple to the conduction electrons through the Ruderman-Kittel-Kasuya-Yosida (RKKY) exchange interaction among the PM impurities, and thus induce weak ferromagnetism [75]. However, it is uncertain that such a FM state above T_N could quantitatively cause a ~ 100 meV gap as found, which inevitably leads to a significantly higher transition temperature at the surface. The residual FM at the surface is supposed to be captured by monitoring the s_z components of the TSS from the spin-ARPES measurements [56]. We performed such measurements on an undoped sample and found large, antiparallel z polarization of the spin at $\bar{\Gamma}$. As shown in Fig. S11 [45], the s_z components are observed to be as large as 30%, in drastic contrast to the case of nonmagnetic TIs where $s_z = 0$ at $\bar{\Gamma}$. However, due to the limitation of the energy resolution of spin-ARPES, one cannot rule out the bulk contribution although the penetration effect predominately counts the topmost Sb-MnBi₂Te₄ layer at the surface [58]. Another possible scenario is that this gap does not result from the surface FM, but rather the effect of dephasing and Coulomb scattering from charged impurities, such as vacancies (Section S15 [45]) [62]. We note that such speculation simultaneously fulfills the two anomalous features of the TSS gap, i.e., remaining above T_N and increasing upon doping, but it does not perfectly fit the observed shape of the gapped bands. Other mechanisms, such as the effect of hybridization with alien d electrons from transition-metal elements [76] and lattice-distortion induced symmetry breaking [77], seem unlikely to happen here.

More evidence that exposes the underlying mechanism of the anomalous gap is thus called for.

In summary, a sizable global energy gap in the topological surface state of a magnetic topological insulator, Sb-doped MnBi_2Te_4 , is discovered experimentally. Our systematic ARPES measurements found that this gap increases in size from near vanishing to more than 100 meV at low doping levels, but remains constant in both the low-temperature AFM and the high-temperature PM phases. The transition between the two phases is identified by the merging of two bulk conduction bands at T_N , observed both in our ARPES measurements and DFT calculations. Restoration of surface FM, weak ferromagnetism introduced by RKKY interaction, as well as the combined effect of charged impurity and quasi-particle dephasing are discussed as possible origins of the TSS gap. Remarkably, these possibilities do not hinder the topological nontriviality of the system. It is nonetheless a large, robust surface state gap with inverted band order in the bulk. Our results show unambiguously that the gap at the topological surface state of MnBi_2Te_4 can be tuned in a systematic way via Sb substitution. Taken collectively, we suggest that Sb-doped MnBi_2Te_4 , comprising a single massive Dirac cone caused either by the broken \mathcal{T} symmetry or the charged impurities, might be thus far the simplest material system to observe the signatures of the high-temperature axion insulator state.

We thank Prof. Xin-Cheng Xie, Haiwen Liu, Hai-Zhou Lu, Weiqiang Chen, Dr. Zhi Wang, and Dr. Wen Huang

for inspiring discussions. ARPES experiments were performed with the approval of the Hiroshima Synchrotron Radiation Center (HSRC), Hiroshima, Japan under Proposals 19BG044, 19BU002, 19BU005 and 19BU012. Work at SUSTech was supported by the National Key R&D Program of China (Nos. 2020YFA0308900 and 2019YFA0704900), the National Natural Science Foundation of China (NSFC) (Nos. 12074161, 11874195, 12074163, 11804144, 11804402, and 11974156), NSFC Guangdong (No. 2016A030313650), the Guangdong Innovative and Entrepreneurial Research Team Program (Nos. 2016ZT06D348, 2017ZT07C062, and 2019ZT08C044), the Guangdong Provincial Key Laboratory of Computational Science and Material Design (No. 2019B030301001), the University Innovative Team in Guangdong Province (No. 2020KCXTD001), the Shenzhen Key Laboratory (No. ZDSYS20170303165926217), the Science, Technology and Innovation Commission of Shenzhen Municipality (Nos. KYTDPT20181011104202253 and KQTD20190929173815000), the Center for Computational Science and Engineering of SUSTech, and also with the assistance of SUSTech Core Research Facilities, especially technical support from Pico-Centre that receives support from the Presidential fund and Development and Reform Commission of Shenzhen Municipality. J.S. is supported by the SUSTech Presidential Postdoctoral Fellowship. C.C. is supported by the Shenzhen High-level Special Fund (Nos. G02206304, G02206404). Ch.L. acknowledges support from the Highlight Project (No. PHYS-HL-2020-1) of the College of Science, SUSTech.

- [1] Y. Tokura, K. Yasuda, and A. Tsukazaki, Magnetic topological insulators, *Nat. Rev. Phys.* **1**, 126 (2019).
- [2] N. P. Armitage and L. Wu, On the matter of topological insulators as magnetoelectrics, *SciPost Phys.* **6**, 046 (2019).
- [3] P. Tang, Q. Zhou, G. Xu, and S.-C. Zhang, Dirac fermions in an antiferromagnetic semimetal, *Nat. Phys.* **12**, 1100 (2016).
- [4] R. S. K. Mong, A. M. Essin, and J. E. Moore, Antiferromagnetic topological insulators, *Phys. Rev. B* **81**, 245209 (2010).
- [5] J. Wang, B. Lian, X.-L. Qi, and S.-C. Zhang, Quantized topological magnetoelectric effect of the zero-plateau quantum anomalous Hall state, *Phys. Rev. B* **92**, 081107(R) (2015).
- [6] M. Mogi, M. Kawamura, R. Yoshimi, A. Tsukazaki, Y. Kozuka, N. Shirakawa, K. S. Takahashi, M. Kawasaki, and Y. Tokura, A magnetic heterostructure of topological insulators as a candidate for an axion insulator, *Nat. Mater.* **16**, 516 (2017).
- [7] D. Xiao, J. Jiang, J.-H. Shin, W. Wang, F. Wang, Y.-F. Zhao, C. Liu, W. Wu, M. H. W. Chan, N. Samarth, and C.-Z. Chang, Realization of the Axion Insulator State in Quantum Anomalous Hall Sandwich Heterostructures, *Phys. Rev. Lett.* **120**, 056801 (2018).
- [8] R. Yu, W. Zhang, H.-J. Zhang, S.-C. Zhang, X. Dai, and Z. Fang, Quantized anomalous Hall effect in magnetic topological insulators, *Science* **329**, 61 (2010).
- [9] C.-Z. Chang, J. Zhang, X. Feng, J. Shen, Z. Zhang, M. Guo, K. Li, Y. Ou, P. Wei, L.-L. Wang, Z.-Q. Ji, Y. Feng, S. Ji, X. Chen, J. Jia, X. Dai, Z. Fang, S.-C. Zhang, K. He, Y. Wang, L. Lu, X.-C. Ma, and Q.-K. Xue, Experimental observation of the quantum anomalous Hall effect in a magnetic topological insulator, *Science* **340**, 167 (2013).
- [10] X.-L. Qi, T. L. Hughes, and S.-C. Zhang, Topological field theory of time-reversal invariant insulators, *Phys. Rev. B* **78**, 195424 (2008); **81**, 159901(E) (2010).
- [11] L. Wu, M. Salehi, N. Koirala, J. Moon, S. Oh, and N. P. Armitage, Quantized Faraday and Kerr rotation and axion electrodynamics of a 3D topological insulator, *Science* **354**, 1124 (2016).
- [12] D. J. E. Marsh, K. C. Fong, E. W. Lentz, L. Šmejkal, and M. N. Ali, Proposal to Detect Dark Matter using Axionic Topological Antiferromagnets, *Phys. Rev. Lett.* **123**, 121601 (2019).
- [13] D. Zhang, M. Shi, T. Zhu, D. Xing, H. Zhang, and J. Wang, Topological Axion States in the Magnetic Insulator MnBi_2Te_4 with the Quantized Magnetoelectric Effect, *Phys. Rev. Lett.* **122**, 206401 (2019).
- [14] J. Li, Y. Li, S. Du, Z. Wang, B.-L. Gu, S.-C. Zhang, K. He, W. Duan, and Y. Xu, Intrinsic magnetic topological insulators in van der Waals layered MnBi_2Te_4 -family materials, *Sci. Adv.* **5**, eaaw5685 (2019).
- [15] Y. Gong, J. Guo, J. Li, K. Zhu, M. Liao, X. Liu, Q. Zhang, L. Gu, L. Tang, X. Feng, D. Zhang, W. Li, C. Song, L. Wang, P. Yu, X. Chen, Y. Wang, H. Yao, W. Duan, Y. Xu, S.-C. Zhang, X. Ma, Q.-K. Xue, and K. He, Experimental realization of an intrinsic magnetic topological insulator, *Chin. Phys. Lett.* **36**, 076801 (2019).

- [16] M. M. Otrokov, I. I. Klimovskikh, H. Bentmann, D. Estyunin, A. Zeugner, Z. S. Aliev, S. Gaß, A. U. B. Wolter, A. V. Koroleva, A. M. Shikin, M. Blanco-Rey, M. Hoffmann, I. P. Rusinov, A. Yu. Vyazovskaya, S. V. Eremeev, Yu. M. Koroteev, V. M. Kuznetsov, F. Freyse, J. Sánchez-Barriga, I. R. Amiraslanov, M. B. Babanly, N. T. Mamedov, N. A. Abdullayev, V. N. Zverev, A. Alfonsov, V. Kataev, B. Büchner, E. F. Schwier, S. Kumar, A. Kimura, L. Petaccia, G. Di Santo, R. C. Vidal, S. Schatz, K. Kißner, M. Ünzelmann, C. H. Min, Simon Moser, T. R. F. Peixoto, F. Reinert, A. Ernst, P. M. Echenique, A. Isaeva, and E. V. Chulkov, Prediction and observation of an antiferromagnetic topological insulator, *Nature* **576**, 416 (2019).
- [17] E. D. L. Rienks, S. Wimmer, J. Sánchez-Barriga, O. Caha, P. S. Mandal, J. Růžička, A. Ney, H. Steiner, V. V. Volobuev, H. Groiss, M. Albu, G. Kothleitner, J. Michalička, S. A. Khan, J. Minár, H. Ebert, G. Bauer, F. Freyse, A. Varykhalov, O. Rader, and G. Springholz, Large magnetic gap at the Dirac point in $\text{Bi}_2\text{Te}_3/\text{MnBi}_2\text{Te}_4$ heterostructures, *Nature* **576**, 423 (2019).
- [18] Y. Deng, Y. Yu, M. Z. Shi, Z. Guo, Z. Xu, J. Wang, X. H. Chen, and Y. Zhang, Quantum anomalous Hall effect in intrinsic magnetic topological insulator MnBi_2Te_4 , *Science* **367**, 895 (2020).
- [19] C. Liu, Y. Wang, H. Li, Y. Wu, Y. Li, J. Li, K. He, Y. Xu, J. Zhang, and Y. Wang, Robust axion insulator and Chern insulator phases in a two-dimensional antiferromagnetic topological insulator, *Nat. Mater.* **19**, 522 (2020).
- [20] T. Hirahara, S. V. Eremeev, T. Shirasawa, Y. Okuyama, T. Kubo, R. Nakanishi, R. Akiyama, A. Takayama, T. Hajiri, S.-I. Ideta, M. Matsunami, K. Sumida, K. Miyamoto, Y. Takagi, K. Tanaka, T. Okuda, T. Yokoyama, S.-I. Kimura, S. Hasegawa, and E. V. Chulkov, Large-gap magnetic topological heterostructure formed by subsurface incorporation of a ferromagnetic layer, *Nano Lett.* **17**, 3493 (2017).
- [21] K. G. S. Ranmohotti, H. Djieutedjeu, and P. F. P. Poudeu, Chemical manipulation of magnetic ordering in $\text{Mn}_{1-x}\text{Sn}_x\text{Bi}_2\text{Se}_4$ solid-solutions, *J Am. Chem. Soc.* **134**, 14033 (2012).
- [22] J. Wu, F. Liu, M. Sasase, K. Ienaga, Y. Obata, R. Yukawa, K. Horiba, H. Kumigashira, S. Okuma, T. Inoshita, and H. Hosono, Natural van der Waals heterostructural single crystals with both magnetic and topological properties, *Sci. Adv.* **5**, eaax9989 (2019).
- [23] M. Z. Shi, B. Lei, C. S. Zhu, D. H. Ma, J. H. Cui, Z. L. Sun, J. J. Ying, and X. H. Chen, Magnetic and transport properties in the magnetic topological insulators $\text{MnBi}_2\text{Te}_4(\text{Bi}_2\text{Te}_3)_n$ ($n = 1, 2$), *Phys. Rev. B* **100**, 155144 (2019).
- [24] J.-Q. Yan, Q. Zhang, T. Heitmann, Z. Huang, K. Y. Chen, J.-G. Cheng, W. Wu, D. Vaknin, B. C. Sales, and R. J. McQueeney, Crystal growth and magnetic structure of MnBi_2Te_4 , *Phys. Rev. Mater.* **3**, 064202 (2019).
- [25] A. Zeugner, F. Nietschke, A. U. B. Wolter, S. Gaß, R. C. Vidal, T. R. F. Peixoto, D. Pohl, C. Damm, A. Lubk, R. Hentrich, S. K. Moser, C. Fornari, C. H. Min, S. Schatz, K. Kißner, M. Ünzelmann, M. Kaiser, F. Scaravaggi, B. Rellinghaus, K. Nielsch, C. Hess, B. Büchner, F. Reinert, H. Bentmann, O. Oeckler, T. Doert, M. Ruck, and A. Isaeva, Chemical aspects of the candidate antiferromagnetic topological insulator MnBi_2Te_4 , *Chem. Mater.* **31**, 2795 (2019).
- [26] L. Ding, C. Hu, F. Ye, E. Feng, N. Ni, and H. Cao, Crystal and magnetic structures of magnetic topological insulators MnBi_2Te_4 and MnBi_4Te_7 , *Phys. Rev. B* **101**, 020412(R) (2020).
- [27] C. Hu, L. Ding, K. N. Gordon, B. Ghosh, H.-J. Tien, H. Li, A. G. Linn, S.-W. Lien, C.-Y. Huang, S. Mackey, J. Liu, P. V. S. Reddy, B. Singh, A. Agarwal, A. Bansil, M. Song, D. Li, S.-Y. Xu, H. Lin, H. Cao, T.-R. Chang, D. Dessau, and N. Ni, Realization of an intrinsic ferromagnetic topological state in $\text{MnBi}_8\text{Te}_{13}$, *Sci. Adv.* **6**, eaba4275 (2020).
- [28] C. Hu, K. N. Gordon, P. Liu, J. Liu, X. Zhou, P. Hao, D. Narayan, E. Emmanouilidou, H. Sun, Y. Liu, H. Brawer, A. P. Ramirez, L. Ding, H. Cao, Q. Liu, D. Dessau, and N. Ni, A van der Waals antiferromagnetic topological insulator with weak interlayer magnetic coupling, *Nat. Commun.* **11**, 97 (2020).
- [29] Y.-J. Hao, P. Liu, Y. Feng, X.-M. Ma, E. F. Schwier, M. Arita, S. Kumar, C. Hu, R. Lu, M. Zeng, Y. Wang, Z. Hao, H.-Y. Sun, K. Zhang, J. Mei, N. Ni, L. Wu, K. Shimada, C. Chen, Q. Liu, and C. Liu, Gapless Surface Dirac Cone in Antiferromagnetic Topological Insulator MnBi_2Te_4 , *Phys. Rev. X* **9**, 041038 (2019).
- [30] H. Li, S.-Y. Gao, S.-F. Duan, Y.-F. Xu, K.-J. Zhu, S.-J. Tian, J.-C. Gao, W.-H. Fan, Z.-C. Rao, J.-R. Huang, J.-J. Li, D.-Y. Yan, Z.-T. Liu, W.-L. Liu, Y.-B. Huang, Y.-L. Li, Y. Liu, G.-B. Zhang, P. Zhang, T. Kondo, S. Shin, H.-C. Lei, Y.-G. Shi, W.-T. Zhang, H.-M. Weng, T. Qian, and H. Ding, Dirac Surface States in Intrinsic Magnetic Topological Insulators EuSn_2As_2 and $\text{MnBi}_{2n}\text{Te}_{3n+1}$, *Phys. Rev. X* **9**, 041039 (2019).
- [31] Y. J. Chen, L. X. Xu, J. H. Li, Y. W. Li, H. Y. Wang, C. F. Zhang, H. Li, Y. Wu, A. J. Liang, C. Chen, S. W. Jung, C. Cacho, Y. H. Mao, S. Liu, M. X. Wang, Y. F. Guo, Y. Xu, Z. K. Liu, L. X. Yang, and Y. L. Chen, Topological electronic structure and its temperature evolution in antiferromagnetic topological insulator MnBi_2Te_4 , *Phys. Rev. X* **9**, 041040 (2019).
- [32] B. Chen, F. Fei, D. Zhang, B. Zhang, W. Liu, S. Zhang, P. Wang, B. Wei, Y. Zhang, Z. Zuo, J. Guo, Q. Liu, Z. Wang, X. Wu, J. Zong, X. Xie, W. Chen, Z. Sun, S. Wang, Y. Zhang, M. Zhang, X. Wang, F. Song, H. Zhang, D. Shen, and B. Wang, Intrinsic magnetic topological insulator phases in the Sb doped MnBi_2Te_4 bulks and thin flakes, *Nat. Commun.* **10**, 4469 (2019).
- [33] Y. Hu, L. Xu, M. Shi, A. Luo, S. Peng, Z. Y. Wang, J. J. Ying, T. Wu, Z. K. Liu, C. F. Zhang, Y. L. Chen, G. Xu, X.-H. Chen, and J.-F. He, Universal gapless Dirac cone and tunable topological states in $(\text{MnBi}_2\text{Te}_4)_m(\text{Bi}_2\text{Te}_3)_n$ heterostructures, *Phys. Rev. B* **101**, 161113(R) (2020).
- [34] P. Swatek, Y. Wu, L.-L. Wang, K. Lee, B. Schunk, J.-Q. Yan, and A. Kaminski, Gapless Dirac surface states in the antiferromagnetic topological insulator MnBi_2Te_4 , *Phys. Rev. B* **101**, 161109(R) (2020).
- [35] N. H. Jo, L.-L. Wang, R.-J. Slager, J. Yan, Y. Wu, K. Lee, B. Schunk, A. Vishwanath, and A. Kaminski, Intrinsic axion insulating behavior in antiferromagnetic $\text{MnBi}_6\text{Te}_{10}$, *Phys. Rev. B* **102**, 045130 (2020).
- [36] X.-M. Ma, Z. Chen, E. F. Schwier, Y. Zhang, Y.-J. Hao, S. Kumar, R. Lu, J. Shao, Y. Jin, M. Zeng, X.-R. Liu, Z. Hao, K. Zhang, W. Mansuer, C. Song, Y. Wang, B. Zhao, C. Liu, K. Deng, J. Mei, K. Shimada, Y. Zhao, X. Zhou, B. Shen, W. Huang, C. Liu, H. Xu, and C. Chen, Hybridization-induced gapped and gapless states on the surface of magnetic topological insulators, *Phys. Rev. B* **102**, 245136 (2020).
- [37] X. Wu, J. Li, X.-M. Ma, Y. Zhang, Y. Liu, C.-S. Zhou, J. Shao, Q. Wang, Y.-J. Hao, Y. Feng, E. F. Schwier, S. Kumar, H. Sun, P. Liu, K. Shimada, K. Miyamoto, T. Okuda, K. Wang, M. Xie, C. Chen, Q. Liu, C. Liu, and Y. Zhao, Distinct Topological Surface

- States on the Two Terminations of MnBi_4Te_7 , *Phys. Rev. X* **10**, 031013 (2020).
- [38] K. N. Gordon, H. Sun, C. Hu, A. G. Linn, H. Li, Y. Liu, P. Liu, S. Mackey, Q. Liu, N. Ni, and D. Dessau, Strongly gapped topological surface states on protected surfaces of antiferromagnetic MnBi_4Te_7 and $\text{MnBi}_6\text{Te}_{10}$, [arXiv:1910.13943](https://arxiv.org/abs/1910.13943) (2019).
- [39] R. C. Vidal, H. Bentmann, T. R. F. Peixoto, A. Zeugner, S. Moser, C.-H. Min, S. Schatz, K. Kißner, M. Ünzelmann, C. I. Fornari, H. B. Vasili, M. Valvidares, K. Sakamoto, D. Mondal, J. Fujii, I. Vobornik, S. Jung, C. Cacho, T. K. Kim, R. J. Koch, C. Jozwiak, A. Bostwick, J. D. Denlinger, E. Rotenberg, J. Buck, M. Hoesch, F. Diekmann, S. Rohlf, M. Kalläne, K. Rossnagel, M. M. Otrokov, E. V. Chulkov, M. Ruck, A. Isaeva, and F. Reinert, Surface states and Rashba-type spin polarization in antiferromagnetic $\text{MnBi}_2\text{Te}_4(0001)$, *Phys. Rev. B* **100**, 121104(R) (2019).
- [40] R. C. Vidal, A. Zeugner, J. I. Facio, R. Ray, M. H. Haghighi, A. U. B. Wolter, L. T. C. Bohorquez, F. Caglieris, S. Moser, T. Figgemeier, T. R. F. Peixoto, H. B. Vasili, M. Valvidares, S. Jung, C. Cacho, A. Alfonsov, K. Mehlawat, V. Kataev, C. Hess, M. Richter, B. Büchner, J. van den Brink, M. Ruck, F. Reinert, H. Bentmann, and A. Isaeva, Topological Electronic Structure and Intrinsic Magnetization in MnBi_4Te_7 : A Bi_2Te_3 Derivative with a Periodic Mn Sublattice, *Phys. Rev. X* **9**, 041065 (2019).
- [41] W. Ko, M. Kolmer, J. Yan, A. D. Pham, M. Fu, F. Lüpke, S. Okamoto, Z. Gai, P. Ganesh, and A.-P. Li, Realizing gapped surface states in the magnetic topological insulator $\text{MnBi}_{2-x}\text{Sb}_x\text{Te}_4$, *Phys. Rev. B* **102**, 115402 (2020).
- [42] D. O. Scanlon, P. D. King, R. P. Singh, A. de la Torre, S. M. Walker, G. Balakrishnan, F. Baumberger, and C. R. Catlow, Controlling bulk conductivity in topological insulators: Key role of anti-site defects, *Adv. Mater.* **24**, 2154 (2012).
- [43] J. Zhang, C.-Z. Chang, Z. Zhang, J. Wen, X. Feng, K. Li, M. Liu, K. He, L. Wang, X. Chen, Q.-K. Xue, X. Ma, and Y. Wang, Band structure engineering in $(\text{Bi}_{1-x}\text{Sb}_x)_2\text{Te}_3$ ternary topological insulators, *Nat. Commun.* **2**, 574 (2011).
- [44] M. Neupane, S.-Y. Xu, L. A. Wray, A. Petersen, R. Shankar, N. Alidoust, C. Liu, A. Fedorov, H. Ji, J. M. Allred, Y. S. Hor, T.-R. Chang, H.-T. Jeng, H. Lin, A. Bansil, R. J. Cava, and M. Z. Hasan, Topological surface states and Dirac point tuning in ternary topological insulators, *Phys. Rev. B* **85**, 235406 (2012).
- [45] See Supplemental Information at <http://link.aps.org/supplemental/10.1103/PhysRevB.103.L121112> for Methods, Sections S1-S15 and Figures S1-S14. References [30,32,46–64] are included.
- [46] Z. S. Aliev, I. R. Amiraslanov, D. I. Nasonova, A. V. Shevelkov, N. A. Abdullayev, Z. A. Jahangirli, E. N. Orujlu, M. M. Otrokov, N. T. Mamedov, M. B. Babanly, and E. V. Chulkov, Novel ternary layered manganese bismuth tellurides of the $\text{MnTe-Bi}_2\text{Te}_3$ system: Synthesis and crystal structure, *J. Alloys Compd.* **789**, 443 (2019).
- [47] T. Okuda, K. Miyamoto, A. Kimura, H. Namatame, and M. Taniguchi, A double VLEED spin detector for high-resolution three dimensional spin vectorial analysis of anisotropic Rashba spin splitting, *J. Elec. Spec. Rel. Phenom.* **201**, 23 (2015).
- [48] G. Kresse and J. Furthmüller, Efficient iterative schemes for *ab initio* total-energy calculations using a plane-wave basis set, *Phys. Rev. B* **54**, 11169 (1996).
- [49] J. P. Perdew, K. Burke, and M. Ernzerhof, Generalized Gradient Approximation Made Simple, *Phys. Rev. Lett.* **77**, 3865 (1996).
- [50] V. I. Anisimov, J. Zaanen, and O. K. Andersen, Band theory and Mott insulators: Hubbard U instead of Stoner I , *Phys. Rev. B* **44**, 943 (1991).
- [51] G. Kresse and D. Joubert, From ultrasoft pseudopotentials to the projector augmented-wave method, *Phys. Rev. B* **59**, 1758 (1999).
- [52] T. B. Boykin, N. Kharche, G. Klimeck, and M. Korkusinski, Approximate bandstructures of semiconductor alloys from tight-binding supercell calculations, *J. Phys.: Condens. Matter* **19**, 036203 (2007).
- [53] T. B. Boykin and G. Klimeck, Practical application of zone-folding concepts in tight-binding calculations, *Phys. Rev. B* **71**, 115215 (2005).
- [54] P. V. C. Medeiros, S. Stafström, and J. Björk, Effects of extrinsic and intrinsic perturbations on the electronic structure of graphene: Retaining an effective primitive cell band structure by band unfolding, *Phys. Rev. B* **89**, 041407(R) (2014).
- [55] P. V. C. Medeiros, S. S. Tsirkin, S. Stafström, and J. Björk, Unfolding spinor wave functions and expectation values of general operators: Introducing the unfolding-density operator, *Phys. Rev. B* **91**, 041116(R) (2015).
- [56] S.-Y. Xu, M. Neupane, C. Liu, D. Zhang, A. Richardella, L. A. Wray, N. Alidoust, M. Leandersson, T. Balasubramanian, J. Sánchez-Barriga, O. Rader, G. Landolt, B. Slomski, J. H. Dil, J. Osterwalder, T.-R. Chang, H.-T. Jeng, H. Lin, A. Bansil, N. Samarth, and M. Z. Hasan, Hedgehog spin texture and Berry's phase tuning in a magnetic topological insulator, *Nat. Phys.* **8**, 616 (2012).
- [57] J. Sánchez-Barriga, A. Varykhalov, J. Braun, S.-Y. Xu, N. Alidoust, O. Kornilov, J. Minár, K. Hummer, G. Springholz, G. Bauer, R. Schumann, L. V. Yashina, H. Ebert, M. Z. Hasan, and O. Rader, Photoemission of Bi_2Se_3 with Circularly Polarized Light: Probe of Spin Polarization or Means for Spin Manipulation? *Phys. Rev. X* **4**, 011046 (2014).
- [58] X. Zhang, Q. Liu, J.-W. Luo, A. J. Freeman, and A. Zunger, Hidden spin polarization in inversion-symmetric bulk crystals, *Nat. Phys.* **10**, 387 (2014).
- [59] T. Sato, K. Segawa, K. Kosaka, S. Souma, K. Nakayama, K. Eto, T. Minami, Y. Ando, and T. Takahashi, Unexpected mass acquisition of Dirac fermions at the quantum phase transition of a topological insulator, *Nat. Phys.* **7**, 840 (2011).
- [60] J. Sánchez-Barriga, A. Varykhalov, G. Springholz, H. Steiner, R. Kirchschlager, G. Bauer, O. Caha, E. Schierle, E. Weschke, A. A. Ünal, S. Valencia, M. Dunst, J. Braun, H. Ebert, J. Minár, E. Golias, L. V. Yashina, A. Ney, V. Holý, and O. Rader, Nonmagnetic band gap at the Dirac point of the magnetic topological insulator $(\text{Bi}_{1-x}\text{Mn}_x)_2\text{Se}_3$, *Nat. Commun.* **7**, 10559 (2016).
- [61] T. Yilmaz, A. Pertsova, W. Hines, E. Vescovo, K. Kaznatcheev, A. V. Balatsky, and B. Sinkovic, Gap-like feature observed in the non-magnetic topological insulators, *J. Phys. Condens. Matter* **32**, 145503 (2020).
- [62] H. Liu, H. Jiang, Q. F. Sun, and X. C. Xie, Dephasing Effect on Backscattering of Helical Surface States in 3D Topological Insulators, *Phys. Rev. Lett.* **113**, 046805 (2014).
- [63] F. Delgado and J. Fernández-Rossier, Spin decoherence of magnetic atoms on surfaces, *Prog. Surf. Sci.* **92**, 40 (2017).

- [64] L. Bellaiche and D. Vanderbilt, Virtual crystal approximation revisited: Application to dielectric and piezoelectric properties of perovskites, *Phys. Rev. B* **61**, 7877 (2000).
- [65] S. V. Eremeev, M. M. Otrokov, and E. V. Chulkov, Competing rhombohedral and monoclinic crystal structures in MnPn_2Ch_4 compounds: An *ab-initio* study, *J Alloys Compd.* **709**, 172 (2017).
- [66] J. Q. Yan, S. Okamoto, M. A. McGuire, A. F. May, R. J. McQueeney, and B. C. Sales, Evolution of structural, magnetic, and transport properties in $\text{MnBi}_{2-x}\text{Sb}_x\text{Te}_4$, *Phys. Rev. B* **100**, 104409 (2019).
- [67] L. Zhou, Z. Tan, D. Yan, Z. Fang, Y. Shi, and H. Weng, Topological phase transition in the layered magnetic compound MnSb_2Te_4 : Spin-orbit coupling and interlayer coupling dependence, *Phys. Rev. B* **102**, 085114 (2020).
- [68] Y. Chen, Y.-W. Chuang, S. H. Lee, Y. Zhu, K. Honz, Y. Guan, Y. Wang, K. Wang, Z. Mao, J. Zhu, C. Heikes, P. Quarterman, P. Zajdel, J. A. Borchers, and W. Ratcliff, II, Ferromagnetism in van der Waals compound $\text{MnSb}_{1.8}\text{Bi}_{0.2}\text{Te}_4$, *Phys. Rev. Mater.* **4**, 064411 (2020).
- [69] M. H. Du, J. Yan, V. R. Cooper, and M. Eisenbach, Tuning Fermi levels in intrinsic antiferromagnetic topological insulators MnBi_2Te_4 and MnBi_4Te_7 by defect engineering and chemical doping, *Adv. Funct. Mater.* **31**, 2006516 (2021).
- [70] A. Zunger, S.-H. Wei, L. G. Ferreira, and J. E. Bernard, Special Quasirandom Structures, *Phys. Rev. Lett.* **65**, 353 (1990).
- [71] T_N is found to decrease monotonically with increasing x , from 23.89 K for $x = 0$ (S1) to ~ 23 K for $x_{\text{nominal}} = 0.1$ (S5).
- [72] Note that a nonvanishing TSS gap is found on the undoped sample from our multipeak fitting procedure (Fig. S6). This gap is much smaller than what the DFT calculation predicts (~ 80 meV). Such behavior is consistent with the near gapless feature found by ARPES in Refs. [29–32,34], among which Ref. [30] pointed out specifically the existence of a gap of about 10 meV.
- [73] Note that previous ARPES studies on $\text{Sb-MnBi}_2\text{Te}_4$ observe a continuous *p*-doping behavior with increasing x values and an *n-p* transition at $x \sim 0.3$ [32]; evidence of a sizable gap at $x = 0.32$ (where the system is *p*-typed) is provided by studying the quasiparticle interference pattern [41], but no momentum-resolved information is available prior to this work on how the surface and the bulk gaps evolve either with x or with temperature.
- [74] T. Murakami, Y. Nambu, T. Koretsune, X. Gu, T. Yamamoto, C. M. Brown, and H. Kageyama, Realization of interlayer ferromagnetic interaction in MnSb_2Te_4 toward the magnetic Weyl semimetal state, *Phys. Rev. B* **100**, 195103 (2019).
- [75] Q. Liu, C.-X. Liu, C. Xu, X.-L. Qi, and S.-C. Zhang, Magnetic Impurities on the Surface of a Topological Insulator, *Phys. Rev. Lett.* **102**, 156603 (2009).
- [76] A. Polyakov, C. Tusche, M. Ellguth, E. D. Crozier, K. Mohseni, M. M. Otrokov, X. Zubizarreta, M. G. Vergniory, M. Geilhufe, E. V. Chulkov, A. Ernst, H. L. Meyerheim, and S. S. P. Parkin, Instability of the topological surface state in Bi_2Se_3 upon deposition of gold, *Phys. Rev. B* **95**, 180202(R) (2017).
- [77] P. S. Mandal, G. Springholz, V. V. Volobuev, O. Caha, A. Varykhalov, E. Golias, G. Bauer, O. Rader, and J. Sánchez-Barriga, Topological quantum phase transition from mirror to time reversal symmetry protected topological insulator, *Nat. Commun.* **8**, 968 (2017).

Observation of Spin-Momentum-Layer Locking in a Centrosymmetric Crystal

Ke Zhang^{1,*}, Shixuan Zhao^{2,*}, Zhanyang Hao^{2,*}, Shiv Kumar³, Eike. F. Schwier^{3,6,7}, Yingjie Zhang², Hongyi Sun², Yuan Wang², Yujie Hao², Xiaoming Ma², Cai Liu², Le Wang², Xiaoxiao Wang³, Koji Miyamoto³, Taichi Okuda³, Chang Liu², Jiawei Mei², Kenya Shimada^{3,†}, Chaoyu Chen^{2,‡} and Qihang Liu^{2,4,5,§}

¹*Department of Physical Science, Graduate School of Science, Hiroshima University, Hiroshima 739-0046, Japan*

²*Shenzhen Institute for Quantum Science and Technology and Department of Physics, Southern University of Science and Technology, Shenzhen 518055, China*

³*Hiroshima Synchrotron Radiation Center, Hiroshima University, Hiroshima 739-0046, Japan*

⁴*Guangdong Provincial Key Laboratory for Computational Science and Material Design, Southern University of Science and Technology, Shenzhen 518055, China*

⁵*Shenzhen Key Laboratory of Advanced Quantum Functional Materials and Devices, Southern University of Science and Technology, Shenzhen 518055, China*

⁶*Experimentelle Physik VII, Universität Würzburg, Am Hubland, D-97074 Würzburg, Germany*

⁷*Würzburg-Dresden Cluster of Excellence ct.qmat, Germany*



(Received 18 February 2021; accepted 30 July 2021; published 14 September 2021)

The spin polarization in nonmagnetic materials is conventionally attributed to the outcome of spin-orbit coupling when the global inversion symmetry is broken. The recently discovered hidden spin polarization indicates that a specific atomic site asymmetry could also induce measurable spin polarization, leading to a paradigm shift in research on centrosymmetric crystals for potential spintronic applications. Here, combining spin- and angle-resolved photoemission spectroscopy and theoretical calculations, we report distinct spin-momentum-layer locking phenomena in a centrosymmetric, layered material, BiOI. The measured spin is highly polarized along the Brillouin zone boundary, while the same effect almost vanishes around the zone center due to its nonsymmorphic crystal structure. Our work demonstrates the existence of momentum-dependent hidden spin polarization and uncovers the microscopic mechanism of spin, momentum, and layer locking to each other, thus shedding light on the design metrics for future spintronic materials.

DOI: 10.1103/PhysRevLett.127.126402

Introduction.—Strategies for generating and controlling highly spin-polarized electronic states in nonmagnetic solids have been explored extensively, taking a crucial step towards the realization of novel spintronic devices [1–6]. It is generally believed that such processes require breaking the space inversion symmetry. This is because a combination of both time-reversal and inversion symmetries inevitably yields spin-degenerate energy levels; further, a spin splitting induced by the spin-orbit coupling (SOC) Hamiltonian [7] is typically classified as the Dresselhaus type [8] or Rashba type [9], according to the specific form of inversion symmetry breaking. Recently published studies have indicated that local symmetry breaking (e.g., polar field) within a part of a unit cell (termed as a “sector”) can intrinsically lead to a form of “hidden spin polarization” (HSP) in most centrosymmetric crystals [10,11]. The global inversion symmetry ensures the existence of an inversion counterpart for a given sector, manifesting exactly opposite HSP and thus leading to spin-degenerate energy bands in the momentum space. However, in the real space, there are indeed spin polarizations localized on both sectors [11–14]. Instead of the arbitrary choices of sector partition in a centrosymmetric

system (the wave function basis according to different choices of sectors can be connected by a unitary transformation), when an individual part is predominantly detected by the probe, the partition of the whole unit cell into sectors is naturally selected. As a result, the choice for the sector could be a van der Waals layer (e.g., in bulk WSe₂ [15]), a sublattice [16], or even an atomic layer (e.g., Se in the PtSe₂ monolayer [17]), and the corresponding HSP effect can be measured by spin- and angle-resolved photoemission spectroscopy (spin-ARPES) [15,17–24] as well as by polarized optical measurements [25–27]. Hence, the experimental evidence of HSP have been reported based on various layered materials such as bulk and monolayer transition metal dichalcogenides [15,17,18,22], BaNiS₂ [20], LaO_{0.55}F_{0.45}BiS₂ [23], and Bi2212 cuprate superconductor [24].

Exploring different quantum materials with strong HSP effects could considerably expand the choice of materials for nonmagnetic spintronic devices. However, while the local symmetry breaking in the real space is the essential characteristic of the HSP, its underlying physics, involving the microscopic mechanism of the way the spin, momentum,

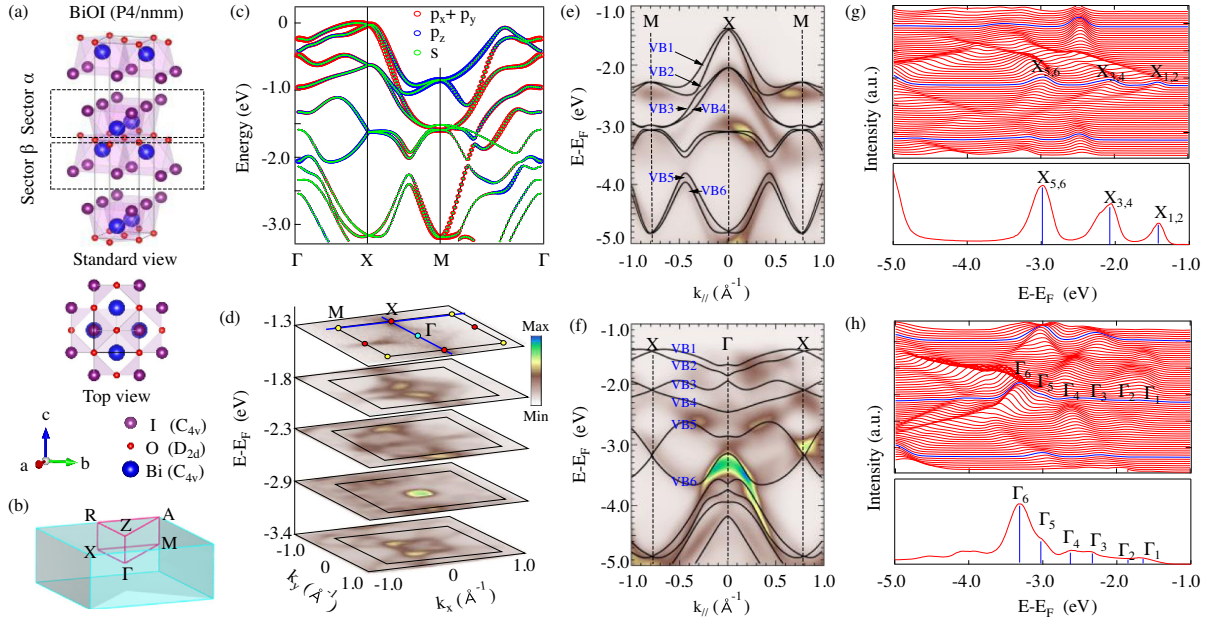


FIG. 1. (a) The crystal structure of BiOI. The unit cell consists of two BiI layers as inversion partners, labeled as a sector α and β . (b) The bulk Brillouin zone. (c) DFT-calculated bulk band dispersion with orbital projection. (d) ARPES-measured CECs of the valence bands at different energies. (e), (f) ARPES-measured spectra along the $X-M$ and $\Gamma-X$ high symmetry lines, overlaid by DFT calculated dispersions (solid black lines). (g), (h) EDCs corresponding to the spectra shown in (e) and (f), respectively. The lower parts are the EDCs at the X and Γ points, respectively, from which one can resolve the spectral peaks corresponding to the top six valence bands.

and sector lock to each other, remains elusive. Recent theoretical works predicted that the magnitude of the HSP effect is distinct around the Brillouin zone (BZ) center and the BZ boundary [16]. Here, by using systematic spin-ARPES measurements, we have investigated the electronic structure and particularly, the spin polarization of a single crystal BiOI with nonsymmorphic symmetry. We have observed up to 80% net spin polarization along the BZ boundary ($X-M$) but almost zero net spin polarization around Γ , indicating a unique momentum dependence of the HSP effect. Our tight-binding (TB) model, as well as density functional theory (DFT) calculations, revealed that in contrast to the Γ point, the nonsymmorphic symmetry minimizes the spin compensation between adjacent sectors at the BZ boundary, thus successfully retaining the local spin polarization of each sector. Our findings reveal the delicate interplay between spin-momentum-sector locking and symmetry protection in HSP systems, thus shedding light on the possibility of all-electrical manipulation.

Electronic structure.—BiOI is an ideal semiconductor, with the Fermi level being easily tunable by doping; therefore, it has been extensively used in the visible light photocatalysis studies [28]. BiOI has a tetragonal crystal structure with a centrosymmetric space group $P4/nmm$ containing nonsymmorphic operations of a glide mirror $\{M_z | (\frac{1}{2}, \frac{1}{2}, 0)\}$ and two screw axes $\{C_{2x} | (\frac{1}{2}, 0, 0)\}$, $\{C_{2y} | (0, \frac{1}{2}, 0)\}$. The inversion center is located in the middle of two inequivalent O atoms (site point group D_{2d}), while the Bi and I atoms occupy the noncentrosymmetric polar sites with the site point

group C_{4v} . The polyhedrons coordinated by Bi and I atoms are intersected by the O plane. Hence, the quasi-2D unit cell is divided into two sectors α and β , respectively, as shown in Fig. 1(a). The global centrosymmetric structure creates opposite local polar fields along the c axis felt by each BiI layer, which is a prerequisite for the HSP effect [16].

The BZ and DFT-calculated electronic structures of BiOI with SOC are shown in Figs. 1(b) and 1(c) [29]. The valence band maximum (VBM) is close to the X point. It is noticeable that at the points X and M , the glide reflection symmetry $\{M_z | (\frac{1}{2}, \frac{1}{2}, 0)\}$ anticommutes with the inversion operator, leading to an extra twofold degeneracy between two pairs of Kramer's degeneracy, i.e., fourfold degeneracy including the spin. Such a fourfold degeneracy is maintained along the entire $X-M$ line in the absence of SOC [29]. Thus, the band splitting along the $X-M$ line shown in Fig. 1(c) is caused by SOC solely. In analogy to the conventional Rashba-Dresselhaus effect, such a splitting is composed of two sets of spin splitting bands originating from the sectors α and β [16]. In comparison, the splitting along the $\Gamma-X$ line is contributed by both the orbital repulsions and the SOC effect, and is thus larger than that along the $X-M$ line. The orbital projection analysis shows that in the vicinity of the points Γ and X , the top two valence bands (designated as VB1 and VB2) are mainly composed of the $p_x + p_y$ and s orbitals, while VB3-VB6 are dominated by the p_z and s orbitals.

The high quality BiOI samples in this study has been confirmed by core-level photoemission spectroscopy and

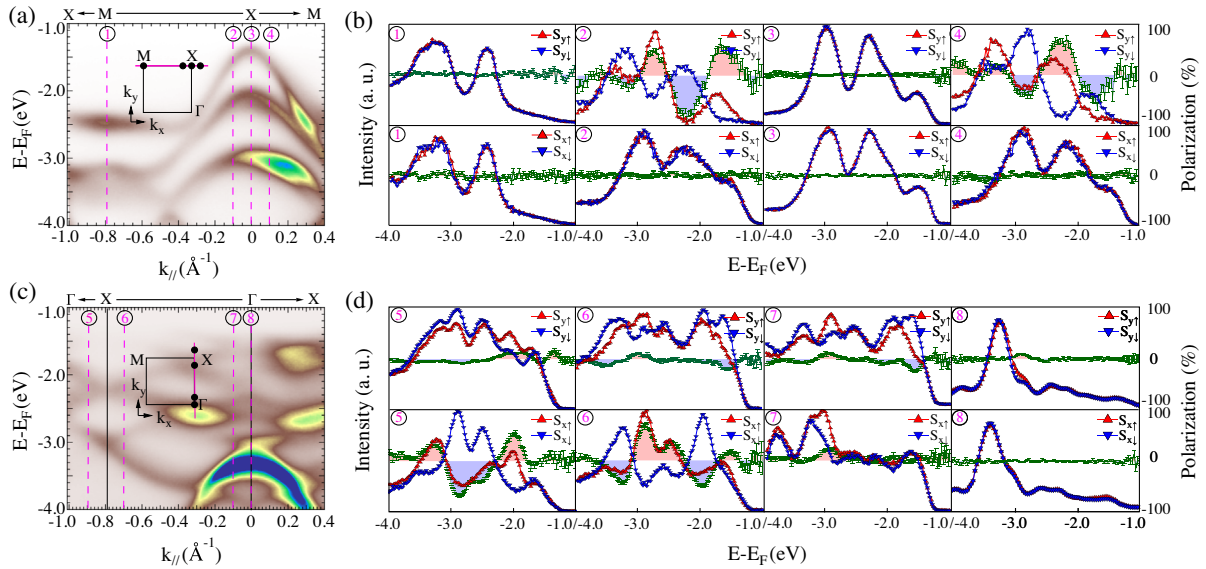


FIG. 2. (a),(c) Band dispersion along the $M - X$ and $\Gamma - X$ directions, respectively. The inset shows the BZ, with black dots indicating the momentum positions where the spin-resolved EDCs are measured. (b),(d) Spin-resolved EDCs and spin polarizations. Each panel's number corresponds to the momentum point denoted by the pink dashed lines in (a),(c). The green curves present the spin polarizations with statistical error bars proportional to $1/\sqrt{N}$, where N is the photoemission intensity.

x-ray diffraction [29]. The electronic structures of BiOI obtained by both DFT calculation and ARPES measurement [29] consistently show a 2D behavior with a relatively flat dispersion along the c axis. The ARPES results measured at a photon energy of 65 eV are shown in Fig. 1(d) [constant energy contours (CECs)], Figs. 1(e) and 1(f) (band dispersions) and Figs. 1(g) and 1(h) [energy-distribution curves (EDCs)]. As evident from our systematic photon energy-dependent measurement [29], this photon energy covers the 6th bulk Γ point, and a squarelike CEC exists at -1.3 eV, with corners located at X points. As the energy decreases, the CEC features at the X point expand and eventually form contours surrounding the M point, merging with those centered at the Γ point. This holelike behavior is presented in the ARPES spectra along the $M - X - M$ line in Fig. 1(e). From the CECs and spectra results, we have found that the VBM is located around the bulk X point, ~ 1.4 eV below the experimental Fermi level.

By directly comparing the calculated bulk band structure with the ARPES data shown in Figs. 1(e) and 1(f), a good agreement is found, indicating that the surface effect that breaks the global inversion symmetry is relatively weak. The predicted fourfold degeneracy at the X and M points and the splitting twofold degenerate branches (VB1 to VB6) away from X and M are all supported by the ARPES measured dispersion. Furthermore, Figs. 1(g) and 1(h) show the EDCs measured along the $M - X - M$ and $X - \Gamma - M$ directions. At the X point, the degenerate peaks, i.e., $X_{1,2}$, $X_{3,4}$, and $X_{5,6}$ are unambiguously present, while at the Γ point, each of the degenerate peak splits into two individual peaks, i.e., Γ_1 to Γ_6 . Consequently, three

pairs of Rashba-like hole-type valence bands are formed at the X and M points, with the band crossing points located around -1.4 , -2.1 , and -3.0 eV for the X point, respectively [Fig. 1(e)]. These results agree well with our calculation that only the time-reversal invariant momenta at the BZ boundary (e.g., the X point) demonstrate a fourfold degeneracy, while the Γ point does not exhibit such behavior, thus confirming the nonsymmorphic feature of the material. We next use spin-ARPES measurements to further demonstrate that the HSP effects for two high-symmetry points (X and M) are clearly distinguishable.

Hidden spin polarization.—Figure 2 presents the in-plane spin polarization of BiOI measured by spin ARPES using photon energies of 65 eV for panels (a),(b) and 30 eV for panels (c),(d). Moreover, the spin-polarized EDCs from the horizontal $X - M$ direction, vertical $\Gamma - X$ direction, and horizontal $\Gamma - X$ direction are measured comprehensively as displayed in Ref. [29]. The wide-ranging measurements involving different photon energies and geometries verified that the observed spin polarization and spin textures are essentially intrinsic. The representative spin EDCs for the three pairs of twofold degenerate bands VB1–VB6 are shown in Figs. 2(b) and 2(d), with the upper (lower) row showing the spin-resolved EDCs and the corresponding S_y (S_x) spin component. At three time-reversal invariant points M , X , and Γ (momentum points ①, ③ and ⑥), the spin-resolved EDCs overlap, indicating negligible spin polarization; this is consistent with the spin degeneracy originating from Kramer's pairs.

When the momenta moved away from the X point, we have observed significant spin polarization (up to 80%) along both k_x and k_y directions (momentum points ②, ④, ⑤

and ⑥ [37]). For momenta ⑤ and ⑥, nearly all the six VBs were resolved as the individual polarizations peaked with opposing polarization signs in each pair. This is because the band splitting along $\Gamma - X$ direction was more significant compared to the splitting along the $X - M$ direction [Figs. 1(c), 1(e), and 1(f)]. In sharp contrast, the spin polarization surrounding the Γ point was very weak ($<30\%$) for momentum point ⑦ and [29], along both k_x and k_y directions. It is worth noting that, for all the spin-resolved EDCs shown in Figs. 2(b) and 2(d), the sums of each pair as spin-integrated EDCs coincide with EDCs measured by regular ARPES in the overall spectral shape [29], a proof of accuracy and self-consistency of our measurement.

Because of the short photoelectron escape depth, $\sim 5 \text{ \AA}$ [38], for the photoelectron kinetic energies of 20–100 eV, and a large lattice constant $c = 9.12 \text{ \AA}$ [39], the detected photoemission signal mainly arises from the topmost sector (α) of the cleaved BiOI single crystal, which is favorable to detect the spin polarization from a local sector. Compared with the previous measurements of HSP materials such as WSe_2 [15], PtSe_2 [17], $\text{LaO}_{0.55}\text{F}_{0.45}\text{BiS}_2$ [23], and Bi_{2212} [24], which focus on the spin-momentum locking around a single high-symmetry point, our work revealed the distinct polarization features surrounding different high-symmetry points, i.e., BZ center (Γ) and BZ boundary (X), and observed a sharp contrast between them. Such observations suggest that momentum-dependent spin polarization originates from the HSP rather than merely from the surface potential gradient; further, these observations suggest the key factors affecting the HSP effect, such as the non-symorphic symmetry and orbital characters.

Spin-momentum-layer locking.—In addition to the momentum dependence and high spin polarization, there is another feature of the HSP at the X point, namely, the spin texture that is localized on the measured sector, manifesting a novel way of spin-momentum-layer locking [40–42]. As shown in Fig. 2 and Ref. [29], for the horizontal $M - X$ line and horizontal $\Gamma - X$ line, the S_y component is strong, while the S_x component vanishes. Similarly, for the vertical $\Gamma - X$ line, the S_x component is strong, while the S_y component vanishes. Since the S_z component is considerably less intense than the in-plane ones [29], this finding indicates a perpendicular spin orientation to the wave vector lying in the $k_x - k_y$ plane. We have further confirmed the specific spin texture for all the three pairs of valance bands, as illustrated in Figs. 3(a) and 3(b); note that only the spin textures of VB1, VB3, and VB5 are shown in Fig. 3(b), while the spin orientations of VB2, VB4, and VB6 are opposite to their counterparts. Surprisingly, while the VB1-2 pair shows a weak spin polarization, VB3-4 and VB5-6 pairs exhibit Dresselhaus-type spin textures with large magnitude, rather than the Rashba spin polarization induced by the local polar field.

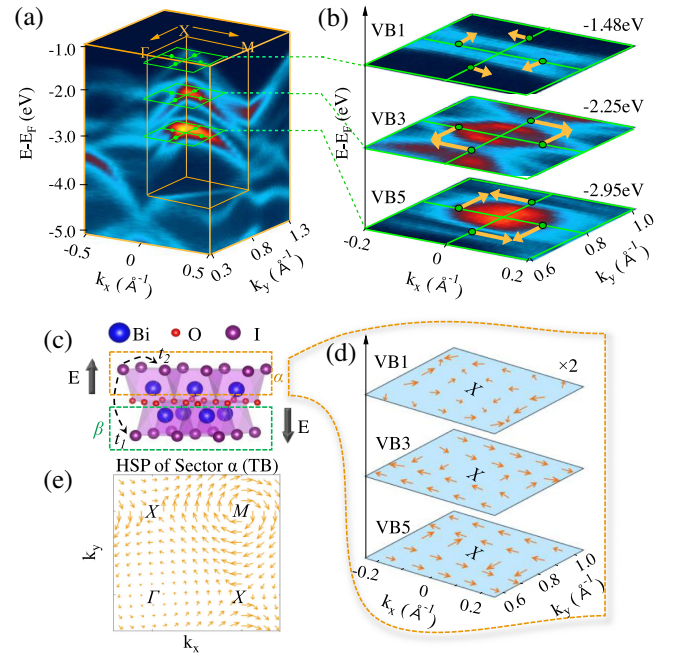


FIG. 3. (a) Overview of ARPES-measured spectra of BiOI plotted in the $k_x - k_y - E$ space. (b) Schematic sketch of the measured spin textures of VB1, VB3, and VB5 by spin ARPES, with the momentum cross sections denoted by the green squares in panel (a). (c) The layered structure of BiOI with two BiI sectors experiencing opposite local dipole fields (black arrows). (d) DFT calculation for p_z -projected HSP of VB1, VB3, and VB5 around X for the sector α . The spin magnitude of VB1 is multiplied by a factor of 2. (e) Spin texture for the sector α calculated by our tight-binding model, showing Dresselhaus and Rashba type HSP effects for X and M , respectively.

Here we employed the p -polarization geometry, where the vector potential of the incident photon lies on the incidence plane. Based on the dipole selection rule [43,44], the p_x and p_z orbitals are selectively detected. Furthermore, by changing the incidence angle of photons, one can change the ratio of the vector potential components parallel (A_{\parallel}) and perpendicular (A_{\perp}) to the sample surface. The dipole transition matrix element for the p_z (p_x) orbital is in proportion to the magnitude of the A_{\perp} (A_{\parallel}) component, and A_{\perp} is larger than A_{\parallel} in the present geometry. In our orbital-projected band calculation in Fig. 1(c), the VB3-6 bands at the X point and the VB1-2 bands at the M point are mainly derived from the p_z orbital. Therefore, we have performed DFT calculations on the p_z -projected spin textures localized on the top BiI layer, i.e., sector α , as shown in Figs. 3(c) and 3(d). We found qualitative agreement with the counterparts measured by spin ARPES in Fig. 3(b). All three VB pairs exhibited weak spin polarization ($<20\%$) around the Γ point [29]. As shown in Fig. 3(d), in the vicinity of X , only the VB1-2 pair manifested very weak spin polarization due to the tiny contribution of the p_z orbital of these bands [see Fig. 1(c)]. In comparison, the spin textures of VB3-4 and VB5-6 around X exhibited a

Dresselhaus type pattern with considerable magnitude. Moreover, the spin patterns of VB3 and VB5 are opposite to each other, which also agrees with the experiment. Thus, we have concluded that the DFT results successfully reproduce the features of the experimental observations, confirming the fact that the measured spin polarization originates from the intrinsic HSP in BiOI.

To further understand the mechanism of the momentum-dependent HSP effect and the corresponding spin-momentum locking, especially the Dresselhaus spin textures at the X point, we have constructed a single-orbital tight-binding model of a nonsymmorphic $P4/nmm$ structure. Two p_z orbitals of the iodine atoms on the adjacent sectors α and β , connected by the glide mirror operation $\{M_z | (\frac{1}{2}, \frac{1}{2}, 0)\}$, were chosen, as shown in Fig. 3(c). Under the basis of $\{|\alpha\uparrow\rangle, |\alpha\downarrow\rangle, |\beta\uparrow\rangle, |\beta\downarrow\rangle\}$, the model Hamiltonian can be written as [16]

$$H(k) = t_1 \cos \frac{k_x}{2} \cos \frac{k_y}{2} \tau_x \otimes \sigma_0 + t_2 (\cos k_x + \cos k_y) \tau_0 \otimes \sigma_0 + \lambda \tau_z \otimes (\sigma_y \sin k_x - \sigma_x \sin k_y). \quad (1)$$

Here, τ and σ are Pauli matrices under the basis of $\{|\alpha\rangle, |\beta\rangle\}$ and $\{|\uparrow\rangle, |\downarrow\rangle\}$, respectively; t_1 (t_2) is the intersector (intrasector) electron hopping that contributes to the Hamiltonian's diagonal (off-diagonal) terms. The third term of Eq. (1) describes the SOC effect induced by the local symmetry breaking for each sector, parametrized by λ . It is noticeable that at the boundary of the BZ, e.g., the $X-M$ line, Eq. (1) naturally becomes block diagonal for $\{|\alpha\uparrow\rangle, |\alpha\downarrow\rangle\}$ and $\{|\beta\uparrow\rangle, |\beta\downarrow\rangle\}$, having opposite local spin polarizations for each sector. When the probe sees sector α predominately, i.e., after breaking the symmetry between α and β , Eq. (1) is naturally decomposed into two matrices for each sector, and thus, the HSP of the sector α is measurable. In contrast, the HSP effect is substantially suppressed around the Γ point due to the intersector coupling t_1 term, as shown in Fig. 3(e), leading to the negligible spin signal measured from spin ARPES. We note that besides nonsymmorphic symmetry, the inclusion of multiple orbitals (such as three p orbitals) could lead to a different type of interference effect that modulates the momentum-dependent spin polarization [16,24].

Our tight-binding model also helps to understand the specific spin textures around different high-symmetry momenta. The low-energy effective $k \cdot p$ Hamiltonian derived from Eq. (1) has the form of $(k_x \sigma_y - k_y \sigma_x) \tau_z$ at M and $(k_x \sigma_y + k_y \sigma_x) \tau_z$ at X , indicating Rashba and Dresselhaus type HSP, respectively, and the latter perfectly explaining the measured spin polarization around the X point. Such results indicate that although a (local) polar field existing in a crystal in general supports a (hidden) Rashba-type spin polarization, a (hidden) Dresselhaus-type spin polarization would also be accompanied [11], depending on the specific symmetry of given momenta.

In summary, combining spin-ARPES measurements and theoretical calculations, we report distinct spin-momentum-layer locking phenomena at different BZ positions in a centrosymmetric material BiOI. The measured spin polarization localized on a specific BiI layer is highly polarized along the BZ boundary but almost vanishes around the zone center due to its nonsymmorphic crystal structure. The layer-resolved spin texture, either Rashba or Dresselhaus type, reflects the symmetry of both real space and k space. Our findings experimentally demonstrate the existence of the HSP effect and shed light on the design metrics to utilize high spin polarization in centrosymmetric materials by revealing the intimate interplay between spin, orbital, and layer degrees of freedom.

This work is supported by National Natural Science Foundation of China (NSFC) (Grants No. 11874195 and No. 12074163), the Shenzhen High-level Special Fund (Grants No. G02206304, No. G02206404), the Guangdong Innovative and Entrepreneurial Research Team Program (Grant No. 2019ZT08C044), the Shenzhen Science and Technology Program (Grant No. KQTD20190929173815000), the Innovative Team of High School in Guangdong Province (Grant No. 2020KCXTD001), Guangdong Provincial Key Laboratory for Computational Science and Material Design under Grant No. 2019B030301001, JSPS KAKENHI Grants No. 18H01954 and the Center for Computational Science and Engineering of Southern University of Science and Technology. ARPES and spin-ARPES measurements were performed with the approval of the Proposal Assessing Committee of the Hiroshima Synchrotron Radiation Center (Proposals No. 19AG004, No. 19BG014). We would also like to thank the N-BARD, Hiroshima University for supplying liquid He.

*These authors contributed equally to this work.

[†]kshimada@hiroshima-u.ac.jp

[‡]chency@sustech.edu.cn

[§]liuqh@sustech.edu.cn

- [1] S. Datta and B. Das, Electronic analog of the electro-optic modulator, *Appl. Phys. Lett.* **56**, 665 (1990).
- [2] I. Žutić, J. Fabian, and S.D. Sarma, Spintronics: Fundamentals and applications, *Rev. Mod. Phys.* **76**, 323 (2004).
- [3] H. C. Koo, J. H. Kwon, J. Eom, J. Chang, S. H. Han, and M. Johnson, Control of spin precession in a spin-injected field effect transistor, *Science* **325**, 1515 (2009).
- [4] A. Manchon, H. C. Koo, J. Nitta, S. Frolov, and R. Duine, New perspectives for Rashba spin-orbit coupling, *Nat. Mater.* **14**, 871 (2015).
- [5] A. Soumyanarayanan, N. Reyren, A. Fert, and C. Panagopoulos, Emergent phenomena induced by spin-orbit coupling at surfaces and interfaces, *Nature (London)* **539**, 509 (2016).

- [6] X. Lin, W. Yang, K.L. Wang, and W. Zhao, Two-dimensional spintronics for low-power electronics, *National electronics review* **2**, 274 (2019).
- [7] *Spin-Orbit Coupling in Two-Dimensional Electron and Hole Systems*, edited by R. Winkler, S. Papadakis, E. De Poortere, and M. Shayegan (Springer, New York, 2003).
- [8] G. Dresselhaus, Spin-orbit coupling effects in zinc blende structures, *Phys. Rev.* **100**, 580 (1955).
- [9] E.I. Rashba, Properties of semiconductors with an extremum loop. 1. Cyclotron and combinational resonance in a magnetic field perpendicular to the plane of the loop, *Sov. Phys. Solid State* **2**, 1109 (1960), <https://www.elibrary.ru/item.asp?id=21757915>.
- [10] Q. Liu, Y. Guo, and A. J. Freeman, Tunable Rashba effect in two-dimensional LaOBiS₂ films: Ultrathin candidates for spin field effect transistors, *Nano Lett.* **13**, 5264 (2013).
- [11] X. Zhang, Q. Liu, J.-W. Luo, A. J. Freeman, and A. Zunger, Hidden spin polarization in inversion-symmetric bulk crystals, *Nat. Phys.* **10**, 387 (2014).
- [12] L. Yuan, Q. Liu, X. Zhang, J.-W. Luo, S.-S. Li, and A. Zunger, Uncovering and tailoring hidden Rashba spin-orbit splitting in centrosymmetric crystals, *Nat. Commun.* **10**, 906 (2019).
- [13] Q. Liu, X. Zhang, and A. Zunger, Intrinsic Circular Polarization in Centrosymmetric Stacks of Transition-Metal Dichalcogenide Compounds, *Phys. Rev. Lett.* **114**, 087402 (2015).
- [14] Q. Liu, X. Zhang, H. Jin, K. Lam, J. Im, A. J. Freeman, and A. Zunger, Search and design of nonmagnetic centrosymmetric layered crystals with large local spin polarization, *Phys. Rev. B* **91**, 235204 (2015).
- [15] J.M. Riley, F. Mazzola, M. Dendzik, M. Michiardi, T. Takayama, L. Bawden, C. Granerød, M. Leandersson *et al.*, Direct observation of spin-polarized bulk bands in an inversion-symmetric semiconductor, *Nat. Phys.* **10**, 835 (2014).
- [16] Y. Zhang, P. Liu, H. Sun, S. Zhao, H. Xu, and Q. Liu, Symmetry-assisted protection and compensation of hidden spin polarization in centrosymmetric systems, *Chin. Phys. Lett.* **37**, 087105 (2020).
- [17] W. Yao, E. Wang, H. Huang, K. Deng, M. Yan, K. Zhang, K. Miyamoto, T. Okuda *et al.*, Direct observation of spin-layer locking by local Rashba effect in monolayer semiconducting PtSe₂ film, *Nat. Commun.* **8**, 14216 (2017).
- [18] M. Gehlmann, I. Aguilera, G. Bihlmayer, E. Młyńczak, M. Eschbach, S. Döring, P. Gospodarič, S. Cramm *et al.*, Quasi 2D electronic states with high spin-polarization in centrosymmetric MoS₂ bulk crystals, *Sci. Rep.* **6**, 26197 (2016).
- [19] K. Deng, M. Yan, C.-P. Yu, J. Li, X. Zhou, K. Zhang, Y. Zhao, K. Miyamoto *et al.*, Crossover from 2D metal to 3D Dirac semimetal in metallic PtTe₂ films with local Rashba effect, *Sci. Bull.* **64**, 1044 (2019).
- [20] D. Santos-Cottin, M. Casula, G. Lantz, Y. Klein, L. Petaccia, P. Le Fèvre, F. Bertran, E. Papalazarou, M. Marsi, and A. Gauzzi, Rashba coupling amplification by a staggered crystal field, *Nat. Commun.* **7**, 11258 (2016).
- [21] J. Tu, X. Chen, X. Ruan, Y. Zhao, H. Xu, Z. Chen, X. Zhang, X. Zhang *et al.*, Direct observation of hidden spin polarization in 2H-MoTe₂, *Phys. Rev. B* **101**, 035102 (2020).
- [22] E. Razzoli, T. Jaouen, M.-L. Mottas, B. Hildebrand, G. Monney, A. Pisoni, S. Muff, M. Fanciulli *et al.*, Selective Probing of Hidden Spin-Polarized States in Inversion-Symmetric Bulk MoS₂, *Phys. Rev. Lett.* **118**, 086402 (2017).
- [23] S.-L. Wu, K. Sumida, K. Miyamoto, K. Taguchi, T. Yoshikawa, A. Kimura, Y. Ueda, M. Arita *et al.*, Direct evidence of hidden local spin polarization in a centrosymmetric superconductor LaO_{0.55}F_{0.45}BiS₂, *Nat. Commun.* **8**, 1919 (2017).
- [24] K. Gottlieb, C.-Y. Lin, M. Serbyn, W. Zhang, C. L. Smallwood, C. Jozwiak, H. Eisaki, Z. Hussain, A. Vishwanath, and A. Lanzara, Revealing hidden spin-momentum locking in a high-temperature cuprate superconductor, *Science* **362**, 1271 (2018).
- [25] R. Suzuki, M. Sakano, Y. Zhang, R. Akashi, D. Morikawa, A. Harasawa, K. Yaji, K. Kuroda *et al.*, Valley-dependent spin polarization in bulk MoS₂ with broken inversion symmetry, *Nat. Nanotechnol.* **9**, 611 (2014).
- [26] R. Oliva, T. Woźniak, F. Dybala, J. Kopaczek, P. Scharoch, and R. Kudrawiec, Hidden spin-polarized bands in semiconducting 2H-MoTe₂, *Mater. Res. Lett.* **8**, 75 (2020).
- [27] Y. Huang, A. Yartsev, S. Guan, L. Zhu, Q. Zhao, Z. Yao, C. He, L. Zhang *et al.*, Hidden spin polarization in the centrosymmetric MoS₂ crystal revealed via elliptically polarized terahertz emission, *Phys. Rev. B* **102**, 085205 (2020).
- [28] M. Arumugam and M. Y. Choi, Recent progress on bismuth oxyiodide (BiOI) photocatalyst for environmental remediation, *J. Ind. Eng. Chem.* **81**, 237 (2020).
- [29] See Supplemental Material at <http://link.aps.org/supplemental/10.1103/PhysRevLett.127.126402> for theoretical and experimental methods, DFT calculated bands of BiOI, sample characterization, photon energy dependent ARPES results, spin polarizations along vertical and horizontal $\Gamma - X$ lines, spin components along the $\Gamma - X$ and $M - X$ directions, out-of-plane spin polarization, and spin textures of six valence bands in the first BZ, which includes Refs. [11,16,28,30–36].
- [30] *Very High Resolution Photoelectron Spectroscopy*, edited by S. Hüfner (Springer, New York, 2007).
- [31] H. Iwasawa, K. Shimada, E. Schwier, M. Zheng, Y. Kojima, H. Hayashi, J. Jiang, M. Higashiguchi *et al.*, Rotatable high-resolution ARPES system for tunable linear-polarization geometry, *J. Synchrotron Radiat.* **24**, 836 (2017).
- [32] T. Okuda, K. Miyamoto, H. Miyahara, K. Kuroda, A. Kimura, H. Namatame, and M. Taniguchi, Efficient spin resolved spectroscopy observation machine at Hiroshima Synchrotron Radiation Center, *Rev. Sci. Instrum.* **82**, 103302 (2011).
- [33] G. Kresse and D. Joubert, From ultrasoft pseudopotentials to the projector augmented-wave method, *Phys. Rev. B* **54**, 11169 (1996).
- [34] P. Hohenberg and W. Kohn, Inhomogeneous electron gas, *Phys. Rev. B* **136**, B864 (1964).
- [35] W. Kohn and L. J. Sham, Self-consistent equations including exchange and correlation effects, *Phys. Rev.* **140**, A1133 (1965).
- [36] G. Kresse and D. Joubert, From ultrasoft pseudopotentials to the projector augmented-wave method, *Phys. Rev. B* **59**, 1758 (1999).

- [37] We note that a trade-off between the measurement efficiency and energy resolution in the spin-ARPES measurement must be considered. We have chosen the current resolution configuration to experiment within a reasonable time, consequently sacrificing the ability to resolve all the individual VB peaks in spin-resolved EDCs.
- [38] C. J. Powell, A. Jablonski, I. Tilinin, S. Tanuma, and D. R. Penn, Surface sensitivity of Auger-electron spectroscopy and X-ray photoelectron spectroscopy, *J. Electron Spectrosc. Relat. Phenom.* **98–99**, 1 (1999).
- [39] C. Yu, C. Fan, C. Y. Jimmy, W. Zhou, and K. Yang, Preparation of bismuth oxyiodides and oxides and their photooxidation characteristic under visible/UV light irradiation, *Mater. Res. Bull.* **46**, 140 (2011).
- [40] A. M. Jones, H. Yu, J. S. Ross, P. Klement, N. J. Ghimire, J. Yan, D. G. Mandrus, W. Yao, and X. Xu, Spin-layer locking effects in optical orientation of exciton spin in bilayer WSe₂, *Nat. Phys.* **10**, 130 (2014).
- [41] X. Xu, W. Yao, D. Xiao, and T. F. Heinz, Spin and pseudospins in layered transition metal dichalcogenides, *Nat. Phys.* **10**, 343 (2014).
- [42] X. Xi, Z. Wang, W. Zhao, J.-H. Park, K. T. Law, H. Berger, L. Forró, J. Shan, and K. F. Mak, Ising pairing in superconducting NbSe₂ atomic layers, *Nat. Phys.* **12**, 139 (2016).
- [43] A. Damascelli, Z. Hussain, and Z.-X. Shen, Angle-resolved photoemission studies of the cuprate superconductors, *Rev. Mod. Phys.* **75**, 473 (2003).
- [44] Y. Cao, J. Waugh, X. Zhang, J.-W. Luo, Q. Wang, T. Reber, S. Mo, Z. Xu *et al.*, Mapping the orbital wavefunction of the surface states in three-dimensional topological insulators, *Nat. Phys.* **9**, 499 (2013).

Half-Magnetic Topological Insulator with Magnetization-Induced Dirac Gap at a Selected Surface

Ruie Lu^{1,*}, Hongyi Sun^{1,*}, Shiv Kumar^{2,*}, Yuan Wang^{1,*}, Mingqiang Gu,¹ Meng Zeng¹, Yu-Jie Hao¹, Jiayu Li¹, Jifeng Shao,¹ Xiao-Ming Ma¹, Zhanyang Hao¹, Ke Zhang,² Wumiti Mansuer,² Jiawei Mei,¹ Yue Zhao¹, Cai Liu¹, Ke Deng¹, Wen Huang¹, Bing Shen³, Kenya Shimada², Eike F. Schwier^{2,†}, Chang Liu^{1,‡}, Qihang Liu^{1,4,§} and Chaoyu Chen^{1,||}

¹Shenzhen Institute for Quantum Science and Engineering (SIQSE) and Department of Physics, Southern University of Science and Technology (SUSTech), Shenzhen 518055, China

²Hiroshima Synchrotron Radiation Centre, Hiroshima University, Higashi-Hiroshima, Hiroshima 739-0046, Japan

³School of Physics, Sun Yat-Sen University, Guangzhou 510275, China

⁴Guangdong Provincial Key Laboratory for Computational Science and Material Design, Southern University of Science and Technology, Shenzhen 518055, China



(Received 9 September 2020; revised 17 November 2020; accepted 13 January 2021; published 25 February 2021)

Topological magnets are a new family of quantum materials providing great potential to realize emergent phenomena, such as the quantum anomalous Hall effect and the axion-insulator state. Here, we present our discovery that the stoichiometric ferromagnet $\text{MnBi}_8\text{Te}_{13}$ with natural heterostructure $\text{MnBi}_2\text{Te}_4/(\text{Bi}_2\text{Te}_3)_3$ is an unprecedented “half-magnetic topological insulator,” with the magnetization existing at the MnBi_2Te_4 surface but not at the opposite surface terminated by triple Bi_2Te_3 layers. Our angle-resolved photoemission spectroscopy measurements unveil a massive Dirac gap at the MnBi_2Te_4 surface and a gapless Dirac cone on the other side. Remarkably, the Dirac gap (about 28 meV) at the MnBi_2Te_4 surface decreases monotonically with increasing temperature and closes right at the Curie temperature, thereby representing the first smoking-gun spectroscopic evidence of a magnetization-induced topological surface gap among all known magnetic topological materials. We further demonstrate theoretically that the half-magnetic topological insulator is desirable to realize the surface anomalous Hall effect, which serves as direct proof of the general concept of axion electrodynamics in condensed matter systems.

DOI: [10.1103/PhysRevX.11.011039](https://doi.org/10.1103/PhysRevX.11.011039)

Subject Areas: Condensed Matter Physics

I. INTRODUCTION

Magnetic topological insulators (TI) showcase quantum magnetism and nontrivial band topology, thereby providing a unique playground for exploring exotic quantum phenomena in condensed matter physics [1–16]. One

paradigmatic example is the so-called axion-insulator phase, which exhibits bulk topological magnetoelectric response with the phase angle $\theta = \pi$ protected by either inversion or time-reversal symmetry [10,15,16]. The resultant bulk-boundary correspondence is the predicted half-quantized surface Hall conductance $e^2/2h$ in the absence of an external magnetic field given that a magnetic gap exists at the surface. The intrinsic magnetic TI $\text{MnBi}_2\text{Te}_4/(\text{Bi}_2\text{Te}_3)_n$ ($n = 1, 2, 3, \dots$), comprising alternating layers of magnetic TI MnBi_2Te_4 and nonmagnetic TI Bi_2Te_3 , has the potential for realizing both the quantum anomalous Hall (QAH) insulator and the axion-insulator phases [1–4,17–22]. In principle, these compounds are ideal candidates for the inversion-preserved axion insulators with a persistent surface gap originating from the long-range magnetic order. However, it remains controversial whether the topological surface states (TSS) of $\text{MnBi}_2\text{Te}_4/(\text{Bi}_2\text{Te}_3)_n$ are gapped or gapless [23–31]. Recent angle-resolved photoemission spectroscopy (ARPES) measurements unexpectedly revealed an almost gapless surface Dirac cone in MnBi_2Te_4 and MnBi_2Te_4 termination of

*These authors contributed equally to this work.

†Corresponding author.

Eike.schwieger@physik.uni-wuerzburg.de

‡Corresponding author.

liuc@sustech.edu.cn

§Corresponding author.

liugh@sustech.edu.cn

||Corresponding author.

chency@sustech.edu.cn

Published by the American Physical Society under the terms of the [Creative Commons Attribution 4.0 International license](https://creativecommons.org/licenses/by/4.0/). Further distribution of this work must maintain attribution to the author(s) and the published article's title, journal citation, and DOI.

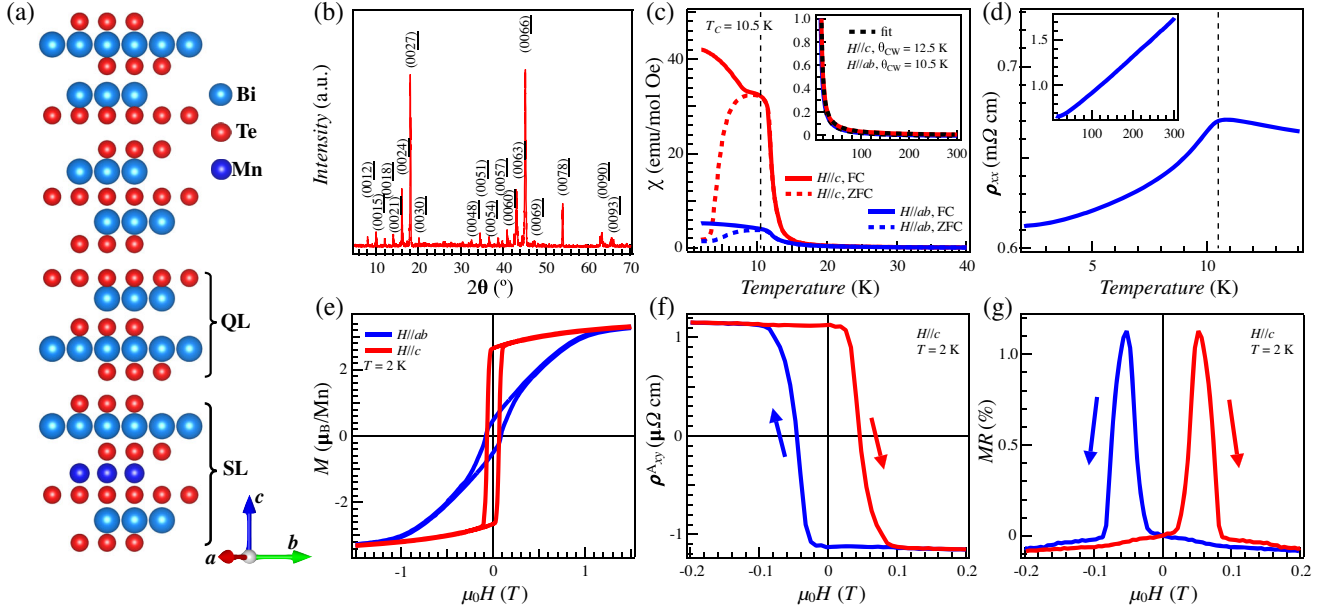


FIG. 1. Ferromagnetism and anomalous Hall effect in $\text{MnBi}_8\text{Te}_{13}$ single crystals. (a) Schematic crystal structure with one unit of -SL-QL-QL-QL- sequences. (b) Single-crystal x-ray diffraction result taken at 300 K. (c) Zero-field-cooled (ZFC, dashed line) and field-cooled (FC, solid line) magnetic susceptibility (χ) vs temperature (T) for magnetic field $H = 100$ Oe parallel to the ab plane (blue) and the c axis (red), respectively. The inset shows the Curie-Weiss fitting for a temperature range of 150 K–300 K. (d) Zero-field in-plane resistivity (ρ_{xx}) vs T . The inset shows the results up to 300 K. (e) Field-dependent magnetization hysteresis at 2 K for $H//ab$ (blue) and $H//c$ (red). (f) Field-dependent anomalous Hall resistivity (ρ_{xy}^A) at 2 K for $H//c$. (g) Field-dependent transverse resistivity change ($MR = [\rho_{xx}(H)/\rho_{xx}(0)] - 1$) at 2 K for $H//c$.

MnBi_4Te_7 [32–34], which may be attributed to reduced effective magnetic moments due to the extension of the surface states to the bulk [28,35]. On the other hand, various surface gaps have been reported in this material family [1,2,25,35], where the speculated mechanisms of the gap opening are from magnetization, hybridization, dephasing, Coulomb scattering, and so on. Furthermore, none of these reported gaps has been directly proved to originate from magnetic orders since they remain open within the high-temperature paramagnetic (PM) phase [25,35–37], which makes the realization of the axion-insulator phase obsolete.

Here, we conduct ARPES measurements on stoichiometric $\text{MnBi}_8\text{Te}_{13}$ [$\text{MnBi}_2\text{Te}_4/(\text{Bi}_2\text{Te}_3)_n$ with $n = 3$], with an intrinsic ferromagnetic (FM) ground state. At the MnBi_2Te_4 septuple-layer (SL) termination, we have directly revealed a surface gap of about 28 meV below the Curie temperature of $T_C = 10.5$ K, which decreases monotonically with increasing temperature and closes right at T_C to form a gapless Dirac cone, proving its magnetic nature. These results represent the first direct spectroscopic evidence of a magnetization-induced topological surface gap among all known magnetic topological materials. In sharp contrast, a gapless Dirac cone with negligible FM proximity is observed on the opposite surface terminated by the triple Bi_2Te_3 quintuple layers (QL), analogous to the situation in non-magnetic TI Bi_2Te_3 . Recalling that a typical magnetic TI manifests magnetic gaps at both surfaces (e.g., top and

bottom) perpendicular to the magnetic moment, here we refer to the ferromagnet $\text{MnBi}_8\text{Te}_{13}$ as a “half-magnetic TI,” in which the MnBi_2Te_4 SL surface is gapped by surface magnetization while the opposite triple- Bi_2Te_3 QL surface remains nonmagnetic and thus gapless. Utilizing density functional theory (DFT) calculations, we find half-QAH conductivity well localized at the SL termination, regardless of the cleavage of the other termination. Therefore, the half-magnetic TI provides an ideal platform for observing the half-QAH effect at a single surface and the related axion physics.

II. $\text{MnBi}_8\text{Te}_{13}$ SINGLE CRYSTAL WITH FM GROUND STATE

Single-crystal $\text{MnBi}_8\text{Te}_{13}$ has a trigonal structure [38], with a space group of $R\bar{3}m$. The lattice of $\text{MnBi}_8\text{Te}_{13}$ consists of one MnBi_2Te_4 SL and three Bi_2Te_3 QLs stacking alternately along the c axis [Fig. 1(a)]. These SLs or QLs are coupled through weak van der Waals (vdW) forces. Cleaving the single crystal perpendicular to the c axis could yield four possible terminations, namely, the S termination, Q termination, QQ termination, and QQQ termination. The crystallinity was examined by x-ray diffraction (XRD). As shown in Fig. 1(b), all of the diffraction peaks, particularly the low-angle ones, can be well indexed by the $(00l)$ reflections with lattice parameter $c \approx 132.6$ Å (calculated from the Rietveld

refinement of powder XRD, as shown in Fig. S1 in the Supplemental Material [39]), in agreement with previous work [40].

The temperature-dependent anisotropic magnetic susceptibility [Fig. 1(c)] shows Curie-Weiss (CW) behavior above 150 K (inset) with the characteristic temperature $\theta_{CW} = 12.5$ K and 10.5 K for $H//c$ and $H//ab$, respectively, through a fitting with $\chi(T) = \chi_0 + C/(T - \theta_{CW})$. Around $T_C = 10.5$ K, a FM transition was revealed by magnetic susceptibility [Fig. 1(c)] and resistivity measurements [Fig. 1(d)]. The frustration parameter (θ_{CW}/T_C) for $H//c$ was calculated to be about 2, indicating a moderate magnetic frustration. For $H//c$, the observed larger bifurcation between zero-field cooling (ZFC) and field cooling (FC) magnetization [Fig. 1(c)] and magnetic hysteresis loop [Fig. 1(e)] indicate an easy axis along the c axis and an Ising-type exchange interaction between adjacent Mn layers. The saturation moment $M_{sa} = 3.58 \mu_B/\text{Mn}$ is close to that of $3.56 \mu_B/\text{Mn}$ in MnBi_2Te_4 [41] and $3.5 \mu_B/\text{Mn}$ in MnBi_4Te_7 [29]. The above magnetic properties suggest a FM order with an out-of-plane magnetic moment configuration in $\text{MnBi}_8\text{Te}_{13}$, in contrast to the A-type AFM ground states found in other $\text{MnBi}_2\text{Te}_4/(\text{Bi}_2\text{Te}_3)_n$ compounds ($n = 0, 1, 2$) [42,43].

The field-dependent Hall resistivity [$\rho_{xy}(H)$] and magnetoresistivity [$\text{MR} = [\rho_{xx}(H)/\rho_{xx}(0)] - 1$] are shown in Figs. 1(f) and 1(g), as well as Fig. S3 in the Supplemental Material [39]. The negative slope of $\rho_{xy}(H)$ in Fig. S3(f) indicates electron-type carriers, and the obvious anomalous Hall effect is observed for $H//c$. In a ferromagnet, the Hall resistivity is described by the formula $\rho_{xy} = R_0 H + \rho_{xy}^A = R_0 H + R_s M$, where R_0 is the ordinary Hall coefficient, ρ_{xy}^A is the anomalous Hall resistivity, R_s is the anomalous Hall coefficient, and M is the magnetization. Above T_C (20 K), $\rho_{xy}(H)$ exhibits the same slope at all H [see Fig. S3(f)], indicating a constant R_0 , which allows us to subtract the ordinary Hall resistivity to obtain the anomalous part, as shown in Fig. 1(f). Note that R_s scales well with the M - H curve to the anomalous part of the Hall resistivity and is calculated to be $R_s = 1.76 \times 10^{-6} \text{ m}^3/\text{C}$, 2 orders of magnitude larger than $R_0 = 1.15 \times 10^{-8} \text{ m}^3/\text{C}$. Unlike the previous report [40], the MR from both increasing and decreasing field measurements maintains a near-vanishing value ($<0.1\%$) and exhibits sharp peaks without any overlap at the appearance of the anomalous Hall plateau. This feature is reminiscent of the MR behavior in Cr-doped $(\text{Bi}, \text{Sb})_2\text{Te}_3$ films when approaching the quantum anomalous Hall region [11,12].

III. GAPPED AND GAPLESS TSS DIRAC CONE IN $\text{MnBi}_8\text{Te}_{13}$

We employ a μ -laser-ARPES system [44], with a focused laser spot size of about $5 \mu\text{m}$, to measure the

termination-sensitive band structure of $\text{MnBi}_8\text{Te}_{13}$. Figures S4 and S5 present the spectra in a high-symmetry direction, as well as a set of constant energy contours for all four terminations. In Fig. 2, we highlight the band structure of the S termination and its opposite cleaving plane, the QQQ termination. Shown are spectra taken at 7 K and 20 K, which correspond to FM and PM phases, respectively. In the FM phase, the S termination shows an unambiguous energy gap of about 28 meV at the Dirac point [Fig. 2(c)], which is in sharp contrast to other Mn-Bi-Te family members such as MnBi_2Te_4 [30,32–34], MnBi_4Te_7 [24,30,36], and $\text{MnBi}_6\text{Te}_{10}$ [28,30], whose S terminations consistently show no apparent gap opening at the Dirac point below the magnetic transition [45]. Above T_C in the PM phase, a gapless Dirac cone is observed [Fig. 2(d)]. Comparison between the FM and PM phases suggests that the origin of the surface gap for the S termination is magnetism. The gap opening is captured by an effective massive Dirac Hamiltonian $H_{\text{surf}}(k) = (\sigma_x k_y - \sigma_y k_x) + m_{\text{eff}} \sigma_z$, where the first two terms describe a Dirac cone and the last the effective Zeeman field induced by the ferromagnetically ordered Mn atoms. The gap size, $m_{\text{eff}} \sim 28$ meV, is in qualitative agreement with our DFT prediction [Fig. 2(b)]. The detailed comparison between the DFT and the ARPES results is provided in Fig. S4.

At the QQQ termination, the gapless Dirac surface states appear to persist below T_C . At first sight, this case seems to contradict the broken time-reversal symmetry. However, given the considerable spatial separation between the top Bi_2Te_3 QL and the magnetic MnBi_2Te_4 SL, it is reasonable to assume a negligibly small effective Zeeman field for the surface states. Such a conjecture is indeed supported by our DFT calculation, which also reproduces the gapless Dirac cone despite a magnetic ground state [Fig. 2(f)]. Here, we note that the DFT surface-only spectra agree with the ARPES spectra better than the DFT bulk spectra, likely because of the limited photoemission probing depth [47]. Similar gapless Dirac cones have been observed by ARPES at the FM phase for both Q and QQ terminations, owing to the hybridization between the TSS and the bulk bands that buries the Dirac point [28], shown in Fig. S6. To sum up, $\text{MnBi}_8\text{Te}_{13}$ is a half-magnetic topological insulator. The time-reversal symmetry is broken at the S termination, which shows a temperature-dependent gap, while it is approximately preserved at the other surface, which shows a gapless state.

Furthermore, in contrast to the unambiguous temperature evolution of the TSS, we find the band-structure change of the bulk states between the FM [Fig. 2(c), 7 K] and PM [Fig. 2(d), 20 K] to be negligible, which is probably attributed to the reduced effective magnetic moments that the particular bulk band feels.

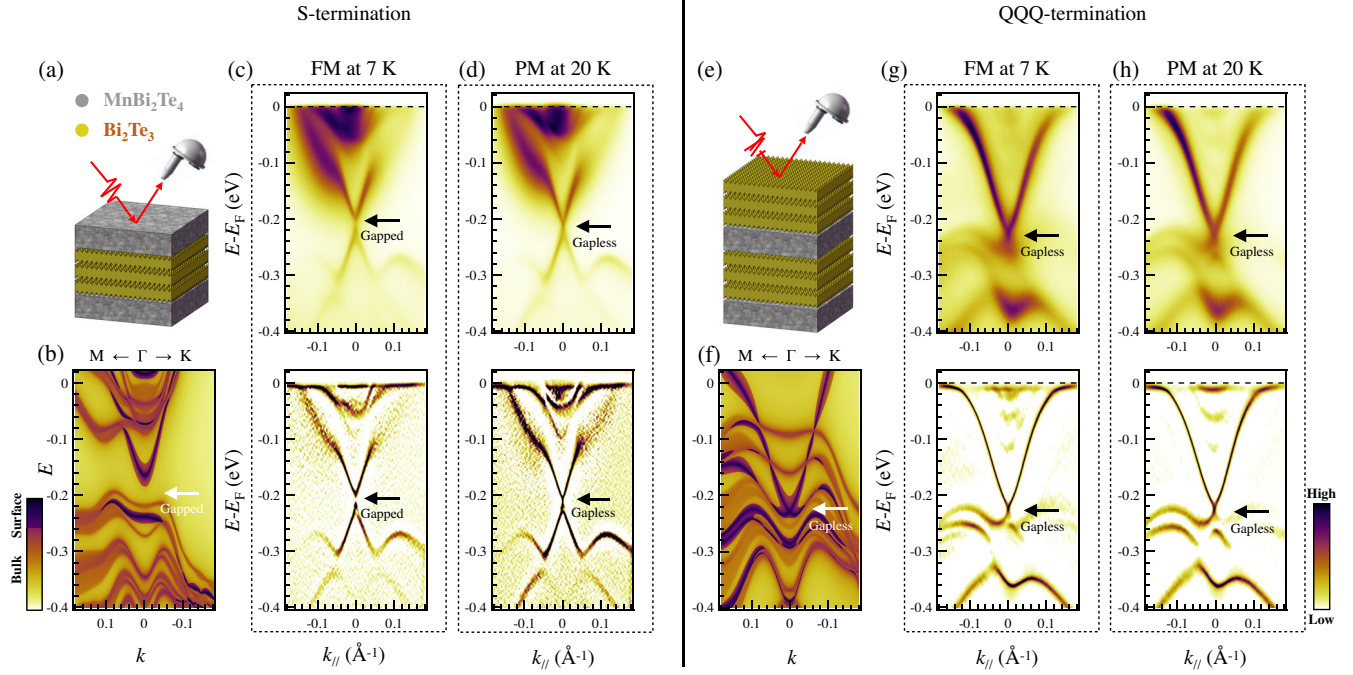


FIG. 2. Temperature evolution of the TSS Dirac cone gap at the S and QQQ termination of $\text{MnBi}_8\text{Te}_{13}$. (a)–(d) ARPES results for the S termination. (a) Schematic structural stacking configuration of the S termination. (b) DFT band structure calculated for the FM state, with the surface-only states (dark violet to black) being superposed on the bulk states (yellow, orange, and light violet). (c) Band structure along $\bar{M} - \bar{\Gamma} - \bar{M}$ measured at 7 K (FM state). (d) Band structure along $\bar{M} - \bar{\Gamma} - \bar{M}$ measured at 20 K (PM state). Data in panels (c) and (d) are shown in the form of the ARPES original spectra (top panel) and the 2D curvature spectra [46] (bottom panel). (e)–(h) Same as panels (a)–(d) but for the QQQ termination. Clearly, entering the FM state opens a gap at the TSS Dirac cone for the S termination, while no such gap is observed for the QQQ termination.

IV. NATURE OF THE TSS DIRAC GAP AT S TERMINATION

Having established a TSS Dirac-point gap opening in the S termination of FM $\text{MnBi}_8\text{Te}_{13}$, we now demonstrate that this gap is indeed opened because of the long-range FM order of the magnetic moments. A zoomed-in ARPES $k - E$ map of the S termination in the PM state (15 K) is shown in Fig. 3(a), while that in the FM state (7 K) is shown in Fig. 3(d). The magnetic-order-induced spectral change is concentrated at the Dirac point, as highlighted in Figs. 3(b) and 3(e). For the PM S termination, a gapless “X”-shape Dirac cone can be clearly resolved, with its Dirac point being indicated by the black arrow in Fig. 3(b). The corresponding energy distribution curve (EDC) taken across the Dirac point can be fitted with two Lorentzian peaks, with the dominating one (dark blue) centered at the Dirac-point energy $E_D \approx -0.21$ eV [Fig. 3(c)].

For the FM S termination, as presented in Fig. 3(e), the upper and lower Dirac cones are separated in energy by a sizable gap, with the two cones clearly detaching from each other. Fitting the corresponding EDC yields three Lorentzian peaks. The two dark-blue peaks, located at $E_1 \approx -0.19$ eV and $E_2 \approx -0.22$ eV, correspond to the upper Dirac cone minimum and lower Dirac cone maximum,

respectively. These two peaks originate from the splitting of the gapless Dirac-point peak centered at $E_D \approx -0.21$ eV [Fig. 3(c)], resulting in a Dirac-point gap of $\Delta = E_1 - E_2 \approx 28$ meV [Fig. 3(f)]. The light-blue peak corresponds to a weak shoulder found in both PM and FM EDCs, whose peak position remains at the same energy at different temperatures and potentially originates from disorder.

In Fig. 3(g), systematic Lorentzians fitting to the $\bar{\Gamma}$ EDCs at various temperatures below and above the bulk PM-FM transition (10.5 K) are presented. The constant energy mapping and dispersions corresponding to each temperature are shown in Figs. S7 and S8, allowing us to unambiguously extract the dispersion at the Γ point. At the lowest temperature (6 K), similarly, three Lorentzian peaks are needed to fit the EDC, of which two dark-blue peaks (E_1 and E_2) correspond to the split Dirac cone. The Dirac cone gap size $\Delta = E_1 - E_2$, and its temperature evolution is plotted in Fig. 3(h). With increasing temperature, E_1 and E_2 move closer to each other (Δ decreases) and eventually merge into one Lorentzian peak at 11 K (gap closes), strongly suggesting a clear correlation between the size of this Dirac-point gap and the FM exchange interaction. It is worth noting that, while, similarly, we can also assume two dark-blue peaks (E_1 and E_2) for the EDCs measured at $T \geq 11$ K, the fitting iterations always result in

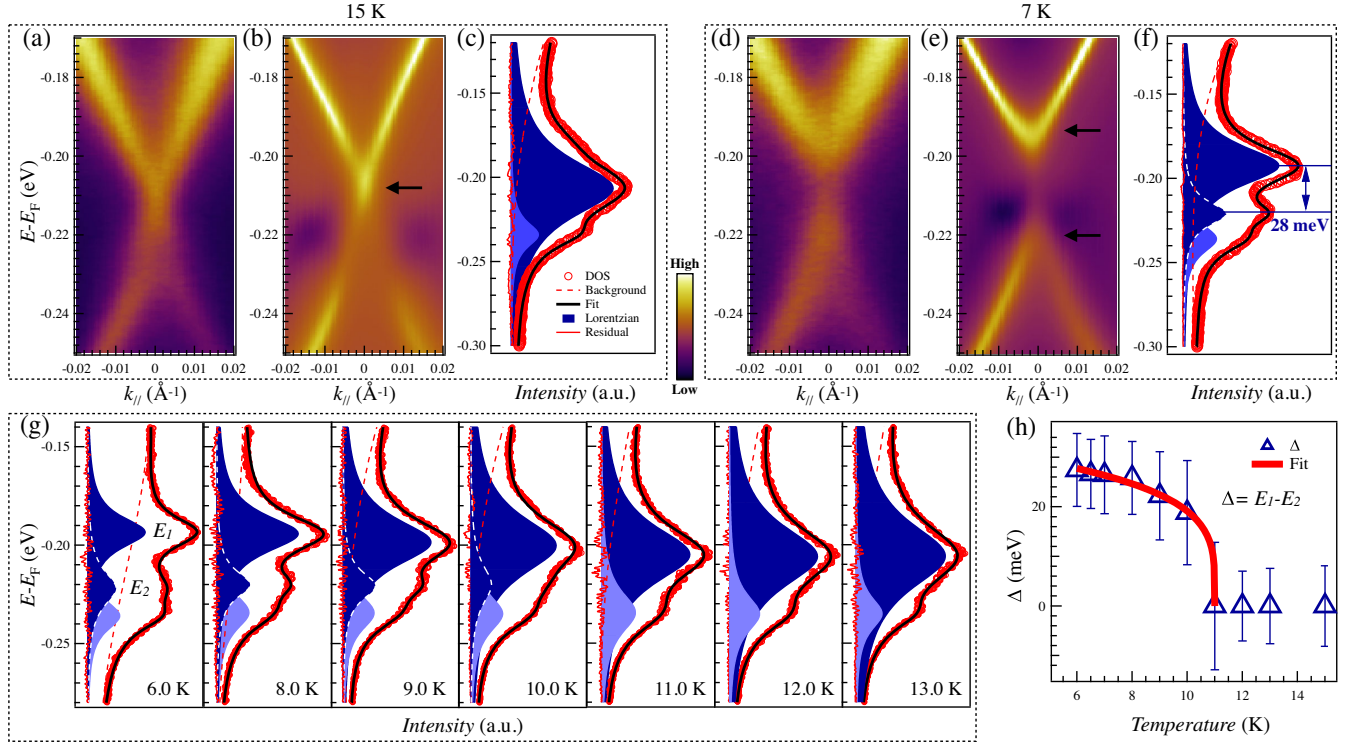


FIG. 3. Temperature dependence of the TSS gap in the S termination of MnBi₈Te₁₃. (a) Enlarged ARPES spectrum of the S termination measured at 15 K (PM phase). (b) Two-dimensional curvature plot for the spectrum in panel (a). (c) Energy distribution curve (EDC) at $\bar{\Gamma}$ (integrated over a ± 0.001 Å⁻¹ momentum window) and its fitting with multiple Lorentzian peaks. (d)–(f) Same plots as those in panels (a)–(c) but for data measured at 7 K (FM phase). (g) EDC fitting analysis at various temperatures, showing a clear gap opening for $T \leq 10.0$ K. The EDCs for each temperature are extracted from the corresponding spectra shown in Fig. S6 integrated over a ± 0.001 Å⁻¹ momentum $k_{||}$ window. Furthermore, the spectra for each temperature are extracted from the corresponding map shown in Fig. S5 integrated over a ± 0.002 Å⁻¹ momentum (k_y) window. (h) TSS Dirac cone gap size (blue triangles) evolution with temperature and its fitting (red solid line) using a power-law curve. The error bar of the gap size is defined as $e = \sqrt{w_1^2 + w_2^2}$, where w_1 and w_2 represent the half width at half maximum for peaks E_1 and E_2 , respectively. We note that the EDC fitting in panel (g) yields the standard deviation of the peak positions much smaller (less than 1 meV) than the error bars shown in panel (h).

a vanishing or even negative area of peak E_2 , and $\Delta = E_1 - E_2 \leq 3$ meV, which is negligible compared to the width of the Lorentzian peaks. In short, the gaplessness of the Dirac cone at temperatures above 11 K is well established.

Assuming a linear relation between this exchange splitting and the magnetic moment, the gap should be well described by a power-law curve [48] $\Delta \sim E_0(1 - T/T_0)^{2\beta}$, where E_0 represents the saturated exchange splitting energy at $T = 0$ K. Fitting the $\Delta(T)$ curve with this power-law function yields $T_0 = 11 \pm 1$ K and $\beta = 0.23 \pm 0.02$. The fitted onset temperature T_0 matches the susceptibility-derived Curie temperature well within the fitting error. The saturated exchange splitting energy is fitted as $E_0 = 33 \pm 1$ meV. We thus established a FM-induced Dirac-point gap in the S termination of MnBi₈Te₁₃. It is noteworthy that, although Dirac-point gaps have been reported for other members of the Mn-Bi-Te family [25,35–37], these observations are still controversial

[24,28,30,32–34]. In particular, all the reported gaps remain open above the magnetic transition temperature, contradicting the scenario of the restoration of time-reversal symmetry. Consequently, our results—that a TSS Dirac cone gap decreases monotonically with increasing temperature and closes right at T_C , forming a gapless Dirac cone—represent the first smoking-gun evidence of TSSs gapped by the magnetic order among all known magnetic topological materials.

One may wonder why this magnetic gap can be observed in FM MnBi₈Te₁₃ but not in its other AFM sisters. While the mechanism of the gapless Dirac cone in AFM Mn-Bi-Te family members remains an open issue, in the study of the surface band structure of MnBi₆Te₁₀, we pointed out that surface-bulk band hybridization may cause the surface Dirac cone distribution to extend to the bulk [28]. In an AFM background, this extension could result in much-reduced effective magnetic moments, which the surface state can feel, thus a (nearly) gapless Dirac cone

with AFM order. In a FM background, the redistribution of the surface state does not change the effective magnetic moments, leading to the gapped Dirac cone.

V. SURFACE ANOMALOUS HALL CONDUCTANCE AS A SIGNATURE OF AXION INSULATOR

So far, we have demonstrated a magnetic gap at the S termination and a gapless feature at the QQQ termination of $\text{MnBi}_8\text{Te}_{13}$, rendering the material a “half-magnetic topological insulator.” To further identify its topological nature, we next theoretically analyze the surface anomalous Hall conductance (AHC) of this gapped surface and the corresponding experimental signatures. Because of the inversion symmetry, the band structure of $\text{MnBi}_8\text{Te}_{13}$ may be characterized by a higher-order topological invariant, i.e., the Z_4 number (the symmetry indicator of inversion [49,50]). Our explicit computation shows that $\text{MnBi}_8\text{Te}_{13}$ has $Z_4 = 2$, in agreement with a previous study [40] (Fig. S10 and Table S1 in Ref. [39]). For a FM compound, while $Z_4 = 1$ or 3 implies a Weyl semimetal, $Z_4 = 2$ corresponds to an axion insulator or a 3D Chern insulator, with distinct surface AHC behavior [13]. Therefore, we compute the surface AHC by integrating the local Chern numbers through surface-related layers for two-dimensional slabs of $\text{MnBi}_8\text{Te}_{13}$, expressed as

$$\sigma_{xy}(L) = \frac{e^2}{h} \frac{4\pi}{A} \text{Im} \sum_{l=0}^L \frac{1}{N_k} \sum_k \sum_{v'v''} X_{vck} Y_{v'ck}^\dagger \rho_{vv''}(l), \quad (1)$$

where X and Y are the position operators along the x and y directions, respectively, which are directly computed from the velocity operators through $X(Y)_{vck} = \langle \psi_{vk} | i\hbar v_{x(y)} | \psi_{ck} \rangle / (E_{ck} - E_{vk})$. The indices v and c denote the valence and conduction bands, respectively. Here, $\rho_{vv''}(l)$ is the projection matrix on the corresponding layer l , which implies a summation over all atoms within a vdW layer. To uncover the locality of the surface AHC, we construct two slabs with different thicknesses. For the S termination of a 16-vdW-layer slab, when E_F lies in the gap of this surface, the layer-integrated AHC reaches about $e^2/2h$ at the second layer from the S termination [Fig. 4(a)]. On the other hand, the metallic QQQ surface does not have a well-defined surface Chern number because E_F inevitably cuts the surface bands (Fig. S11). In comparison, the slab with 17 vdW layers is symmetric and has a global band gap, leading to a well-defined integer-quantized Chern number for the whole slab, i.e., $C = 1$. Figure 4(b) clearly shows that both top and bottom surfaces contribute a half-quantized AHC, while the internal layers do not contribute to the global AHC. In the bulk, there is an oscillation around $e^2/2h$ with a period of the unit cell thickness (four vdW layers) starting from the fourth layer from the surface. Therefore, the half-quantized AHC of $\text{MnBi}_8\text{Te}_{13}$ is a local quantity at the S termination, indicating an axion-insulator phase.

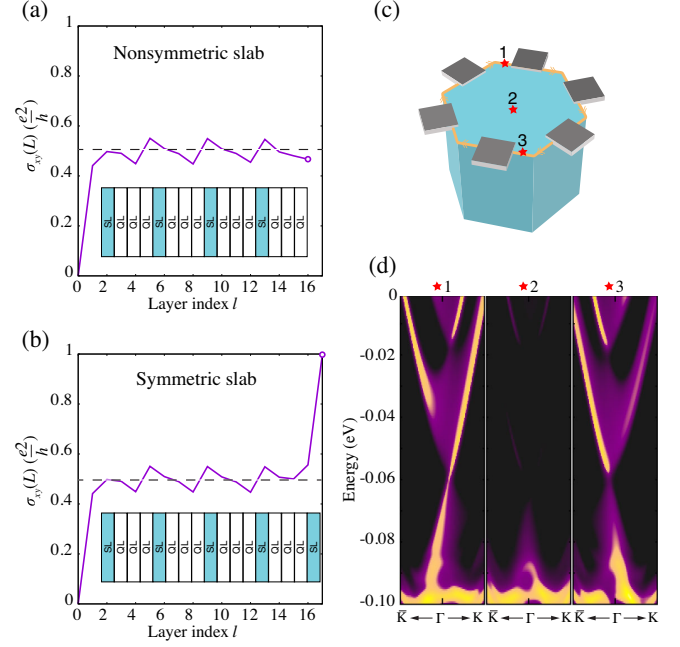


FIG. 4. Half-quantized surface AHC at the S termination. (a,b) Integrated, layer-projected, anomalous Hall conductance for the slabs with 16 and 17 vdW layers, respectively. The 16-layer slab is not symmetric, containing four unit cells as a half-magnetic topological insulator, while the 17-layer slab is symmetric with a global band gap and nontrivial Chern number, as shown in the insets. (c) Schematic plot for the nonlocal transport measurement with a hexagonal six-contact-probing setup. (d) Spectral functions at three spots denoted in panel (c), showing spectral chiral hinge states at the S termination that manifest the half-QAH effect.

Though direct experimental measurement of the half-quantized surface AHC is challenging for various reasons—including sample quality, possible electrode scattering, actual size of the surface gap, and the electron chemical potential in the sample—numerical validation in $\text{MnBi}_2\text{Te}_4/(\text{Bi}_2\text{Te}_3)_n$ [13] and an experimental proposal based on nonlocal transport measurement have recently been provided [14], with a hexagonal six-contact-probing setup shown in Fig. 4(c). In the case of $\text{MnBi}_8\text{Te}_{13}$, as discussed above, magnetism opens a gap in the S termination surface. We compute the spectral functions at the hinges and the center of the top surface (S termination) [Fig. 4(d)], validating the existence of the chiral hinge state at the S termination. It clearly shows that, although the center of the S termination [point 2 in Fig. 4(c)] has a gap, nonvanishing chiral states exist near the boundary formed by the $x-y$ top surface and the $x-z$ side surface, i.e., points 1 and 3, with opposite velocity. Such chiral hinge states are embedded within the side surface states, causing imbalanced density of states at the two sides of the Dirac cone. In this sense, $\text{MnBi}_8\text{Te}_{13}$ is an excellent candidate for observing the signature of the long-sought axion insulator and topological magnetoelectric effect.

ACKNOWLEDGMENTS

We thank Ni Ni, Haizhou Lu, and Hu Xu for helpful discussions. This work is supported by National Key R&D Program of China (Grants No. 2020YFA0308900 and No. 2019YFA0704900), the National Natural Science Foundation of China (NSFC) (Grants No. 12074163, No. 12074161, No. 11804144, No. 11674149, No. 11874195, and No. 11804402), the Shenzhen High-level Special Fund (Grants No. G02206304 and No. G02206404), the Guangdong Innovative and Entrepreneurial Research Team Program (Grants No. 2019ZT08C044, No. 2017ZT07C062, and No. 2016ZT06D348), Shenzhen Science and Technology Program (Grant No. KQTD20190929173815000), the University Innovative Team in Guangdong Province (No. 2020KCXTD001), the Technology and Innovation Commission of Shenzhen Municipality (No. JCYJ20150630145302240 and No. KYTDPT20181011104202253), the Highlight Project (No. PHYS-HL-2020-1) of the College of Science at SUSTech, Guangdong Provincial Key Laboratory for Computational Science and Material Design under Grant No. 2019B030301001, and Center for Computational Science and Engineering of Southern University of Science and Technology. ARPES measurements were performed with the approval of the Proposal Assessing Committee of the Hiroshima Synchrotron Radiation Center (Proposals No. 19BG044, No. 19BU002, No. 19BU005, and No. 19BU012).

APPENDIX: MATERIALS AND METHODS

1. Sample growth

MnBi₈Te₁₃ single crystals were grown by the conventional high-temperature solution method using Bi₂Te₃ as the flux. Mn (purity 99.98%), Bi (purity 99.999%), and Te (99.999%) blocks were placed in an alumina crucible with a molar ratio of Mn:Bi:Te = 1:12.3:19.4. Then, the alumina crucible was sealed in a quartz tube under the argon environment. The assembly was first heated up in a box furnace to 950°C, held for 10 hrs, and then cooled down slowly to 574°C over 120 hrs. After this heating procedure, the quartz tube was taken out quickly and then decanted into the centrifuge to remove the excess flux from the single crystals. Because the temperature window for the growth of MnBi₈Te₁₃ is very narrow and Bi₂Te₃ is an inevitable by-product, we cut the single crystals into thin pieces and checked using single-crystal x-ray diffraction on both sides to select only the pure phase of MnBi₈Te₁₃ single crystals.

2. Transport and magnetic measurements

The structure of the crystals was characterized by x-ray diffraction with Cu *K* α radiation at room temperature using a Rigaku Miniex diffractometer. The diffraction pattern can be well indexed by the (00*l*) reflections with

$\Delta_{2\theta} \sim 2^\circ$ for adjacent peaks, especially at lower angles ($<20^\circ$). Resistivity measurements were performed by a Quantum Design (QD) Physical Properties Measurement System (PPMS) with a standard six-probe method, using a drive current of 8 mA. The current flows in the *ab* plane, and the magnetic field is perpendicular to the current direction. Magnetic measurements were performed using the QD Magnetic Property Measurement System (MPMS) with the Vibrating Sample Magnetometer (VSM) mode. Temperature-dependent magnetization results were collected with an external magnetic field of 100 Oe, both along and perpendicular to the (001) direction of the sample.

3. ARPES measurement

The μ -laser-ARPES [44] measurements were performed at the Hiroshima Synchrotron Radiation Center (HSRC), Hiroshima, Japan with a VG Scienta R4000 electron analyzer and a photon energy of 6.36 eV. The energy and angular resolution were better than 3 meV and less than 0.05° , respectively. Samples were cleaved *in situ* along the (001) crystal plane under ultrahigh-vacuum conditions with pressure better than 5×10^{-11} mbar and temperatures below 20 K.

4. First-principles calculations

DFT calculations [51,52] were conducted by using the projector-augmented wave (PAW) pseudopotentials [53], and exchange correlation was described by the Perdew-Burke-Ernzerhof (PBE) version of the GGA functional [54,55] as implemented in the Vienna *ab-initio* Simulation Package (VASP) [56]. Considering the transition-metal element Mn in MnBi₈Te₁₃, the PBE + U functional with $U = 5$ eV was used for Mn 3*d* orbitals for all the results in this work [57]. The *k*-mesh, energy cutoff, and total energy tolerance for the self-consistent calculations were $5 \times 5 \times 5$, 500 eV, and 10^{-5} eV, respectively. The experimental lattice constants ($a_0 = 4.37$ Å and $c_0 = 132.32$ Å) were taken, while the atomic positions were fully relaxed until the force on each atom was less than 10^{-2} eV/Å. Spin-orbit coupling was included in the calculations self-consistently. We constructed Wannier representations by projecting the Bloch states from the first-principles calculations of bulk materials onto Mn-*d*, Bi-*p*, and Te-*s* orbitals. The TSS, as well as the surface anomalous Hall conductivity, were calculated in tight-binding models constructed by these Wannier representations, as implemented in the WannierTools package [58–61].

-
- [1] M. M. Otrokov *et al.*, *Prediction and Observation of an Antiferromagnetic Topological Insulator*, *Nature (London)* **576**, 416 (2019).

- [2] E. D. L. Rienks *et al.*, *Large Magnetic Gap at the Dirac Point in $\text{Bi}_2\text{Te}_3/\text{MnBi}_2\text{Te}_4$ Heterostructures*, *Nature (London)* **576**, 423 (2019).
- [3] Y. Deng *et al.*, *Quantum Anomalous Hall Effect in Intrinsic Magnetic Topological Insulator MnBi_2Te_4* , *Science* **367**, 895 (2020).
- [4] C. Liu *et al.*, *Robust Axion Insulator and Chern Insulator Phases in a Two-Dimensional Antiferromagnetic Topological Insulator*, *Nat. Mater* **19**, 522 (2020).
- [5] R. S. K. Mong, A. M. Essin, and J. E. Moore, *Antiferromagnetic Topological Insulators*, *Phys. Rev. B* **81**, 245209 (2010).
- [6] E. Liu *et al.*, *Giant anomalous Hall Effect in a Ferromagnetic Kagome-Lattice Semimetal*, *Nat. Phys.* **14**, 1125 (2018).
- [7] D. F. Liu *et al.*, *Magnetic Weyl Semimetal Phase in a Kagomé Crystal*, *Science* **365**, 1282 (2019).
- [8] N. Morali, R. Batabyal, P. K. Nag, E. Liu, Q. Xu, Y. Sun, B. Yan, C. Felser, N. Avraham, and H. Beidenkopf, *Fermi-Arc Diversity on Surface Terminations of the Magnetic Weyl Semimetal $\text{CO}_3\text{Sn}_2\text{S}_2$* , *Science* **365**, 1286 (2019).
- [9] Y. Tokura, K. Yasuda, and A. Tsukazaki, *Magnetic Topological Insulators*, *Nat. Rev. Phys.* **1**, 126 (2019).
- [10] N. P. Armitage and L. Wu, *On the Matter of Topological Insulators as Magnetoelectrics*, *SciPost Phys.* **6**, 046 (2019).
- [11] C.-Z. Chang *et al.*, *Experimental Observation of the Quantum Anomalous Hall Effect in a Magnetic Topological Insulator*, *Science* **340**, 167 (2013).
- [12] C. Z. Chang, W. Zhao, D. Y. Kim, H. Zhang, B. A. Assaf, D. Heiman, S.-C. Zhang, C. Liu, M. H. W. Chan, and J. S. Moodera, *High-Precision Realization of Robust Quantum Anomalous Hall State in a Hard Ferromagnetic Topological Insulator*, *Nat. Mater.* **14**, 473 (2015).
- [13] M. Gu, J. Li, H. Sun, Y. Zhao, C. Liu, J. Liu, and Q. Liu, *Spectral Signatures of the Surface Anomalous Hall Effect in Magnetic Axion Insulators*, *arXiv:2005.13943*.
- [14] R. Chen, S. Li, H.-P. Sun, Y. Zhao, H.-Z. Lu, and X. C. Xie, *Using Nonlocal Surface Transport to Identify the Axion Insulator*, *arXiv:2005.14074*.
- [15] X.-L. Qi, T. L. Hughes, and S.-C. Zhang, *Topological Field Theory of Time-Reversal Invariant Insulators*, *Phys. Rev. B* **78**, 195424 (2008).
- [16] A. M. Essin, J. E. Moore, and D. Vanderbilt, *Magnetoelectric Polarizability and Axion Electrodynamics in Crystalline Insulators*, *Phys. Rev. Lett.* **102**, 146805 (2009).
- [17] J. Ge *et al.*, *High-Chern-Number and High-Temperature Quantum Hall Effect without Landau Levels*, *Natl. Sci. Rev.* **7**, 1280 (2020).
- [18] Y. Gong *et al.*, *Experimental Realization of an Intrinsic Magnetic Topological Insulator*, *Chin. Phys. Lett.* **36**, 076801 (2019).
- [19] J. Li, Y. Li, S. Du, Z. Wang, B.-L. Gu, S.-C. Zhang, K. He, W. Duan, and Y. Xu, *Intrinsic Magnetic Topological Insulators in van der Waals Layered MnBi_2Te_4 -Family Materials*, *Sci. Adv.* **5**, eaaw5685 (2019).
- [20] M. M. Otrokov, I. P. Rusinov, M. Blanco-Rey, M. Hoffmann, A. Yu. Vyazovskaya, S. V. Eremin, A. Ernst, P. M. Echenique, A. Arnau, and E. V. Chulkov, *Unique Thickness-Dependent Properties of the van der Waals Interlayer Antiferromagnet MnBi_2Te_4 Films*, *Phys. Rev. Lett.* **122**, 107202 (2019).
- [21] H. Sun, B. Xia, Z. Chen, Y. Zhang, P. Liu, Q. Yao, H. Tang, Y. Zhao, H. Xu, and Q. Liu, *Rational Design Principles of the Quantum Anomalous Hall Effect in Superlattice-like Magnetic Topological Insulators*, *Phys. Rev. Lett.* **123**, 096401 (2019).
- [22] D. Zhang, M. Shi, T. Zhu, D. Xing, H. Zhang, and J. Wang, *Topological Axion States in the Magnetic Insulator MnBi_2Te_4 with the Quantized Magnetoelectric Effect*, *Phys. Rev. Lett.* **122**, 206401 (2019).
- [23] K. N. Gordon, H. Sun, C. Hu, A. G. Linn, H. Li, Y. Liu, P. Liu, S. Mackey, Q. Liu, N. Ni, and D. Dessau, *Strongly Gapped Topological Surface States on Protected Surfaces of Antiferromagnetic MnBi_4Te_7 and $\text{MnBi}_6\text{Te}_{10}$* , *arXiv:1910.13943*.
- [24] L. X. Xu, *et al.*, *Persistent Gapless Surface States in $\text{MnBi}_2\text{Te}_4/\text{Bi}_2\text{Te}_3$ Superlattice Antiferromagnetic Topological Insulator*, *arXiv:1910.11014*.
- [25] N. H. Jo, L.-L. Wang, R.-J. Slager, J. Yan, Y. Wu, K. Lee, B. Schunk, A. Vishwanath, and A. Kaminski, *Intrinsic Axion Insulating Behavior in Antiferromagnetic $\text{MnBi}_6\text{Te}_{10}$* , *Phys. Rev. B* **102**, 045130 (2020).
- [26] S. Tian *et al.*, *Magnetic Topological Insulator $\text{MnBi}_6\text{Te}_{10}$ with a Zero-Field Ferromagnetic State and Gapped Dirac Surface States*, *Phys. Rev. B* **102**, 035144 (2020).
- [27] R. C. Vidal *et al.*, *Topological Electronic Structure and Intrinsic Magnetization in MnBi_4Te_7 : A Bi_2Te_3 Derivative with a Periodic Mn Sublattice*, *Phys. Rev. X* **9**, 041065 (2019).
- [28] X.-M. Ma *et al.*, *Hybridization-Induced Gapped, and Gapless States on the Surfaces of Magnetic Topological Insulators*, *Phys. Rev. B* **102**, 245136 (2020).
- [29] C. Hu *et al.*, *A van der Waals Antiferromagnetic Topological Insulator with Weak Interlayer Magnetic Coupling*, *Nat. Commun.* **11**, 97 (2020).
- [30] Y. Hu *et al.*, *Universal Gapless Dirac Cone and Tunable Topological States in $(\text{MnBi}_2\text{Te}_4)_m(\text{Bi}_2\text{Te}_3)_n$ Heterostructures*, *Phys. Rev. B* **101**, 161113 (2020).
- [31] X. Wu *et al.*, *Distinct Topological Surface States on the Two Terminations of MnBi_4Te_7* , *Phys. Rev. X* **10**, 031013 (2020).
- [32] Y. J. Chen *et al.*, *Topological Electronic Structure and Its Temperature Evolution in Antiferromagnetic Topological Insulator MnBi_2Te_4* , *Phys. Rev. X* **9**, 041040 (2019).
- [33] Y.-J. Hao *et al.*, *Gapless Surface Dirac Cone in Antiferromagnetic Topological Insulator MnBi_2Te_4* , *Phys. Rev. X* **9**, 041038 (2019).
- [34] P. Swatek, Y. Wu, L.-L. Wang, K. Lee, B. Schunk, J. Yan, and A. Kaminski, *Gapless Dirac Surface States in the Antiferromagnetic Topological Insulator MnBi_2Te_4* , *Phys. Rev. B* **101**, 161109 (2020).
- [35] A. M. Shikin *et al.*, *Nature of the Dirac Gap Modulation and Surface Magnetic Interaction in Axion Antiferromagnetic Topological Insulator MnBi_2Te_4* , *Sci. Rep.* **10**, 13226 (2020).
- [36] H. Li *et al.*, *Dirac Surface States in Intrinsic Magnetic Topological Insulators EuSn_2As_2 and $\text{MnBi}_{2n}\text{Te}_{3n+1}$* , *Phys. Rev. X* **9**, 041039 (2019).

- [37] X.-M. Ma *et al.*, *Spectroscopic Realization of Large Surface Gap in a Doped Magnetic Topological Insulator*, [arXiv:2004.09123](https://arxiv.org/abs/2004.09123).
- [38] I. I. Klimovskikh *et al.*, *Tunable 3D/2D Magnetism in the (MnBi₂Te₄)(Bi₂Te₃)_m Topological Insulators Family*, *npj Quantum Mater.* **5**, 54 (2020).
- [39] See Supplemental Material at <http://link.aps.org/supplemental/10.1103/PhysRevX.11.011039> for more information on x-ray diffraction, magnetic and electric properties, comparison between DFT and ARPES results, and the determination of the band topology.
- [40] C. Hu *et al.*, *Realization of an Intrinsic Ferromagnetic Topological State in MnBi₈Te₁₃*, *Sci. Adv.* **6**, eaba4275 (2020).
- [41] J. Q. Yan, S. Okamoto, M. A. McGuire, A. F. May, R. J. McQueeney, and B. C. Sales, *Evolution of Structural, Magnetic, and Transport Properties in MnBi₂-Sb_xTe₄*, *Phys. Rev. B* **100**, 104409 (2019).
- [42] L. Ding, C. Hu, F. Ye, E. Feng, N. Ni, and H. Cao, *Crystal and Magnetic Structures of Magnetic Topological Insulators MnBi₂Te₄ and MnBi₄Te₇*, *Phys. Rev. B* **101**, 020412 (2020).
- [43] J. Q. Yan, Y. H. Liu, D. S. Parker, Y. Wu, A. A. Aczel, M. Matsuda, M. A. McGuire, and B. C. Sales, *A-Type Antiferromagnetic Order in MnBi₄Te₇ and MnBi₆Te₁₀ Single Crystals*, *Phys. Rev. Mater.* **4**, 054202 (2020).
- [44] H. Iwasawa, E. F. Schwier, M. Arita, A. Ino, H. Namatame, M. Taniguchi, Y. Aiura, and K. Shimada, *Development of Laser-Based Scanning Micro-ARPES System with Ultimate Energy and Momentum Resolutions*, *Ultramicroscopy* **182**, 85 (2017).
- [45] It is still controversial whether a topological surface gap exists in MnBi₂Te₄. While one recent work (Ref. [36]) reports two types of gaps that persist at AFM and PM phases (nonmagnetic), we always observe a gapless Dirac cone in MnBi₂Te₄ at AFM and PM phases (Ref. [24]).
- [46] P. Zhang, P. Richard, T. Qian, Y.-M. Xu, X. Dai, and H. Ding, *A Precise Method for Visualizing Dispersive Features in Image Plots*, *Rev. Sci. Instrum.* **82**, 043712 (2011).
- [47] C. J. Powell, A. Jablonski, I. S. Tilinin, S. Tanuma, and D. R. Penn, *Surface Sensitivity of Auger-Electron Spectroscopy and X-Ray Photoelectron Spectroscopy*, *J. Electron Spectrosc. Relat. Phenom.* **98–99**, 1 (1999).
- [48] D. A. Estyunin *et al.*, *Signatures of Temperature Driven Antiferromagnetic Transition in the Electronic Structure of Topological Insulator MnBi₂Te₄*, *APL Mater.* **8**, 021105 (2020).
- [49] J. Kruthoff, J. de Boer, J. van Wezel, C. L. Kane, and R.-J. Slager, *Topological Classification of Crystalline Insulators through Band Structure Combinatorics*, *Phys. Rev. X* **7**, 041069 (2017).
- [50] W. Haruki, P. H. Chun, and V. Ashvin, *Structure and Topology of Band Structures in the 1651 Magnetic Space Groups*, *Sci. Adv.* **4**, eaat8685 (2018).
- [51] P. Hohenberg and W. Kohn, *Inhomogeneous Electron Gas*, *Phys. Rev.* **136**, B864 (1964).
- [52] W. Kohn and L. J. Sham, *Self-Consistent Equations Including Exchange and Correlation Effects*, *Phys. Rev.* **140**, A1133 (1965).
- [53] G. Kresse and D. Joubert, *From Ultrasoft Pseudopotentials to the Projector Augmented-Wave Method*, *Phys. Rev. B* **59**, 1758 (1999).
- [54] J. P. Perdew, K. Burke, and M. Ernzerhof, *Generalized Gradient Approximation Made Simple*, *Phys. Rev. Lett.* **77**, 3865 (1996).
- [55] J. P. Perdew, K. Burke, and M. Ernzerhof, *Generalized Gradient Approximation Made Simple*, *Phys. Rev. Lett.* **77**, 3865 (1996); *Phys. Rev. Lett.* **78**, 1396 (1997).
- [56] G. Kresse and J. Furthmüller, *Efficient Iterative Schemes for *ab initio* Total-Energy Calculations Using a Plane-Wave Basis Set*, *Phys. Rev. B* **54**, 11169 (1996).
- [57] S. L. Dudarev, G. A. Botton, S. Y. Savrasov, C. J. Humphreys, and A. P. Sutton, *Electron-Energy-Loss Spectra and the Structural Stability of Nickel Oxide: An LSDA + U Study*, *Phys. Rev. B* **57**, 1505 (1998).
- [58] N. Marzari and D. Vanderbilt, *Maximally Localized Generalized Wannier Functions for Composite Energy Bands*, *Phys. Rev. B* **56**, 12847 (1997).
- [59] I. Souza, N. Marzari, and D. Vanderbilt, *Maximally Localized Wannier Functions for Entangled Energy Bands*, *Phys. Rev. B* **65**, 035109 (2001).
- [60] A. A. Mostofi, J. R. Yates, G. Pizzi, Y.-S. Lee, I. Souza, D. Vanderbilt, and N. Marzari, *An Updated Version of Wannier90: A Tool for Obtaining Maximally-Localised Wannier Functions*, *Comput. Phys. Commun.* **185**, 2309 (2014).
- [61] Q. Wu, S. Zhang, H.-F. Song, M. Troyer, and A. A. Soluyanov, *WannierTools: An Open-Source Software Package for Novel Topological Materials*, *Comput. Phys. Commun.* **224**, 405 (2018).

RESEARCH ARTICLE

THERMOELECTRICS

High thermoelectric performance in low-cost $\text{SnS}_{0.91}\text{Se}_{0.09}$ crystals

Wenke He¹, Dongyang Wang¹, Haijun Wu², Yu Xiao¹, Yang Zhang², Dongsheng He³, Yue Feng³, **Yu-Jie Hao³**, Jin-Feng Dong⁴, Raju Chetty⁵, Lijie Hao⁶, Dongfeng Chen⁶, Jianfei Qin⁶, Qiang Yang⁷, Xin Li⁷, Jian-Ming Song⁷, Yingcai Zhu⁸, Wei Xu⁸, Changlei Niu⁹, Xin Li⁹, Guangtao Wang¹⁰, Chang Liu^{3,11}, Michihiro Ohta⁵, Stephen J. Pennycook², Jiaqing He³, Jing-Feng Li⁴, Li-Dong Zhao^{1*}

Thermoelectric technology allows conversion between heat and electricity. Many good thermoelectric materials contain rare or toxic elements, so developing low-cost and high-performance thermoelectric materials is warranted. Here, we report the temperature-dependent interplay of three separate electronic bands in hole-doped tin sulfide (SnS) crystals. This behavior leads to synergistic optimization between effective mass (m^*) and carrier mobility (μ) and can be boosted through introducing selenium (Se). This enhanced the power factor from ~ 30 to ~ 53 microwatts per centimeter per square kelvin ($\mu\text{W cm}^{-1} \text{K}^{-2}$ at 300 K), while lowering the thermal conductivity after Se alloying. As a result, we obtained a maximum figure of merit ZT (ZT_{max}) of ~ 1.6 at 873 K and an average ZT (ZT_{ave}) of ~ 1.25 at 300 to 873 K in $\text{SnS}_{0.91}\text{Se}_{0.09}$ crystals. Our strategy for band manipulation offers a different route for optimizing thermoelectric performance. The high-performance SnS crystals represent an important step toward low-cost, Earth-abundant, and environmentally friendly thermoelectrics.

Thermoelectric technology enables invertible conversion between thermal energy and electricity, providing an environmentally friendly route for power generation through harvesting waste heat, as well as for refrigeration by solid-state cooling (1, 2). The conversion efficiency of thermoelectric technology is determined by the dimensionless figure of merit (ZT) for a given thermoelectric material, expressed by $ZT = S^2\sigma T / (\kappa_{\text{lat}} + \kappa_{\text{ele}})$, where S is the Seebeck coefficient, σ is the electrical conductivity, T is the temperature (in kelvin), and κ_{lat} and κ_{ele} are the phonon and carrier contributions to the thermal conductivity, respectively. These thermoelectric parameters are intertwined, making manipulation of any single parameter targeted to improving the overall thermoelectric performance a challenge. Several strategies have emerged for improving ZT s. Optimizing power factors ($PF = S^2\sigma$) can be accomplished through band convergence (3, 4), band flattening (5, 6), or density of states (DOS) distortion (7, 8). Reducing thermal conductivity is possible by introducing nanostructures (9–11) or all-scale hierarchical architectures (12, 13). Decoupling thermoelectric parameters can be done through embedding magnetic nanoparticles (14, 15). Finally, entirely new materials can be developed with intrinsic

ally low thermal conductivity (16–19) or large power factor (4, 20, 21), or by seeking high-performance thermoelectrics through reliable high-throughput material screening (22).

High-performance thermoelectrics are often the widely studied group IV–VI compounds, such as GeTe (23), PbTe (7, 12, 24), PbSe (25, 26), PbS (27), and SnTe (8, 28). The scarcity of Ge and Te , combined with the toxicity of Pb , makes compounds such as SnSe (16) promising thermoelectric materials, as they do not contain these elements. Moreover, SnSe has a high ZT due to its strong anharmonicity (16, 29, 30), multiple valence bands (31–33), and three-dimensional (3D) charge and 2D phonon transport (34–36). An analog compound of SnSe is SnS , which is also predicted to be an attractive thermoelectric candidate. The lower cost and more Earth-abundant S is appealing for large-scale commercial applications. However, the low carrier mobility results in poor electrical transport properties and impedes high thermoelectric performance in polycrystalline SnS (37). Nevertheless, the carrier mobility in SnS crystals can be boosted by one order of magnitude by making use of its layer structure, leading to a high room-temperature PF of ~ 20 to $30 \mu\text{W cm}^{-1} \text{K}^{-2}$ (38, 39). To further exploit the thermoelectric potentialities of SnS crystals, we

sought to manipulate its electronic band structure (4, 31, 40).

Manipulating the electronic band structure involves optimizing a dimensionless quality factor (β) for a given thermoelectric material (41, 42), characterized by $\beta \propto (m^*)^{3/2}\mu$, where m^* and μ are the effective mass and carrier mobility, respectively. The behavior of m^* and μ is usually anticorrelated, and synergistically optimizing them is challenging. The quality factor in the single parabolic band (SPB) structure can be optimized by lowering m^* and enhancing μ through sharpening electronic bands (43). In a two-band structure, two-band convergence can improve m^* but cause μ to deteriorate (3, 40), whereas two-band divergence can boost μ but lower m^* (36). Therefore, we sought new band structures to optimize m^* and μ simultaneously.

In contrast to the well-known two-band convergence and divergence, other types of band interaction have not been well explored for thermoelectric materials (40, 44, 45). In this study, we synthesized $\text{SnS}_{1-x}\text{Se}_x$ crystals using the temperature gradient method (figs. S1 and S2) with Na doped at 2% to investigate the role of Se (38). We reported the temperature-dependent evolution and interplay of three separate electronic bands, involving the interplay of two-band convergence, two-band divergence, and two-band crossing. The three interplaying bands became sharper with rising temperature. We obtained temperature-dependent electronic band structures using density function theory (DFT) calculations, which are based on the atomic positions derived from the high-temperature synchrotron radiation x-ray diffraction (SR-XRD) data. Our DFT calculations and angle-resolved photoemission spectroscopy (ARPES) measurements confirmed the band interactions. The outstanding behavior—interplay of three separate electronic bands—could be promoted through substitution of S with Se , allowing successful optimization of m^* and μ . Thus, we enhanced the PF from ~ 30 to $\sim 53 \mu\text{W cm}^{-1} \text{K}^{-2}$ at 300 K. The Se substitution was confirmed with aberration-corrected scanning transmission electron microscopy (STEM) and x-ray absorption fine structure spectroscopy (XAFS). Our inelastic neutron scattering (INS) measurements show that the optical phonons are softened by Se substitution and further coupled with acoustic branches. This leads to a lower thermal conductivity. Collectively, we achieved a maximum ZT (ZT_{max}) of ~ 1.6 at 873 K and an average ZT (ZT_{ave}) of ~ 1.25 at 300 to 873 K in $\text{SnS}_{0.91}\text{Se}_{0.09}$ crystals.

Electrical transport properties

The room-temperature electrical conductivity increased from ~ 692 to $\sim 1279 \text{ S cm}^{-1}$ after 9% Se

¹School of Materials Science and Engineering, Beihang University, Beijing 100191, China. ²Department of Materials Science and Engineering, National University of Singapore, Singapore 117575, Singapore. ³Department of Physics, Southern University of Science and Technology, Shenzhen 518055, China. ⁴Key Laboratory of New Ceramics and Fine Processing, School of Materials Science and Engineering, Tsinghua University, Beijing 100084, China. ⁵Research Institute for Energy Conservation, National Institute of Advanced Industrial Science and Technology (AIST), Tsukuba, Ibaraki 305-8568, Japan. ⁶Department of Nuclear Physics, Neutron Scattering Laboratory, China Institute of Atomic Energy, Beijing 102413, China. ⁷Key Laboratory of Neutron Physics and Institute of Nuclear Physics and Chemistry, China Academy of Engineering Physics, Mianyang 621900, China. ⁸Beijing Synchrotron Radiation Facility, Institute of High Energy Physics, Chinese Academy of Sciences, Beijing 100049, China. ⁹Department of Isotope, China Institute of Atomic Energy, Beijing 102413, China. ¹⁰College of Physics and Materials Science, Henan Normal University, Xinxiang 453007, China. ¹¹Shenzhen Key Laboratory of Quantum Science and Engineering, Shenzhen Institute for Quantum Science and Engineering, Shenzhen 518055, China.

*Corresponding author. Email: zhaolindong@buaa.edu.cn

alloying, whereas the carrier concentration decreased from $\sim 3.4 \times 10^{19}$ to $\sim 2.6 \times 10^{19} \text{ cm}^{-3}$ (Fig. 1A). This implies that the improvement of electrical conductivity stemmed from the enhanced carrier mobility. At a doping level of $\sim 10^{19} \text{ cm}^{-3}$, all the samples possessed large Seebeck coefficients (Fig. 1B), namely, $\sim +211 \mu\text{V K}^{-1}$ for SnS, and maintained a large value of $\sim +203 \mu\text{V K}^{-1}$ for $\text{SnS}_{0.91}\text{Se}_{0.09}$. The Seebeck coefficients in $\text{SnS}_{1-x}\text{Se}_x$ crystals were higher than that of the enhancement through activating multiple valence bands found in SnSe (Fig. 1B) (31). The combination of increased electrical conductivity and large Seebeck coefficient gave rise to a PF of $\sim 53 \mu\text{W cm}^{-1} \text{ K}^{-2}$ for $\text{SnS}_{0.91}\text{Se}_{0.09}$ at 300 K (Fig. 1C). When we compared the PF of $\text{SnS}_{0.91}\text{Se}_{0.09}$ to those of other thermoelectric materials in the group IV–VI compounds (24, 25, 27, 28), we found that it exceeded those of the other compounds in the range from 300 to 523 K (Fig. 1D).

To elucidate the high electrical transport properties in SnS crystals, we performed DFT calculations to obtain the electronic band structures. Using the atomic position parameters that we extracted from the temperature-dependent SR-XRD data (fig. S3 and tables S1 and S2), our DFT calculations show the evolution of band structures with rising temperature in SnS (Fig. 2A). Three valence bands lie close to each other in the energy range from ~ -0.20 to ~ -0.07 eV. The first valence band maximum (VBM1) lies in the Γ -Z direction, the second VBM (VBM2) is located on the U point, and the third VBM (VBM3) lies in the Γ -Y direction (Fig. 2A). The schematic diagram displays the dynamic evolution of these three valence bands and the energy offset between them as a function of temperature (Fig. 2B). The changes in energy offsets between these three valence bands are also evidence of the triple-band evolution with temperature. The energy offset between VBM1 and VBM2 is ~ 0.07 eV at 323 K, expanding to ~ 0.13 eV with increasing temperature. Conversely, the energy offset between VBM1 and VBM3 is ~ 0.12 eV at 323 K and gradually decreases to a convergence at 873 K. After Se alloying, the band convergence between VBM2 and VBM3 advances from ~ 650 to ~ 600 K, and the band convergence between VBM1 and VBM3 also takes place at lower temperature. With rising temperature, both VBM1 and VBM3 increase, but VBM3 moves faster than VBM1 while VBM2 decreases. That is, VBM1 and VBM2 diverge whereas VBM3 and VBM1 converge at elevated temperatures. VBM2 and VBM3 eventually cross one another, converging at a temperature of ~ 650 K before diverging. The increased hole concentration at high temperature may come from the band convergence of VBM2 and VBM3, resulting in a carrier redistribution (3, 34, 45) (fig. S6). Thereafter, the divergence from VBM3 (lighter band) rising and VBM2 (heavier band) dropping may contribute to the enhancement of carrier mobility (3, 36). This behavior would transfer to lower temperature after Se alloying (fig. S6).

With rising temperature, the band sharpening decreases the effective masses, which is further reduced after Se alloying, thus resulting in an

improved carrier mobility (Fig. 2C and fig. S6). Hence, introducing Se promotes the interplay of the three valence bands in SnS, which is responsible for the optimization between m^* and μ . That is, μ is improved through lowering m^* as a result of both band divergence and band sharpness (3), whereas the larger Seebeck coefficient is achieved as a result of multiple electronic bands, because the interplay of these three valence bands occurs within ~ 0.16 eV. The energy difference of ~ 0.16 eV in SnS is comparable to the ~ 0.15 eV difference between the first light and the second heavy valence bands of PbTe, in which the contribution from the heavy band becomes considerable with rising temperature (3, 40).

On the basis of the DFT calculated band structure, we investigated the variations of m^* and μ to clarify the higher electrical transport properties in $\text{SnS}_{1-x}\text{Se}_x$ crystals. Our DFT calculations show that the density of states (DOS) effective mass (m_d^*) of VBM1 decreases from $\sim 0.74 m_e$ for SnS to $\sim 0.66 m_e$ for $\text{SnS}_{0.91}\text{Se}_{0.09}$ (table S1). We have calculated Pisarenko lines with single Kane band (SKB), double Kane band (DKB), and triple Kane band (TKB) models to estimate the experimental Seebeck coefficient data (Fig. 2D). It is clearly seen that the experimental values obtained in $\text{SnS}_{1-x}\text{Se}_x$ crystals ($x = 0$ to 0.12) are higher than the Pisarenko line with the SKB model, indicating the contribution of multiple bands. When the

three bands are considered, the TKB model can well elucidate that the enhanced Seebeck coefficients come from three or more bands involved in electrical transport in the $\text{SnS}_{1-x}\text{Se}_x$ system. After Se alloying, the Hall carrier mobility increases (Fig. 2E), which can be well explained by the decreasing effective masses of three bands after introducing Se. We have adopted different band models to simulate the carrier mobility versus carrier concentration. The TKB model is consistent with our experimental data before and after Se alloying in SnS, indicating one good three-valence-band transporting feature. The product of Seebeck coefficient and carrier mobility can reflect the coordination between effective mass (m^*) and carrier mobility (μ) in $\text{SnS}_{1-x}\text{Se}_x$ crystals. The value reaches a maximum at a Se fraction of 9%, which is consistent with the TKB model (Fig. 2F). The power factors also have been simulated with different models to elucidate the contributions from the interplay of three bands (Fig. 2G). The TKB transport model appears to be superior to the SKB and DKB models in $\text{SnS}_{1-x}\text{Se}_x$ crystals. After 9% Se alloying, the TKB model accurately predicts the high power factor, consistent with the experimental data that we obtained. In addition, the competing parameters m^* and μ have been optimized and the quality factor has peaked in SnS with the 9% Se fraction (Fig. 2G, inset). Therefore, three-band transport plays an important part in the improvement of

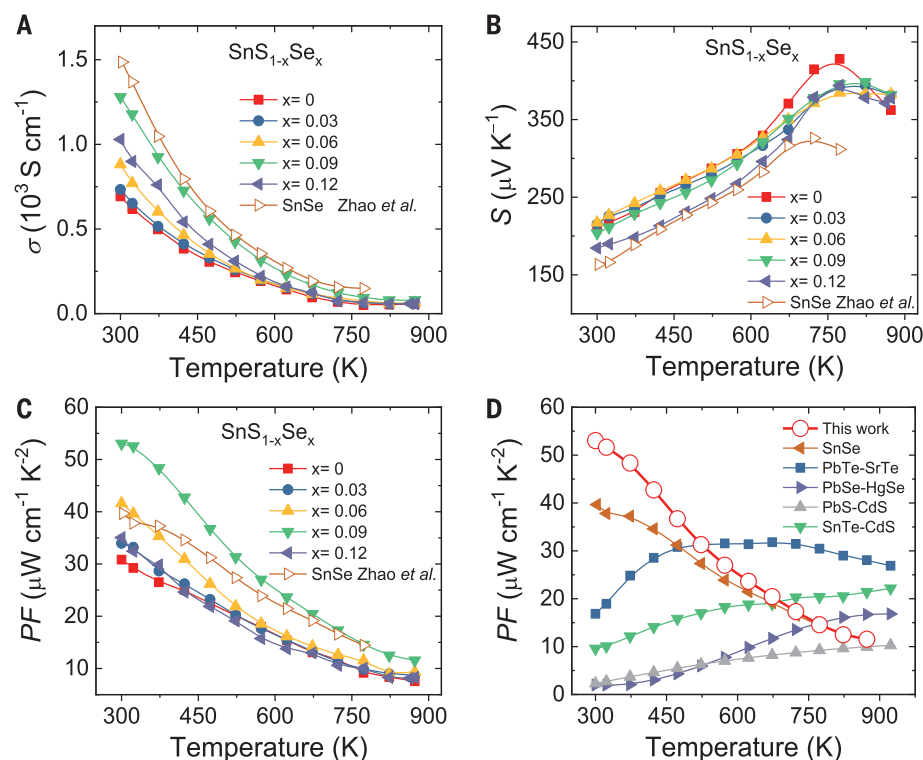


Fig. 1. Electrical transport properties as a function of temperature for $\text{SnS}_{1-x}\text{Se}_x$ crystals.

(A) Electrical conductivity. (B) Seebeck coefficient. (C) Power factor. The electrical properties of SnSe crystals are also added for comparison (31). (D) Power factor comparisons of p-type lead and tin chalcogenides (24, 25, 27, 28, 31). The power factor achieved for SnS indicates a more complex band structure of SnS than of other thermoelectrics.

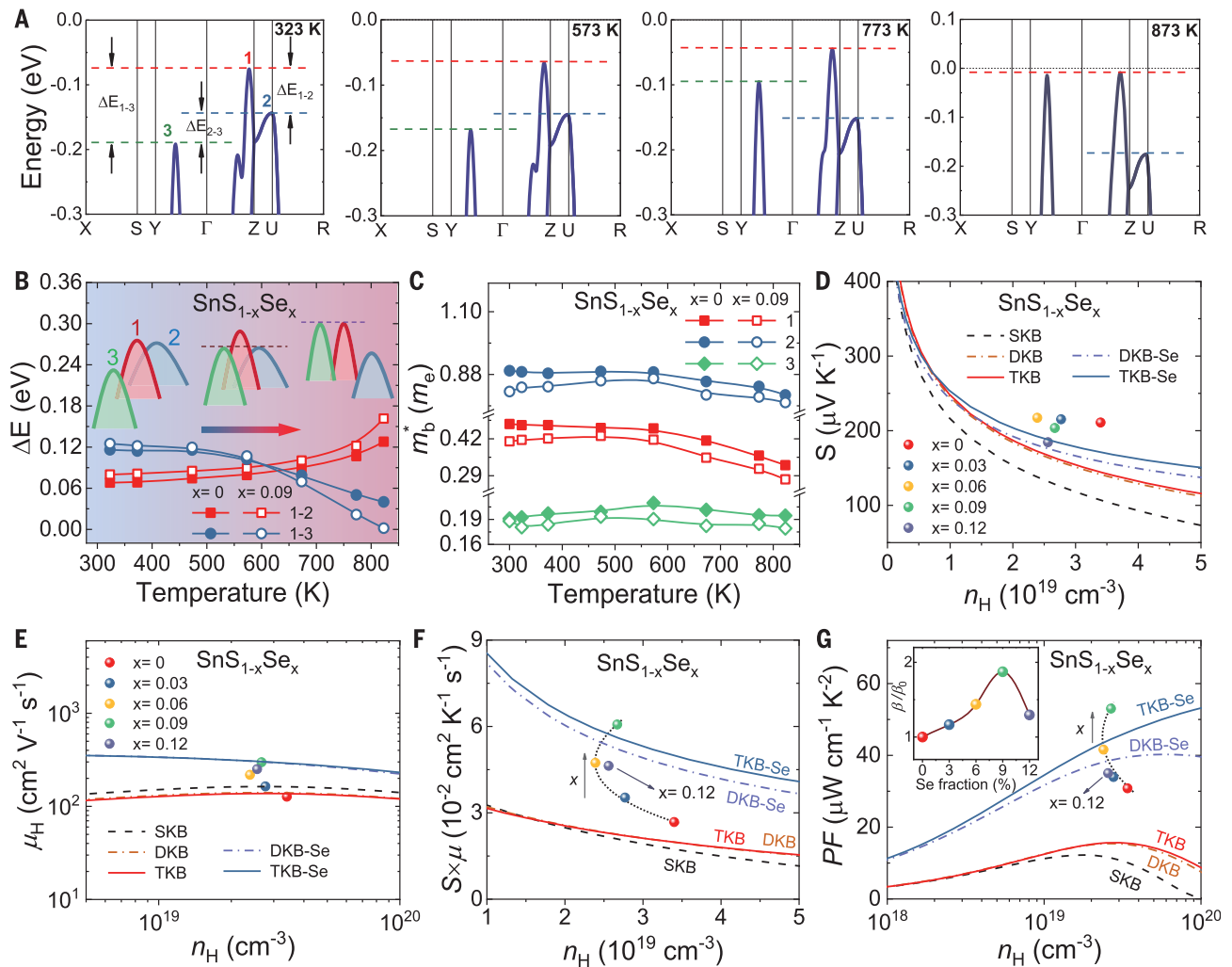


Fig. 2. Temperature-dependent electronic band structure and theoretical simulations on electrical transport properties. (A) Electronic band structure as a function of temperature. (B) Schematic of dynamic evolution of three separate valence bands with increasing temperature for SnS. (Top) As the temperature increases, VBM2 (blue) separates away from VBM1 (red), while VBM3 (green) approaches VBM1, and VBM2 crosses VBM3. (Bottom) The energy gap (ΔE) between VBM1 and VBM2, and between VBM1 and VBM3, as a function of temperature in $\text{SnS}_{1-x}\text{Se}_x$. (C) The effective masses as a function of temperature for VBM1, VBM2, and VBM3 in $\text{SnS}_{1-x}\text{Se}_x$, indicating that effective masses decrease after Se alloying. (D) Pisarenko plots showing the Seebeck coefficients as a

function of carrier concentration with different band models. (E) Carrier mobility as a function of carrier concentration with different band models. (F) The product of the Seebeck coefficient and carrier mobility as a function of carrier concentration in $\text{SnS}_{1-x}\text{Se}_x$ crystals, elucidating the advanced interplay of three separate bands. (G) The simulated power factor as a function of carrier concentration with different band models. The inset shows the ratio of quality factor (β/β_0) in $\text{SnS}_{1-x}\text{Se}_x$ crystals to that in SnS. The experimental data are consistent with the simulations with the TKB model, indicating the contribution of three bands. SKB indicates a single Kane band; DKB, a double Kane band; and TKB, a triple Kane band.

electrical transport properties (power factor) in $\text{SnS}_{1-x}\text{Se}_x$ crystals.

Electronic band structures

We observed the electronic band structure of SnS crystals by ARPES. We plot the three valence bands along different directions and their relative energy levels using triple cuts in the 3D Brillouin zone (Fig. 3A) and the calculated band structure (Fig. 2A) as a reference (Fig. 3B). The triple cuts clearly illustrate the band dispersion of the three VBMs of SnS. The valence band structure along the Γ -Z direction shows that VBM1 is located at the Fermi energy level ($E_1 =$

0 eV) and that VBM3 along the Γ -Y direction is located at $E_3 = -0.30$ eV. The parabolic energy distribution curve (EDC) fitting gives VBM2 at $k = 0.69 \text{ \AA}^{-1}$, which is located at $E_2 = -0.05$ eV (Fig. 3C). Therefore, the energy offset between VBM1 and VBM2 is ~ 0.05 and ~ 0.30 eV between VBM1 and VBM3 at 20 K. We also observed the electronic band structures in the Y- Γ -Z plane at different temperatures. The energy offset between VBM1 (Γ -Z direction) and VBM3 (Γ -Y direction) is ~ 0.50 eV at 5 K, and then decreases to ~ 0.30 eV at 80 K (Fig. 3, D and E). When the temperature is fixed at 80 K, the energy offset between VBM1 and VBM3 decreases from ~ 0.30 eV for SnS to

~ 0.15 eV (Fig. 3, D and E). Both the declining trend with rising temperature and the approach of VBM1 toward VBM3 after Se alloying are consistent with our DFT results (Fig. 2A).

Thermal transport properties

With increasing Se alloying fraction, the thermal conductivities (κ_{tot} and κ_{lat}) of SnS decrease. At room temperature, the total thermal conductivity (κ_{tot}) decreases from ~ 3.3 to $\sim 2.5 \text{ W m}^{-1} \text{ K}^{-1}$, and the lattice thermal conductivity (κ_{lat}) decreases from ~ 3.0 to $\sim 1.7 \text{ W m}^{-1} \text{ K}^{-1}$ for $\text{SnS}_{0.91}\text{Se}_{0.09}$. The thermal conductivity in SnS reaches a minimum at 873 K. After alloying with 9% Se, the κ_{tot}

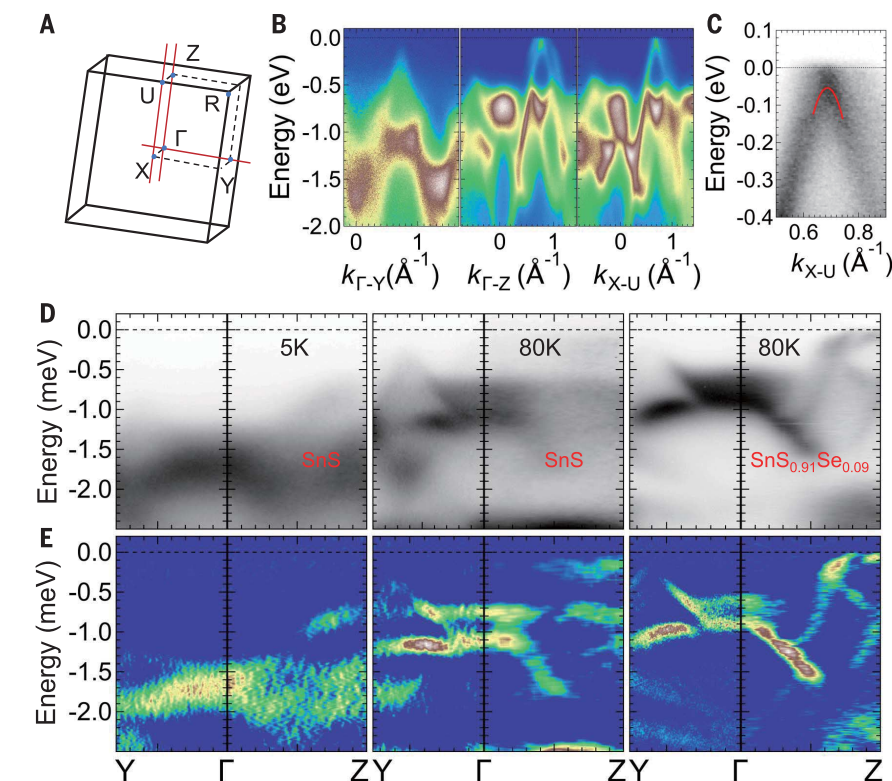


Fig. 3. Brillouin zone and band structures observed by ARPES. (A) Brillouin zone of SnS, and sketch of the three cuts in the Brillouin zone. (B) ARPES band structures of SnS along the Γ -Y, Γ -Z, and X-U directions. The VBM3 (Γ -Y) is located at $E_3 = -0.30$ eV, VBM1 (Γ -Z) is located at the Fermi level ($E_1 = 0$ eV), and VBM2 (X-U) is located at $E_2 = -0.05$ eV. Three cuts illustrate the band dispersion of the three VBMs in SnS. (C) ARPES band structure along the X-U direction. Parabolic fit of the energy distribution curve gives VBM2 at $k = 0.69 \text{ \AA}^{-1}$, $E_2 = -0.05$ eV. (D) Electronic band structures for $\text{SnS}_{1-x}\text{Se}_x$ ($x = 0, 0.09$) along the Y- Γ -Z plane at 5 and 80 K, respectively. The energy gaps (ΔE) between VBM1 and VBM2 are 0.50 eV (5 K, SnS), 0.30 eV (80 K, SnS), and 0.15 eV (80 K, $\text{SnS}_{0.91}\text{Se}_{0.09}$), respectively. (E) Second-derivative maps (with respect to energy) along the Y- Γ -Z plane for $\text{SnS}_{1-x}\text{Se}_x$ ($x = 0, 0.09$).

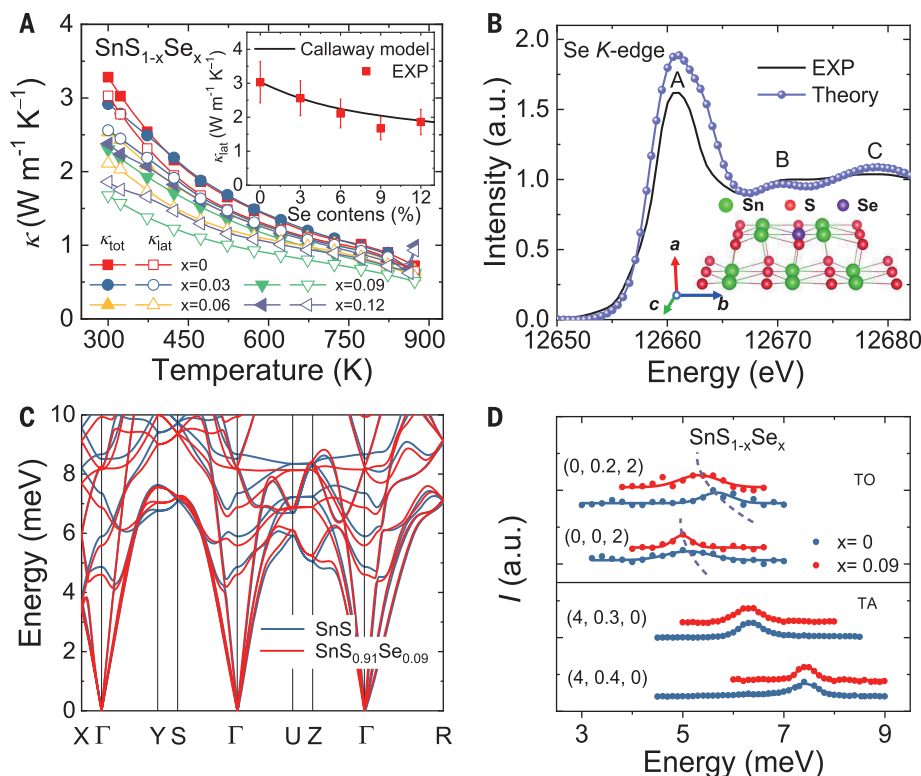


Fig. 4. Thermal conductivity as a function of temperature and phonon band structure. (A) Total and lattice thermal conductivity for $\text{SnS}_{1-x}\text{Se}_x$ crystals. Inset shows the room-temperature lattice thermal conductivities fitted with the Callaway model. (B) Comparison of the experimental and theoretical Se K-edge XANES spectra. Inset: A sketch of the atomic structure indicating Se substituting for S in SnS. (C) Phonon band structure of $\text{SnS}_{1-x}\text{Se}_x$ ($x = 0, 0.09$). (D) Typical constant-Q scans of the TO mode at $Q = (0, 0, 2)$ and $(0, 0.2, 2)$, and TA mode at $Q = (4, 0.3, 0)$ and $(4, 0.4, 0)$, which indicates that the phonon energy of the TO mode decreases after Se alloying, whereas the TA mode changes only slightly.

decreases from ~ 0.72 to $\sim 0.61 \text{ W m}^{-1} \text{ K}^{-1}$, and the κ_{lat} decreases from ~ 0.65 to $\sim 0.51 \text{ W m}^{-1} \text{ K}^{-1}$ at 873 K. Our calculations with the Callaway model (46, 47) are consistent with these reductions being due to Se substitution (Fig. 4A, inset). We

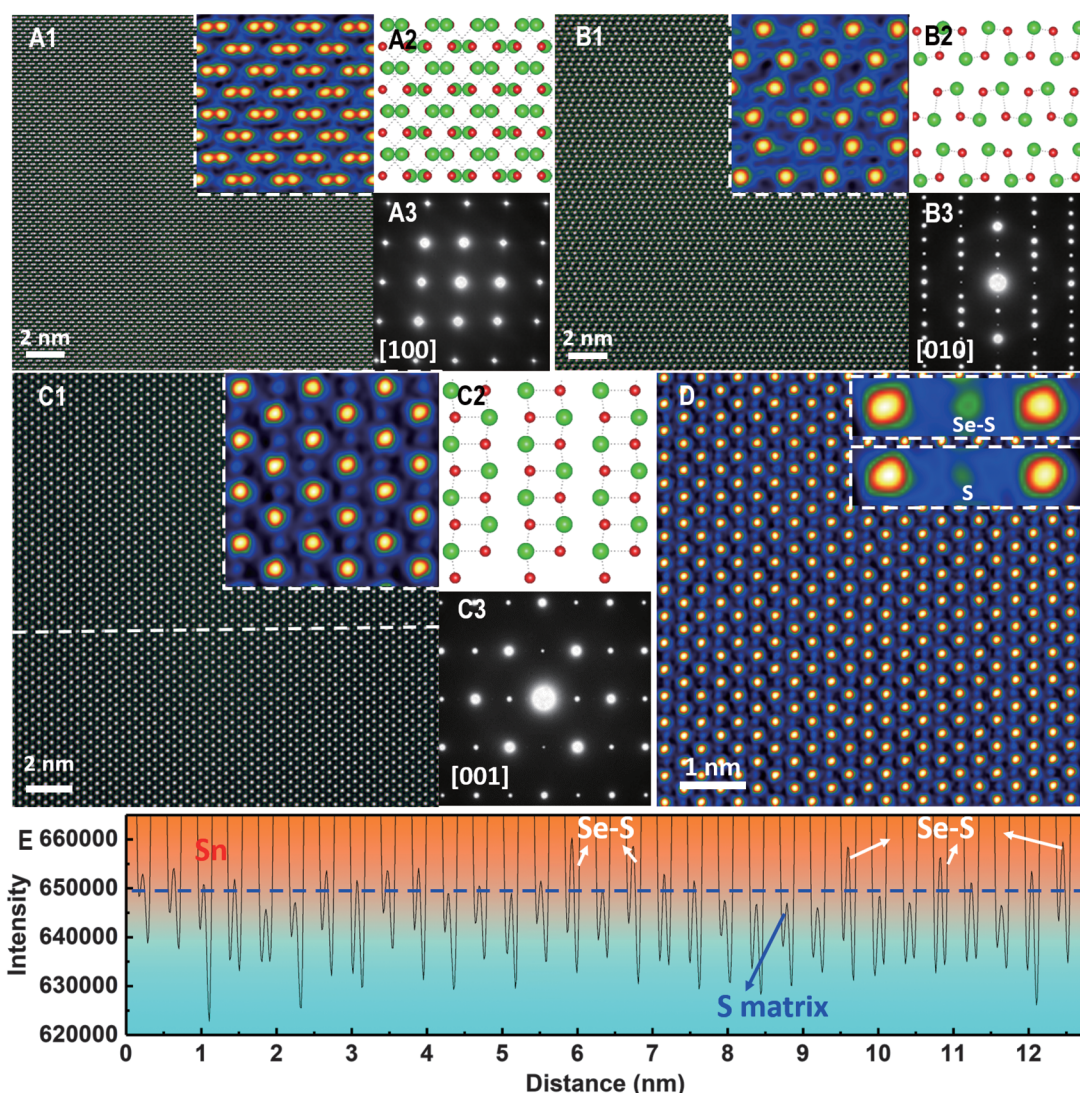
performed x-ray absorption fine structure spectroscopy (XAFS) analysis on $\text{SnS}_{1-x}\text{Se}_x$ crystals to identify the Se substitution. Our XAFS results for $\text{SnS}_{0.91}\text{Se}_{0.09}$ show that the Se K-edge x-ray absorption near-edge structure (XANES)

spectrum contains three major features (Fig. 4B). Peak A originates from 1s to 4p transitions, which could present both geometric and electronic structural information (48). The subsequent features B and C correspond to multiple scattering of the

Fig. 5. Atomic-scale structures of high-performance $\text{SnS}_{0.91}\text{Se}_{0.09}$ crystal. (A1, B1, C1)

Atomically resolved STEM HAADF images along the [100], [010], and [001] zone axes, respectively, with enlarged images shown in the insets. (A2, B2, C2) The respective structural models. (A3, B3, C3) The respective electron diffraction patterns.

(D) Atomically resolved STEM HAADF image along the [001] zone axis, with enlarged images showing the intensity difference between Se-substituted S and the SnS matrix. (E) Intensity profile from the dashed line of (C1) showing the higher intensity of Se-substituted S, compared with the SnS matrix.



photoelectrons by the atoms coordinated in different shells surrounding Se, and the substitution of S by Se is schematically shown in the inset of Fig. 4B. We reproduced all three major features of the experimental Se K-edge XANES with a simulated spectrum using a Se substitution model for SnS. This result indicates the successful introduction of Se into the SnS lattice by occupation of the S site. We observed this feature in all $\text{SnS}_{1-x}\text{Se}_x$ crystals (fig. S2).

We investigated the phonon band structures of both SnS and $\text{SnS}_{0.91}\text{Se}_{0.09}$ with DFT calculations. The optical branches show a softening trend in the whole Brillouin zone after Se substitution, which is more pronounced than that in the acoustic branches (Fig. 4C). The softening of optical branches can be coupled with acoustic branches, and this optical-acoustic mode coupling leads to lower lattice thermal conductivity (49). We performed inelastic neutron scattering (INS) experiments on SnS and $\text{SnS}_{0.91}\text{Se}_{0.09}$ crystals with constant-Q scans for the transverse acoustic (TA) and transverse optical (TO) modes along the Γ -Y direction (fig. S8). After the introduction of Se,

the excitation peaks shifted to lower energy for the TO mode whereas the TA mode showed no substantial change (Fig. 4D and fig. S8). The phonon dispersions that we measured for TA and TO modes along Γ -Y show excellent agreement with the $S(Q, E)$ spectra simulated by our first-principles calculation (fig. S8). Therefore, we conclude that the softening of optical phonons in SnS crystals derives from Se substitution and that the coupling between optical and acoustic phonons contributes to the lower thermal conductivity.

Microstructures

We observed the atomic-scale Se substitutions on S sites in $\text{SnS}_{0.91}\text{Se}_{0.09}$ through aberration-corrected STEM, because STEM high-angle annular dark-field (HAADF) produces a contrast image that can be interpreted by mass thickness (the number of atoms) or atomic number (Z) contrast (50). We obtained atomically resolved STEM HAADF images along [100] (*a* axis), [010] (*b* axis), and [001] (*c* axis), respectively (Fig. 5, A1 to C1). We also obtained the structural modes

and electron diffraction patterns (Fig. 5). Because the structures of SnSe and SnS both show a dumbbell-like atomic arrangement along the *a* axis (51), viewing the Se substitutions along this axis is difficult, as the two atom columns of each dumbbell are close in intensity. To better observe the Se substitutions on the S sites, we turned to the *b* or *c* axis, along which the Sn and S atom columns are well separated in the Z-contrast image, where the heavier Se (*Z* = 34) substitutions may be more visible in the lighter S (*Z* = 16) matrix. The abnormally brighter contrast on S sites is consistent with Se substitutions (Fig. 5D). The Se and S atoms are well distinguished through line profiles with intensity difference. The peaks with abnormally higher intensity are the Se-substituted ones, compared with the S matrix (Fig. 5E and fig. S9).

ZT values and conversion efficiency

The combination of exceptionally high *PF* and low thermal conductivity generates a maximum *ZT* (ZT_{max}), which increases from ~1.0 for SnS to ~1.6 for $\text{SnS}_{0.91}\text{Se}_{0.09}$ at 873 K (Fig. 6A). We

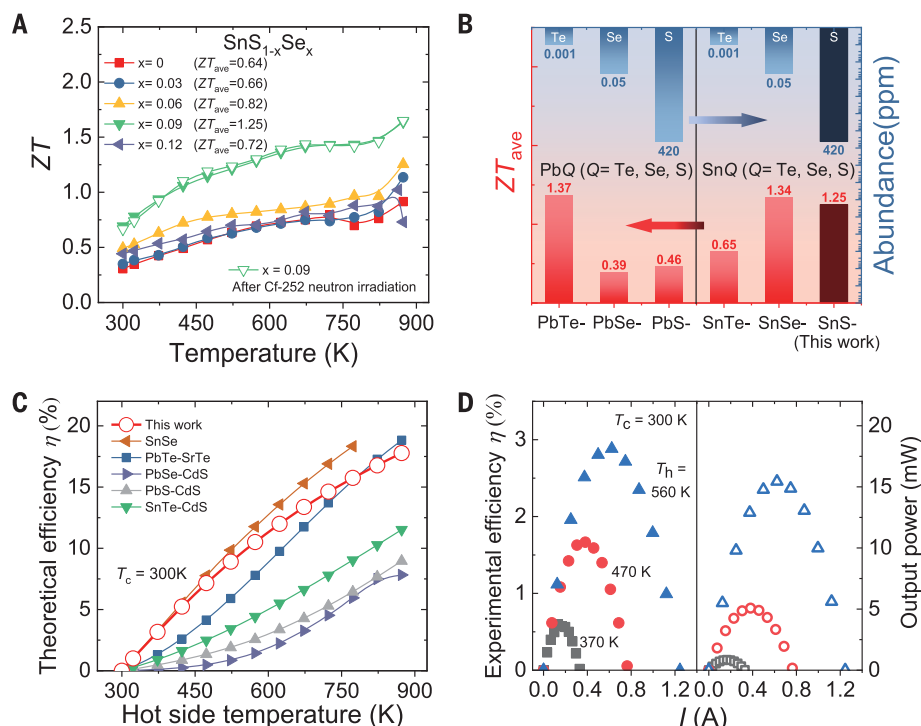


Fig. 6. ZT values, Earth-abundance, and projected power generation efficiency. (A) ZT values as a function of temperature for SnS_{1-x}Se_x crystals with corresponding ZT_{ave} values. (B) Comparisons of ZT_{ave} for p-type lead and tin chalcogenides and element abundance in Earth (24, 25, 27, 28, 31). (C) Theoretical power generation efficiency as a function of hot-side temperature (cold-side temperature is 300 K) for SnS_{0.91}Se_{0.09}, compared to reported lead and tin chalcogenides (24, 25, 27, 28, 31). (D) Experimental power generation efficiency and output power for SnS_{0.91}Se_{0.09}.

found good thermoelectric stability for such high-performance SnS_{0.91}Se_{0.09} samples with three heating-cooling cycle measurements (fig. S10). Notably, the thermoelectric properties of SnS_{0.91}Se_{0.09} also show excellent stability after neutron (Cf-252) irradiation for 432 hours. The radiation resistance of SnS crystals (fig. S11) is important for radioisotope thermoelectric generators geared for deep-space exploration (1, 3). We can maintain the high ZT values over a large temperature range (300 to 873 K), which results in a high average ZT (ZT_{ave}) of ~1.25 in SnS_{0.91}Se_{0.09}. This value is twice that of SnS (ZT_{ave} = 0.64). Noticeably, the ZT_{ave} of SnS is comparable to those of the state-of-the-art PbTe and SnSe crystals (24, 31). Moreover, the abundance of S in the Earth is 420 parts per million (ppm), which far exceeds that of Te (0.001 ppm) and Se (0.05 ppm) (52) (Fig. 6B). Hence, compared with these group IV–VI thermoelectric materials, such as Pb- and Sn-based chalcogenides (24, 25, 27, 28, 31), SnS is far superior when considering toxicity and elemental abundance. The ZT_{ave} must be high over the entire working temperature range, because it determines the thermoelectric conversion efficiency (η) (53). For SnS_{0.91}Se_{0.09}, the theoretical conversion efficiency (η) is ~18% at 873 K and exceeds those of most of thermoelectric materials in the group IV–VI compounds (24, 25, 27, 28, 31) (Fig. 6C). To experimentally investigate the power

efficiency, we attempted to carry out the measurement using the high-performance SnS_{0.91}Se_{0.09} crystals. At the hot-side temperature of ~560 K, which is the highest temperature that is allowed for lower electrical resistivity from the contact materials (Au and Cu), we obtained an efficiency of ~3.0% and an output power of ~15 mW (Fig. 6D). These values are far lower than the theoretical value (fig. S14). The experimental conversion efficiency that we obtained in SnS is comparable to the reported efficiency in p-type half-Heusler at the same hot-side temperature (54). Because the S is quite reactive with the contact materials (fig. S15), a diffusion barrier must be developed. A higher experimental efficiency for SnS with low cost and high performance can be expected through future optimizing contact materials. Nevertheless, the great potential of SnS may make it competitive in large-scale applications.

REFERENCES AND NOTES

- C. Uher, Ed., *Materials Aspect of Thermoelectricity* (CRC press, 2017).
- J. Mao et al., *Science* **365**, 495–498 (2019).
- Y. Ravich, B. Efimova, I. Smirnov, *Semiconducting lead chalcogenides*. (Plenum, New York, 1970).
- W. Liu et al., *Phys. Rev. Lett.* **108**, 166601 (2012).
- X. Qian et al., *Energy Environ. Sci.* **12**, 1969–1978 (2019).
- Y. Xiao et al., *Energy Environ. Sci.* **11**, 2486–2495 (2018).
- J. P. Heremans et al., *Science* **321**, 554–557 (2008).

- Q. Zhang et al., *Proc. Natl. Acad. Sci. U.S.A.* **110**, 13261–13266 (2013).
- K. F. Hsu et al., *Science* **303**, 818–821 (2004).
- M. Zhou, J. F. Li, T. Kita, *J. Am. Chem. Soc.* **130**, 4527–4532 (2008).
- K. Biswas et al., *Nat. Chem.* **3**, 160–166 (2011).
- K. Biswas et al., *Nature* **489**, 414–418 (2012).
- X. Su et al., *Adv. Mater.* **29**, 1602013 (2017).
- W. Zhao et al., *Nature* **549**, 247–251 (2017).
- W. Zhao et al., *Nat. Nanotechnol.* **12**, 55–60 (2017).
- L. D. Zhao et al., *Nature* **508**, 373–377 (2014).
- L. D. Zhao et al., *Energy Environ. Sci.* **7**, 2900–2924 (2014).
- M. D. Nielsen, V. Ozolins, J. P. Heremans, *Energy Environ. Sci.* **6**, 570–578 (2013).
- H. Liu et al., *Nat. Mater.* **11**, 422–425 (2012).
- T. Zhu, C. Fu, H. Xie, Y. Liu, X. Zhao, *Adv. Energy Mater.* **5**, 1500588 (2015).
- X. Shi et al., *J. Am. Chem. Soc.* **133**, 7837–7846 (2011).
- L. Xi et al., *J. Am. Chem. Soc.* **140**, 10785–10793 (2018).
- S. K. Plachova, *Phys. Status Solidi, A Appl. Res.* **83**, 349–355 (1984).
- Y. Xiao, L. D. Zhao, *npj Quantum Materials* **3**, 55 (2018).
- J. M. Hodges et al., *J. Am. Chem. Soc.* **140**, 18115–18123 (2018).
- H. Wang, Y. Pei, A. D. LaLonde, G. J. Snyder, *Adv. Mater.* **23**, 1366–1370 (2011).
- L. D. Zhao et al., *J. Am. Chem. Soc.* **134**, 16327–16336 (2012).
- G. Tan et al., *J. Am. Chem. Soc.* **137**, 5100–5112 (2015).
- C. W. Li et al., *Nat. Phys.* **11**, 1063–1069 (2015).
- A. T. Duong et al., *Nat. Commun.* **7**, 13713 (2016).
- L. D. Zhao et al., *Science* **351**, 141–144 (2016).
- K. Peng et al., *Energy Environ. Sci.* **9**, 454–460 (2016).
- L. D. Zhao, C. Chang, G. Tan, M. G. Kanatzidis, *Energy Environ. Sci.* **9**, 3044–3060 (2016).
- K. Kutorasinski, B. Wiendlocha, S. Kaprzyk, J. Tobola, *Phys. Rev. B Condens. Matter Mater. Phys.* **91**, 205201 (2015).
- J. Yang, G. Zhang, G. Yang, C. Wang, Y. X. Wang, *J. Alloys Compd.* **644**, 615–620 (2015).
- C. Chang et al., *Science* **360**, 778–783 (2018).
- Q. Tan et al., *J. Mater. Chem. A Mater. Energy Sustain.* **2**, 17302–17306 (2014).
- W. He et al., *J. Mater. Chem. A Mater. Energy Sustain.* **6**, 10048–10056 (2018).
- H. Wu et al., *Adv. Energy Mater.* **8**, 1800087 (2018).
- Y. Pei et al., *Nature* **473**, 66–69 (2011).
- W. Liu et al., *Energy Environ. Sci.* **9**, 530–539 (2016).
- J. He, T. M. Tritt, *Science* **357**, eaak9997 (2017).
- Y. Xiao et al., *J. Am. Chem. Soc.* **140**, 13097–13102 (2018).
- X. Zhang, L. D. Zhao, *J. Materiomics* **1**, 92–105 (2015).
- G. Tan, L. D. Zhao, M. G. Kanatzidis, *Chem. Rev.* **116**, 12123–12149 (2016).
- J. Callaway, *Phys. Rev.* **113**, 1046–1051 (1959).
- J. Callaway, H. C. von Baeyer, *Phys. Rev.* **120**, 1149–1154 (1960).
- W. Xu, Y. Liu, A. Marcelli, P. P. Shang, W. S. Liu, *Mater. Today Phys.* **6**, 68–82 (2018).
- O. Delaire et al., *Nat. Mater.* **10**, 614–619 (2011).
- H. Wu et al., *Ultramicroscopy* **194**, 182–192 (2018).
- B. Qin et al., *J. Am. Chem. Soc.* **141**, 1141–1149 (2019).
- L. D. Zhao et al., *J. Am. Chem. Soc.* **134**, 7902–7912 (2012).
- D. Rowe, *CRC Handbook of Thermoelectrics: Macro to Nano* (CRC/Taylor and Francis, Boca Raton, FL, 2006).
- C. Fu et al., *Nat. Commun.* **6**, 8144 (2015).

ACKNOWLEDGMENTS

We thank BL14B1 and BL14W1 (Shanghai Synchrotron Radiation Facility) for the SR-XRD and XAFS experiments, and BL21B1 (National Synchrotron Radiation Research Center, Hsinchu, Taiwan) for the ARPES measurements. We thank L. Chen, S. Bai, and X. Xia for help measuring the thermoelectric conversion efficiency based on the two-leg module. **Funding:** This work was supported by The Basic Science Center Project of National Natural Science Foundation of China (grant no. 51788104), National Key Research and Development Program of China (grant nos. 2018YFA0702100 and 2018YFB0703600), National Natural Science Foundation of China (51772012, 51632005, 51571007, 11504159, 11674406, 11875238, 51602143, 51788104, and U1532128), the Beijing Natural Science Foundation (JQ18004), and 111 Project (B17002). H.W. acknowledges financial support from Singapore Ministry of Education Tier 1 research grant for Lee Kuan Yew Postdoctoral Fellow. The work at AIST was supported as part of the International Joint Research Program for Innovative Energy Technology funded by Ministry of Economy, Trade and Industry

(METI), Japan. C.L. is grateful to the Guangdong Innovative and Entrepreneurial Research Team Program (no. 2016ZT06D348) and the Shenzhen Key Laboratory (no. ZDSYS20170303165926217).

Author contributions: W.H. and L.-D.Z. synthesized the samples, designed and carried out the experiments, analyzed the results, and wrote the paper. D.W. and G.W. carried out the DFT calculations. H.W., Y.Z., and S.J.P. carried out STEM measurements. Y.F., Y.-J.H., and C.L. carried out ARPES measurements. J.-F.D. and J.-F.L. carried out the Hall measurements. J.-F.L. provided helpful discussion. R.C. and M.O. performed the thermoelectric conversion efficiency measurements. L.H., D.C., and J.Q. carried out

INS measurements at reactor BER II at Helmholtz-Zentrum Berlin, Germany. X.L. and J.-M.S. carried out INS measurements at instrument Kunpeng in Mianyang research reactor (CMRR), China. D.H. and J.H. conducted microscopy experiments. Y.Z. and W.X. carried out XAFS measurements. C.N. performed neutron radiation measurements. W.H. carried out the high-temperature SR-XRDs and Rietveld refinements. All authors conceived the experiments, analyzed the results, and coedited the manuscript.

Competing interests: The authors declare no competing interests. **Data and materials availability:** All data are in the main text and the supplementary materials.

SUPPLEMENTARY MATERIALS

science.sciencemag.org/content/365/6460/1418/suppl/DC1
Materials and Methods
Figs. S1 to S16
Tables S1 to S6
References (55–81)

5 April 2019; resubmitted 26 April 2019
Accepted 30 August 2019
10.1126/science.aax5123

High thermoelectric performance in low-cost $\text{SnS}_{0.91}\text{Se}_{0.09}$ crystals

Wenke He, Dongyang Wang, Haijun Wu, Yu Xiao, Yang Zhang, Dongsheng He, Yue Feng, Yu-Jie Hao, Jin-Feng Dong, Raju Chetty, Lijie Hao, Dongfeng Chen, Jianfei Qin, Qiang Yang, Xin Li, Jian-Ming Song, Yingcai Zhu, Wei Xu, Changlei Niu, Xin Li, Guangtao Wang, Chang Liu, Michihiro Ohta, Stephen J. Pennycook, Jiaqing He, Jing-Feng Li and Li-Dong Zhao

Science **365** (6460), 1418-1424.
DOI: 10.1126/science.aax5123

Lower-cost thermoelectrics

Thermoelectric materials convert heat to electricity, making them attractive for heat harvesting or cooling applications. However, many high-performance thermoelectrics are made of expensive or toxic materials. He *et al.* found that a material composed of primarily tin and sulfur could be optimized to have relatively good thermoelectric properties. Introducing about 10% selenium to tin sulfide helped tune these properties by electronic band manipulation. This material is a step toward more earth-abundant, less toxic, and lower-cost thermoelectrics than the telluride-based materials currently in use.

Science, this issue p. 1418

ARTICLE TOOLS

<http://science.sciencemag.org/content/365/6460/1418>

SUPPLEMENTARY MATERIALS

<http://science.sciencemag.org/content/suppl/2019/09/25/365.6460.1418.DC1>

REFERENCES

This article cites 75 articles, 7 of which you can access for free
<http://science.sciencemag.org/content/365/6460/1418#BIBL>

PERMISSIONS

<http://www.sciencemag.org/help/reprints-and-permissions>

Use of this article is subject to the [Terms of Service](#)

Science (print ISSN 0036-8075; online ISSN 1095-9203) is published by the American Association for the Advancement of Science, 1200 New York Avenue NW, Washington, DC 20005. The title *Science* is a registered trademark of AAAS.

Copyright © 2019 The Authors, some rights reserved; exclusive licensee American Association for the Advancement of Science. No claim to original U.S. Government Works

证书号第10802502号



实用新型专利证书

实用新型名称：一种新型超高真空多样品转移装置

发明人：王渊；谢卓晋；马小明；郝宇杰；陈朝宇

专利号：ZL 2019 2 1935110.1

专利申请日：2019年11月11日

专利权人：南方科技大学

地址：518055 广东省深圳市南山区西丽学苑大道1088号

授权公告日：2020年06月23日

授权公告号：CN 210823656 U

国家知识产权局依照中华人民共和国专利法经过初步审查，决定授予专利权，颁发实用新型专利证书并在专利登记簿上予以登记。专利权自授权公告之日起生效。专利权期限为十年，自申请日起算。

专利证书记载专利权登记时的法律状况。专利权的转移、质押、无效、终止、恢复和专利权人的姓名或名称、国籍、地址变更等事项记载在专利登记簿上。



局长
申长雨

申长雨



证书号 第10802502号



专利权人应当依照专利法及其实施细则规定缴纳年费。本专利的年费应当在每年11月11日前缴纳。未按照规定缴纳年费的，专利权自应当缴纳年费期满之日起终止。

申请日时本专利记载的申请人、发明人信息如下：

申请人：

南方科技大学

发明人：

王渊；谢卓晋；马小明；郝宇杰；陈朝宇



荣誉证书

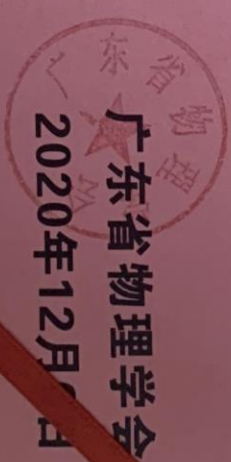
HONORARY CREDENTIAL



郝宇杰同学:

您的论文 “Gapless Surface Dirac Cone in Antiferromagnetic Topological Insulator”
(WuB, 2014)

荣获2020年广东省物理学会年会张贴报告 三 等奖。



荣誉证书

郝宇杰 博士

荣获“2021 第五届全国磁性材料与器件大会”

研究生学术新锐奖

2021 第五届全国磁性材料与器件大会



2021 第五届全国磁性材料与器件大会

5th National Congress of magnetic materials and devices

郝宇杰 博士

经组委会审议，特邀您出席2021年07月16-18日于成都举办的“2021 第五届全国磁性材料与器件大会”，并作 Gapless Surface Dirac Cone in Antiferromagnetic

Topological Insulator MnBi₂Te₄ 专题报告。



欢迎扫码
进入会议交流群



欢迎扫码
登录会议官网

2021 第五届全国磁性材料与器件大会

